Technische Universität München

Fakultät für Chemie

Lehrstuhl I für Technische Chemie

Model Development for
Oxidative Dehydrogenation of Ethane:
Transport Phenomena and Kinetics

Philipp Johannes Donaubauer

Vollständiger Abdruck der von der Fakultät für Chemie der Technischen Universität München zur Erlangung des akademischen Grades eines

Doktor-Ingenieurs (Dr.-Ing.)

genehmigten Dissertation.

Vorsitzender: Prof. Dr. Johannes A. Lercher

Prüfer der Dissertation: 1. Prof. Dr.-Ing. Kai-Olaf Hinrichsen

2. Prof. Dr.-Ing. Harald Klein

3. Prof. Dr. Dr. h.c. Frerich Keil (schriftliche Beurteilung)

Hon.-Prof. Dr. Richard W. Fischer (mündliche Beurteilung)

Die Dissertation wurde am 20.09.2019 bei der Technischen Universität München eingereicht und durch die Fakultät für Chemie am 04.02.2020 angenommen.

*So eine Arbeit wird eigentlich nie fertig, man muß sie für fertig erklären,
wenn man nach Zeit und Umständen das Möglichste getan hat.*
-Johann Wolfgang von Goethe

Danksagung

Diese Dissertation wäre ohne die Hilfe und Unterstützung zahlreicher Personen niemals möglich gewesen. Ihnen allen gebührt mein herzlichster Dank! Die letzten vier Jahre waren voller wissenschaftlicher und anderer Herausforderungen und gleichzeitig geprägt von neuen Eindrücken, einzigartigen Erfahrungen sowie einer Menge Spaß.

Insbesondere möchte ich mich bei Prof. Olaf Hinrichsen für die Aufnahme in seinen Arbeitskreis und das entgegengebrachte Vertrauen bedanken. Darüber hinaus bin ich dankbar für die freien Entfaltungsmöglichkeiten, die allgegenwärtige Unterstützung und die zahlreichen Möglichkeiten meine Ergebnisse in der Fachwelt zu präsentieren. Mein Dank gilt auch den weiteren Mitgliedern der Prüfungskommission: Prof. Johannes Lercher für die inspirierende Zusammenarbeit während des ODH-Projekts und die Übernahme des Prüfungsvorsitzes; Prof. Harald Klein in seiner Funktion als zweiter Prüfer sowie für die Zusammenarbeit während meiner Master's Thesis und der daraus entstandenen Publikation; Prof. Frerich Keil für die Anfertigung des Drittgutachtens und Prof. Richard Fischer für die entsprechende mündliche Beurteilung.

Mein umfassender Dank gebührt auch allen Kollegen und zugleich Freunden am TC1 Lehrstuhl, ohne die diese Aufgabe deutlich schwieriger und die vergangene Zeit um ein Vielfaches langweiliger gewesen wäre. Insbesondere bedanke ich mich bei Sebastian für unzählige Diskussionen über fachliche und andere Dinge; bei meinen Bürokollegen Chris, Daniel, Flo, Johanna, Julia und Thomas für die unvergessliche gemeinsame Zeit in CH36304, den inspirierenden Austausch und den täglichen Wahnsinn; bei Heidi und Thomas für die Unterstützung bei allen großen und kleinen administrativen Problemen sowie den etwas anderen Blick auf manche Dinge; und bei Franz, Franz, Jennie, Matthias, Moritz, My, Stefan und Tabea für die einzigartige Atmosphäre, den kollegialen Zusammenhalt und den familiären Charakter am Lehrstuhl. Besonders hervorzuheben sind die Frühstücks- und Kaffeerunden, diverse Grillabende und allen voran die gemeinsame Zeit auf nationalen und internationalen Konferenzen.

Ein großes Dankeschön gebührt Daniel für die reibungslose Zusammenarbeit im ODH-Projekt und die damit verbundenen zahllosen Stunden in denen er für mich im Labor stand. Das kinetische Modell wäre ohne seine praktischen Fertigkeiten, experimentelle Genauigkeit und Geduld nicht möglich gewesen. Ebenso möchte ich mich auch bei Maricruz, Klaus und Gerhard für die ergiebigen Projekttreffen im Rahmen von MuniCat bedanken.

Während meiner Zeit als Doktorand durfte ich mit einer Vielzahl von Studierenden zusammenarbeiten, die alle zum Gelingen dieser Arbeit beigetragen haben. Vielen Dank an Alvin, Jonas,

Abstract

Oxidative dehydrogenation of ethane is a promising alternative to the classical production route to ethene via steam cracking, which is a highly unselective and energy-intensive process. Main challenges for potential industrial applications are the formulation of a suitable catalytic material and the associated integrated design of the chemical process. For the latter, a reliable multi-scale description of transport phenomena as well as an adequate kinetic model are inevitable. This thesis focuses on model development with a view to an accurate description of dominant transport processes relevant for the selective production of ethene via oxidative dehydrogenation of ethane.

The basis of model development in chemical reaction engineering consists of a comprehensive analysis of the respective chemical transformation, culminating in a mathematical description of desired accuracy and reliability. This includes deliberate handling of species, mass, heat and momentum transport equations and their mutual interplay. In this work, special focus is given to multicomponent transport phenomena in porous media superimposed with heterogeneously catalyzed reactions. Moreover, the coupling of fluid flow and chemical reactions in fixed-bed reactions is re-evaluated. Finally, a kinetic description of ethane conversion over $MoVTeNbO_x$ M1 phase complements the integral reactor design.

Transport process inside porous catalysts are frequently described by means of multicomponent diffusion models, combining Maxwell-Stefan with Knudsen diffusion and viscous Darcy flow. Here, the well-established dusty-gas model competes with several alternatives, e.g. the mean-transport pore model and the binary friction model. It is shown, that these diffusion models result in very similar behavior when applied to three different heterogeneously catalyzed reactions. A global, Monte-Carlo-based sensitivity analysis of overall effectiveness factors is used to investigate the impact of the above mentioned diffusion models in comparison to uncertainties in catalyst properties. At equal uncertainty levels, highest sensitivity was observed for the pellet porosity. In general, the choice of the diffusion model appears to become negligible for transport properties having minimal degree of uncertainty. Finally, the binary friction model proved as most reliable, due to inconsistencies in the treatment of the viscous flux terms by the other two approaches. These conclusions can be adapted to any reaction-diffusion problem occurring in porous media. Furthermore, the applied global sensitivity method can be recommended as a robust tool for analyses of nonlinear models.

When applied to industrial scale problems, the effectiveness factor of particles is a crucial parameter to evaluate transport limitations occurring inside the catalytic material. For this purpose, a variety of catalyst shapes are proposed to overcome transport problems. Hence, a

rigorous description of multicomponent diffusion-reaction problems in complex geometries is of high relevance. For the first time, the binary friction model is solved in three dimensional catalyst pellets using an analytical solution of the implicit flux relations. It is found, that the interplay of reaction and diffusion significantly depends on the volume-to-surface ratio and the curvature of the bodies. In order to allow efficient coupling to reactor models, a one-dimensional approximation method is adopted, which robustly describes the investigated multicomponent systems. Overall, these findings contribute to an integral description of reaction-diffusion phenomena in mesoporous catalytic materials.

Regarding the design and optimization of fixed-bed reactors for heterogeneously catalyzed reactions, continuum models persist as highly established strategy. However, accurate description of the convective and dispersive transport together with appropriate assumptions on the bed configuration are the core of a reliable design. A pseudo-homogeneous continuum model, fully accounting for 2D fluid flow, heat and species dispersion in axial and radial direction, is applied to different configurations of packed beds. Here, application of two discretization techniques for fluid flow as well as heat and species transport allow a robust solution. By taking void inlet regions into account, conventional artificial boundary conditions become obsolete and the evolution of fluid flow in front of the bed is observable. Moreover, beds of ideal spheres exhibited deviating behavior due to oscillations in the radial porosity profile. By investigating variable reaction stoichiometries, the effect of changes in fluid density and superficial velocity highlight the importance of an adequate description of the interplay between fluid flow and chemical reaction in fixed-bed reactors.

Finally, an intrinsic kinetic model for oxidative dehydrogenation of ethane over the M1 phase of $MoVTeNbO_x$ is developed. It gives insights to the formation of ethene and the side products acetic acid, carbon monoxide and carbon dioxide. The reaction scheme is based on two different oxygen sites, assuming seven irreversible surface reactions. Here, carbon-hydrogen bond cleavage is attributed to lattice oxygen sites, while the formation of carbon-oxygen bonds is proposed to exclusively happen with the use of electrophilic surface oxygen. Decarboxylation of surface acetate species is capable to fully describe carbon dioxide production, whereas ethene decomposes to carbon monoxide only. The strong impact of the initial carbon-hydrogen cleavage on the production of ethene is established by local sensitivity analyses. Moreover, at oxygen-lean conditions, regeneration of lattice oxygen sites is found to become rate-determining.

Contents

Contents

1 Introduction

1.1 Motivation and Background

1.1.1 Ethene Production: Status and Perspective

Ethene is ranked as the most important hydrocarbon base chemical with an annual worldwide production of 120 Mt/a in 2008 [1] and increased production capacities of 160 Mt/a in 2016 [2]. The scheme in Figure 1.1 depicts major intermediates and chemicals produced with ethene as base chemical.
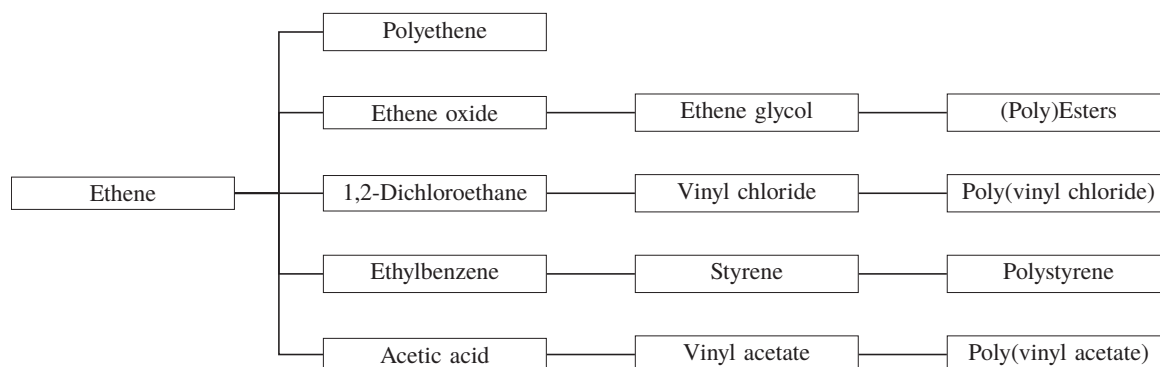
Figure 1.1: Overview of major petrochemical products from ethene processing. Scheme adapted from Moulijn et al. [3].

Up to 60 % of the ethene available is consumed in the production of low- and high-density polyethene [3]. Other prevalent secondary products are ethene oxide, 1,2-dichloroethane, ethylbenzene and acetic acid [3], all of them being key intermediates for the production of polymers.

Moreover, the demand for light olefins continuously increased over the past decades and will continue to rise, which requires enhanced production capacities in the near future [4]. In addition, accelerated shale gas development in the United States leads to unused ethane surpluses at remote destinations [5]. However, extensive fracking has severe environmental impacts [6] and, hence, undoubtedly is a debatable technology.

Conventionally, ethene is mainly produced through pyrolytic processes, like steam and catalytic cracking of ethane and naphtha [3]. Major drawbacks of these routes are the high energy demand with accompanying emissions, limited ethene selectivities and coke formation [7, 8]. An established alternative is the dehydration of ethanol obtained by fermentation [1, 3].

1

From an economical and ecological point of view, the selective production of olefins from abundant alkanes in medium-scale units can become a key part of future supply chains [4]. A perspective route towards a selective and environmentally more acceptable production of ethene is through oxidative dehydrogenation of ethane (ODHE) [9]

$$C_2H_6 + \frac{1}{2} O_2 \longrightarrow C_2H_4 + H_2O, \qquad \Delta_r H^{\circ}_{25\,^{\circ}C} = -105 \frac{kJ}{mol}.$$

Similar to other selective oxidation reactions, ODHE is premised on thermodynamic advantages arising from the exothermic character of the reaction. Due to possible thermal runaway through total oxidation, a prospective ODHE process demands sophisticated control of the reaction and, hence, thorough overall process design. Amongst others, this includes:

- a sufficiently active, highly selective and stable catalyst;

- a balanced reactor concept, based on:

    - particle design,

    - integral optimization of transport processes,

    - sufficient cooling or heating;

- comprehensive process safety analyses;

- and an economic basis.

Such integrated design requirements presuppose key disciplines of chemical reaction engineering on multiple scales.

1.1.2 Multi-Scale Design of Chemical Processes

Modeling of chemical processes based on heterogeneously catalyzed reactions is an inherently multidimensional task. While elementary steps and catalytic cycles occur on a molecular scale within a split second, a chemical plant easily captures the size of a football pitch and is designed to operate over multiple years, up to decades.

Figure 1.2 sketches the interplay of time and length scales related to selected disciplines of chemical reaction engineering. Microscopic description of the catalyst structure, elementary steps and molecular transport are core targets of quantum mechanic and molecular dynamic studies [11, 12]. Ideally, resolution of chemical reactions and transport phenomena down to the molecular level over the full scale would yield an exact description of the integral process. However, despite tremendously increased computational power over the last decades, a full-scale model remains infeasible due to the extreme spacial and temporal ranges. Hence, multiscale
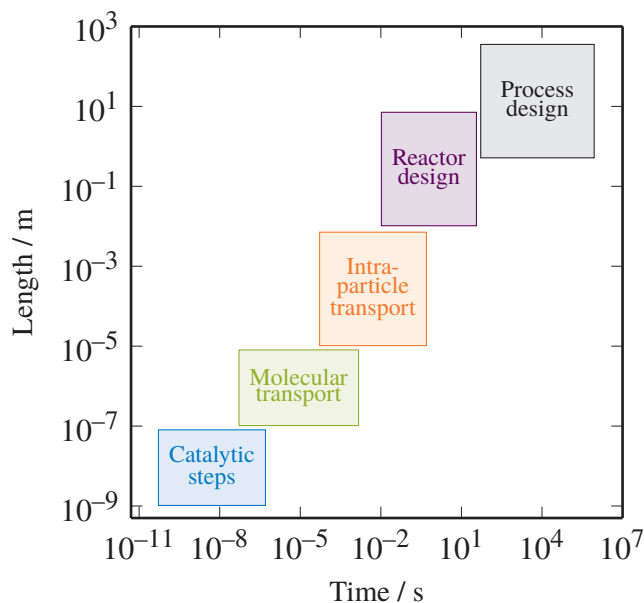
Figure 1.2: Length and time scales of a heterogeneously catalyzed process. Representation compiled from [3, 10–12].

modeling requires strategies to adequately link the different scale domains, allowing an integrated design [12].

Frequently, the nature and density of active sites as well as detailed reaction mechanisms are not fully unraveled. Hence, it is convenient to apply so-called mean-field approximations, which are based on an averaged activity assuming homogeneous and independent surface coverages [13]. This allows development of intrinsic kinetic models obtained from catalytic measurements. Other transport effects, like diffusion phenomena inside the porous structure of the catalyst particle, heat and mass transfer at the fluid-solid interface as well as mixing and transport inside of the reactor, have to be decoupled from a kinetic description to enable reliable scale-up.

For fixed-bed reactors, meso- and macroscopic models for these transport phenomena are well-established on a semi-empirical basis. Fluid and solid phases inside porous particles are commonly described using one pseudo-homogeneous continuum phase. Transport through the packed-bed structure can either be described by the same concept of continuous phases [14], or by using a discrete particle approach resolving void and solid regions of the reactor [15]. While the latter strategy was in the focus of research during the last years, continuum models will persist in the design of fixed-bed reactors due to computational benefits [16].

Besides the regions depicted in Figure 1.2, changes of the catalytic material, like surface restructuring, phase segregation, recrystallization and sintering can pose requirements and constraints for an overall process design on multidimensional time scales [10–12].

1.1.3 Oxidative Dehydrogenation of Ethane: Catalysts and Reactors

Oxidative dehydrogenation of ethane presents an attractive alternative for a selective and sustainable production of ethene [8, 9, 17, 18]. Since dissociation energy of the weakest C–H bond in the product ethene exceeds the corresponding value of the reactant ethane, selectivities towards ethene can reach high values [19].

Over the past decades different catalytic systems for ODHE have been investigated, e.g. [9, 20]:

- nickel oxide-based systems [21, 22];

- materials using alkali metals [23, 24];

- materials based on boron [25–27].

- (supported) transition metal oxides:

    – vanadia [28–30],

    – molybdenum oxide [31, 32],

    – rare earth metal oxides [33],

    – mixed metal oxides forms [34–36].

One of the most promising materials is the M1 phase of a mixed metal oxide composed of molybdenum, vanadium, niobium and tellurium [37, 38].

For selective oxidation reactions, an integral reactor concept imposes requirements and constraints on the functionality and shape of the catalyst particles and vice versa. In fixed-bed reactors, particle design can be optimized with regard to pressure drop, overall lifetime, conversion behavior, or hot-spot formation. Here, size and shape of the pellets, catalyst loading and distribution, pore-structure and bed layering represent adjustable parameters. For moving or fluidized beds, properties like fluidization behavior and resistance to mechanical attrition become essential and have to be considered.

For ODHE, a variety of reactor types and concepts have been reported in literature. In general, these approaches resemble strategies proposed for other selective oxidation reactions, like the production of ethylene oxide [39], or maleic anhydride [40] and phthalic anhydride [41]. The key challenge is to control the reaction by suppression of total oxidation and effective removal of the heat of reaction. This tasks are tackled by various approaches.

The concentration and nature of the oxidant define the overall process, which leads to a distinction between oxygen- and air-based concepts. The former uses an undiluted oxidant, which allows compact reactor design and reduces purification cost, but requires an air separation unit for the provision of oxygen and results in an increased effort for safety precautions. The latter uses nitrogen as co-feed, which inherently reduces risks of flammability and facilitates

reaction control, but at the same time increases the required reactor volume and expenses for purification [42].

As indicated above, effective cooling is a key task for selective oxidation reactions. Polytropic multitubular fixed-bed reactors are characterized by an effective lateral heat removal and a sophisticated temperature control using circulating thermal fluids or molten salts in the reactor jacket [43]. To reach adequate conversion levels in selective oxidation reactions, the design of these reactors requires either high inlet concentration of the reactants or substantial recycle of unreacted feed. The former configuration, however, imposes large chemical potentials at the reactor inlet, which are sensitive to fluctuations in feed or temperature and, hence, can lead to thermal runaway of the reactor.

Several theoretical studies on industrial scale ODHE in multitubular fixed-bed reactors have been published over the last 15 years [44–47]. For example, López et al. [44] emphasized the need of effective cooling and temperature control as well as the danger of too high oxygen partial pressures. Using a transient study, Che-Galicia et al. [46] stressed the importance of a sophisticated reactor model, which covers hydrodynamic effects inside reactors operated with low tube-to-particle ratio. Furthermore, ethane inlet partial pressure and coolant temperature were determined as important parameters influencing the reactor performance [46, 47].

Besides feed dilution, staged feeding of oxidant is an alternative design option. Here, two basic strategies are available: on the one hand, multiple adiabatic beds in series with interstage feeding of oxidant and simultaneous quenching (if desired with product water removal); on the other hand, continuous feeding of oxidant along the reactor axis by membrane technology. While the former approach represents a widely industrialized concept, e.g. for the production of sulfuric acid in adiabatic beds [3], membrane technology has not yet been industrialized for large-scale applications in heterogeneously catalyzed systems [48].

For oxidative dehydrogenation of ethane, López et al. [44] stressed the advantage of low oxygen partial pressures and higher ethene selectivity of a two-bed multitubular reactor compared to a single-bed design. This concept was extended up to a five-stage design by Fattahi et al. [45], who additionally highlighted the improved reactor stability in terms of thermal runaway. Recently, Fazlinezhad et al. [49] used a design of up to 20 beds with interstage water removal for ODHE over MoVTeNbO$_x$ catalysts, yielding advanced temperature control and enhanced ethene selectivities compared to single-pass operation.

Due to the defined distribution of oxygen, without the increased piping expenses arising for multi-bed designs, membrane technology is considered as a promising option for future reactor concepts in selective oxidation reactions [50]. Lab-scale experiments for ODHE in membrane reactors have already been performed in the 1990s, e.g. by Gobina and Hughes [51] and Coronas et al. [52]. Hamel et al. [53] performed pilot-scale experiments for single- and multi-stage packed-bed membrane reactors (PBMR). They achieved significantly higher selectivities compared to a conventional fixed-bed reactor and backed their experimental findings by a modeling study. Rodríguez et al. [42] theoretically evaluated an industrial-scale multitubular

PBMR with one-[42] and two-dimensional models [54], achieving high ethene selectivities at elevated ethane conversions and mild temperature profiles. However, the authors stressed the danger arising from possible mechanical failure of membrane tubes and the accompanied formation of explosive mixtures [42].

A further alternative reactor concept is the use of fluidized-bed reactors. Advantages over fixed-bed reactors are the possibility of continuous regeneration of catalyst and the uniform temperature inside of the reactor. This is contrasted with reduced selectivities due to pronounced backmixing and challenging scale-up [55, 56]. For ODHE, de Lasa and co-workers [57, 58] used a lab-scale fluidized-bed reactor for kinetic investigations. Rischard et al. [59] investigated a two-zone fluidized-bed reactor for the oxidative dehydrogenation of n-butane. Popov and coworkers reported the impact of reaction temperature and contact time for ODHE over supported mixed metal oxide catalysts in a riser reactor [60, 61].

In addition, reactor types based on short contact times, similar to a riser setup, have been proposed in the past for ODHE [9]. Metallic catalyst on structured supports allowed autothermal operation [62] and improved heat integration [63] at minimal pressure drop. Moreover, Brussino et al. [64] successfully coated cordierite monoliths with NiCe/γ-Al$_2$O$_3$ demonstrating the effect of catalyst loading on the overall ethene yield.

Integrated designs, combining two or more of the above-mentioned reactor types, allow additional flexibility and potential for optimization. Membrane-assisted fluidized beds could be a potential approach for oxidative dehydrogenation reactions [65]. Alternatively, classic fixed-bed reactors can be combined with membranes or monoliths in a staged design.

Depending on the proposed reactor design, different requirements for the catalyst material arise. While for fixed-bed applications size and shape are crucial design parameters and fluidized systems require sufficient mechanical stability, monolithic reactors apply the active phases in form of washcoats to minimize pressure losses. In addition, overall transport phenomena are inherently dependent on the kinetics of the ODHE reaction, as well as on the geometry of the active phase and the reactor type. Furthermore, fluid flow and accompanied dispersive transport phenomena are linked by a mutual interplay with transport properties of all phases involved.

1.2 Objectives

The main objective of this thesis is a model-based analysis of the multi-scale transport phenomena arising in the oxidative dehydrogenation of ethane over a MoVTeNbO$_x$ catalyst. This selective oxidation reaction represents a promising perspective production route for ethene as one of the major bulk products in chemical industry.

Modeling of this heterogeneously-catalyzed and highly exothermic system comprise open challenges in chemical reaction engineering. The presence of a gaseous multicomponent system touches fields of research in the description of diffusive transport phenomena inside porous media. Moreover, a reliable fixed-bed reactor design requires consistent and extensive description of hydrodynamics and dispersive transport. Finally, a reliable kinetic description of the ethane conversion and (side) product formation is the linchpin of accurate multi-scale design. The thesis is divided into following parts, including the secluded Chapters 3 to 6 based on independent studies, containing individual introductions and theoretical backgrounds.

Chapter 2 introduces the physical background of transport phenomena based on non-equilibrium thermodynamics. An overview of relevant transport processes is the basis for a detailed description of multicomponent diffusion and its differences to other approaches. Furthermore, the concept of dispersion is briefly presented and put into this context.

Chapter 3 presents a global sensitivity analysis of different multicomponent diffusion models inside porous catalyst pellets. Here, the uncertainty in the estimation of transport parameter is compared to three concepts using an elaborated statistical method. Application to different example reactions and conditions yield a universal recommendation on the future use of multicomponent diffusion models in heterogeneous catalysis. This chapter was published in similar form as P. J. Donaubauer, O. Hinrichsen, "A Monte-Carlo-Based Sensitivity Analysis of Multicomponent Diffusion in Porous Catalysts", *Chem. Eng. Sci.* **2018**, *185*, 282–291, DOI 10.1016/j.ces.2018.03.048.

Chapter 4 deals with the numerically challenging problem of an adequate description of multicomponent transport in three-dimensional catalyst pellets. A Maxwell-Stefan-based model is compared to classic Fickian representation of intraparticle diffusion for nine different catalyst geometries. The resulting conclusions are used to adapt a mapping method for a robust approximation of these complex structures with a straightforward one-dimensional approach. This chapter was published in similar form as P. J. Donaubauer, O. Hinrichsen, "Evaluation of Effectiveness Factors for Multicomponent

Diffusion Models inside 3D Catalyst Shapes", *Ind. Eng. Chem. Res.* **2019**, *58*, 110–119, DOI 10.1021/acs.iecr.8b04922.

Chapter 5 addresses the interplay of fluid flow and chemical reaction in classical two-dimensional fixed-bed reactor models. A novel numerical scheme is presented to efficiently solve and couple this two parts. By investigating the impact of radial porosity profiles on the reactor performance, the study emphasizes the necessity of an adequate handling of fluid flow phenomena in chemical reactor design. This chapter was published in similar form as P. J. Donaubauer, L. Schmalhorst, O. Hinrichsen, "2D Flow Fields in Fixed-Bed Reactor Design: a Robust Methodology for Continuum Models", *Chem. Eng. Sci.* **2019**, *208*, 115137, DOI 10.1016/j.ces.2019.07.055.

Chapter 6 covers an intrinsic kinetic study on the oxidative dehydrogenation of ethane over the M1 phase of MoVTeNb mixed metal oxides. Role and functionality of two different oxygen species are discriminated, resulting in a novel approach for describing selective oxidation reactions. Seven surface reactions allow to adequately represent the kinetic transformation into ethene as well as the side products acetic acid, carbon monoxide and carbon dioxide. Finally, local sensitivity analyses reveal the degree of rate control of each individual kinetic parameter on the overall ethene formation. This chapter was submitted in similar form as P. J. Donaubauer, D. Melzer, K. Wanninger, G. Mestl, M. Sanchez-Sanchez, J. A. Lercher, O. Hinrichsen, "Intrinsic Kinetic Model for Oxidative Dehydrogenation of Ethane over MoVTeNb Mixed Metal Oxides: a Mechanistic Approach", *Chem. Eng. J.* **2020**, *383*, 123195, DOI 10.1016/j.cej.2019.123195.

Chapter 7 summarizes the obtained findings and classifies them with regards to an integrated multi-scale fixed-bed reactor design for oxidative dehydrogenation of ethane. Furthermore, the perspective applications of the developed methods are outlined, by adapting the findings of this work in a pilot-scale reactor design.

2 Theoretical Background

Besides adequate intrinsic kinetic models, description and design of chemical reactors inherently rely on an adequate formulation of relevant transport phenomena. From a general perspective, every form of transport originates from an irreversible process described via principles of non-equilibrium thermodynamics. In Section 2.1, this principle is introduced following the representation of de Groot and Mazur [66]. Subsequently, a brief introduction to multicomponent mass and heat transport with focus on fixed-bed tubular reactors is given in Sections 2.2 and 2.3, respectively.

2.1 Non-Equilibrium Thermodynamics

Elementary transport processes, like momentum exchange, thermal conduction, molecular diffusion, or electric conduction, arise in systems, which are in a non-equilibrium state. All fluxes $\widetilde{J}_j$ emerging from this state are irreversible and cause production of entropy. The overall rate of this entropy production σ_S can be regarded as linear combination of the corresponding fluxes

$$\sigma_S = \sum_j \widetilde{J}_j \delta_j, \tag{2.1}$$

where δ_j represents respective thermodynamic forces [67]. From the linear system in Equation (2.1), the fluxes $\widetilde{J}_j$ can be expressed through

$$\widetilde{J}_j = \sum_k L_{jk} \delta_k \tag{2.2}$$

using phenomenological coefficients L_{jk} [66]. Here, $\widetilde{J}_j$ can for example represent: individual molar (or mass) fluxes $\widetilde{J}_i$, the heat flux $\widetilde{J}_q$, or the electric current density $\widetilde{J}_e$. Thermodynamic driving forces δ_k are chosen to decouple individual phenomena and, hence, enable a derivation of the phenomenological coefficients L_{jk}.

Table 2.1 gives an overview of selected driving forces and the resulting transport phenomena. Diagonal entries cover intuitive processes, e.g.: electric current (density) as a result of differences in the electric potential ϕ (Ohm's law), a temperature gradient leading to thermal conduction (Fourier's law), or diffusion as a molar flux arsing from gradients of the chemical potential μ at

Table 2.1: Phenomenological representation of driving forces and corresponding transport processes in non-equilibrium thermodynamics. Compilation freely adapted from de Groot and Mazur [66].

		Thermodynamic force δ_j		
		$\frac{1}{T}\nabla_{p,T}\mu$	$\frac{1}{T^2}\nabla T$	$\frac{1}{T}\nabla\phi$
Flux $\widetilde{J_j}$	$\widetilde{J_i}$	Diffusion[a] (Fick's law)	Soret effect	Electrochem. diffusion
	$\widetilde{J_q}$	Dufour effect	Thermal conduction (Fourier's law)	Peltier effect
	$\widetilde{J_e}$	–	Seebeck effect	Electricity (Ohm's law)

[a]Diffusion in itself represents interdependent transport processes for non-equilibrated multicomponent mixtures.

isobaric and isothermal conditions (Fick's law). The latter provides the basis of multicomponent transport and will be introduced in detail in Section 2.2.1.

Moreover, any thermodynamic driving force can lead to other interactions. Well-known are, for example, the Peltier effect, which describes cooling or heating through electric potentials, or its reversal, the Seebeck effect, as the basis of photovoltaic applications. One key feature of such cross-phenomena is their reciprocity

$$L_{jk} = L_{kj}, \tag{2.3}$$

which was established by Onsager [67, 68]. Equation (2.3) directly implies that a mathematical representation of Table 2.1 yields a symmetric matrix. Hence, coefficients L_{jk} describing the Soret and Dufour effect or, respectively, the Peltier and Seebeck effect are identical. Furthermore, when applied to multicomponent mass transport, Equation (2.3) allows an adequate description of diffusive transport phenomena (cf. Section 2.2.1.3).

In addition to the compilation in Table 2.1, viscous, magnetic, or other body forces contribute to the individual fluxes $\widetilde{J_j}$. The Navier-Stokes equations represent one example for the interaction of different internal and external driving forces, resulting in an overall fluid transport. Another effect arising from external forces is piezoelectricity, which describes separation of charge inside certain solids caused by applied mechanical stress.

Modeling of transport phenomena in chemical reaction engineering comprises an adequate choice of relevant transport phenomena, determination of respective transport parameters (here L_{jk}) and solution of the resulting mass, component, energy and momentum balances.

2.2 Mass Transport

As introduced in the previous section, transport processes originate from a variety of driving forces. For chemical reaction engineering, transport of reactive species, superimposed by chemical reactions, represents the predominant pathway of interest. In the following, the theoretical background of molecular diffusion and dispersive transport are introduced in concise form for mixtures of ideal gases.

2.2.1 Molecular Diffusion

The driving force δ_i for molecular diffusion of a species i is based on its gradient of the chemical potential μ_i (cf. Equation (A.12)), expressed as

$$\delta_i = \frac{y_i}{\mathcal{R}T} \, \nabla_{p,T}\mu_i \tag{2.4}$$

at isobaric and isothermal conditions [69], with the respective mole fraction y_i, the ideal gas constant $\mathcal{R}$ and the temperature T. For an ideal mixture of ideal gases (cf. Appendix A), Equation (2.4) simplifies to

$$\delta_i = \frac{1}{p}\nabla p_i. \tag{2.5}$$

An alternative representation of Equation (2.4) describes non-ideal behavior of the multicomponent mixture by binary thermodynamic factors Γ_{ij}:

$$\delta_i = \sum_{j=1}^{n_{\text{species}}-1} \Gamma_{ij}\nabla y_i. \tag{2.6}$$

The coefficients Γ_{ij} are calculated using the dependency of activity, or fugacity coefficients, on the mixture composition, which can be obtained from an adequate equation-of-state [69].

Moreover, for systems of n_{species} species with constant temperature T and pressure p the Gibbs-Duhem relation [70] can be expressed

$$\sum_{i=1}^{n_{\text{species}}} y_i\mathrm{d}\mu_i = \sum_i \delta_i = 0, \tag{2.7}$$

allowing only $n_{\text{species}} - 1$ driving forces to be independent [69].

2.2.1.1 Maxwell-Stefan Relations

In the late 19th century, Maxwell [71] and Stefan [72] derived a model for the description of diffusive transport based on molecular collisions and accompanied momentum exchange between several species of different kind. This theory can be generalized to allow a universal description of multicomponent mass transport.

In the following, the basic principles of Maxwell-Stefan diffusion are introduced based on the concepts and representation in the monograph of Taylor and Krishna [69]. Applying momentum conservation, a collision between two different kinds (1 and 2) of molecules having a mass of m_1 and m_2, respectively, can be described by the change of momentum

$$\Delta P = m_1 \left(u_1 - u_1' \right) = m_2 \left(u_2 - u_2' \right), \tag{2.8}$$

where u_i and u_i' represent the velocities of the molecules before and after the collision, respectively. The latter can be calculated using the system's center of mass [72], which yields

$$\Delta P = \frac{m_1 m_2 \left(u_1 - u_2 \right)}{m_1 + m_2}. \tag{2.9}$$

Based on the considerations above, a force balance on a differential control volume allows to quantify the impact of these molecular collisions on molecules of type '1'. Hence, the internal rate of change of momentum has to be proportional to the average amount of momentum exchange of one collision ($u_1 - u_2$) and the frequency of collisions between molecules of type '1' and '2' inside the control volume ($y_1 y_2$) [69]. This is balanced by the external surface forces acting on the control volume. If shear stresses, body forces and velocity gradients are neglected, the gradient of the respective partial pressure yields [69]

$$-\nabla p_1 \propto y_1 y_2 \left(u_1 - u_2 \right). \tag{2.10}$$

Using the Maxwell-Stefan Diffusion coefficient $Ð_{12}$ as 'drag-like' proportionality constant, Equation (2.10) becomes

$$\frac{1}{p} \nabla p_1 = -\frac{y_1 y_2 \left(u_1 - u_2 \right)}{Ð_{12}}. \tag{2.11}$$

The left hand side of Equation (2.11) is equivalent to the external driving force δ_i of an ideal system for molecular diffusion, introduced in Equation (2.5). Extending this principle to n_{species} species results in [69]

$$\delta_i = -\sum_{i=1}^{n_{\text{species}}} \frac{y_i y_j \left(u_i - u_j \right)}{Ð_{ij}}. \tag{2.12}$$

Finally, the species velocities are replaced by diffusive fluxes

$$J_i = y_i c_t u_i \tag{2.13}$$

using the total molar concentration c_t. Hence, combining Equations (2.12) and (2.13) yield the general representation for Maxwell-Stefan diffusion

$$\delta_i = \sum_{j=1}^{n_{\text{species}}} \frac{y_i J_j - y_j J_i}{c_t D_{ij}}. \tag{2.14}$$

If the transport process is of purely diffusive nature, Equation (2.7) holds, which leads to an inevitable conservation of the diffusive fluxes

$$\sum_{i=1}^{n_{\text{species}}} J_i = 0. \tag{2.15}$$

By rearranging Equation (2.14), the diffusive fluxes J_i can be expressed through a linear system of the size $n_{\text{species}} - 1$ [69]

$$\vec{J} = -c_t [B]^{-1} \vec{\delta} \tag{2.16}$$

with the coefficients of matrix $[B]$ defined as

$$\begin{aligned}
B_{ii} &= \frac{y_i}{D_{in_{\text{species}}}} + \sum_{\substack{k=1 \\ k \neq i}}^{n_{\text{species}}} \frac{y_k}{D_{ik}} \qquad i = 1, \ldots, n_{\text{species}} - 1, \\
B_{ij} &= -y_i \left(\frac{1}{D_{ij}} - \frac{1}{D_{in_{\text{species}}}} \right) \quad i, j = 1, \ldots, n_{\text{species}} - 1.
\end{aligned} \tag{2.17}$$

Inserting the driving forces δ_i given in Equation (2.6) in matrix representation Equation (2.16) leads to

$$\vec{J} = -c_t [B]^{-1} [\Gamma] \nabla \vec{y}. \tag{2.18}$$

For ideal mixtures of ideal gases, the thermodynamic matrix $[\Gamma]$ reduces to the identity matrix.

Using this representation of multicomponent mass transport, it can be shown that for ideal gases the binary diffusion coefficients D_{ij} are [69]

- independent of composition: $D_{ij} \neq f\left(y_1, \ldots, y_{n_{\text{species}}}\right)$,

- non-negative: $D_{ij} \geq 0$,

- and symmetric: $D_{ij} = D_{ji}$.

The latter property is equivalent to Onsager's reciprocal relation (2.3). For ideal gases the semi-empirical relation of Fuller et al. [73] is frequently applied to calculate binary diffusion coefficients $Đ_{ij}$ and their dependency on pressure and temperature (cf. Appendix A.4).

In addition to the gradient of the chemical potential at isobaric and isothermal conditions (2.4), a multitude of other driving forces δ_i can affect multicomponent diffusion. At mechanical equilibrium, which establishes significantly faster compared to chemical equilibrium [69], gradients of the total pressure, temperature, and electrical potential as well as centrifugal and magnetic forces can have an impact on the molar flux (cf. Table 2.1). If, however, any of these additional driving forces is present, mass transport is no longer purely diffusive and molar fluxes N_i have to be used instead of diffusive fluxes J_i. This follows from the fact that the conditions for the Gibbs-Duhem relation are no longer fulfilled. Hence, Equation (2.15) is not valid for molar fluxes N_i and, moreover, Equations (2.14) and (2.16) become linear systems of the size n_{species}.

2.2.1.2 Fick's Law of Diffusion

Fick [74] concluded from experimental analyses, that for a binary system the diffusive flux J_1 is proportional to the gradient of its partial concentration

$$J_1 \propto \nabla c_1, \tag{2.19}$$

which yields a well-established form of Fick's law

$$J_1 = -c_\text{t} D_{12} \nabla y_1. \tag{2.20}$$

For binary systems, Fick's law is identical to the Maxwell-Stefan relation in Equation (2.14), leading to $D_{12} = Đ_{12}$. However, for systems composed of more than two components Equation (2.20) becomes [69]

$$J_i = -c_\text{t} \sum_{k=1}^{n_{\text{species}}-1} D_{ik} \nabla y_k. \tag{2.21}$$

In this generalized form, Fickian diffusion coefficients D_{ij} are dependent on composition and not necessarily symmetric $D_{ij} \neq D_{ji}$, or can have negative values [69].

A convenient approximation of Fickian diffusion behavior based on an average molecular diffusion coefficient $D_{i,\text{m}}$ was proposed by Fairbanks and Wilke [75]

$$J_i = -c_\text{t} D_{i,\text{m}} \nabla y_i. \tag{2.22}$$

Here, the coefficient $D_{i,\text{m}}$ is derived from the respective values of the binary Maxwell-Stefan diffusion coefficients $Đ_{ij}$ and the composition of the multicomponent mixture (cf. Appendix A.4).

Furthermore, by this simplification the diffusive flux J_i is assumed to be dependent on the gradient of the corresponding mole fraction ∇y_i only.

Equation (2.22) is frequently used as basis for simplifications in the description mass transfer phenomena. For example, in the concept of species dispersion (cf. Section 2.2.3) the average molecular diffusion coefficient is replaced by a dispersion parameter $\mathcal{D}_i$, yielding

$$J_i = \mathcal{D}_i \nabla c_i. \tag{2.23}$$

Another example is two-film theory. Here, interphase mass transport is described by mass transfer coefficients β_i, assuming constant gradients within the boundary layer of a thickness δ

$$J_i = D_{i,\mathrm{m}} \frac{\Delta c_i}{\delta} = \beta_i \Delta c_i. \tag{2.24}$$

In both cases, any interaction between the molar flux J_i and concentration gradients of other components within the multicomponent mixture is neglected.

2.2.1.3 Interaction Effects

To emphasize the importance of a correct representation of multicomponent transport, Figure 2.1 illustrates possible diffusion phenomena of a general multicomponent system.
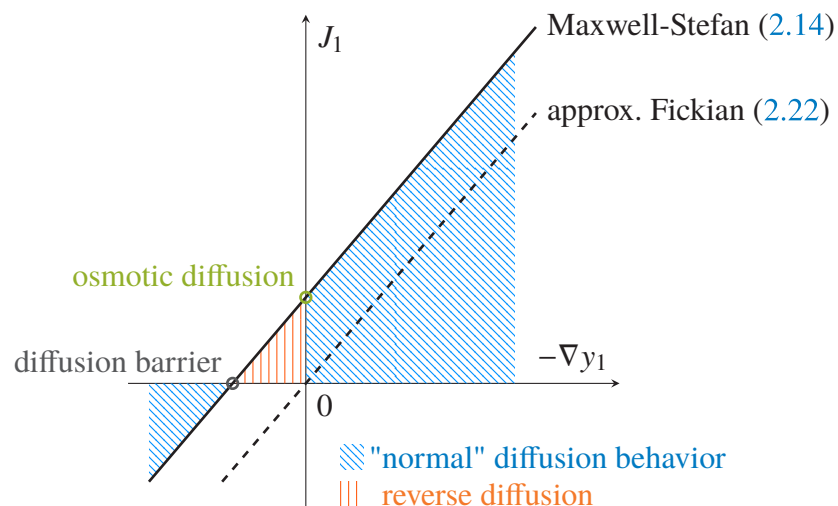
Figure 2.1: Exemplary dependency of diffusion flux J_1 on composition gradient ∇y_1 for a system with three or more species illustrating phenomenological regions. Representation adapted from Taylor and Krishna [69].

The approximation of Equation (2.22) for Fickian fluxes can describe multicomponent systems exclusively by a proportionality to the respective composition gradient. However, several prominent effects, such as osmotic or reverse diffusion as well as a diffusion barrier, demand an elaborate description of the transport phenomena. Moreover, already for simple ternary

gaseous mixtures Maxwell-Stefan-theory was found to be essential for a correct description of the diffusion behavior (e.g. H_2/CO_2/N_2 [76]).

2.2.2 Molar Flux

The molar flux N_i of a species i is defined by the product of its concentration c_i and velocity u_i [69]:

$$N_i = c_i u_i. \tag{2.25}$$

Hence, for a multicomponent mixture the total molar flux is given to

$$N_t = \sum_{i=1}^{n_{species}} N_i = \sum_{i=1}^{n_{species}} c_i u_i = c_{tot} \sum_{i=1}^{n_{species}} y_i u_i = c_{tot} u^*. \tag{2.26}$$

Here, the molar average velocity u^* represents a fictive velocity, which accounts for the net molar movement of the mixture having a molar concentration c_{tot} [69]. The deviation of the species velocity from the molar average velocity u^* describes the diffusive fluxes

$$J_i = c_i \left(u_i - u^* \right) \tag{2.27}$$

introduced in Section 2.2.1.

Finally, individual molar fluxes N_i (2.25) can be expressed by the total molar flux N_t (2.26) and appropriate diffusive fluxes J_i through

$$N_i = y_i N_t + J_i. \tag{2.28}$$

Depending on the regarded system, mass or volume average approaches are favorable [69].

2.2.3 The Concept of Dispersion

A key concept in the description of species transport in chemical reaction engineering is called (fluid) dispersion [77]. With this approach, a multitude of effects are combined into a diffusion-like dispersion parameter $\mathcal{D}$ using the approximated Fickian representation (2.22). For a species i, the transient convection-dispersion balance can be expressed as

$$\frac{\partial c_i}{\partial t} = -\nabla \cdot (cu)_i + \nabla \cdot (\mathcal{D}\nabla c_i) + \dot{R}_i. \tag{2.29}$$

The temporal change of the molar concentration c_i is balanced by the divergence of the respective convective fluxes $(cu)_i$, dispersive fluxes $\mathcal{D}\nabla c_i$ and the volumetric net rate of production $\dot{R}_i$, representing sources or sinks of the species.

Dispersion models arose from the description of axial backmixing in 1D-tubular flow. In particular, the convective transport of tracer species was found to be superimposed by an apparent [78], or virtual [79] coefficient of diffusion, which exceeds molecular diffusion in axial direction (cf. Section 2.2.1). For laminar flow, radial variations in the axial velocity component lead to axial dispersion [79] additive to pure molecular diffusion [80]. Moreover, fluctuations originating from turbulent flow can enhance axial backmixing dependent on the Fanning friction factor [80, 81].

This methodology of an apparent diffusion coefficient can be generalized and applied to both axial and radial transport in either empty, or packed tubes [82, 83]. However, depending on the nature of flow, longitudinal and lateral dispersion can exhibit significant differences in their magnitude [84]. For packed beds, species dispersion is additively composed of a stagnant and a dynamic contribution. The former represents an isotropic measure dependent on the molecular diffusion coefficient and bed porosity (cf. Equation (A.38)) for the fluid-filled packed bed without flow. In addition, dynamic dispersion due to fluid flow is a macroscopic interpretation of finite displacements of fluid elements, occurring due to the random flow within bed voidages [85]. This methodology is also commonly applied to thermal dispersion inside packed beds, considering transport phenomena inside and between fluid and solid phase, respectively [85, 86].

In summary, dispersion models for species transport are used as a (semi-)empirical method to predict complex flow phenomena, which are independent of the average convective transport, by a diffusion-like parameter. The combination of all these effects accounts for the overall degree of longitudinal and lateral mixing and, hence, the residence time inside a tubular reactor [84].

Nowadays, direct numerical simulations of transport phenomena are capable of a full spatial and temporal resolution of turbulences making an approximation via dispersion coefficients obsolete. However, due to the high computational costs of such studies, a full-scale description of transport process in chemical reaction engineering, e.g. within a packed bed obtained by discrete particle approaches [87], remains impracticable for full-scale models of chemical reactors. Simpler, and a less computationally-demanding, Reynolds-averaged methods are in its nature similar to the concept of species dispersion, as they decouple turbulences by an averaging procedure [77].

2.3 Heat Transport

As introduced in Section 2.1, overall heat transport is dependent on several driving forces. The three basic principles for the transport of energy occur through thermal conduction, bulk motion and radiation [77]. In the following, thermal conduction and effective thermal transport are introduced in brief, in analogy to diffusive and dispersive mass transport.

2.3.1 Thermal Conduction

Fourier empirically found that the heat flux Q by thermal conduction is proportional to the temperature gradient of the system

$$Q = -\lambda \nabla T \tag{2.30}$$

with the thermal conductivity λ as constant of proportionality [88].

For fluid systems, it is possible to predict thermal conductivity values through kinetic theory, while solid materials require experimental basis.

2.3.2 Effective Thermal Conductivity

A common concept for the description of heat transport through inhomogeneous materials is the application of effective thermal conductivities λ^{eff}. Here, superimposed energy transport phenomena through a heterogeneous material are combined to one parameter to allow a macroscopic description using a modified proportionality constant for Fourier's law (2.30) [77].

Especially porous media are frequently described through an effective parameter λ^{eff}. For porous particles Harriott [89] related λ^{eff} to the thermal conductivity of the solid matrix and the enclosed fluid in combination with pressure effects inside of corresponding pores (cf. Appendix A.3.2). This effective parameter can be regarded as interconnection of relevant transport resistances.

For packed beds filled with a stagnant fluid, Zehner, Bauer and Schlünder [90, 91] proposed a method for the effective bed thermal conductivity (cf. Appendix A.5.1). In addition to the contributions in porous particles, effects of bed porosity, radiation and the form of the particles are included.

Finally, these stagnant effects can be superimposed by a dynamic contribution arising from heat transport through fluid motion. As described in Section 2.2.3 for mass transport, complex flow phenomena can lead to an enhancement of longitudinal and lateral transport, which exceeds average convective transport. For heat transport, this concept of dispersion is applicable in a similar way. A prominent example for dispersive heat transport is the description of effective thermal conductivity of packed beds in fluid flow, which is frequently referred to as thermal dispersion.

3 Sensitivity Analysis of Multicomponent Diffusion Models

Molar fluxes inside porous catalysts can be calculated by means of multicomponent diffusion models. The state-of-the-art dusty-gas model competes with several alternatives, best-known the mean-transport pore model and the binary friction model. All three approaches combine Maxwell-Stefan-based transport with Knudsen diffusion and viscous Darcy flow. However, the models have not yet been compared theoretically, when applied to actual diffusion-reaction problems. It is successively shown that these diffusion models result in very similar behavior when applied to CO_2 methanation, methanol synthesis and oxidative dehydrogenation of ethane. By comparing mole fractions, temperature and pressure profiles, latter revealed the most striking deviations between the models. Monte-Carlo-based, global sensitivity analyses on the catalyst effectiveness factors exhibit significant impact of catalyst properties, even at low uncertainties. At equal uncertainty levels, highest sensitivity was observed for the pellet porosity, followed by the tortuosity factor and the pore diameter. Overall, the choice of the diffusion model appears to have low influence on the regarded reaction-diffusion models. Hence, the binary friction model is recommended as most reliable, since both other approaches suffer from inconsistencies in the treatment of the viscous flux terms. These findings can be used as valuable basis for modeling multicomponent diffusion inside porous catalysts employed in heterogeneously-catalyzed gas-phase reactions.
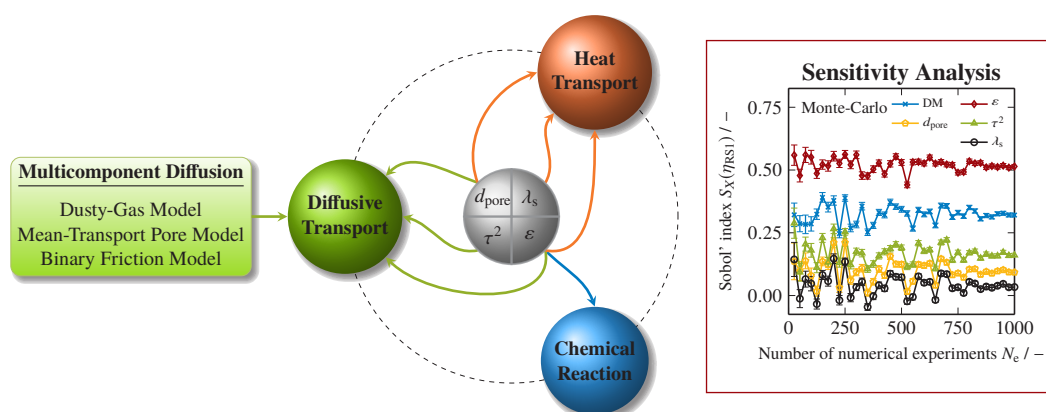
3.1 Introduction

Theoretical studies of diffusive transport and reaction in porous media have been in the focus of chemical reaction engineering for almost 80 years. The pioneer work of Damköhler [92] and Thiele [93], based on Fick's law of diffusion in cylindrical pores, was subsequently applied and advanced by many authors. Efforts on Thiele's reaction-diffusion representation were summarized in multiple monographs and articles, e.g. by Aris [94, 95] and Emig [96]. Herein a wide range of applications, such as non-isothermal effects, influence of boundary conditions, multiple reactions and stability of steady-state solutions are covered. Kinetic models – starting from simple power-law approaches up to reversible reactions of the Langmuir-Hinshelwood type – can be combined with the method of Thiele. However, the main drawback in this type of model is the use of Fick's law for the diffusive transport [74], together with constant effective diffusion coefficients. This description applied to multicomponent gas mixtures even fails to predict qualitative diffusion phenomena and, hence, can lead to severe errors [97].

In fact, the model developed by Maxwell [71] and Stefan [72] based on the mechanical interaction between the gas molecules was used as basis to tackle this problem. The first approach of this type is the dusty-gas model (DGM), which can combine multiple transport processes, such as bulk, Knudsen, and surface diffusion as well as ion transport and viscous flow [98]. Some of the main contributors in the development of the DGM were Mason and co-workers [99–104], starting in the early 1960s. The model is currently the most widely used method for theoretical representation of diffusive transport through porous media. Besides heterogeneously catalyzed reactions [105–108], fluid transport inside porous fuel cell matrices [109–112] is the most frequent application of the multicomponent diffusion models.

In this study, a consecutive comparison of the DGM to two competing approaches is provided. For this purpose, CO_2 methanation, methanol synthesis and oxidative dehydrogenation of ethane are used as model reaction systems. A global, Monte-Carlo-based sensitivity analysis gives insights to the influence of diffusion models in comparison to uncertainties of four selected catalyst properties such as porosity, pore diameter, tortuosity factor and thermal conductivity.

3.2 Model Definition

In the following section, the principals of multicomponent diffusion are introduced for the purpose of modeling heterogeneous diffusion-reaction problems. Therefore, a set of governing equations for species, heat and total mass is successively presented. Three model reaction systems complete the problem definition. Details on applied thermodynamic correlations are given in Appendix 3.A. Effective diffusion coefficients are calculated as defined in the following section.

3.2.1 Diffusional Transport in Porous Media

The binary diffusion coefficients $\mathcal{D}_{ij}$ are calculated by the semi-empirical correlation of Fuller et al. [73]

$$\left[\frac{\mathcal{D}_{ij}}{\mathrm{m^2/s}}\right] = \frac{10^{-7}\left[\frac{T}{\mathrm{K}}\right]^{1.75}\left(\left[\frac{M_i}{\mathrm{g/mol}}\right]^{-1} + \left[\frac{M_j}{\mathrm{g/mol}}\right]^{-1}\right)^{\frac{1}{2}}}{\left[\frac{p}{\mathrm{atm}}\right]\left(\left[\frac{\Delta v_i}{\mathrm{cm^3}}\right]^{\frac{1}{3}} + \left[\frac{\Delta v_j}{\mathrm{cm^3}}\right]^{\frac{1}{3}}\right)^2}, \tag{3.1}$$

which goes back to an empirical extension of the kinetic theory of gases proposed by Gilliland [113]. Herein, temperature T, total pressure p, molar masses $M_{i/j}$ and specific diffusive volumes $\Delta v_{i/j}$ are used. Latter are defined by measured incremental values, listed in an updated publication [114], as a sum of all structural groups of the regarded species i/j. In contrast to Fickian diffusion, the symbol $\mathcal{D}_{ij}$ denotes the Maxwell-Stefan representation. For ideal gases, these coefficients are symmetric and independent of composition [69].

Knudsen diffusion coefficients inside pores are defined as a function of temperature T, molar mass M_i of species i, and pore diameter d_{pore},

$$D_{i,\mathrm{Kn}} = \frac{d_{\mathrm{pore}}}{3}\sqrt{\frac{8\mathcal{R}T}{\pi M_i}}. \tag{3.2}$$

Both diffusion coefficients given in Equations (3.1) and (3.2) are used as effective parameters to encounter the flow inside porous media:

$$\begin{aligned}\mathcal{D}_{ij}^{\mathrm{eff}} &= \frac{\varepsilon}{\tau^2}\mathcal{D}_{ij}; \\ D_{i,\mathrm{Kn}}^{\mathrm{eff}} &= \frac{\varepsilon}{\tau^2}D_{i,\mathrm{Kn}}.\end{aligned} \tag{3.3}$$

While the porosity ε represents the void fraction of the catalyst pellet, the tortuosity factor τ^2 can be regarded as an empirical quantity [94, 115, 116]. Furthermore, the pressure-driven viscous flux N_{visc} inside single pores is commonly described via Darcy's law

$$N_{\mathrm{visc}} = -\frac{B_0 c_\mathrm{t}}{\eta}\frac{\partial p}{\partial r}, \tag{3.4}$$

with the total molar concentration c_t, the fluid viscosity η and the permeability B_0 of the porous medium. Latter is expressed via Hagen-Poiseuille's law

$$B_0 = \frac{\varepsilon}{\tau^2}\frac{d_{\mathrm{pore}}^2}{32} \tag{3.5}$$

for effective flow in the pellet matrix. Surface diffusion can be neglected, since comparatively small molecules without strong surface interaction in mesoporous pellets are regarded in this study (c.f. [98]). Hence, a combination of molecular diffusion (3.1), Knudsen diffusion (3.2) and viscous flow (3.4) is suitable to adequately describe diffusion and momentum transport in porous catalysts.

3.2.2 Maxwell-Stefan Transport Models

Besides the above introduced DGM, the mean-transport pore model (MTPM) developed by Schneider and co-workers [117–121] as well as the binary friction model (BFM) derived by Kerkhof [122–124] are based on Maxwell-Stefan diffusional transport [116].

Adapting the representation of Čapek and Seidel-Morgenstern [125], DGM, MTPM and BFM can be summarized in a generalized representation

$$-c_t \frac{\partial y_i}{\partial r} - \alpha_i \frac{y_i}{\mathcal{R}T} \frac{\partial p}{\partial r} = \sum_{\substack{j=1 \\ j \neq i}}^{n_{species}} \frac{y_j N_i - y_i N_j}{\mathcal{D}_{ij}^{eff}} + \beta_i N_i, \qquad i = 1, \ldots, n_{species}; \tag{3.6}$$

which is valid for an ideal multicomponent mixture of ideal gases. Furthermore, thermophoresis (Soret effect) is assumed to be negligible. The different placeholders for α_i and β_i are listed in Table 3.1. Gradients of mole fractions y_i and total pressure p act as driving forces. The first term on the right-hand-side (RHS) reflects the classical Maxwell-Stefan momentum exchange, while the second term accounts for the viscous flux.

Table 3.1: Transport placeholders α_i and β_i according to Equation (3.6), for the DGM, the BFM, and the MTPM.

Model	α_i	β_i
DGM	$\dfrac{B_0 p}{\eta D_{i,Kn}^{eff}} + 1$	$\dfrac{1}{D_{i,Kn}^{eff}}$
MTPM[a]	$\dfrac{B_i}{D_{i,Kn}^{eff}} + \sum_{j=1, j \neq i}^{n_{species}} \dfrac{y_j (B_i - B_j)}{\mathcal{D}_{ij}^{eff}}$ $B_i = D_{i,Kn}^{eff} + B_0 \dfrac{p}{\eta}$	$\dfrac{1}{D_{i,Kn}^{eff}}$
BFM[b]	1	$\left(D_{i,Kn}^{eff} + \dfrac{B_0}{\kappa_i} \right)^{-1}$ $\kappa_i = \dfrac{1}{p} \dfrac{\eta_i^0}{\sum\limits_{j=1}^{n_{species}} y_j \zeta_{ij}}$

[a] Slip at the pore wall is neglected [126].
[b] Interspecies friction at zero pressure is neglected [123].

Equation (3.6) can easily be rearranged to the following matrix form, giving a linear system of equations for the molar fluxes

$$\vec{N} = -c_{\mathrm{t}} \left[C\right]^{-1} \left(\frac{\partial \vec{y}}{\partial r} + \vec{\alpha} \frac{\vec{y}}{p} \frac{\partial p}{\partial r} \right). \tag{3.7}$$

The transport matrix $[C]$ consists of different contributions to the diffusive transport. The entries for the three models are calculated by

$$
\begin{aligned}
c_{i,i} &= \beta_i + \sum_{\substack{k=1 \\ k \neq i}}^{n_{\mathrm{species}}} \frac{y_k}{\mathcal{D}_{ik}^{\mathrm{eff}}}, \\
c_{i,j} &= -\frac{y_i}{\mathcal{D}_{i,j}^{\mathrm{eff}}}.
\end{aligned}
\tag{3.8}
$$

For given fields of pressure p, temperature T and mole fractions y_i, Equation (3.7) reduces to one set of linear equations in radial direction.

The DGM is based on a serial combination of bulk and Knudsen diffusion together with a pressure gradient induced viscous flow in parallel. Especially the later aspect has been targeted in a controversial debate [123, 127]. Kerkhof demonstrated that the parallel viscous flux is a conceptional mistake, since the effect should be included via frictional forces between the wall of the porous media and the species [122, 128]. Furthermore, the viscous nature of the fluid-wall interactions is missing in the description of the friction forces. However, for not too small Knudsen numbers, both errors seem to compensate [116].

The MTPM, on the other hand, assumes major diffusion through cylindrical pores with a radii distribution. However, as derived in Appendix 3.B, the MTPM suffers from the two inconsistencies described above in a similar way.

The BFM overcomes these theoretical discrepancies by a straightforward derivation from Boltzmann transport equations [128]. Here, viscous fluxes and Knudsen diffusion are regarded as correlated parallel processes [116], which eliminates both above mentioned problems.

3.2.3 Governing Equations

An entire description of multicomponent diffusion-reaction problem inside porous materials can be achieved by solving species and heat governing equations together with overall mass conservation. However, due to the fact that molar fluxes are given implicitly, cf. Equation (3.7), the set of unknown variables increases. Besides $n_{\mathrm{species}} - 1$ mole fractions y_i, pressure p and temperature T, there are n_{species} molar fluxes N for the coordinate r.

For steady-state conditions net rate of production $\dot{R}_i$ for each component equals the divergence of its molar fluxes N_i

$$\frac{1}{r^2} \frac{\partial}{\partial r} \left(r^2 N_i \right) = \varrho_s \left(1 - \varepsilon \right) \dot{R}_i; \qquad i = 1, \ldots, n_{\text{species}} - 1. \tag{3.9}$$

Latter are calculated by the respective diffusional transport models introduced in the previous Section 3.2.2. The heat balance of the pellets writes

$$\frac{1}{r^2} \frac{\partial}{\partial r} \left(r^2 Q \right) = \varrho_s \left(1 - \varepsilon \right) \sum_{j=1}^{n_r} \dot{r}_j \cdot \left(-\Delta_r H_j^\circ \right), \tag{3.10}$$

with the energy fluxes Q given by Fourier's law

$$Q = -\lambda^{\text{eff}} \left(\lambda_s, \lambda_{\text{fl}}, \varepsilon, d_{\text{pore}} \right) \frac{\partial T}{\partial r}. \tag{3.11}$$

The heat consumed or produced via chemical reaction is expressed via the sum of the individual reaction rates $\dot{r}_j$ times the respective standard enthalpy of reaction $\Delta_r H_j^\circ$. The effective thermal conductivity λ^{eff} of the porous pellet is a function of various parameters calculated by the correlation of Harriott [89]. Furthermore, similar to thermophoresis also the reciprocal process (Dufour effect) [67, 68] is neglected within this work.

Finally, the conservation of total mass is used to complete the set of equations

$$\frac{1}{r^2} \frac{\partial}{\partial r} \left(r^2 \sum_{i=1}^{n_{\text{species}}} M_i N_i \right) = 0. \tag{3.12}$$

3.2.4 Model Reaction Systems

Multicomponent diffusion-reaction problems are inherently impractical to be generalized by dimensionless numbers, as it is done with the common Fickian approach. Therefore, three different model reaction systems (RS) are regarded, to obtain a broad statement. The overall reactions are summarized below. For detailed information on the respective kinetic models, including rate and adsorption parameters, it is referred to the original publications [129–131] and Appendix B.

3.2.4.1 Carbon Dioxide Methanation (RS1)

CO_2 methanation is a highly exothermic single reaction with four species:

$$CO_2 + 4\,H_2 \rightleftharpoons CH_4 + 2\,H_2O, \qquad\qquad \Delta_r H_{25\,°C}^\circ = -165\,\frac{kJ}{mol}. \tag{3.13}$$

Langmuir-Hinshelwood-Hougen-Watson kinetics of Koschany et al. [129] are applied for a porous $NiAlO_x$ catalyst ($\varrho_s = 4700\,kg/m^3$).

3.2.4.2 Methanol Synthesis (RS2)

As second model reaction system, methanol (MeOH) synthesis from CO_2 together with the reverse of the water-gas-shift reaction

$$CO_2 + 3\,H_2 \rightleftharpoons MeOH + H_2O, \qquad \Delta_r H^\circ_{25\,°C} = -49\,\frac{kJ}{mol}; \qquad (3.14)$$

$$CO_2 + H_2 \rightleftharpoons CO + H_2O, \qquad \Delta_r H^\circ_{25\,°C} = 41\,\frac{kJ}{mol}; \qquad (3.15)$$

on a ternary $Cu/ZnO/Al_2O_3$ catalyst ($\varrho_s = 4500\,kg/m^3$) is used. Kinetics are given by the power-law model of Peter et al. [130].

3.2.4.3 Oxidative Dehydrogenation of Ethane (RS3)

Finally, the third model system is oxidative dehydrogenation of ethane on a $MoVTeNbO_x$ mixed metal oxide catalyst ($\varrho_s = 4370\,kg/m^3$). The main reaction is given to

$$C_2H_6 + \frac{1}{2}\,O_2 \longrightarrow C_2H_4 + H_2O, \qquad \Delta_r H^\circ_{25\,°C} = -105\,\frac{kJ}{mol}. \qquad (3.16)$$

In addition, partial and total oxidation of the C_2 species take place

$$C_2H_6 + \frac{7}{2}\,O_2 \longrightarrow 2\,CO_2 + 3\,H_2O, \qquad \Delta_r H^\circ_{25\,°C} = -1428\,\frac{kJ}{mol}; \qquad (3.17)$$

$$C_2H_6 + \frac{5}{2}\,O_2 \longrightarrow 2\,CO + 3\,H_2O, \qquad \Delta_r H^\circ_{25\,°C} = -862\,\frac{kJ}{mol}; \qquad (3.18)$$

$$C_2H_4 + 3\,O_2 \longrightarrow 2\,CO_2 + 2\,H_2O, \qquad \Delta_r H^\circ_{25\,°C} = -1323\,\frac{kJ}{mol}; \qquad (3.19)$$

$$C_2H_4 + 2\,O_2 \longrightarrow 2\,CO + 2\,H_2O, \qquad \Delta_r H^\circ_{25\,°C} = -757\,\frac{kJ}{mol}. \qquad (3.20)$$

A Langmuir-Hinshelwood-Hougen-Watson kinetic model published by Che-Galicia et al. [131] is applied.

3.3 Methodology

All calculations are performed using MATLAB v2015b. Thermodynamic properties (cf. Appendix 3.A) are treated as variable during the complete solution routine.

3.3.1 Numerical Solution Routine

Variables p, T and N, as well as the spacial coordinate r are used in dimensionless form to allow stable solution of the equations system (3.6), (3.9), (3.10) and (3.12). The coupled boundary value problem in the Equations (3.9), (3.10) and (3.12) is discretized using orthogonal collocation on finite elements (OCFE) [132]. Solution was achieved with five elements consisting of three internal grid points. Unequal element sizes allowed faster convergence. All simulations were stable and did not change by an increase in element or grid point number. More detailed information on the applied OCFE method is given in Appendix 3.C. The nonlinear governing equations are solved for p, T and y_i, for $i = 1, \ldots, n_{species} - 1$, by a constrained trust-region-reflective algorithm. No-flux boundary conditions at the pellet center and Dirichlet-type boundary condition at the respective surface are applied for all variables. At each step the set of linear Equations (3.6) is decomposed by the QR-method, giving the molar fluxes N for each species.

3.3.2 Sensitivity Analysis

As introduced in Section 3.2, definition of the mathematical problem for multicomponent diffusion in heterogeneous catalysts involves a multitude of equations and parameters. First of all, the influence of the diffusional transport model has to be evaluated. Furthermore, these models have to be regarded in the full context of the problem. Due to the strong coupling of diffusional transport with chemical reaction and heat transport, other parameters can also have a significant impact. These parameters are the pore diameter d_{pore}, the pellet porosity ε, the tortuosity factor τ^2 and the thermal conductivity of the non-porous solid phase λ_s. While the choice of the diffusion model (DM) is a parameter with three discrete values, DGM, MTPM, or BFM, the four quantities listed above are continuous. Prior to a reliable simulation of the diffusion-reaction problem inside porous catalysts, the values of the parameters have to be determined. Typically, these quantities also underlie a specific uncertainty ξ and, hence, are not precisely known [133]. This can be caused by inhomogeneities inside the material, a natural distribution of the value and uncertainties in the experimental measurements. To assess the impact of these uncertainties together with the diffusion model, the variable $X \in \mathrm{DM}, d_{pore}, \varepsilon, \tau^2, \lambda_s$ is defined. After assuming X to be independent random variables, a global stochastic sensitivity analysis of the mathematical model is possible [134, 135].

The sensitivity of each variable X on the model output $Y = f(X_1, \ldots, X_N)$ is quantified by first order Sobol' indices [136]

$$S_{X_i} = \frac{\mathrm{Var}(Y|X_i)}{\mathrm{Var}(Y)}. \tag{3.21}$$

Table 3.2: Summary of parameters applied in sensitivity analysis including variable type and reference value at zero uncertainty $\xi_X = 0$. The quantity $\xi_{X,\text{max}}$ indicates the maximum possible uncertainties for two Cases I and II.

X	type	reference state	$\xi^{\text{I}}_{X,\text{max}}/-$	$\xi^{\text{II}}_{X,\text{max}}/-$
DM	discrete	n.a.	n.a.	n.a.
d_{pore}	continuous	15 nm	0.1	0.5
ε	continuous	0.5	0.1	0.1
τ^2	continuous	4	0.1	0.5
λ_{s}	continuous	4 W/(m K)	0.1	0.5

In this case, the model output Y is defined as the catalyst effectiveness factor

$$\eta_j = \frac{3}{(d/2)^3} \frac{\int_0^{d/2} r^2 \dot{r}_j \, \mathrm{d}r}{\dot{r}_{j,\text{surf}}}. \tag{3.22}$$

To estimate the Sobol' indices, in Equation (3.21) a first order Monte-Carlo-based so-called Sobol' pick-freeze scheme is applied [136, 137]. Here Sobol' indices are obtained from the model output Y and its replication, where one value of the variables X is held constant (frozen variables), while the others are varied randomly (picked variables) [134]. For each parameter X, this is repeated for a given number of 'numerical experiments' n_{exp} and the respective model outputs Y and Y^X [134, 138].

$$S_X(Y) = \frac{\frac{1}{n_{\text{exp}}} \sum_{k=1}^{n_{\text{exp}}} Y_k Y_k^X - \left(\frac{1}{n_{\text{exp}}} \sum_{k=1}^{n_{\text{exp}}} \left[\frac{Y_k + Y_k^X}{2}\right]\right)^2}{\frac{1}{n_{\text{exp}}} \sum_{k=1}^{n_{\text{exp}}} \left[\frac{(Y_k)^2 + (Y_k^X)^2}{2}\right] - \left(\frac{1}{n_{\text{exp}}} \sum_{k=1}^{n_{\text{exp}}} \left[\frac{Y_k + Y_k^X}{2}\right]\right)^2}. \tag{3.23}$$

The standard deviation σ of the calculated Sobol' indices is given by [134]

$$\sigma^2_{S_X(Y)} = \frac{1}{[\text{Var}(Y)]^2} \cdot \text{Var}\left[(Y - \text{E}(Y))\left(Y^X - \text{E}(Y)\right) \dots \right.$$
$$\left. - \frac{S_X}{2}\left((Y - \text{E}(Y))^2 + \left(Y^X - \text{E}(Y)\right)^2\right)\right]. \tag{3.24}$$

Table 3.2 lists an overview of the introduced variables X and their reference states, chosen according to typical values [116, 139]. Furthermore, two Cases I and II of different uncertainty ranges are listed. For example, a maximum uncertainty $\xi^{\text{I}}_{d_{\text{pore}},\text{max}} = 0.1$ means that the pore diameter of 15 nm can range from 13.5 to 16.5 nm. For each model reaction systems a global reference state, equal to the conditions at the pellet surface, is defined. For RS1, a temperature of $T = 260\,°\text{C}$, pressure of $p = 8$ bar and a composition of $CO_2/H_2/CH_4/H_2O/N_2 = 22.5/22.5/$

22.5/22.5/10.0 are used. For RS2, the reference conditions are 250 °C, 32.5 bar and $CO_2/H_2/CO/CH_4/H_2O/MeOH/N_2$ = 12/52.5/9/1/0.5/25. The surface conditions for RS3 are chosen to be T = 400 °C, p = 1 bar, $C_2H_6/O_2/C_2H_4/H_2O/CO_2/CO/N_2$ = 21/25/21/21/1/1/10. Furthermore, the pellet diameter is set to d = 2 mm for spherical catalyst pellets in all sensitivity calculations.

3.4 Results and Discussion

In the following, a simple apparent comparison of the three multicomponent diffusion models gives the basis and motivation for the subsequent Monte-Carlo-based global sensitivity analysis described in Section 3.3.2.

3.4.1 Comparison of Multicomponent Diffusion Models

A general evaluation of the selected reaction system in dependence on the different diffusion models gives Table 3.3 together with Figures 3.1 and 3.2. Selected conditions according to the reference states are given in the previous Section 3.3.2.

Table 3.3: Results summary of effectiveness factors, temperature and pressure changes for all reaction systems at reference state conditions, defined in Section 3.3.2.

	DGM	MTPM	BFM
	RS1- CO_2 Methanation		
ΔT_{max} / K	0.9965	0.9963	1.0192
Δp_{max} / mbar	19.9245	19.9211	9.5727
η_1 / −	0.7362	0.7361	0.7444
	RS2 - MeOH Synthesis		
ΔT_{max} / K	0.0594	0.0594	0.0598
Δp_{max} / mbar	−23.9103	−23.9113	−27.2047
η_1 / −	0.8781	0.8783	0.8849
η_2 / −	1.2946	1.2943	1.2861
	RS3 - ODH Ethane		
ΔT_{max}/K	0.0286	0.0286	0.0286
Δp_{max}/mbar	4.1247	4.1248	4.1180
η_1 / −	0.9307	0.9307	0.9311
η_2 / −	0.9509	0.9509	0.9513
η_3 / −	0.9413	0.9413	0.9417
η_4 / −	1.0100	1.0101	1.0100
η_5 / −	1.0007	1.0007	1.0007

Table 3.3 lists overall results like maximum temperature ΔT_{max} and pressure Δp_{max} changes, as well as the respective effectiveness factors η_j. The latter cover a range from 73 to 130 % for

(a) RS1: CO_2 methanation.

(b) RS2: Methanol synthesis.
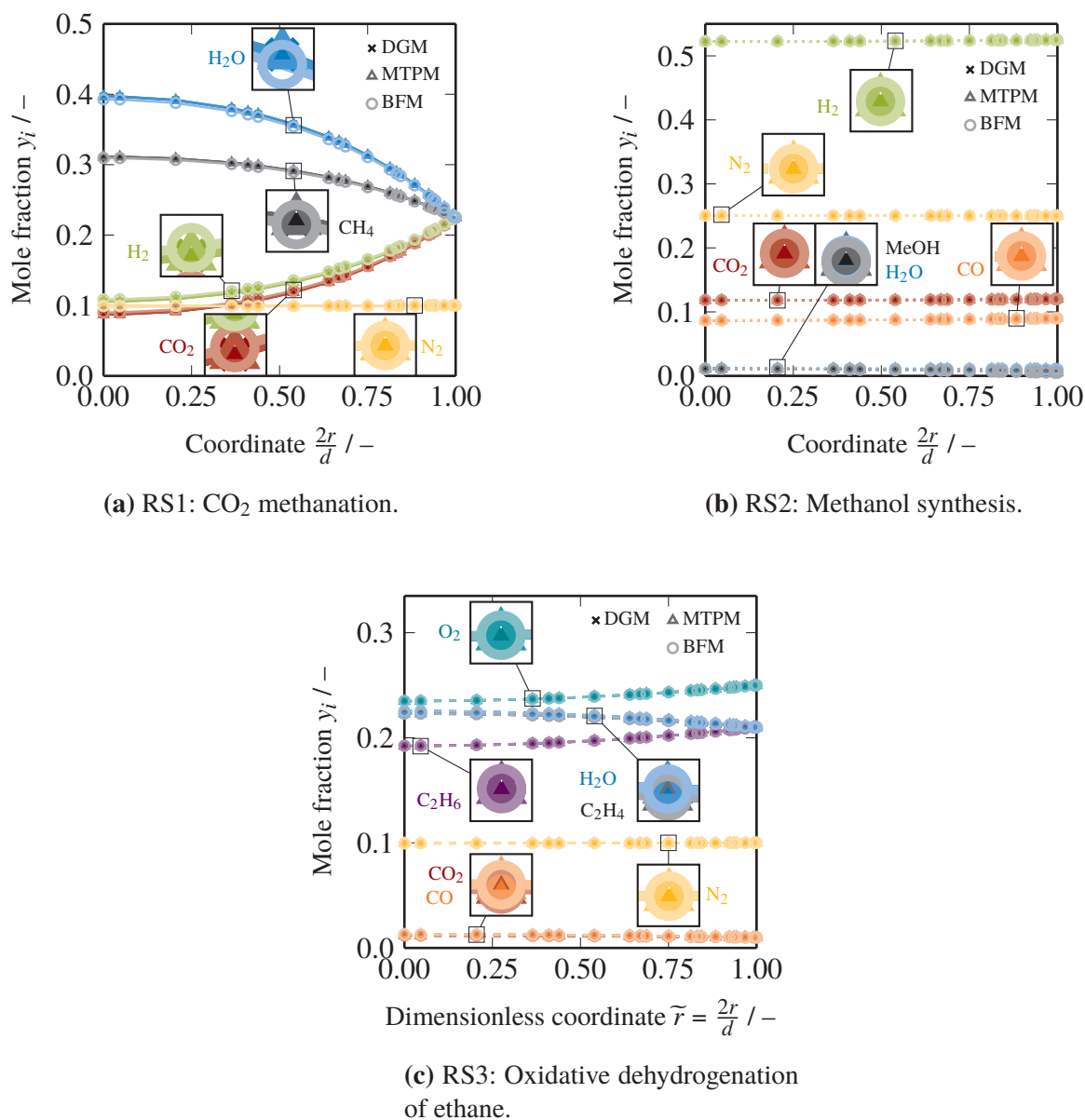

(c) RS3: Oxidative dehydrogenation of ethane.

Figure 3.1: Profiles of mole fractions for model reaction systems with examples at reference state conditions, introduced in Section 3.3.2.

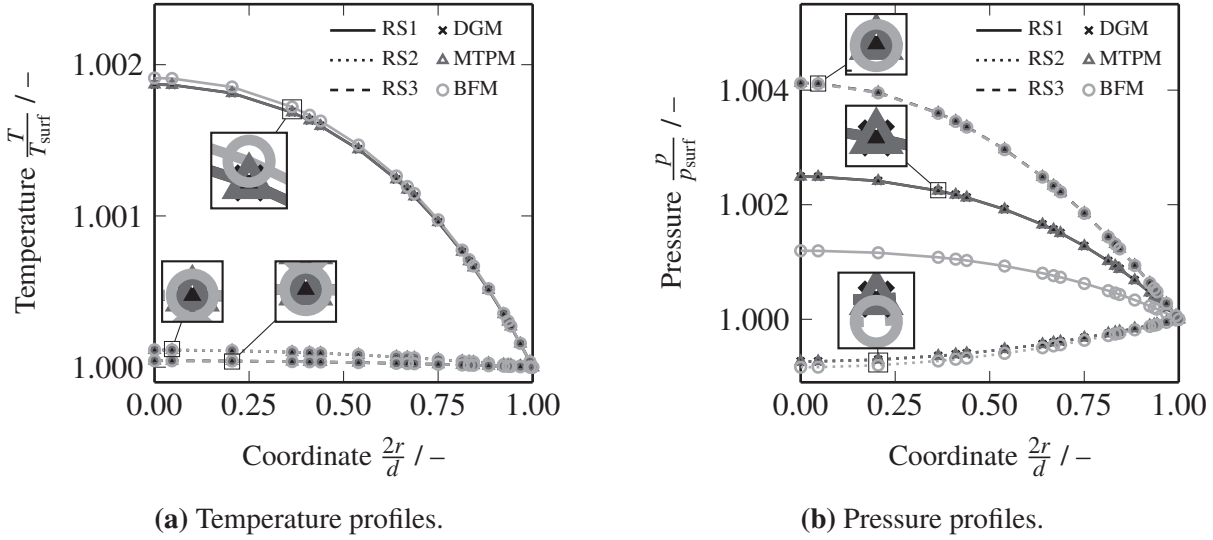**(a)** Temperature profiles.

(b) Pressure profiles.

Figure 3.2: Profiles of the three model reaction systems at reference state conditions introduced in Section 3.3.2.

the three reaction systems. However, only slight deviations between the models occur. While η_j values for RS3 are consistent up to 0.05 percentage points, for RS1 and RS2 the deviations go up to 0.8 percentage points. The difference in the diffusional behavior between the three models is further illustrated in Figure 3.1 showing respective mole fractions over the dimensionless coordinate for all three RS.

Figure 3.1a depicts strong differences in diffusional behavior of the species. Stoichiometrically, H_2 is consumed four times faster than CO_2 (3.13). However, due to a smaller molecule diameter, diffusion is strongly enhanced for H_2 in comparison to the 22-times heavier CO_2. Similar phenomena have been observed by Barrientos et al. [140], who experimentally and numerically investigated pellet size effects in CO methanation. In addition, the fast diffusion of hydrogen leads to an overall pressure change inside the pellet, which is in contradiction to the stoichiometric decrease in volume. As illustrated by the magnified profiles, DGM and MTPM can hardly be discriminated. In contrast, the BFM predicts a slightly lower conversion inside the pellet. Latter can be attributed to the deviating treatment of the viscous fluxes, as introduced in Section 3.2.2, which is further confirmed in the deviating maximum pressure changes Δp_{max}, listed in Table 3.3 and shown in Figure 3.2b. As illustrated by Figure 3.2a, temperature rises ΔT_{max} for the RS1 example are again similar for DGM and MTPM and slightly higher for BFM. This also explains the elevated effectiveness factor for the BFM compared to both other models.

For methanol synthesis (RS2), Figure 3.1b shows flat trends of most species. However, the increase in the MeOH profile close to the pellet surface ($\tilde{r} \rightarrow 1$) and the effectiveness factors of $\eta_1 \approx 0.88$ and $\eta_2 \approx 1.29$ indicate effects of diffusional transport. For RS2, differences in the three transport models are less pronounced. Only the pressure decrease, shown in Figure 3.2b, depicts the above-mentioned discrepancies in viscous fluxes handling. In Figures 3.1c and 3.2 similar trends for RS3 are illustrated. Here, the deviations between all transport models are even

less pronounced for mole fractions y_i, as well as maximum temperature ΔT_{max} and pressure Δp_{max} changes, which is also verified by the values given in Table 3.3.

In summary, the three examples shown within this section illustrate the quality of the reaction-diffusion problems by comparing the reference states of the different diffusion models. In general, these variations can be attributed to the viscous flux handling, which is strengthened by the fact that highest deviations are observed for the total pressure changes of DGM and MTPM compared to the BFM. This variation in viscous transport seems to be enhanced in diffusional regimes, since the differences in the pressure profiles can be related to the deviations of effectiveness factors from unity (see Table 3.3). However, an adequate comparison of the diffusion models requires a rigorous evaluation of all reaction systems. For that purpose, influences of catalyst properties are measured by global sensitivity analysis.

3.4.2 Sensitivity Analysis

As introduced in Section 3.3.2, global sensitivity analysis, following the procedure of Monod et al. [138], is applied for evaluation of parameter uncertainties. First, an adequate number of numerical experiments n_{exp} has to be determined.
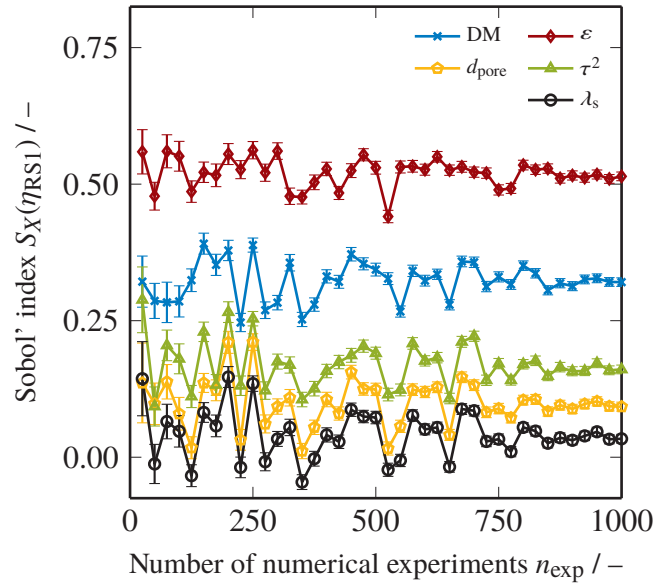
Figure 3.3: Exemplary dependency of Sobol' indices S_X on number of experiments n_{exp} for RS1 Case I with a relative uncertainty $\widetilde{\xi} = \frac{\xi_X}{\xi_{X,max}^I} = 0.25$. For clarity reasons only 40 datasets are displayed. Standard deviations are given by Equation (3.24).

Figure 3.3 gives an exemplary progression of Sobol' indices at altered n_{exp} values for the effectiveness factor η_j as output function. One random Monte-Carlo experiment is repeated for each parameter leading to $6 \cdot n_{exp}$ total simulations for each point. Thus, by increasing n_{exp}, both the individual scattering of all S_X values and the corresponding standard deviations diminish, respectively. Furthermore, above $n_{exp} \approx 800$, all shown Sobol' indices seem to stabilize. Similar

31

behavior is observed for varied uncertainties and reaction systems. Hence, n_{exp} is set to 1000 for all subsequently presented simulations, in order to ensure reliable sensitivity estimates. Per definition, without any uncertainty, $\widetilde{\xi} = 0$, the Sobol' index of the diffusion model S_{DM} is unity, while for all other parameters S_X has to be zero. In addition, it has to be noted that Sobol' indices range by definition from 0 to 1. Small negative values are most likely caused by the numerical approximation. As can be seen by the trends in Figure 3.3, increasing n_{exp} stabilizes the routine. In the following, slightly negative values for S_X are tolerated, as they do not affect the global evaluation.
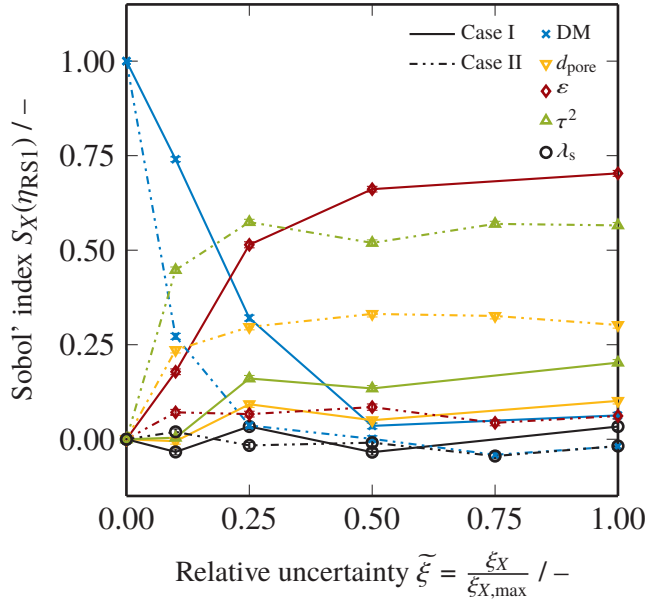
Figure 3.4: Sobol' indices S_X for dependency of CO_2 methanation (3.13) catalyst efficiencies η_{RS1} on relative uncertainty $\widetilde{\xi}$ using Cases I and II, with definitions given in Table 3.2.

As Figure 3.4 depicts for the effectiveness factor of RS1, S_{DM} values decrease rapidly with increased uncertainties for both Cases I and II. Solid lines in Figure 3.4 refer to equal maximum uncertainties or Case I (cf. Table 3.2). Here, pellet porosity ε settles as most sensitive parameter with an Sobol' index above 0.50 for $\widetilde{\xi} = 0.25$ or $\xi_\varepsilon = 0.05$. In contrast, impacts of pore diameter d_{pore} and solid thermal conductivity λ_s on the effectiveness factors are comparatively small.

For Case II (dash-dotted lines), trends are partly shifted. While λ_s remains insignificant, sensitivity values for tortuosity factor S_{τ^2} and pore diameter $S_{d_{pore}}$ are strongly enhanced. In Case II the maximum uncertainty is kept constant for the pellet porosity and increased by a factor of five for all other parameters (c.f. Table 3.2). Hence, the sensitivity of the pellet porosity diminishes. At the same time the Sobol' index for the diffusion model S_{DM} drops even faster, which can be attributed to the higher maximum uncertainties for Case II.

Methanol synthesis (3.14) in Figure 3.5 displays very similar trends. For Case I, at uncertainties ξ_X of 0.05, or a relative uncertainty $\widetilde{\xi} = 0.50$, S_ε exceeds the respective values of the diffusion

model S_{DM}. Also, the Sobol' index for τ^2 is enhanced up to 0.20 for $\xi_{\tau^2} = 0.10$, while d_{pore} and λ_s are insensitive.
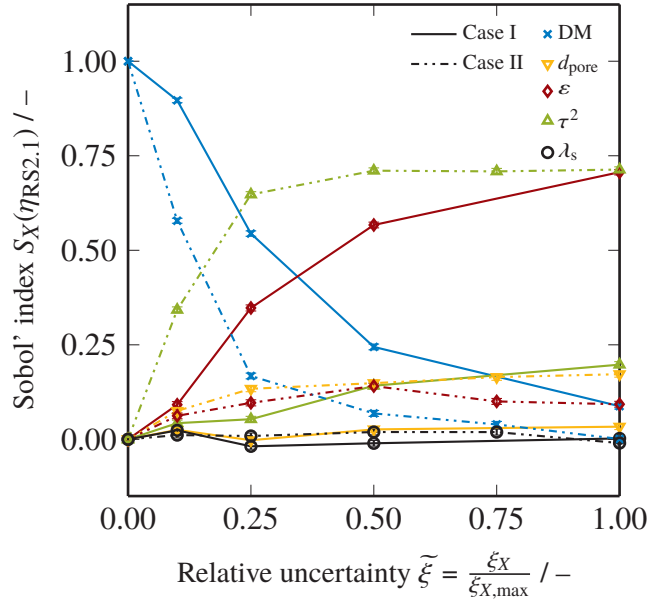

Figure 3.5: Sobol' indices S_X for dependency of methanol synthesis (3.14) catalyst efficiencies $\eta_{RS2.1}$ on relative uncertainty $\widetilde{\xi}$ using Cases I and II, with definitions given in Table 3.2.

Reduced uncertainties for the pellet porosity ε, cf. Case II in Figure 3.5, lead to changed sensitivities of the pellet features. Similar to CO_2 methanation, for RS2 also the tortuosity factor τ^2 exhibits a dominating Sobol' index for relative uncertainties above $\widetilde{\xi} = 0.20$. Other sensitivities are below 0.20 for all parameters. Trends for the second reaction (3.15) of reaction system RS2 are depicted in Figure 3.7 of the Supplementary Material 3.S.1. Here, very similar behavior to the one described for (3.14) in Figure 3.5 is observed.

Oxidative dehydrogenation of ethane (3.16) serves as representative of the third reaction system RS3. As shown in Figure 3.6, sensitivity of the diffusion model S_{DM} drops rapidly with increased relative uncertainty $\widetilde{\xi}$ for both cases. For Case I, again, pellet porosity ε features a high and stable Sobol' index above 0.65 at increased uncertainties. At $\widetilde{\xi} = 1$, S_{τ^2} and $S_{d_{pore}}$ follow with values of 0.15 and 0.11, respectively. Solid thermal conductivity remains negligible on the catalyst effectiveness factor η.

Sobol' indices for case II conform to the trends described above. However, since the maximum uncertainty for ε is decreased, the sensitivity of the tortuosity factor S_{τ^2} and the pore diameter $S_{d_{pore}}$ rise, respectively. Side (3.17), (3.18) and consecutive reactions (3.17), (3.18) of the reaction system are analyzed in a similar way. The respective Figure 3.8 is given in the Supplementary Material 3.S.1. With the exception of ethene partial combustion to CO (3.20), were the slopes are smaller, trends are very alike to the described reactions in Figure 3.6. Nevertheless, also here Sobol' indices of the diffusion model S_{DM} are decreasing with elevated relative uncertainties $\widetilde{\xi}$, as can be seen in Figure 3.8d.
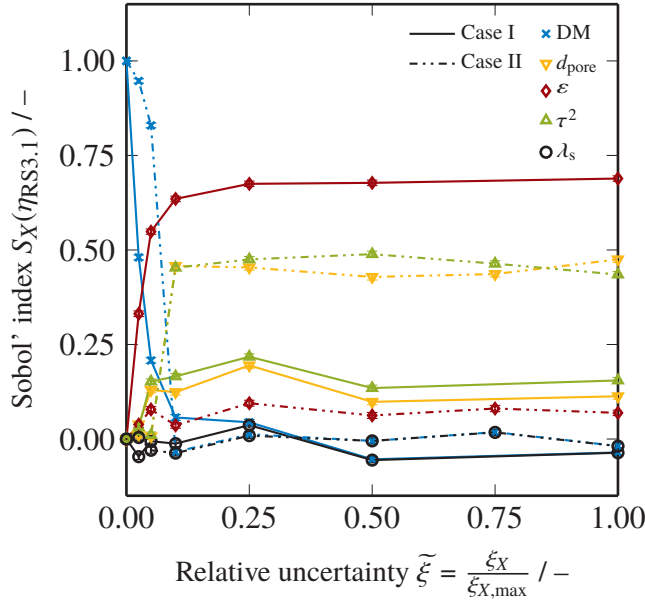
Figure 3.6: Sobol' indices S_X for dependency of oxidative dehydrogenation of ethane (3.16) catalyst efficiencies $\eta_{RS3.1}$ on relative uncertainty $\widetilde{\xi}$ using Cases I and II, with definitions given in Table 3.2.

In general, the results reveal some striking global trends. First of all, sensitivities of diffusion models S_{DM} reduce drastically with increased uncertainties of the continuous parameters d_{pore}, ε, τ^2 and λ_s for all cases. Furthermore, thermal conductivity of the solid seems to be insensitive to all regarded effectiveness factors, as indicated by the consistently low S_{λ_s} values. Also, for equal maximum uncertainty levels, as defined by Case I in Table 3.2, the pellet porosity ε clearly has a dominating effect on the output of the three regarded reaction-diffusion problems. For the reduced $\xi_{\varepsilon,max}^{II}$ value of Case II, this trend is diminished, while the sensitivities of tortuosity factor τ^2 and pore diameter d_{pore} rise.

The impact of pellet dimension on the Monte-Carlo-based global sensitivity analysis made in this study has been evaluated with an additional test for spheres with a diameter of 5 mm for the reaction system RS3 and Case I. Respective modeling results are given in the Supplementary Material 3.S.2. Although effectiveness factors for the reactions are shifted to significantly lower values (see Figures 3.9 and Table 3.4), trends in Sobol' indices are consistent to the ones for the 2 mm pellets (cf. Figure 3.10). Hence, it can be stated that the analyses made in this study are not affected by changes in the physical dimension of the pellet.

These results indicate the strong coupling of mass, heat and momentum transfer to the respective chemical reactions for all three reaction systems. As illustrated in the previous Section 3.4.1, within the regarded regimes, the difference between DGM, MTPM and BFM is quite small, which is why S_{DM} reduces with increased $\widetilde{\xi}$ values. However, it also emphasizes the need for reliable parameter estimates for d_{pore}, ε, τ^2 and λ_s, since their impact on the effectiveness factors can become significantly large compared to the choice of the diffusion

model. This fact is explained by the appearance of the individual parameters within the equation system of Section 3.2. Most abundantly the pellet porosity ε is present. Besides its use to calculate effective diffusion coefficients, Equation (3.3), and permeabilities, Equation (3.5), also the reaction terms in Equations (3.12) and (3.10) and the effective thermal conductivity, cf. Equation (3.11), make direct use of ε. The parameter with the second highest influence is found to be the tortuosity factor τ^2 as demonstrated by the results for Case II. Again, direct influence on effective diffusion coefficients and permeabilities becomes apparent. Pore diameters d_{pore} also exhibit some influence on the effectiveness factors, although these are less pronounced for the cases investigated. However, it has to be stated that for all catalysts regarded in the reaction systems d_{pore}, ε and τ^2 can have a natural distribution. Furthermore, for low pore diameters below 10 nm, not regarded in this study, Knudsen diffusion becomes more dominant [141]. In contrast, λ_s did not show any significant effect on any effectiveness factor, since, via modification of heat transport properties, the solid thermal conductivity only indirectly contributes to the diffusion and reaction inside the pellet.

3.5 Conclusion

With a reasoned comparison and a global sensitivity analysis of state-of-the-art multicomponent diffusion models their minor differences in reaction-diffusion problems are exhibited, using three heterogeneously catalyzed reaction systems. Adopting a procedure of Kerkhof [122], a theoretical derivation reveals inconsistencies of the MTPM, similar to the DGM, leaving the BFM as single consistently derived approach. However, the models resulted in hardly varying mole fraction and temperature profiles. Only the differing handling of momentum transport yields in distinguishable deviations of pressure profiles for BFM, compared to MTPM and DGM. A more detailed investigation by a Monte-Carlo-based global sensitivity analysis emphasizes the small discrepancy between the three diffusion models, when uncertainties in parameter estimation are regarded. For all effectiveness factors, the most influential catalyst property is the pellet porosity, followed by the tortuosity factor and pore diameter. The impact of the choice of diffusional model revealed to become negligible throughout this study, resulting in similar effectiveness factors for all three models and reaction systems. Moreover, the BFM remains as single consistently derived model with a correct treatment of the viscous fluxes. Hence, the BFM is highly recommended to be applied in advanced chemical reactor simulations and to gradually replace the classical DGM.

3.A Thermodynamic Properties

For multicomponent transport, ideal gas behavior is assumed. However, for methanol synthesis, reaction kinetics rely on fugacity coefficients, which are calculated by the Peng-Robinson equation-of-state [70, 142] using binary interaction parameters according to Knapp et al. [143]. It was found that applying real gas behavior to the diffusional transport equation (3.6) by using gradients of the chemical potential as driving forces [98] had an insignificant effect on the overall results and, hence, the ideal gas assumption is sufficiently justified. Temperature-dependent thermodynamic properties according to the polynomials summarized by Kleiber and Joh [144, 145] are used for enthalpies of reaction, thermal conductivities and fluid viscosities. Pressure dependence is regarded as negligible. Excess properties are neglected, while mixture viscosity and thermal conductivity of the fluid are calculated using respective mixing rules [146, 147]. Additional information is provided in Appendix A.

3.B Inconsistencies in Mean-Transport Pore Model

Kerkhof [122] illustratively derived the inconsistencies in the DGM for two concrete examples:

(i) A two-component gaseous Stefan-tube problem is regarded, with air (a) as stagnant and steam (st) as mobile species;

(ii) Flow of a single fluid (fl) in the absence of any external force besides a gradient in total pressure.

In the following both examples are applied to the MTPM. From Equation (3.6) and Table 3.1, it follows for Example (i):

$$
c_{\mathrm{t}} \frac{\partial y_{\mathrm{a}}}{\partial r} - \left(1 + \frac{B_0 p}{\eta D_{\mathrm{a,Kn}}^{\mathrm{eff}}} + \frac{y_{\mathrm{st}} \left(D_{\mathrm{a,Kn}}^{\mathrm{eff}} - D_{\mathrm{st,Kn}}^{\mathrm{eff}} \right)}{\mathcal{D}_{\mathrm{a,st}}^{\mathrm{eff}}} \right) \frac{\partial p}{\partial r} = \frac{y_{\mathrm{a}} N_{\mathrm{st}}}{\mathcal{D}_{\mathrm{a,st}}^{\mathrm{eff}}}.
\tag{3.25}
$$

Applying ideal gas and mixture behavior, this expression can further be rearranged to

$$
\frac{1}{p} \frac{\partial p_{\mathrm{a}}}{\partial r} = \frac{y_{\mathrm{a}} N_{\mathrm{st}}}{c_{\mathrm{t}} \mathcal{D}_{\mathrm{a,st}}^{\mathrm{eff}}} - \frac{y_{\mathrm{a}}}{p} \left(\frac{B_0 p}{\eta D_{\mathrm{a,Kn}}^{\mathrm{eff}}} + \frac{y_{\mathrm{st}} \left(D_{\mathrm{a,Kn}}^{\mathrm{eff}} - D_{\mathrm{st,Kn}}^{\mathrm{eff}} \right)}{\mathcal{D}_{\mathrm{a,st}}^{\mathrm{eff}}} \right) \frac{\partial p}{\partial r}.
\tag{3.26}
$$

The partial pressure gradient of air should arise solely from the intermolecular collisions with steam molecules, since air can be treated as stagnant species [122]. These interactions are reflected by the first term on the RHS of Equation (3.26). However, the additional terms also imply contributions of viscous friction to the pore wall [122] as well as the difference of the

individual permeability of steam and air [119, 148]. Both is against physical intuition since only intermolecular collisions are expected.

For the Example (ii) of a single fluid flow Equation (3.6) reduces to

$$N_{\text{fl}} = -\left(\frac{D_{\text{fl,Kn}}^{\text{eff}}}{\mathcal{R}T} + \frac{B_0 c_{\text{t}}}{\eta}\right)\frac{\partial p}{\partial r} \tag{3.27}$$

for the MTPM, which is identical to the derivation made by Kerkhof for DGM [122]. Hence, the argumentation of Kerkhof applies here in the same way. The friction to the pore walls should be reflected by Darcy's law (3.4) only, as this is the actual definition of the viscous flux. However, both the MTPM and the DGM, lack the viscous nature of the fluid-wall interaction [116, 122].

In summary, the MTPM shows conceptional inconsistencies as previously demonstrated for the DGM by Kerkhof [122]. Furthermore, the structure of the coefficients suggests a similar diffusion behavior of DGM and MTPM.

3.C Orthogonal Collocation on Finite Elements

Orthogonal collocation on finite elements is applied for the entire discretization within in this work. Following the description of Carey and Finlayson [132] using unequal spacing, the element centers are placed at 0.205, 0.539, 0.750, 0.884 and 0.968. Roots of unweighted, modified fourth order Jacobi polynomials serve as the three inner collocation points: 0.1127, 0.5000 and 0.8873. Continuity of variables and their respective slopes between each element is enforced [149]. In total, the procedure yields in 21 grid points for each variable, being a highly stable and cost-effective discretization method [132]. Detailed information on this concept is given in Appendix C.

3.S Supplementary Material

3.S.1 Additional Figures for 2 mm Pellet

Additional results for the cases I and II are given in Figures 3.7 and 3.8.

3.S.2 Analysis of 5 mm Pellet for RS3

The impact of pellet dimension on the Monte-Carlo-based global sensitivity analysis is investigated for a pellet diameter of 5 mm for the third reaction system RS3 and Case I. Table 3.4 lists the integrated parameters for all three diffusion models. Corresponding profiles for the mole fractions are displayed in Figure 3.4. Figure 3.10 shows the respective trends for the Sobol' indices.
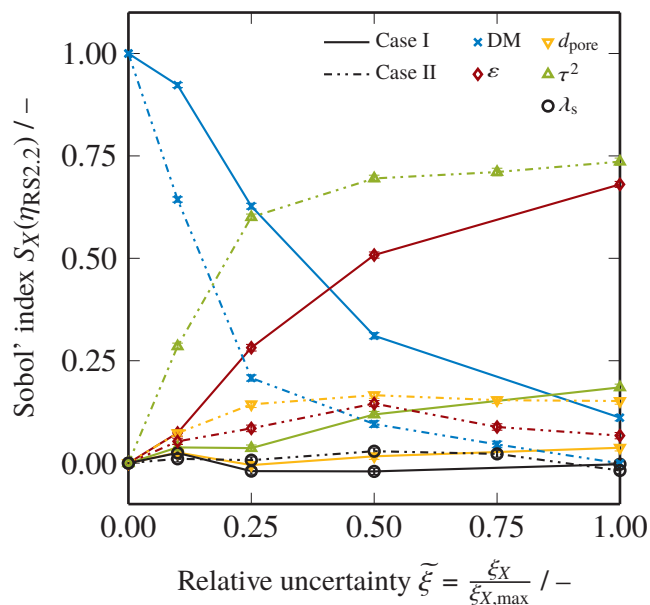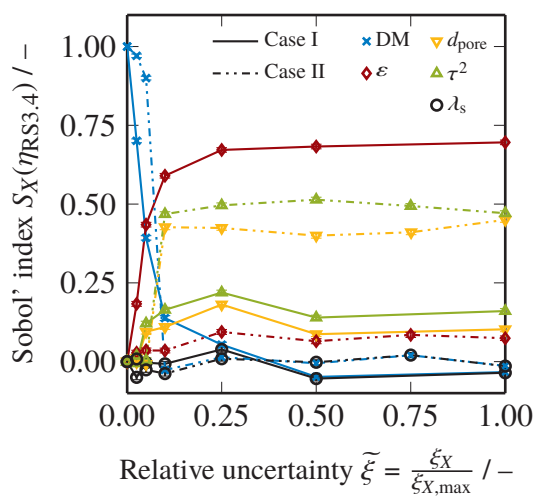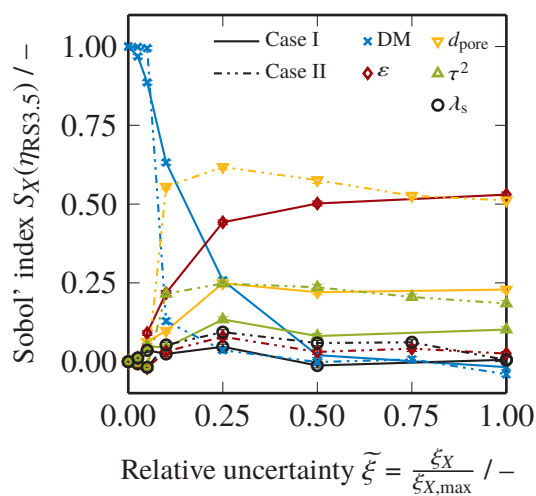
Figure 3.7: Sobol' indices S_X for dependency of reverse-water-gas-shift reaction in methanol synthesis (RS2.2) catalyst efficiencies $\eta_{RS2.2}$ on relative uncertainty $\widetilde{\xi}$ using cases I and II, with definitions given in Table 3.2.

Table 3.4: Results summary of effectiveness factors, temperature and pressure changes for reaction system RS3 at reference state conditions with 5 mm pellet diameter.

	DGM	MTPM	BFM
$\Delta T_{max}/K$	0.1330	0.1333	0.1330
$\Delta p_{max}/mbar$	1.7206	1.7211	1.7208
$\eta_1 / -$	0.7256	0.7268	0.7256
$\eta_2 / -$	0.7966	0.7967	0.7966
$\eta_3 / -$	0.7619	0.7630	0.7619
$\eta_4 / -$	1.0315	1.0314	1.0316
$\eta_5 / -$	0.9871	0.9871	0.9871
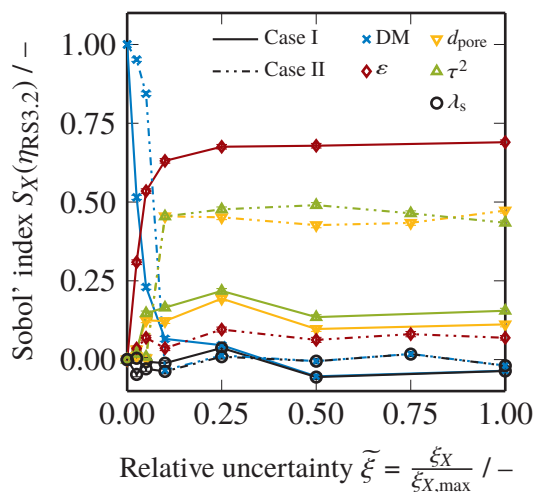
(a) Ethane to CO_2 (RS3.2).
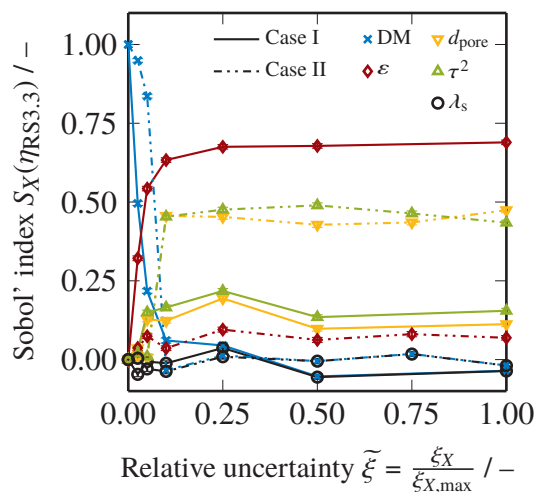
(b) Ethane to CO (RS3.3).

(c) Ethene to CO_2 (RS3.4).

(d) Ethene to CO (RS3.5).

Figure 3.8: Sobol' indices S_X for dependency of oxidative dehydrogenation of ethane catalyst efficiencies on relative uncertainty $\widetilde{\xi}$ using cases I and II, with definitions given in Table 3.2.
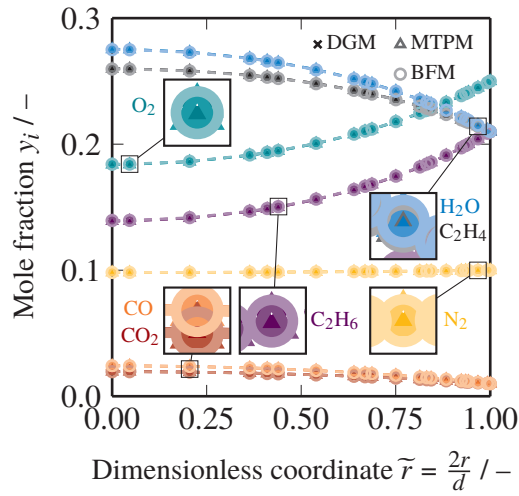
Figure 3.9: Profiles of mole fractions for oxidative dehydrogenation of ethane (RS3) at reference state conditions with 5 mm pellet diameter.

(a) ODH of ethane (RS3.1)

(b) Ethane to CO_2 (RS3.2).
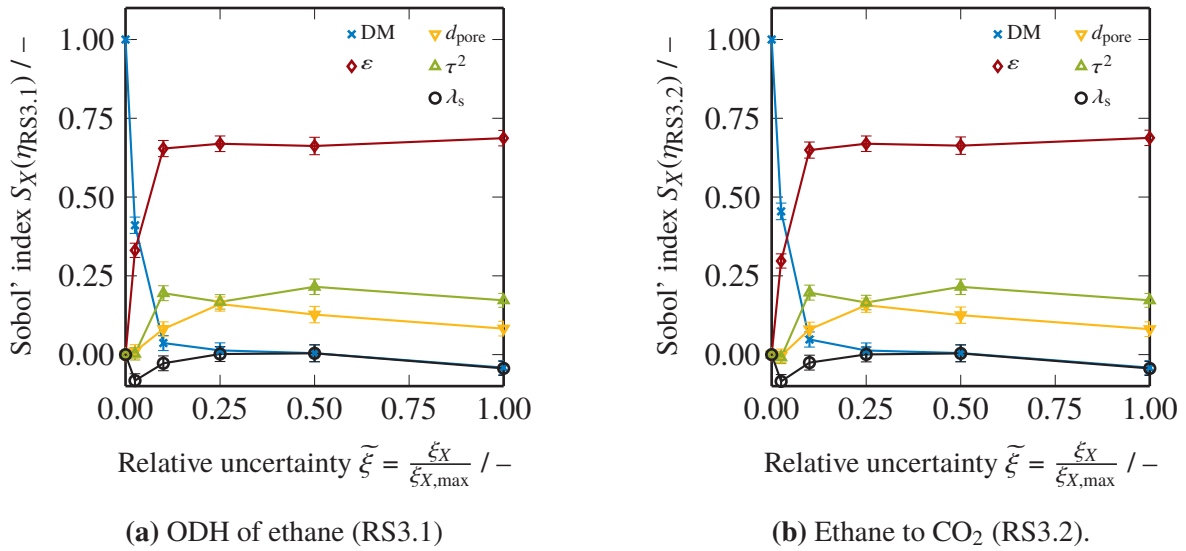
Figure 3.10: Sobol' indices S_X for dependency of oxidative dehydrogenation of ethane catalyst efficiencies on relative uncertainty $\widetilde{\xi}$ using a 5 mm pellet and $n_{exp} = 100$ number of experiments for Cases I, with definitions given in Table 3.2.
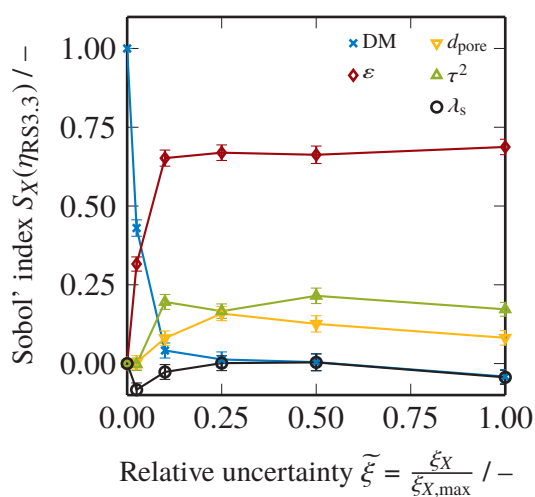
(c) Ethane to CO (RS3.3).
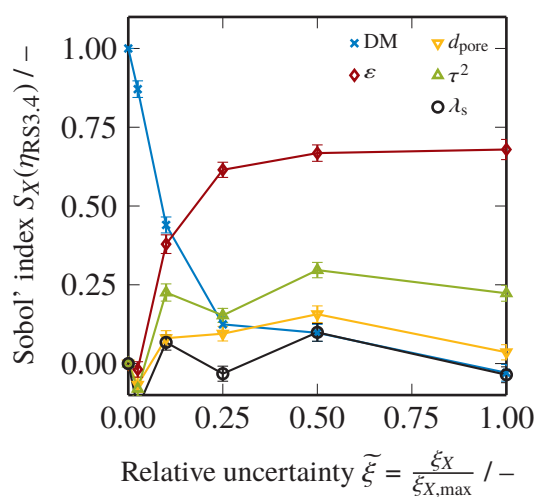
(d) Ethene to CO_2 (RS3.4).
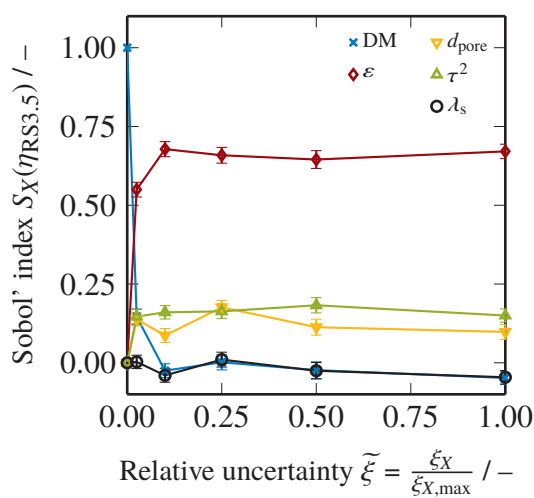
(e) Ethene to CO (RS3.5).

Figure 3.10: *(continued)*.

4 Multicomponent Diffusion inside 3D Shapes

On an industrial scale, the efficiency of heterogeneous catalysis is commonly subject to diffusive transport limitations. The binary friction model (BFM) combines Maxwell-Stefan-type diffusion, pore effects and viscous contributions for multicomponent reaction mixtures. A variety of catalyst shapes have been developed over the years to overcome transport problems. However, rigorous modeling of multicomponent diffusion-reaction problems in 3D geometries remains an ongoing challenge. The BFM is successfully applied to nine shapes, all varying in size and catalyst loading. The volume-to-surface ratio and the curvature of the bodies were found to be the characteristic features of the pellets, describing the reaction-diffusion interplay. With this, the 3D shape can be adequately approximated with straightforward 1D strategies. Finally, a comparison to Fickian diffusion models highlights the similarities and discrepancies to the Maxwell-Stefan concept of the BFM. These findings can contribute to an integral description of 3D reaction-diffusion problems in homogeneously-distributed, mesoporous catalysts.
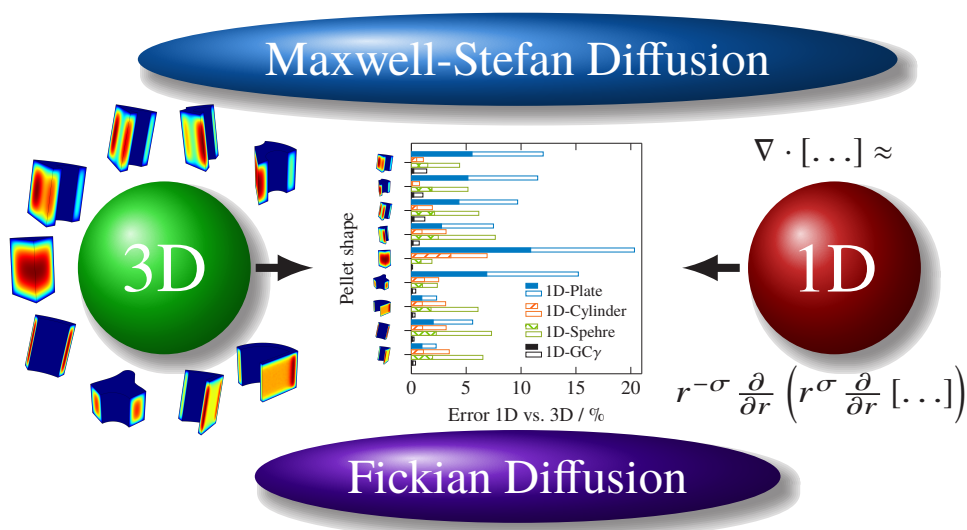
4.1 Introduction

Intraparticle mass transfer is of inherent importance for the integral evaluation of heterogeneously catalyzed chemical reactions. A fundamental understanding of the interplay between reaction and diffusion in porous media has been well established over the years [93, 94, 127]. There are many aspects, which have to be considered in modeling reaction-diffusion processes in catalyst.

First of all, the structure of the porous catalyst has to be adequately represented in a model. Here, a distinction must be made for the scale and the homogeneity of the porous material. Key characteristics comprise the pore structure, i.e. pore size (nano-, micro- and mesopores) [150] and the pore size distribution (mono-, bi- or multimodal) [151] as well as the distribution of the active material (e.g. homogeneously-distributed, coated, egg-shell, or core-shell).

In addition, it is important to distinguish between Fickian and Maxwell-Stefan representation for multicomponent diffusion, especially if the molecular transport is accompanied by the interplay of Knudsen diffusion in pores, surface migration, configurational diffusion and viscous effects. Maxwell-Stefan-based approaches combining these effects are well-known and were originally proposed by Mason and co-workers in the early 1960s in form of the dusty-gas model [103]. The mean transport-pore model by Schneider and co-workers [119], the binary friction model of Kerkhof [122] and the cylindrical pore interpolation model of Young and Todd [152] further developed and extended this theory. Based on the study presented in Chapter 3, the binary friction model (BFM) can be recommended as the method of choice.

Another important element is the actual shape of the catalyst pellet, which was analyzed for ideal 1D geometries by Aris [153]. Here, the volume-to-surface ratio was established as the characteristic length of choice for steady state problems. The major advantage of this work was the ability to give analytical solutions to basic reaction networks and kinetics. Over the past two decades, this concept has been extended by Barreto and co-workers [154–157]. In these studies, parameters were defined to approximate the catalytic behavior for specific 3D pellet shapes, mainly based on their geometrical features.

Furthermore, there have been efforts to actually solve the diffusion problem for higher dimensions. A 2D numerical solution for solid and hollow cylinders was first published by Dixon and Cresswell [158]. In addition, recent advances in particle-resolved modeling of catalytic fixed-bed reactors [159–161] led to an actual need for solving reaction-diffusion problems in 3D pellets as part of the full packed-bed system. For this, Dixon and co-workers [162–164] applied Maxwell-Stefan principles by using effective Fickian diffusivities derived from a modified dusty-gas law, which neglects intraparticle pressure gradients [165]. Nagaraj et al. reported to overcome this simplification by considering the viscous term in the dusty-gas model [166, 167]. Unfortunately, these results have not been published.

In this study, the binary friction model is applied to nine different 3D pellet shapes assuming a homogeneously-distributed, mesoporous structure with monomodal pore size distribution. CO_2 methanation and oxidative dehydrogenation (ODH) of ethane are employed as sample reaction

systems. Based on the catalyst effectiveness factor, all results are compared among themselves as well as to a 1D approximation. Additionally, the shapes are evaluated and compared to two Fickian models in terms of their diffusional behavior. Pressure gradients inside the pellets are enabled throughout this study.

4.2 Theory

Modeling of multi-dimensional diffusion-reaction systems in porous media requires a simultaneous solution of species, mass and energy governing equations. Here, the choice of diffusion model directly influences the complexity of the total equation system.

4.2.1 Mass Transfer in Porous Media

Binary diffusion coefficients $Đ_{ij}$ are calculated by the semi-empirical correlation of Fuller and co-workers [73, 114]

$$\left[\frac{Đ_{ij}}{\text{m}^2/\text{s}}\right] = \frac{10^{-7}\left[\frac{T}{\text{K}}\right]^{1.75}\left(\left[\frac{M_i}{\text{g/mol}}\right]^{-1} + \left[\frac{M_j}{\text{g/mol}}\right]^{-1}\right)^{\frac{1}{2}}}{\left[\frac{p}{\text{atm}}\right]\left(\left[\frac{\Delta v_i}{\text{cm}^3}\right]^{\frac{1}{3}} + \left[\frac{\Delta v_j}{\text{cm}^3}\right]^{\frac{1}{3}}\right)^2}. \tag{4.1}$$

Molecular diffusion coefficients for individual species in a mixture are approximated by the correlation of Fairbanks and Wilke [75] using the binary diffusion coefficients from Equation (4.1)

$$D_{i,\text{m}} = \frac{1 - y_i}{\displaystyle\sum_{\substack{j=1 \\ j \neq i}}^{n_{\text{species}}} \frac{y_j}{Đ_{ij}}}. \tag{4.2}$$

In this context, it is emphasized that although Equation (4.2) is widely used in describing reactive media, it is actually only valid for the case of one species diffusing through a stagnant mixture, or highly diluted systems [14]. More sophisticated approaches use stoichiometry ratios assuming dominating chemical reaction to account for the multicomponent nature of the system [162, 165].

The effects of the pore wall on the diffusion process is expressed by the Knudsen diffusion coefficient

$$D_{i,\text{Kn}} = \frac{d_{\text{pore}}}{3}\sqrt{\frac{8\mathcal{R}T}{\pi M_i}} \tag{4.3}$$

as a function of temperature T, molar mass M_i of species i, and the pore diameter d_{pore}. The impact of Knudsen diffusion on the overall transport process is dependent on the reaction system and conditions, as for example smaller pores and an elevated total pressure increase the significance of the pore wall interactions [141].

The nature of porous catalysts is incorporated using effective transport parameters for the diffusion coefficients $\mathcal{D}_{ij}$ in Equation (4.1) and $D_{i,Kn}$ in Equation (4.3)

$$
\begin{aligned}
\mathcal{D}_{ij}^{eff} &= \frac{\varepsilon}{\tau^2} \mathcal{D}_{ij}; \\
D_{i,Kn}^{eff} &= \frac{\varepsilon}{\tau^2} D_{i,Kn},
\end{aligned}
\tag{4.4}
$$

where ε is the pellet porosity and τ^2 represents the tortuosity factor, an empirical quantity [94, 115, 116]. If required, a pressure-driven viscous flux N_{visc} can be incorporated with Darcy's law

$$
N_{visc} = -\frac{B_0 c_t}{\eta} \nabla p,
\tag{4.5}
$$

dependent on the total molar concentration c_t and the fluid viscosity η. The permeability B_0 of the porous medium is expressed via Hagen-Poiseuille's law

$$
B_0 = \frac{\varepsilon}{\tau^2} \frac{d_{pore}^2}{32}.
\tag{4.6}
$$

This study compares three different approaches for diffusive mass transport inside porous media. The classical Fickian representation for the molar fluxes N_i of species i, is given to

$$
N_i = -D_{i,Fickian}^{eff} \nabla c_i.
\tag{4.7}
$$

Herein, the gradient of the concentration of i-species c_i is directly proportional to the respective flux. The effective diffusion coefficient $D_{i,Fickian}^{eff}$ can be approximated by the well-known Wilke-Bosanquet (WB) equation [168], where $D_{i,WB}^{eff}$ is defined as

$$
D_{i,WB}^{eff} = \left(\frac{1}{D_{i,m}^{eff}} + \frac{1}{D_{i,Kn}^{eff}} \right)^{-1}.
\tag{4.8}
$$

It has be demonstrated [97] that this approach is only valid for idealized situations. However, Equation (4.8) persists in the literature, most likely due to its simplicity and the possible usage

in Thiele-type analytic solutions. The validity of the WB model is limited to situations, where Knudsen diffusion dominates viscous forces [123]. Viscous terms can be incorporated via

$$D_{i,\text{vWB}}^{\text{eff}} = \left(\frac{1}{D_{i,\text{m}}^{\text{eff}}} + \frac{1}{D_{i,\text{Kn}}^{\text{eff}} + \frac{B_0}{\kappa_i}} \right)^{-1}. \tag{4.9}$$

An inherently different approach is based on a Maxwell-Stefan-type description of multicomponent mass transfer, where binary interactions between different components are adequately accounted for. A profound evaluation of the drawbacks of the Fickian representation compared to Maxwell-Stefan diffusion in modeling of intraparticle transport is for example given by Krishna [97]. Molar fluxes for the BFM are calculated via the following linear system [122]

$$N_i = -c_{\text{t}} \left[C \right]^{-1} \left(\nabla y_i + \frac{y_i}{p} \nabla p \right). \tag{4.10}$$

The transport matrix $[C]$ is defined as (cf. Equation (3.8))

$$c_{i,i} = \left(D_{i,\text{Kn}}^{\text{eff}} + \frac{B_0}{\kappa_i} \right)^{-1} \sum_{\substack{k=1 \\ k \neq i}}^{n_{\text{species}}} \frac{y_k}{\mathcal{D}_{ik}^{\text{eff}}}, \tag{4.11a}$$

$$c_{i,j} = -\frac{y_i}{\mathcal{D}_{ij}^{\text{eff}}}. \tag{4.11b}$$

Due to the incorporation of a viscous flux via the permeability B_0, the BFM is able to adequately describe non-equimolar diffusion, which may be caused for example by chemical reactions.

4.2.2 Governing Equations

Transport and chemical conversion for $n_{\text{species}} - 1$ species is described via

$$\nabla \cdot N_i = \varrho_{\text{p}} \dot{R}_i; \quad i = 1, \ldots, n_{\text{species}} - 1; \tag{4.12}$$

where ϱ_{p} is the density of the porous pellet. Total molar fluxes N_i are balanced with the net rate of production for species i, $\dot{R}_i$. The latter is calculated via the sum of all reactions n_{reaction}

$$\dot{R}_i = \sum_{j=1}^{n_{\text{reaction}}} v_{ij} \dot{r}_j. \tag{4.13}$$

Heat transport inside the porous catalyst is described using its effective thermal conductivity $\lambda_\mathrm{p}^\mathrm{eff}$ [127]

$$\nabla \cdot \left(\lambda_\mathrm{p}^\mathrm{eff} \nabla T\right) = \varrho_\mathrm{p} \sum_{j=1}^{n_\mathrm{reaction}} \Delta_\mathrm{r} H_j^\circ \dot{r}_j. \tag{4.14}$$

Conservation of mass is guaranteed with

$$\nabla \cdot \left(\sum_{i=1}^{n_\mathrm{species}} M_i N_i\right) = 0. \tag{4.15}$$

At this point, it is advisable to refer to the pitfalls arising from isobaric conditions inside the pellet. Jackson [127] extensively reviewed pressure variations within catalyst pellets. He pointed out that pressure gradients inside the pellets might be small compared to the ambient pressure, but must exist to free molar fluxes from the constraint of Graham's law. The impact of these pressure variations can be investigated by including Equation (4.15) to the overall problem definition. Nevertheless, assuming isobaric conditions can serve as a valuable approximation, even at industrially relevant conditions [169].

4.2.3 Reaction System

Two examples of reactions systems are investigated to demonstrate their influence on the catalyst effectiveness factor. First, carbon dioxide methanation is used as a single reaction problem

$$CO_2 + 4\,H_2 \rightleftharpoons CH_4 + 2\,H_2O. \tag{4.16}$$

The LHHW-model of Koschany et al. [129] for a $NiAlO_x$ catalyst is used.

Oxidative dehydrogenation of ethane over $MoVTeNbO_x$ serves as a second reaction system [131]

$$1: C_2H_6 + \frac{1}{2}\,O_2 \longrightarrow C_2H_4 + H_2O. \tag{4.17}$$
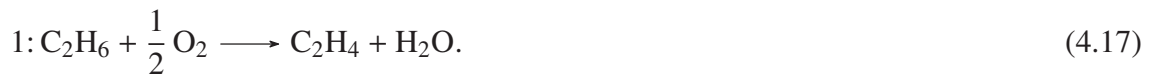
Side reactions comprise partial and total oxidation of ethane

$$2: C_2H_6 + \frac{7}{2}\,O_2 \longrightarrow 2\,CO_2 + 3\,H_2O \tag{4.18}$$

$$3: C_2H_6 + \frac{5}{2}\,O_2 \longrightarrow 2\,CO + 3\,H_2O \tag{4.19}$$

and of ethene

$$4: C_2H_4 + 3\,O_2 \longrightarrow 2\,CO_2 + 2\,H_2O \tag{4.20}$$

$$5: C_2H_4 + 2\,O_2 \longrightarrow 2\,CO + 2\,H_2O. \tag{4.21}$$

A detailed description of both reaction system is given in Appendix B.

4.3 Methodology

Within this study, nine catalyst pellets with a constant aspect ratio of $R/H = 1$ are investigated. Table 4.1 provides schematic illustrations of the individual geometries in top and isometric view. The symmetrical wedges used for computation are sketched by solid lines and correspond to the listed angles. The radii of the small holes of three and four hole cylinders (3H1, 4H1) are $0.25\,R$, like the respective indented versions (3H2, 4H2). The wall thicknesses of the ring filet and the wagon wheel shape are $1/\left(4\sqrt{2}\right)\,R$. Plain rings have an inner diameter of $0.75\,R$, while for double alpha pellets an inner diameter of $0.5\,R$ is chosen. Other features of the latter follow the respective patent literature [170].

The porous medium is described as a pseudo-continuum. Adopted from the study in Chapter 3, the parameters are chosen as follows: porosity $\varepsilon = 0.5$, tortuosity factor $\tau^2 = 4$, mean pore diameter $d_{pore} = 15\,$nm and effective pellet thermal conductivity $\lambda_p^{eff} = 1\,$W/mK.

For the CO_2 methanation reaction surface compositions representing three conversion levels X_{CO_2} of 0, 33.33 and 66.67 % are investigated at different densities of the active catalyst material ϱ_p, namely 500, 1000 and $1500\,$kg$_{cat}$/m^3. An overview of surface compositions is given in Table 4.2. A temperature T_{surf} of 260 °C and a total pressure p_{surf} of 8 bar are applied to shapes with an outer radius R ranging from 0.5 to 4.0 mm.

For oxidative dehydrogenation, 0 and 50 % ethane conversion levels are considered. Table 4.3 lists the respective compositions. Catalyst density is varied between 1000, 1500 and $2000\,$kg$_{cat}$/m^3, while surface conditions are constant at $T_{surf} = 400$ °C and $p_{surf} = 1\,$bar. The outer radius R ranges from 1 to 6 mm.

The 3D domain is discretized using four boundary layers at the outer surfaces with a first layer thickness of $R/250$ and a stretching factor of 1.2. Symmetry boundaries and internal volume are meshed with free tetrahedrals of a specified size of $R/25$. Grid convergence is confirmed on effectiveness factors as well as pressure and temperature changes using the grid convergence index [171]. Details are given in Supplementary Material 4.S.1.

The resulting system of governing equations (4.12), (4.15) and (4.14) is implemented in COMSOL Multiphysics 5.3a using coefficient form PDE modules. Linear Lagrange finite elements are applied to all variables. Due to the high degree of coupling and the strong non-linearities arising from the chemical reactions, a fully-coupled direct MUMPS solver was found

Table 4.1: Definition of pellet shapes, with geometrical features and the angle of the wedge used for computation with COMSOL Multiphysics.
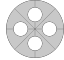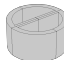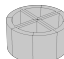
Shape	Abbr.	Hole radius	Wall thickness	Wedge angle	Topview	Isometry
Three Hole (1)	3H1	$0.25\,R$	-	$60°$		
Three Hole (2)	3H2	$0.25\,R$	-	$60°$		
Four Hole (1)	4H1	$0.25\,R$	-	$45°$		
Four Hole (2)	4H2	$0.25\,R$	-	$45°$		
Cylinder	CYL	-	-	$45°$		
Double Alpha	DAL	$0.50\,R$	-	$90°$		
Ring Filet	RIF	-	$\frac{1}{4\sqrt{2}}\,R$	$90°$		
Ring	RIN	$0.75\,R$	$0.25\,R$	$45°$		
Wagon Wheel	WAW	-	$\frac{1}{4\sqrt{2}}\,R$	$45°$		

Table 4.2: Summary of surface compositions for different conversion levels of the CO_2 methanation reaction.

X_{CO_2} %	Mole fraction $y_{i,\text{surf}}$			
	CO_2	H_2	CH_4	H_2O
0	0.8	0.2	0	0
33.33	0.154	0.615	0.077	0.154
66.67	0.091	0.364	0.181	0.364

Table 4.3: Summary of surface compositions for different conversion levels of the ODH reaction.

$X_{C_2H_6}$	Mole fraction $y_{i,\text{surf}}$					
%	C_2H_6	O_2	C_2H_4	H_2O	CO_2	CO
0	0.5	0.4	0	0.1	0	0
50	0.208	0.059	0.208	0.467	0.025	0.033

to be the most robust solution method. The composition dependencies of the transport parameter ($D_{i,\text{WB}}$, $D_{i,\text{vWB}}$, and $[C]$) are fully accounted for during solving. The inverse of the non-singular Maxwell-Stefan transport matrix $[C]$ in Equations (4.10) and (4.11) is obtained analytically in a universal coefficient form, using the algebraic data tool MuPad. In this way, computational effort can be minimized by drastically reducing the degrees of freedom of the system, keeping memory requirements at a reasonable level. The analytical inverse of the respective transport matrices (4.10) for four (CO_2 methanation) and six (ODH of ethane) component systems are provided in Supplementary Material of the original publication.

Computational results are evaluated based on several characteristic values. Most importantly, the catalyst effectiveness factors are obtained for single reactions j

$$\eta_{\dot{r}_j} = \frac{\int_{V_p} \dot{r}_j \mathrm{d}V}{V_p \cdot \dot{r}_{j,\text{surf}}} \tag{4.22}$$

and for the net rate of production $\dot{R}_i$ of a species i

$$\eta_{\dot{R}_i} = \frac{\int_{V_p} \dot{R}_i \mathrm{d}V}{V_p \cdot \dot{R}_{i,\text{surf}}} \tag{4.23}$$

For single reaction systems, both effectiveness factors types (4.22) and (4.23) become identical. Classically, catalyst effectiveness factors are evaluated in dependence on the Thiele modulus Φ. For reactions of the form A $\longrightarrow$ B Aris proposed a generalized form of the Thiele modulus [14, 153]

$$\Phi = \frac{V_p}{A_p} \sqrt{\frac{\varrho_p \dot{r}_{\text{surf}}}{D_{i,\text{m}}^{\text{eff}} c_{i,\text{surf}}}}. \tag{4.24}$$

However, diffusion coefficients $D_{i,\text{m}}^{\text{eff}}$ are generally dependent on the mixture composition inside the pellet and Thiele moduli can not be defined for systems with more than one reaction [14]. Nevertheless, for a homogeneously-distributed catalyst the pellet density ϱ_p

remains an independent and constant parameter for all reactions and compositions. Therefore, it is possible to define a combined shape and material parameter

$$\chi_{\rm p} = \frac{V_{\rm p}}{A_{\rm p}} \cdot \sqrt{\varrho_{\rm p}} \tag{4.25}$$

for each pellet. Hereby, the influence of the catalyst loading, represented by the catalyst density $\varrho_{\rm p}$, and the geometry of the pellet are combined to one parameter. The latter is expressed via the volume-to-surface ratio $V_{\rm p}/A_{\rm p}$, as recommended by Aris [153]. The unit of $\chi_{\rm p}$ is $(\rm kg/m)^{0.5}$.

In addition, the temperature and pressure changes inside the catalyst pellets are investigated:

$$\Delta T = \max{(T)} - T_{\rm surf}; \tag{4.26}$$

$$\Delta p = \begin{cases} \max{(p)} - p_{\rm surf} & \text{for } p \geq p_{\rm surf}, \\ \min{(p)} - p_{\rm surf} & \text{for } p < p_{\rm surf}. \end{cases} \tag{4.27}$$

Different approaches are compared by using the percentage error $PE\,(\rm A,B)$ of two models A and B. For a comparison of an effectiveness factor $\eta_{\dot{r}_j}$, PE is defined as

$$PE_\eta\,(\rm A,B) = \frac{\eta_A - \eta_B}{\eta_B}. \tag{4.28}$$

An overall comparison of models is achieved by the mean absolute percentage error

$$MAPE\,(\rm A,B) = \frac{\left| \sum_{i=1}^{n_{\rm sim}} PE_{\eta,i}\,(\rm A,B) \right|}{n_{\rm sim}} \tag{4.29}$$

for all available simulations $n_{\rm sim}$. Finally, the maximum absolute percentage error

$$MaxAPE\,(\rm A,B) = \max{\left| PE_{\eta,i}\,(\rm A,B) \right|} \tag{4.30}$$

provides insights into the magnitude of the observed deviations.

4.4 Results and Discussion

In a first step, the selected shapes in Table 4.1 are compared using the binary friction model in Equation (4.10) for multicomponent diffusion. Subsequently, an evaluation of 1D approximation procedures for the BFM provides insights into the possibilities and challenges arising from the reduction of the dimensions. Finally, the two presented Fickian approaches WB (4.8) and vWB (4.9) are compared to the Maxwell-Stefan-type BFM. Basic insights to the two reaction diffusion system of this study is provided in the Supplementary Material 4.S.2. Herein, mole fraction profiles inside a CYL-type pellet demonstrate the diffusional behavior.

4.4.1 Influence of Pellet Shape

As a first step, the effectiveness of the nine shapes in Table 4.1 are investigated. From an industrial point of view, the effectiveness of a catalyst for a specific target is most important. In Figure 4.1, species effectiveness factors (4.23) for CH_4 and C_2H_4 are compared to the mass of catalyst pellet. In Section 4.S.3 of the Supplementary Material the surface area and volume of the pellets are evaluated and compared to the results presented in Figure 4.1.
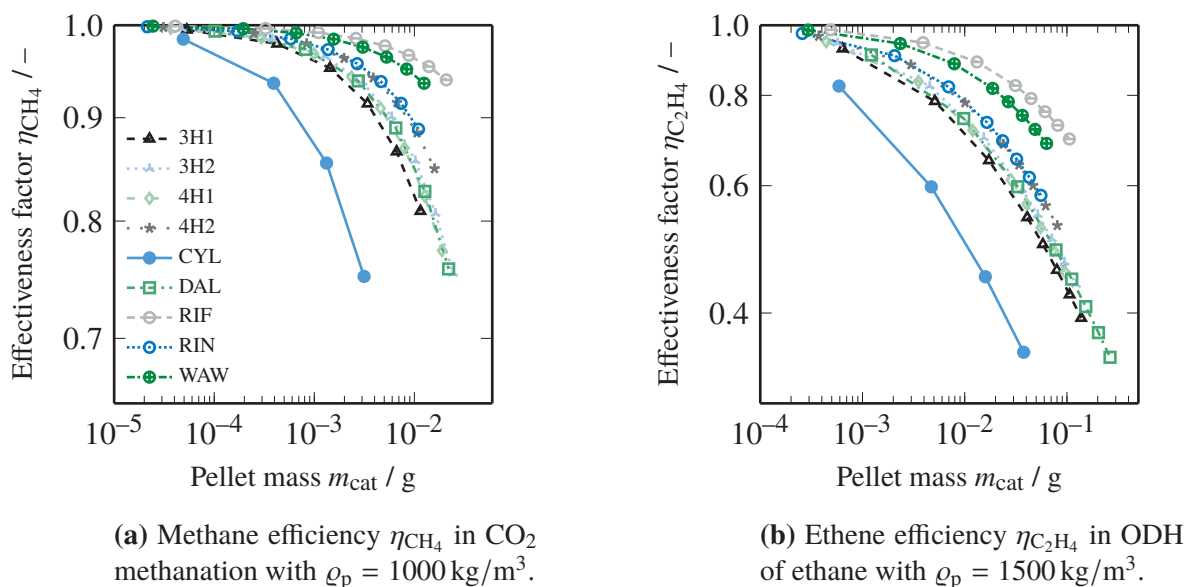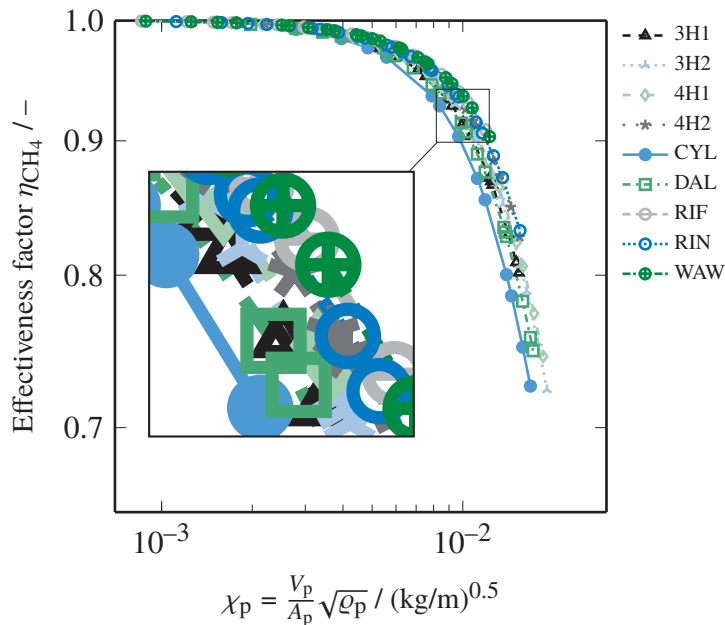

(a) Methane efficiency η_{CH_4} in CO_2 methanation with $\varrho_p = 1000\,\mathrm{kg/m^3}$.

(b) Ethene efficiency $\eta_{C_2H_4}$ in ODH of ethane with $\varrho_p = 1500\,\mathrm{kg/m^3}$.

Figure 4.1: Target product species effectiveness factor for different pellet masses at $0\,\%$ reactant conversion (cf. Tables 4.2 and 4.3). Definition of shapes is given in Table 4.1.

For both reaction systems, similar trends become apparent. While distinct diffusion limitations prevail for the solid cylinder (CYL), internal holes and indentions yield significantly higher effectiveness factors. In both cases, best yield per mass of active material is achieved for RIF-type shapes, while the similar WAW pellets are almost as effective. The difference between RIF and WAW type arises from the representation by pellet mass. For the same mass of active material, the RIF type has a bigger dimension and, hence, provides a higher surface area per mass of catalyst compared to the WAW type (cf. Figure 4.9). Indentions on the outer surface allow a slight increase in efficiency, as demonstrated by the profiles of 3H1 and 4H1 compared to 3H2 and 4H2 shapes, respectively.

The classic volume-to-surface ratio V_p/A_p is combined with the variable catalyst density ϱ_p to a shape-material parameter χ_p, defined in Equation (4.25). Figure 4.2 shows the applicability of this parameter. Besides the dimension of the pellets, also the catalyst density has been varied. In Figure 4.2 effectiveness factors for all nine shapes exhibit similar behavior confirming the suitability of the parameter χ_p.

However, as represented in Figure 4.2, the shape-material parameter does not completely generalize all 3D pellets. Differences in the curvature of the respective geometries affect the

(a) Methane efficiency η_{CH_4} in CO_2 methanation with ϱ_p from 500 to 1500 kg/m^3.
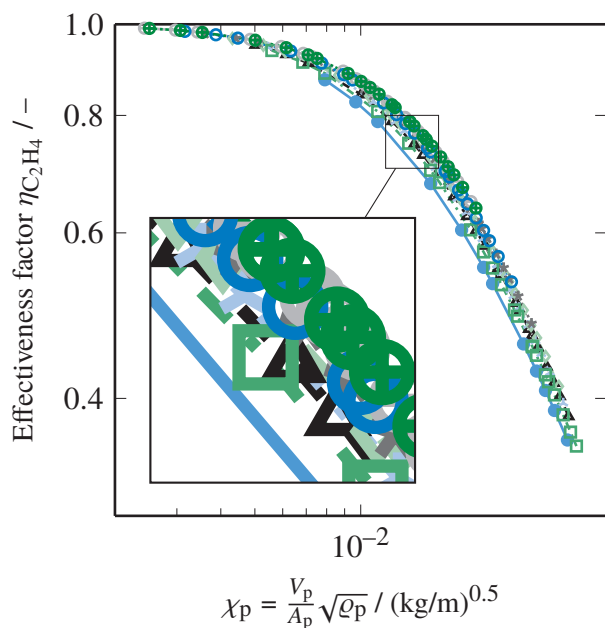
(b) Ethene efficiency $\eta_{C_2H_4}$ in ODH of ethane with ϱ_p 1000 to 2000 kg/m^3.

Figure 4.2: Species effectiveness factor η_i for different shape-material parameters χ_p. Definition of shapes is given in Table 4.1.

Table 4.4: Shape factors σ for pellets defined in Table 4.1 according to the 1D GCγ-model of Mariani et al. [154] Details of the model and solution routine are provided in the Supplementary Material 4.S.4.

Shape	σ
3H1	1.2876
3H2	1.0395
4H1	0.9055
4H2	0.6716
CYL	2.6154
DAL	1.4682
RIF	0.3883
RIN	0.5669
WAW	0.3768

diffusion length inside the catalyst pellets. In this regard, a shape factor σ as part of a 1D generalized cylinder model (1D GC) [172] can be used to evaluate the curvature. Barreto and co-workers developed two strategies to estimate σ values [156]. For constant aspect ratios, the 1D GCγ model of Mariani et al. [154] gives σ values, which are independent of the reaction type and the pellet radius R (cf. Table 4.4). Definition and basic principles of this methodology are given in Section 4.S.4 of the Supplementary Material.

By comparing these values to the 1D geometries of a sphere ($\sigma = 2$), infinite cylinder ($\sigma = 1$) and plate ($\sigma = 0$), it is possible to assess the curvature of the shapes. RIF- and WAW-type shapes, for example, exhibit a low σ value, while the shape factor of CYL-type pellets even exceeds the value for a sphere. The σ value can then be used to classify the shapes within the sequence from infinite 1D plate over infinite 1D cylinder to a regular sphere.

4.4.2 1D Approximation

Reaction-diffusion simulations in 3D structures should draw a more realistic picture of the processes in real catalyst shapes. To incorporate advanced pellet geometries in continuum reactor simulations, it is desirable to mimic the situation in 3D shapes using a straightforward 1D approach.

As described above, this can be achieved by applying the concept of a generalized cylinder [154, 172]. Here, this approach is adopted and applied on Maxwell-Stefan-type diffusion by taking the BFM as example. The basic idea is to replace the divergence operator $\nabla \cdot$ in the species (4.12), heat (4.14) and mass (4.15) balances by a 1D equivalent along the coordinate r. For this purpose, the shape factor σ is used to describe the curvature of the 3D structures. The divergence is approximated by

$$\nabla \cdot [\ldots] \approx r^{-\sigma} \frac{\partial}{\partial r} \left(r^{\sigma} \frac{\partial}{\partial r} [\ldots] \right).$$
(4.31)

Thereby, the dimension of the problem can be reduced to one. Due to the lack of an established method, it is unfortunately common practice to approximate non-spherical catalysts by a 1D cylinder ($\sigma = 1$) or sphere ($\sigma = 2$) using the volume-to-surface ratio as the characteristic length. The 1D GCγ of Mariani et al. [154] allows to use the shape factors σ in Table 4.4 for a promising, alternative approach.

In Figure 4.3, the mean average *MAPE* and the maximum percentage errors *MaxAPE* for both reaction system are compared for different 1D approximations. Estimates by an infinite plate ($\sigma = 0$) partly resulted in very high errors values and are not shown for the purpose of representation. It is noteworthy that, for the RIF and WAW shapes a 1D plate produced acceptable approximations below the 1D cylinder and sphere, respectively. *MAPE* and *MaxAPE* values for all shapes, reactions and approximations are provided in the Supplementary Material 4.S.5.

From a global point of view, the trends for CO_2 methanation in Figure 4.3a and ODH of ethane in Figure 4.3b are similar, although the magnitude of the errors is greater for the latter. In both reaction systems, the highest values for *MaxAPE* and *MAPE* are observed for the 1D sphere approximation. The 1D cylinder model outperforms a spherical approximation for all pellet shapes, except for DAL and CYL. This correlates with the shape factor values listed in Table 4.4, where σ (DAL) = 1.4682 and σ (CYL) = 2.6154 are closest to the value of an ideal sphere, i.e., $\sigma = 2$.

The approximation by the 1D GCγ of Mariani et al. [154] gives remarkably good approximations, which remain below *MAPE* = 0.2 % and *MaxAPE* = 1.5 % for CO_2 methanation and *MAPE* = 1.5 % and *MaxAPE* = 2.5 % for ODH of ethane, respectively (cf. Tables 4.5 to 4.10). However, the comparison of the two reaction systems also illustrates the impact of individual reactions on the diffusion processes inside porous catalysts.

As demonstrated in Figure 4.3b, the 1D cylinder model produces smaller errors compared to the 1D GCγ approximation for the 3H1 and 3H2 shape. This effect can be caused by insufficient handling of the kinetics or of the curvature and edges of the shapes during the approximation [156, 173, 174]. Nevertheless, the 1D GCγ model proves to be flexible, accurate and reliable at the same time, when applied to a multicomponent diffusion model including Maxwell-Stefan, heat and momentum transport. Therefore, the 3D structure can be adequately represented by a single characteristic parameter σ.

In summary, for the reaction systems investigated in this study, it is possible to use the 1D GCγ approximation for 3D shapes. Furthermore, the degrees of freedom needed to solve the reaction-diffusion problem are at least three orders of magnitude smaller for 1D geometries compared to 3D. Hence, the computational effort is drastically reduced and elaborated pellet geometries can be incorporated in commonly used continuum approaches for chemical reactor design.
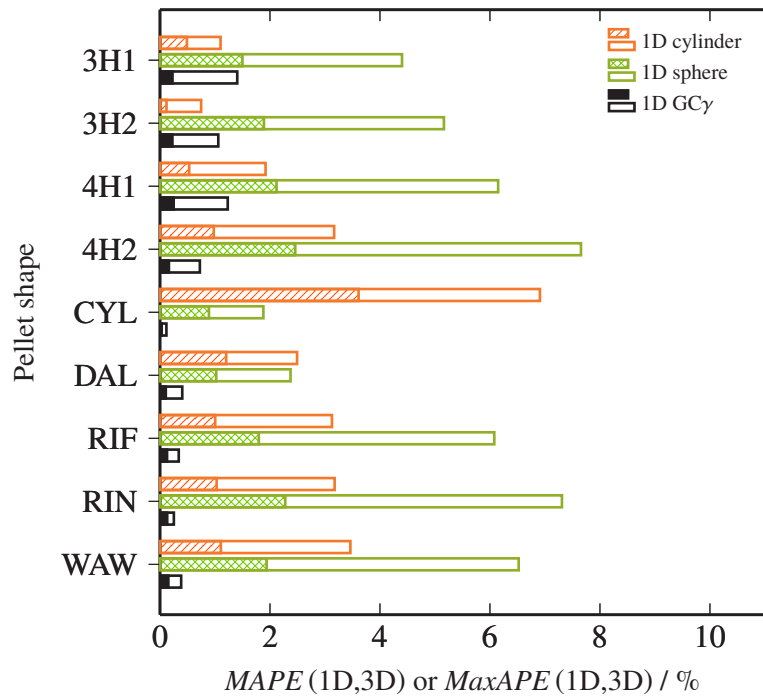
(a) CO_2 methanation reaction (4.16).
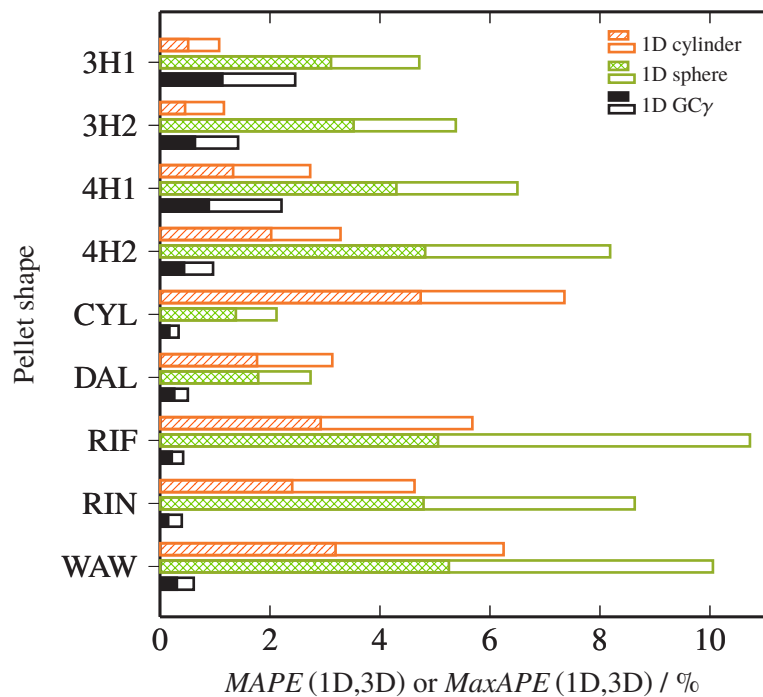
(b) ODH of ethane (4.17).

Figure 4.3: Overview of approximation errors for 1D models compared to 3D simulations. Filled bars represent mean average percentage errors *MAPE* (4.29) and open bars the maximum percentage errors *MaxAPE* (4.30). Values are calculated based on all conversion boundary conditions.

4.4.3 Comparison of Diffusion Models

Finally, the effect of Maxwell-Stefan-type diffusion for the selected reaction systems is evaluated by a comparison to the WB and vWB approaches. The three models differ in two major assumptions. First, while WB and vWB rely on Fickian diffusion, the BFM can account for multicomponent effects, such as diffusive fluxes at zero gradient of the mole fraction. Second, the Fickian approach is based on one effective diffusion coefficient for each species, while the BFM directly couples molecular (4.1) and Knudsen (4.3) diffusion with the viscous flux term (4.6) in a physically consistent way [116].
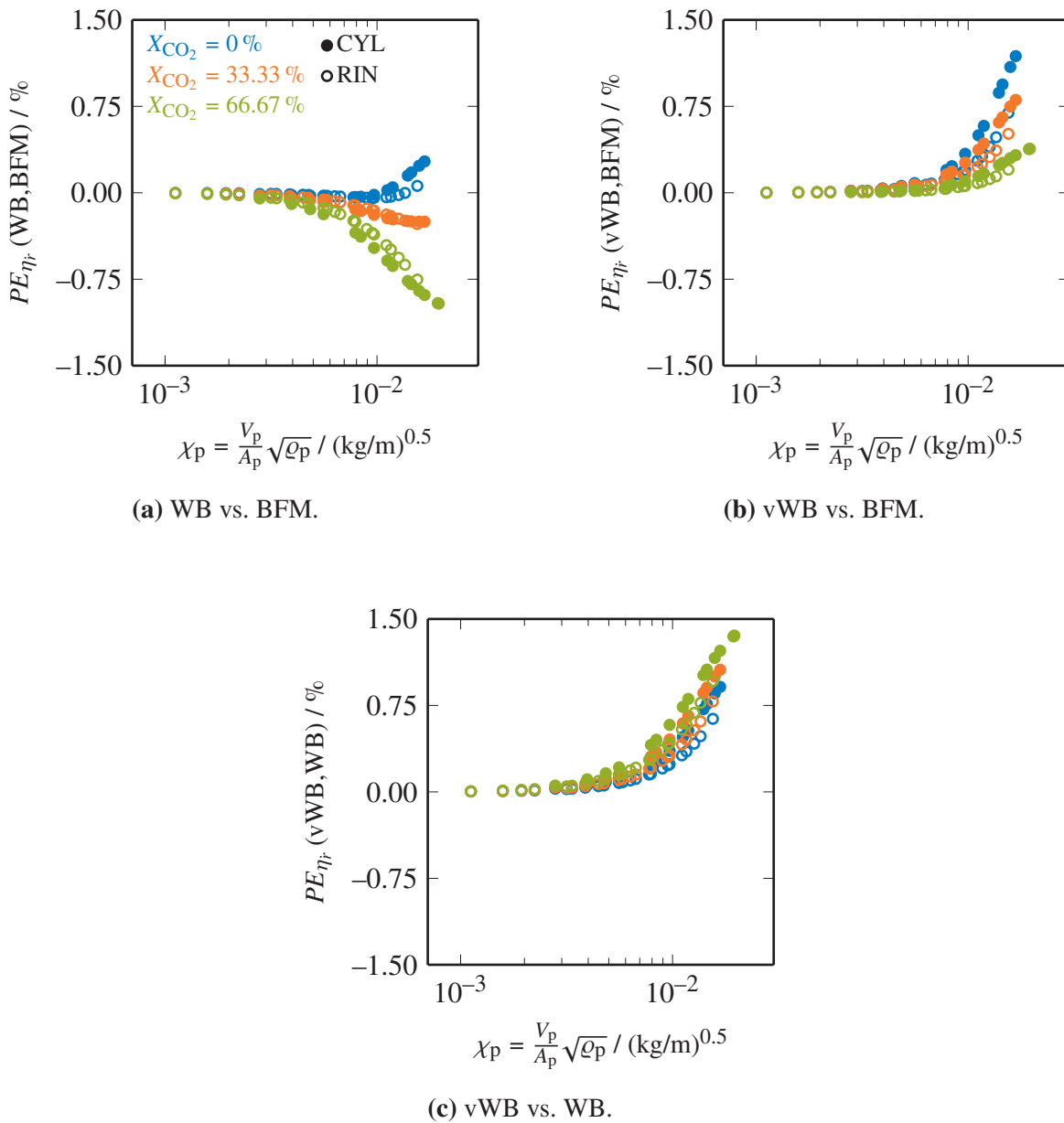

(a) WB vs. BFM.

(b) vWB vs. BFM.

(c) vWB vs. WB.

Figure 4.4: Percentage errors of pellet effectiveness factor (4.22) between diffusion models for CO_2 methanation reaction.

(a) WB vs. BFM.

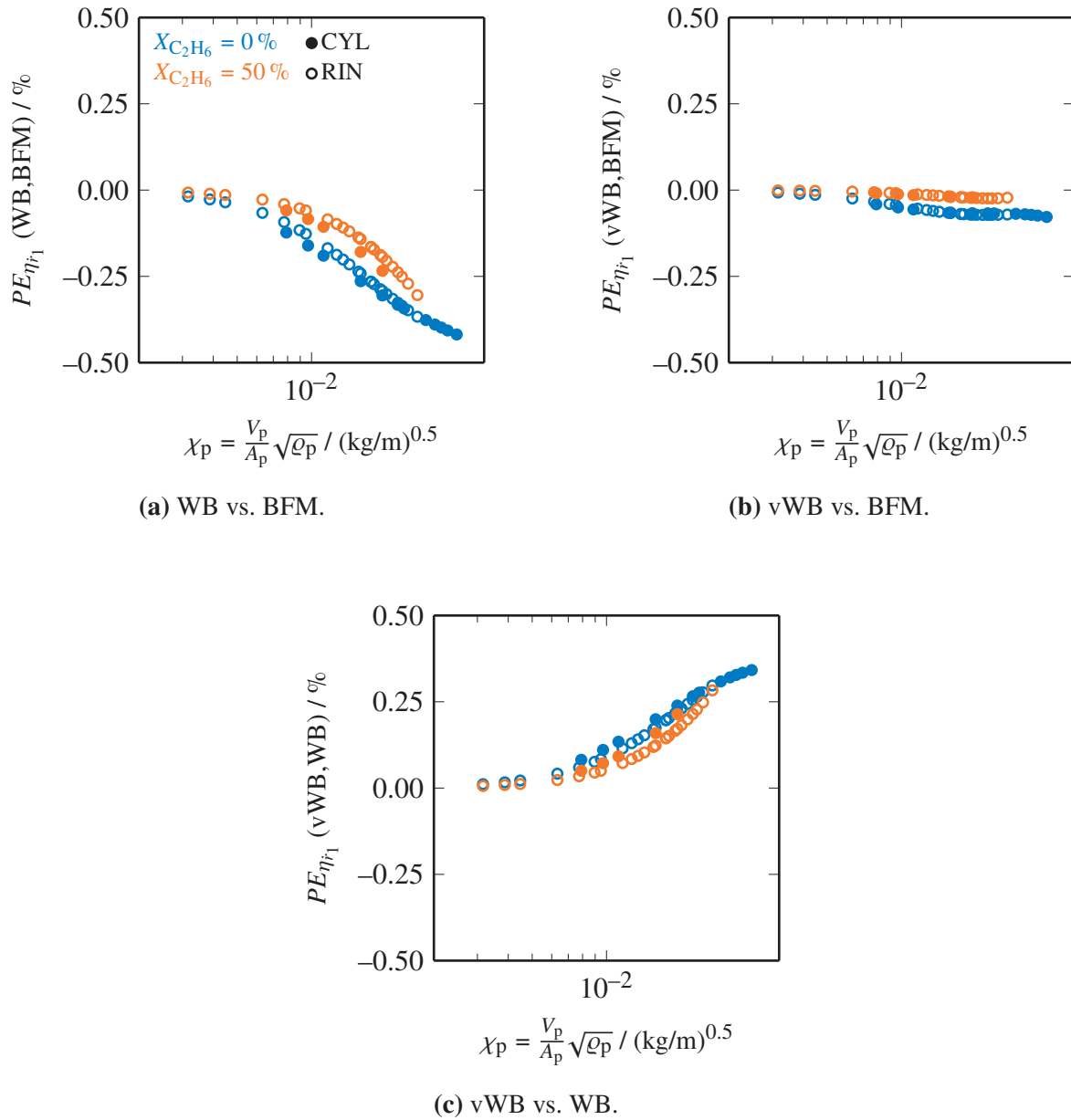(b) vWB vs. BFM.

(c) vWB vs. WB.

Figure 4.5: Percentage errors of pellet effectiveness factor (4.22) between diffusion models for ODH of ethane reaction 1 (4.17).

Figures 4.4 and 4.5 illustrate percentage errors $PE_{\eta_{\dot{r}}}$ between the diffusion models in dependence on the shape-material parameter χ_{p} (4.25) for CYL- and RIN-type pellets. Differences between the three diffusion models for CO_2 methanation are displayed in Figure 4.4 for all boundary compositions (cf. Table 4.2). In general, the differences are moderate and range from -1.5 to $1.0\,\%$. However, $PE_{\eta_{\dot{r}}}$ values directly correlate with the pellet dimension expressed via the shape-material parameter χ_{p}. As can be seen in Figure 4.1a, at small χ_{p} values diffusion is not limiting the reaction ($\eta_{\dot{r}} \approx 1$) and consequently percentage errors $PE_{\eta_{\dot{r}}}$ become zero. At increased pellet dimensions ($\chi_{\mathrm{p}} > 2 \cdot 10^{-3}\,(\mathrm{kg/m})^{0.5}$), evident differences between the models become observable.

Comparing the WB approach to the BFM in Figure 4.4a, distinct trends for each conversion level are observed. While for $X_{CO_2} = 0\,\%$ the WB approach overestimates the values of the BFM, higher conversion levels of 33.33 and 66.67\,\% lead to an underestimation.

The influence of viscous terms is directly visible in Figure 4.4c. Here, for all three conversion levels, the inclusion of a viscous term in the vWB equation leads to higher $\eta_{\dot{r}}$ values relating to the WB approach. Surface compositions, expressed by the CO_2 conversion levels, have only a slight effect on $PE_{\eta_{\dot{r}}}$ (vWB,WB) values.

The comparison of vWB and BFM in Figure 4.4b can, hence, be a direct measure of the difference between Fickian and Maxwell-Stefan-type diffusion models. The differences become observable at shape-material parameters above $10^{-2}\,(\mathrm{kg/m})^{0.5}$. Here, $PE_{\eta_{\dot{r}}}$ (vWB,BFM) curves for the three conversion levels fan out, indicating the inherently different treatment of multicomponent diffusion.
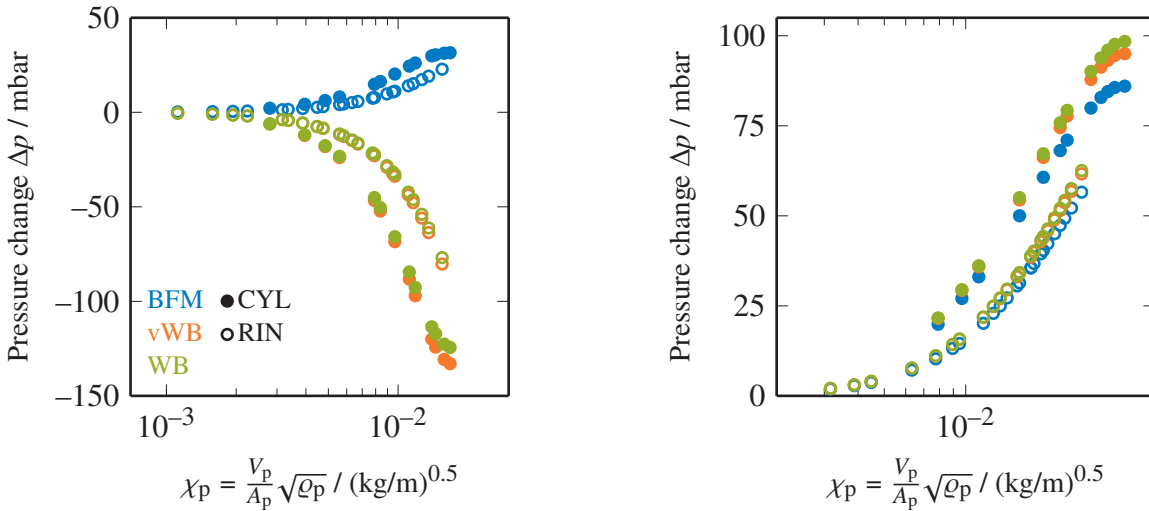
(a) CO_2 methanation (cf. Table 4.2).

(b) ODH of ethane (cf. Table 4.3).

Figure 4.6: Comparison of pressure changes (4.27) at zero conversion surface conditions.

In Figure 4.6a, this mechanistic difference between Fickian and Maxwell-Stefan diffusion models is directly expressed by reversed signs for the pressure changes Δp inside the pellets. While the WB and vWB approaches follow the stoichiometric volume decrease of the

methanation reaction with a mole change from 5 to 3, cf. Equation (4.16), the BFM predicts a pressure increase. This is caused by the fast diffusion of hydrogen combined with the interspecies momentum exchange (cf. Section 3.4.1). The latter is not covered by Fickian approaches, which simply follow the reaction stoichiometry. The absolute Δp values decrease with increased feed concentrations at the pellet surface, shown in Figure 4.10 of the Supplementary Material. The overall pressure change inside the pellets is less than 150 mbar for the selected conditions being relatively small compared to the total pressure of 8 bar. However, a change of 150 mbar inside a CYL pellet can cause a pressure gradient up to 150 bar/m representing a significant driving force for the viscous transport (cf. Equation (4.5)).

For the oxidative dehydrogenation reaction (4.17), differences between the models are less pronounced, as shown in Figure 4.5. On the one hand, this is caused by similar trends for the pressure change (cf. Figure 4.6b), indicating a low impact of the Maxwell-Stefan-type treatment (BFM) on the description of the diffusive fluxes compared to a simple Fickian approach (WB, vWB). On the other hand, the ODH reaction system consists of molecules similar in molecular weight and size, which leads directly to comparable diffusion behavior of each species. For this example, all pressure changes are positive following the reaction stoichiometry (cf. Equations (4.17) to (4.21)). The error of approximating the multicomponent system by Fickian diffusion decreases for the ODH system. This fact is reflected by the low percentage errors $PE_{\eta_{\dot{r}_1}}$ (WB,BFM) and $PE_{\eta_{\dot{r}_1}}$ (vWB,BFM) in Figures 4.5a and 4.5b, respectively. For the latter case, the percentage errors become negligible. Hence, the differences between WB and BFM shown in Figures 4.5a and 4.5c are mainly caused by the missing viscous flux term in the WB approach. Results for the side reactions (4.18) to (4.21), given in the Supplementary Material 4.S.6, further confirm the situation shown in Figure 4.5.

As shown in Figures 4.11 and 4.12 of the Supplementary Material, intraparticle changes in temperature (4.26) for both reaction systems essentially depend on the surface composition as well as on the shape-material parameter χ_p of the pellet. It is noteworthy, that the RIN type pellet exhibits reduced ΔT values throughout all simulations. The constant wall thickness of the shape results in homogeneously-distributed composition and temperature preventing hotspot formation. All other shapes feature either unequal or comparably thick walls allowing for potential internal hotspots (cf. Table 4.1). Furthermore, slight differences between CYL- and RIN-type pellets occur for $PE_{\eta_{\dot{r}}}$ (cf. Figures 4.4 and 4.5) and Δp (cf. Figure 4.6).

In summary, the comparison of Fickian (WB,vWB) and Maxwell-Stefan-type (BFM) strategies for intraparticle diffusion in 3D pellets provide valuable insights. First of all, for the selected conditions, the observed differences between the models are moderate for both reactions systems presented in this study. However, for CO_2 methanation, the different diffusion concepts yield a fundamental discrepancy expressed in the reversed sign of the pressure change Δp. Furthermore, the inclusion of viscous flux terms is the main reason for the differences observed in ODH of ethane.

4.5 Conclusion

The binary friction model, a Maxwell-Stefan-type multicomponent diffusion approach, including viscous flux terms, molecular and Knudsen diffusion, has been successfully applied to industrially relevant 3D pellet geometries built of an equally distributed, mesoporous structure with monomodal pore size distribution. No further assumptions or constraints are needed to solve the coupled transport processes.

A comparison of nine different shapes confirms that the volume-to-surface ratio is a key parameter for predicting the pellet's effectiveness factor. Additionally, the curvature influencing these geometries is adequately described by the shape factor obtained from a method of Mariani et al. [154]. This strategy is adapted to approximate the reaction-diffusion phenomena inside the 3D geometries using a 1D model. An error-based comparison validates the 1D GCγ model as a flexible and robust tool mimicking multicomponent diffusion processes in 3D shapes.

Finally, a Maxwell-Stefan-type approach (BFM) is compared to two Fickian models. For the reaction systems and conditions of this modeling study, all three approaches result in similar values of catalyst effectiveness factors. However, the significance of Maxwell-Stefan diffusion is demonstrated by the reverse sign of the pressure gradient inside all pellets, observable for CO_2 methanation.

For future work, the presented methodology serves as a valuable example for reaction diffusion problems inside 3D pellet shapes. On the one hand, an integral evaluation of the 3D case can be used to justify certain 1D approximations. On the other hand, optimization of the pellet geometry and catalyst loading remains an ongoing challenge.

4.S Supplementary Material

4.S.1 Grid Convergence Study

Grid convergence is confirmed for effectiveness factors as well as pressure and temperature changes using the grid convergence index [171]. The methodology, originally developed for finite volume techniques, is adapted for the finite element environment of COMSOL Multiphysics [175]. For this purpose, a representative mesh size $\overline{h}$ is defined as the arithmetic mean over all nodes [171]

$$\overline{h} = \frac{1}{N_{\text{nodes}}} \sum_{i=1}^{N_{\text{nodes}}} h_i. \tag{4.32}$$

In total, three different mesh sizes of $R/15$, $R/20$ and $R/25$ are tested. The first boundary layer has a thickness of $R/150$, $R/200$ and $R/250$, respectively. Following the procedure recommended by Celik et al., the convergence of the grid can be evaluated using the grid convergence index GCI_{fine} [171].

The catalyst effectiveness factor $\eta_{\dot{r}_1}$ (4.22), the signed temperature ΔT (4.26) and pressure change Δp (4.27) are selected as response variables. In Figure 4.7, the grid convergence indices $GCI_{\text{fine}}^{(R/25)(R/20)}$ are displayed for a selection of shapes for ODH of ethane, cf. Equation (4.17), at a given surface composition of $X_{C_2H_6} = 0\,\%$.

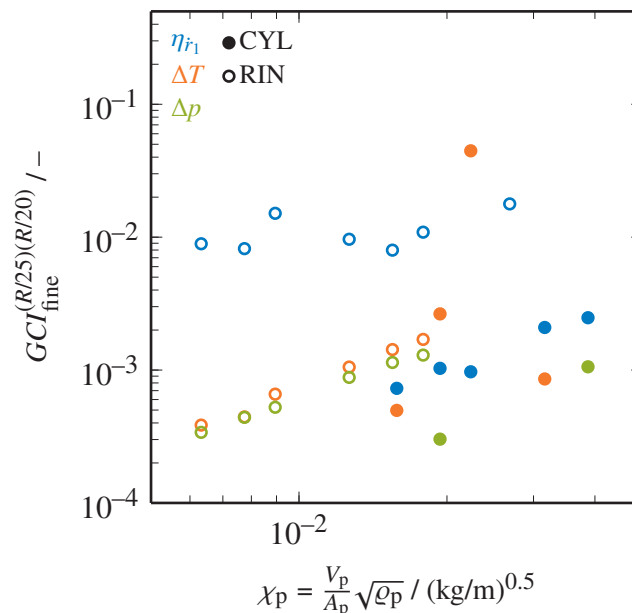**Figure 4.7:** Evaluation of grid convergence for selected shapes for ODH of ethane (4.17) at $X_{C_2H_6} = 0\,\%$.

The $GCI_{\text{fine}}^{(R/25)(R/20)}$ values are below 4.5 % for the selected conditions, which shows that the grid size of $R/25$ is sufficiently fine [171]. Hence, influences of mesh size are expected to be negligible and grid convergence is reached.

4.S.2 Test Cases

Exemplary cases of the plain cylinder (CYL) are evaluated for both reaction systems. Figure 4.8 shows centerline plots at zero conversion applying the binary friction model. For CO_2 methanation, different diffusivities of H_2 and CO_2 become apparent. While close to the pellet center CO_2 is completely consumed, hydrogen is present in excess. This is caused by the fact that the effective diffusivity of H_2 is considerably higher compared to all other species. This leads to a small gradient of the respective mole fraction profile y_{H_2}, deviating from the nominal stoichiometric ratio of 4:1, related to CO_2 (4.16). The example corresponds to a catalyst effectiveness factor of $\eta_{\dot{r}} = 0.75$.

Mole fraction profiles for oxidative dehydrogenation of ethane depict the high production of H_2O arising from the oxidation reactions. For the chosen conditions, CO is formed faster compared to the full oxidation product CO_2. The catalyst effectiveness factor for reaction $\dot{r}_1$ is determined to be $\eta_{\dot{r}_1} = 0.60$ for the selected conditions.

While pressure changes are more pronounced for ODH of ethane compared to CO_2 methanation, temperature rises inside the CYL pellet behave vice versa. Interestingly, for CO_2 methanation an increase in pressure is observed, which is counterintuitive to the nominal stoichiometric volume contraction, cf. Equation (4.16). This can be explained by the above-mentioned fast diffusion of H_2 leading to strong molecular interactions within the multicomponent mixture. This phenomenon is further investigated in Section 4.4.3 of the manuscript.

4.S.3 Evaluation of Surface-to-Volume Ratio

Traditionally, the key characteristic parameter for intraparticle transport is the volume-to-surface ratio V_p/A_p or its reciprocal value, the volume-specific surface area A_p/V_p [94]. For the selected constant aspect ratio $R/H = 1$, the latter is displayed in Figure 4.9.

Naturally, an increased pellet diameter R results in a reduction of the surface-to-volume ratio. From the representation in Figure 4.9, shapes with internal holes or indentions increase the specific surface area. Surface-to-volume ratios in Figure 4.9 are well correlated to the respective trends in Figure 4.1 for most pellet shapes. This correlation is further confirmed by applying the shape-material parameter χ_p (4.25), presented in Figure 4.2.

The effectiveness factor per mass of catalyst for the various pellet types (cf. Figure 4.1) follow the trend of A_p/V_p-ratios. Lower values for A_p/V_p increase transport limitations and consequently reduce the effectiveness factor of the pellet. Solely the DAL type has a slightly increased effectiveness factor and outperforms 3H1 pellets, which is not expected from the
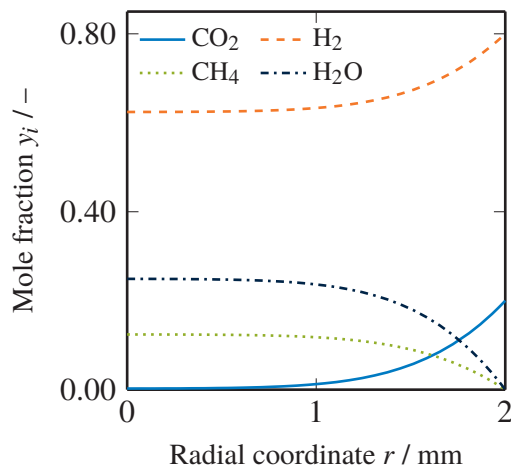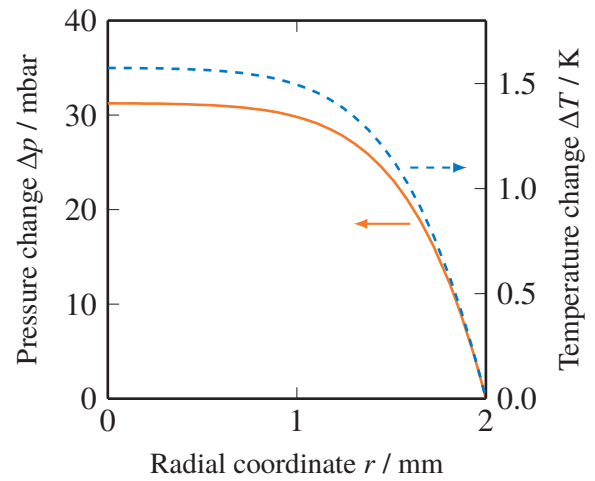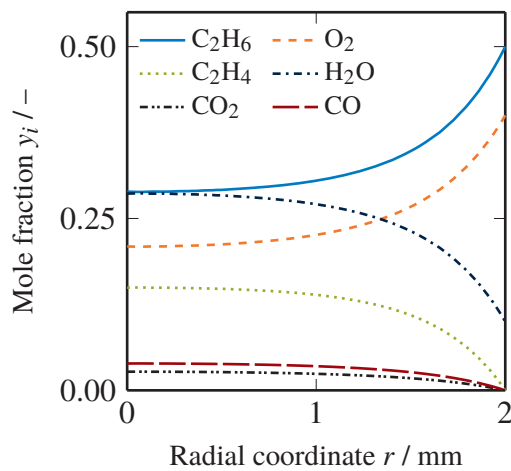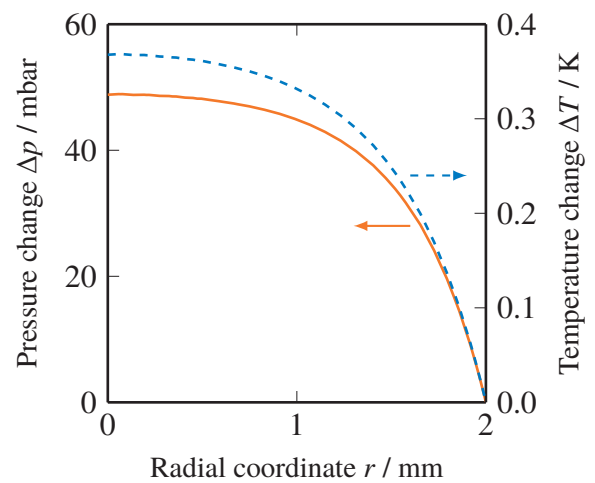
(a) CO_2 methanation: y-profiles.

(b) CO_2 methanation: p/T-profiles.

(c) ODH of ethane: y-profiles.

(d) ODH of ethane: p/T-profiles.

Figure 4.8: Radial centerline profiles of mole fractions (a,c) as well as pressure and temperature change (b,d) for a cylinder with $d = 2\,mm$ calculated using the BFM model. CO_2 methanation with $\varrho_p = 1000\,kg/m^3$ (a,b) and ODH of ethane with $\varrho_p = 1500\,kg/m^3$ (c,d).
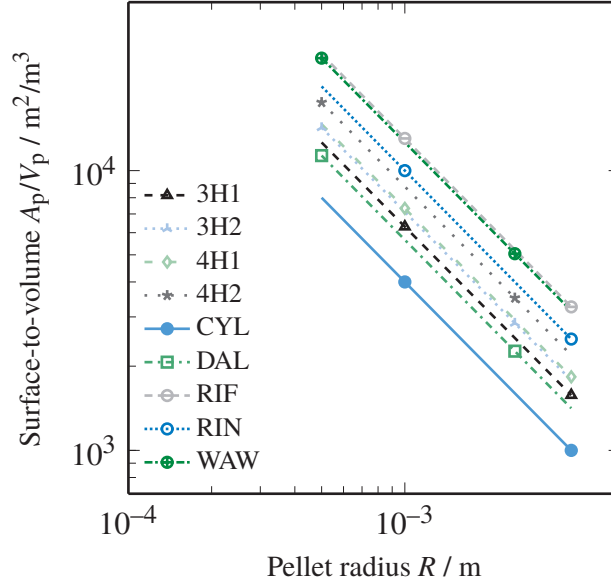
Figure 4.9: Effect of pellet radius R on surface-to-volume ratio $A_\mathrm{p}/V_\mathrm{p}$ for different pellet geometries. Definition of shapes is given in Table 4.1.

$A_\mathrm{p}/V_\mathrm{p}$-ratio. This is related to shorter effective diffusion paths arising from the fin-like double alpha shape and the non-convex outer surface.

4.S.4 The 1D GCγ Model

Mariani et al. [154] developed a straightforward method to predict shape factors for any pellet geometry, the so-called one dimensional generalized cylinder model using the characteristic integral value γ (1D GCγ). The basis of this method is the solution of the dimensionless Poisson problem

$$
\begin{aligned}
\nabla^* \cdot G &= -1 \\
G &= 0 \quad \forall \quad \text{outer surfaces} \\
\nabla^* G &= 0 \quad \forall \quad \text{symmetric surfaces}
\end{aligned}
\tag{4.33}
$$

over the complete pellet volume. By a different treatment of symmetric and outer boundaries, pellet segments are adequate to give exact σ estimates. The dimensionless nabla operator ∇^* is based on the volume-to-surface ratio $V_\mathrm{p}/A_\mathrm{p}$. In COMSOL Multiphysics, this is implemented in the following way

$$
\begin{aligned}
\nabla \cdot G &= \frac{-1}{\left(V_\mathrm{p}/A_\mathrm{p}\right)^2} \\
G &= 0 \quad \forall \quad \text{outer surfaces} \\
\nabla G &= 0 \quad \forall \quad \text{symmetric surfaces}
\end{aligned}
\tag{4.34}
$$

Solving for G, a volume integration gives

$$\gamma = \frac{1}{V_p} \int_{V_p} G dV. \tag{4.35}$$

Finally, the shape factor is calculated to

$$\sigma = \frac{3\gamma - 1}{1 - \gamma}. \tag{4.36}$$

4.S.5 1D Approximation

Tables 4.5 to 4.10 provide values for mean average *MAPE* and maximum percentage errors *MaxAPE* values for all 1D approximations of the BFM. Graphical representations are given in the Supplementary Material of the original publication.

Table 4.5: Summary of mean average *MAPE* and maximum percentage errors *MaxAPE* for 1D approximation of CO_2 methanation reaction (4.16). All values are given in percent.

Shape	1D plate		1D cylinder		1D sphere		1D GCγ	
	MAPE	*MaxAPE*	*MAPE*	*MaxAPE*	*MAPE*	*MaxAPE*	*MAPE*	*MaxAPE*
3H1	5.53	12.02	0.49	1.10	1.50	4.40	0.23	1.40
3H2	5.16	11.52	0.12	0.75	1.89	5.16	0.23	1.06
4H1	4.34	9.69	0.53	1.92	2.12	6.15	0.25	1.23
4H2	2.75	7.49	0.98	3.17	2.46	7.65	0.16	0.72
CYL	10.88	20.33	3.61	6.91	0.89	1.88	0.03	0.12
DAL	6.88	15.22	1.20	2.49	1.02	2.37	0.11	0.41
RIF	0.96	2.31	1.00	3.13	1.80	6.08	0.13	0.34
RIN	1.99	5.59	1.03	3.18	2.28	7.31	0.13	0.25
WAW	0.97	2.26	1.11	3.46	1.94	6.52	0.15	0.39

Table 4.6: Summary of mean average *MAPE* and maximum percentage errors *MaxAPE* for 1D approximation of ODH of ethane reaction 1 (4.17). All values are given in percent.

Shape	1D plate		1D cylinder		1D sphere		1D GCγ	
	MAPE	*MaxAPE*	*MAPE*	*MaxAPE*	*MAPE*	*MaxAPE*	*MAPE*	*MaxAPE*
3H1	9.62	12.75	0.51	1.08	3.11	4.71	1.13	2.46
3H2	8.64	12.05	0.46	1.16	3.52	5.38	0.64	1.42
4H1	7.30	10.04	1.33	2.73	4.30	6.50	0.89	2.21
4H2	5.77	8.32	2.02	3.28	4.82	8.19	0.44	0.96
CYL	14.48	18.69	4.74	7.35	1.38	2.12	0.17	0.34
DAL	12.18	16.19	1.76	3.13	1.79	2.74	0.26	0.51
RIF	2.84	4.88	2.92	5.68	5.06	10.73	0.21	0.42
RIN	5.47	10.79	2.40	4.63	4.79	8.63	0.15	0.40
WAW	2.79	4.61	3.19	6.25	5.25	10.05	0.31	0.61

Table 4.7: Summary of mean average *MAPE* and maximum percentage errors *MaxAPE* for 1D approximation of ODH of ethane reaction 2 (4.18). All values are given in percent.

Shape	1D plate		1D cylinder		1D sphere		1D GCγ	
	MAPE	*MaxAPE*	*MAPE*	*MaxAPE*	*MAPE*	*MaxAPE*	*MAPE*	*MaxAPE*
3H1	6.00	8.14	0.25	0.68	1.94	3.20	0.68	1.64
3H2	5.14	7.64	0.26	0.76	2.17	3.56	0.37	0.96
4H1	4.41	6.60	0.77	1.77	2.67	4.53	0.51	1.41
4H2	3.39	5.85	1.16	2.28	2.79	5.13	0.24	0.60
CYL	8.95	12.93	2.91	4.33	0.85	1.27	0.12	0.25
DAL	7.53	9.92	1.11	1.58	1.11	1.50	0.14	0.32
RIF	1.55	3.37	1.57	3.46	2.72	6.23	0.10	0.20
RIN	2.79	5.63	1.25	2.35	2.68	5.28	0.06	0.11
WAW	1.52	3.20	1.71	3.75	2.87	6.55	0.15	0.38

Table 4.8: Summary of mean average *MAPE* and maximum percentage errors *MaxAPE* for 1D approximation of ODH of ethane reaction 3 (4.19). All values are given in percent.

Shape	1D plate		1D cylinder		1D sphere		1D GCγ	
	MAPE	*MaxAPE*	*MAPE*	*MaxAPE*	*MAPE*	*MaxAPE*	*MAPE*	*MaxAPE*
3H1	7.92	9.95	0.37	0.95	2.55	4.08	0.88	2.00
3H2	6.94	9.49	0.34	0.93	2.88	4.39	0.48	1.17
4H1	5.90	8.08	1.03	2.24	3.51	5.66	0.67	1.78
4H2	4.57	7.16	1.59	2.80	3.84	6.27	0.33	0.77
CYL	11.87	16.28	3.93	5.27	1.15	1.52	0.14	0.28
DAL	9.99	12.43	1.49	2.26	1.49	1.95	0.20	0.41
RIF	2.17	4.11	2.24	4.19	3.90	7.48	0.16	0.28
RIN	4.11	6.98	1.84	3.16	3.77	6.36	0.11	0.36
WAW	2.13	3.90	2.44	4.54	4.07	7.87	0.23	0.49

Table 4.9: Summary of mean average *MAPE* and maximum percentage errors *MaxAPE* for 1D approximation of ODH of ethane reaction 4 (4.20). All values are given in percent.

Shape	1D plate		1D cylinder		1D sphere		1D GCγ	
	MAPE	*MaxAPE*	*MAPE*	*MaxAPE*	*MAPE*	*MaxAPE*	*MAPE*	*MaxAPE*
3H1	0.52	1.52	0.17	0.61	0.09	0.37	0.10	0.33
3H2	0.48	1.37	0.07	0.23	0.17	0.67	0.06	0.18
4H1	0.39	1.11	0.06	0.12	0.16	0.57	0.08	0.23
4H2	0.19	0.51	0.06	0.18	0.31	1.09	0.05	0.11
CYL	0.57	1.53	0.31	1.04	0.11	0.36	0.00	0.01
DAL	0.62	1.92	0.25	0.74	0.16	0.50	0.03	0.06
RIF	0.06	0.22	0.10	0.52	0.23	1.45	0.01	0.03
RIN	0.29	1.43	0.17	0.72	0.30	1.18	0.02	0.18
WAW	0.07	0.29	0.11	0.61	0.21	1.04	0.02	0.03

Table 4.10: Summary of mean average *MAPE* and maximum percentage errors *MaxAPE* for 1D approximation of ODH of ethane reaction 5 (4.21). All values are given in percent.

Shape	1D plate		1D cylinder		1D sphere		1D GCγ	
	MAPE	*MaxAPE*	*MAPE*	*MaxAPE*	*MAPE*	*MaxAPE*	*MAPE*	*MaxAPE*
3H1	3.14	6.43	0.48	1.42	0.64	1.90	0.08	0.32
3H2	2.81	5.91	0.08	0.29	1.02	2.82	0.03	0.10
4H1	2.35	4.90	0.11	0.25	1.06	2.84	0.05	0.18
4H2	1.56	3.01	0.53	1.25	1.72	4.41	0.03	0.06
CYL	3.73	7.85	1.58	4.03	0.50	1.25	0.02	0.04
DAL	3.87	8.09	1.03	2.24	0.81	1.73	0.04	0.13
RIF	0.66	1.69	0.86	2.64	1.70	5.83	0.06	0.20
RIN	1.91	5.59	0.98	2.68	1.78	4.73	0.11	0.48
WAW	0.70	1.81	0.96	2.97	1.67	4.90	0.07	0.21

4.S.6 Comparison of Diffusion Models

In the following, additional results of the comparison between diffusion models are given. Figure 4.10 shows additional results for pressure changes. Signed temperature changes for CO_2 methanation and ODH of ethane are displayed in Figures 4.11 and 4.12, respectively. Percentage errors for ODH reactions (4.17) to (4.21) are presented in the Supplementary Material of the original publication.
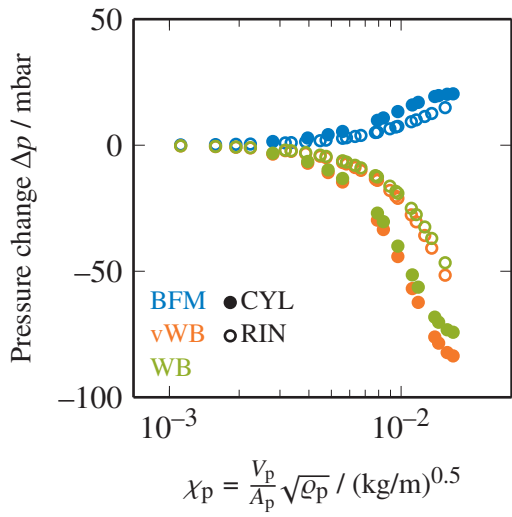
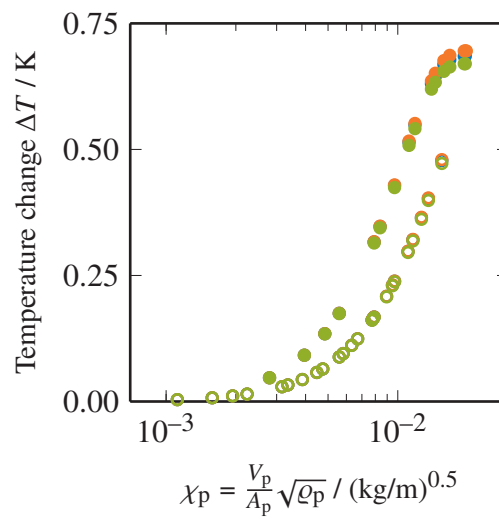**(a)** CO_2 methanation reaction at $X_{CO_2} = 33.33\,\%$.
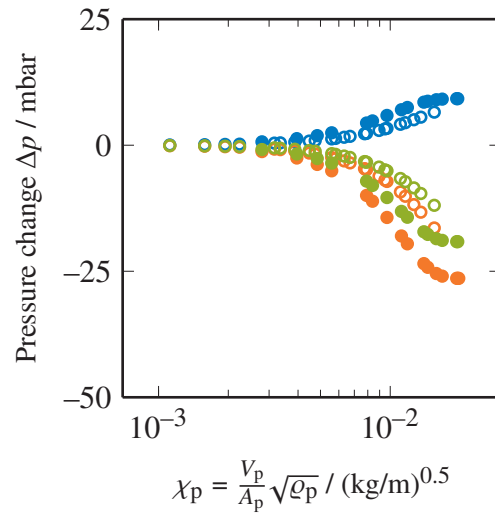
(b) CO_2 methanation reaction at $X_{CO_2} = 66.67\,\%$.
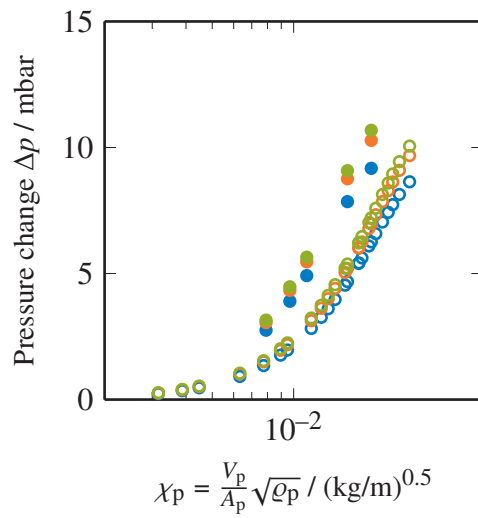
(c) ODH of ethane at $X_{C_2H_6} = 50\,\%$.

Figure 4.10: Comparison of signed pressure changes.
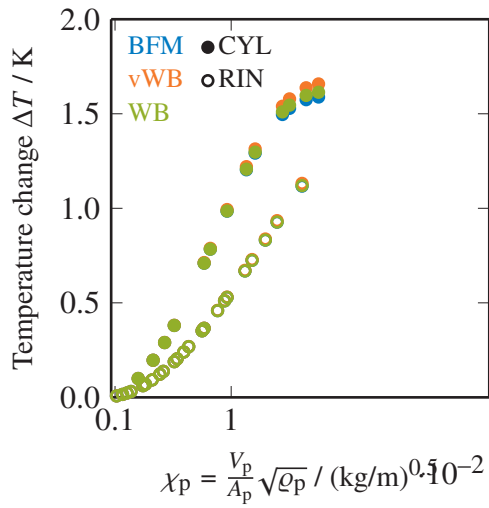
(a) $X_{CO_2} = 0\,\%$.
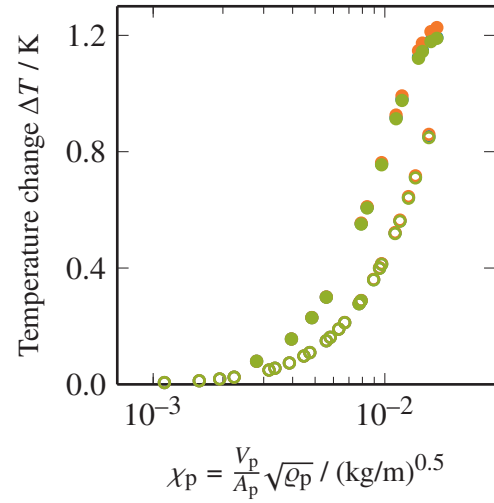
(b) $X_{CO_2} = 33.33\,\%$.

(c) $X_{CO_2} = 66.67\,\%$.

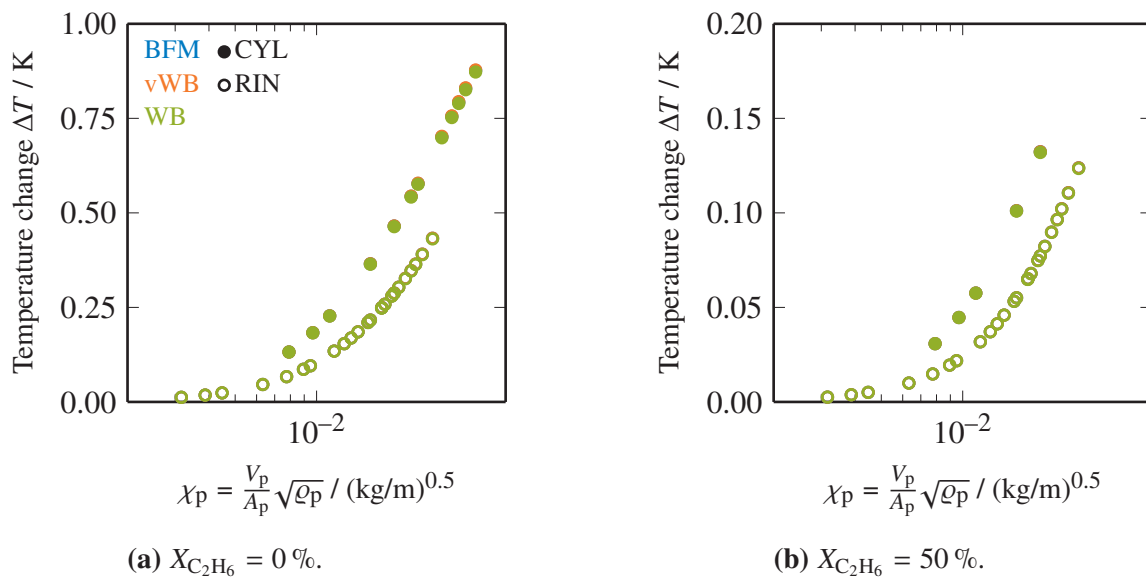**Figure 4.11:** Comparison of temperature changes (4.27) for CO_2 methanation reaction.

(a) $X_{C_2H_6} = 0\,\%$.

(b) $X_{C_2H_6} = 50\,\%$.

Figure 4.12: Comparison of temperature changes (4.27) for ODH of ethane.

5 2D Flow Fields in Fixed-Bed Reactor Design

In combination with computationally demanding, but steadily developing discrete particle simulation techniques, new areas of application for the fixed-bed continuum models, like *in silico* determination of transport parameters, become accessible. Within this study, a pseudo-homogeneous continuum model fully accounting for 2D fluid flow, heat and species dispersion in axial and radial direction is presented and applied to four configurations of packed beds. Application of different discretization techniques for fluid flow as well as heat and species transport provide an efficient and robust solution strategy. Beds of ideal spheres exhibited deviating conversion behavior due to strong oscillation in the radial flow profile. Moreover, the importance of adequate coupling of fluid flow and chemical reaction is highlighted by a variation of reaction stoichiometry. This theoretical evaluation of the continuum approach provides valuable insights on the interplay of fluid flow and chemical reaction in fixed-bed reactors.
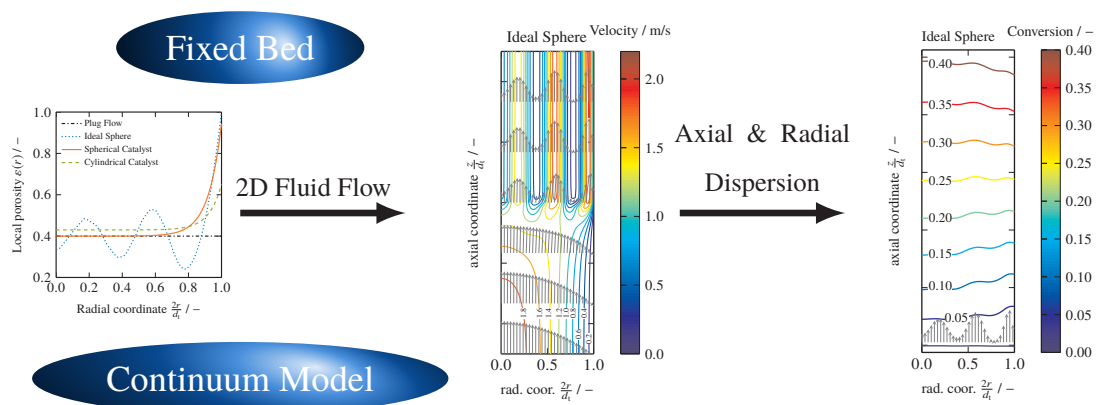
5.1 Introduction

Modeling of chemical reactions in fixed beds has been one of the major fields in chemical reactor design for the last decades. Historically, approaches treating fluid and solid phases as pseudo-continuum became the most applied strategy in academia and industry [176].

Modeling fluid flow inside fixed-bed reactors differs strongly in literature: starting from constant pressure assumption, over Ergun-based artificial plug-flow [46], to finally consideration of radially dependent flow phenomena [177–179]. The latter was found to be essential, in order to describe so-called bypassing effects observed for reactors operated with low tube-to-particle ratios d_t/d_p. This phenomenon arises from the prominent particle-wall interactions and the accompanied higher porosities close to the tube wall. Assuming the radial velocity component to be negligible ($u_r \approx 0$) and neglecting radial pressure variation ($\partial p/\partial r \approx 0$) allows a simplified description of the fluid flow by the extended Brinkmann equation [180, 181]. However, this approach can introduce constraints to the system, as convective radial transport is artificially inhibited yielding an invariable mass flux in axial direction for each radial position.

Changes of heat and species are described by (semi-)empirical models relying on effective transport parameters [14]. Numerous studies have been carried out describing the complex interplay between fluid and solid phase inside fixed-beds. Most prominent the $\Lambda_r(r)$-model of Winterberg et al. [182] proved to be a flexible and reliable model. Herein, the concept of dispersion is used to account for stagnant and dynamic contributions of heat and species transport, respectively.

In recent years, increased computational power made CFD modeling strategies for packed beds feasible and allowed to drop the continuum simplification inside the bed [183]. In discrete, three-dimensional particle models the fluid and solid domains are resolved to their full extent. Dixon [184] compares a 3D discrete particle model to 1D and 2D continuum approaches for steam methane reforming demonstrating similarities and discrepancies of these two approaches. Several other studies demonstrated the applicability and potential of discrete particle modeling for fixed-bed reactor design, cf. Nijemeisland and Dixon [15], Wehinger et al. [160], Das et al. [87], Karthik and Buwa [161], Partopour and Dixon [164, 185, 186]. However, as a consequence of the high resolution in such models, the computational requirements for models of fixed-bed reactors at industrial scale are tremendous. To date, Dixon [184] reported the largest study of a fixed-bed reactor being 70 cm in length and consisting of approximately 800 particles.

In contrast, the classical continuum approach has been extensively validated to be a realistic design tool for industrial applications of fixed-bed chemical reactors and, hence, will persist as a valuable approach in industry and academia [16]. In fact, in recent studies [187–190] insights gained from discrete particle CFD studies are mapped onto conventional continuum approaches, investigating axial and radial dispersion coefficients for mass and heat transport. This strategy provides a promising route for theoretical predictions of transport effects inside packed beds of various particle shapes and its practical applications in fixed-bed continuum models.

However, so far there is neither a universally accepted procedure for extracting dispersion coefficient from discrete particle models nor a consistent use of the concept of dispersion inside packed beds. According to Levenspiel [84] the dispersion describes backmixing during fluid flow in longitudinal or axial direction. Besides molecular diffusion, this mixing originates from fluctuations in flow velocities and turbulent diffusion. Hence, a dispersion coefficient is meant to decouple subordinate forms of transport from the net convective transport by grouping them to one effective, (semi-)empirical parameter. In fixed-bed continuum models this concept is applied to transport of mass, heat and, rarely, momentum. At this point, it is important to stress, that radial inhomogeneities in fluid density, arising from hot spot formation or differences in fluid composition, inevitably lead to convective radial flow, which per definition cannot be described with the concept of dispersion.

In this work, an integrated, pseudo-homogeneous fixed-bed reactor modeling strategy fully accounting for 2D transport including radial and axial dispersion effects is presented. A dual grid method is used to efficiently handle 2D momentum transfer on the one, as well as heat and mass transfer on the other hand. During analyses, special focus is given on the fluid flow at the inlet region of the reactor. Furthermore, coupling effects of reaction induced change in fluid density and stoichiometry in combination with different flow patterns are investigated.

5.2 Theory

In the following, the basis of a 2D, steady-state continuum model for fluid flow and heat and species transport in catalytically active fixed beds is presented.

Convective transport is described by the superficial velocity vector

$$\vec{u} = \begin{pmatrix} u_r \\ u_z \end{pmatrix}, \tag{5.1}$$

composed of the radial u_r and axial u_z velocity component. The magnitude of the velocity vector $\vec{u}$ is given to

$$u = ||\vec{u}|| = \sqrt{u_r^2 + u_z^2}. \tag{5.2}$$

The fixed-bed domain is characterized by a radially dependent porosity $\varepsilon(r)$. Beds of ideal spheres (IS) are represented by the model of Bey and Eigenberger [191].

$$\varepsilon(r) = \begin{cases} 0.24 + (1 - 0.24)\, r^{*2}, & \text{at } r^* < 0; \\ \varepsilon_\infty + (0.24 - \varepsilon_\infty) \exp\left(-\frac{r^*}{4}\right) \cos\left(\frac{\pi r^*}{0.876}\right), & \text{at } r^* \geq 0; \end{cases}$$
$$r^* = \frac{2\,(R - r)}{d_p \left(\frac{d_t}{d_p} - \sqrt{\left(\frac{d_t}{d_p} - 1\right)^2 - 1} \right)} - 1.$$

(5.3)

Depending on the tube-to-particle ratio d_t/d_p, pronounced oscillations in porosity in radial direction are superimposed with an exponential decay towards the tube center (cf. Figure 5.1). The parameter ε_∞ represents the bed porosity for an infinitely expanded bed. A summary of parameters is provided in Table 5.1.

The oscillating behavior observed in beds of perfect spheres, is strongly damped for packings consisting of real catalysts [179]. On the one hand, mass production of catalyst pellets results in a size distribution instead of ideal uniformity. On the other hand, transport of the pellets and filling into the tubes can cause abrasion or breakage, which leads to imperfect shape and deformation of the particles and further broadening of the size distribution. The porosity profiles for such packings of real spherical (SC) and cylindrical catalysts (CC), with an aspect ratio = 1, can be described using the correlation of Giese et al. [179]

$$\varepsilon(r) = \varepsilon_\infty \left(1 + a_{\varepsilon(r)} \exp\left(-b_{\varepsilon(r)} \frac{R - r}{d_p} \right) \right).$$

(5.4)

Values for the empirical parameters $a_{\varepsilon(r)}$ and $b_{\varepsilon(r)}$ are listed in Table 5.1. Averaged porosities $\bar{\varepsilon}$ are calculated by integration of Equations (5.3) and (5.4) over the tube cross-section.

Porosity profiles for the three selected pellet types are given in Figure 5.1 and compared to the reference case of ideal plug flow (PF). Distinct differences for the ideal sphere and spherical particles are observable, as for the latter no oscillation behavior is regarded. Furthermore, IS fulfill the point contact condition at the tube wall, while for SC the wall porosity does not exceed 0.944 due higher contact area arising from their deformed nature. Cylindrical pellets exhibit even better wall contact ($\varepsilon(r = R) = 0.650$) caused by coaxial arrangement of the CC combined with its inhomogeneity [179].

5.2.1 Fluid Flow

One of the special characteristic features of fluid flow inside fixed-bed reactors is its compressibility at low Mach numbers. Changes in fluid density arise from pressure drop caused by friction, temperature gradients arising from heat of reaction and variations of the mixture stoichiometry as a result of non-equimolar chemical reactions.
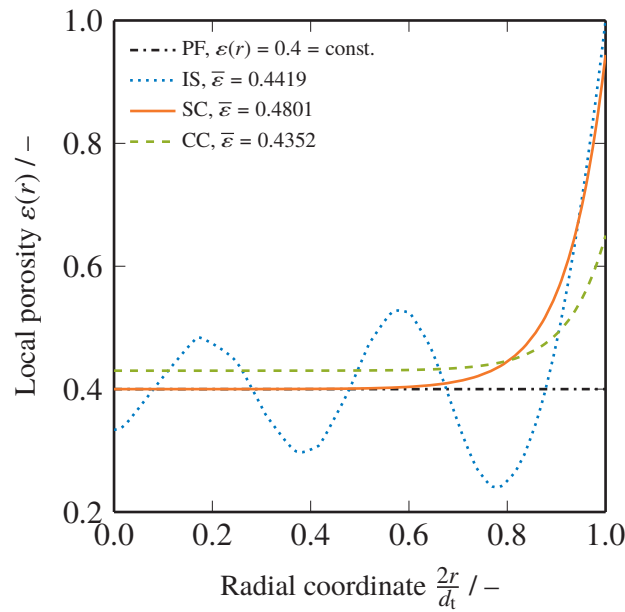
Figure 5.1: Radial porosity profiles using a tube-to-particle ratio of $d_\mathrm{t}/d_\mathrm{p} = 5.0$ for plug flow (PF), beds of ideal spheres (IS), spherical (SC) and cylindrical catalyst (CC) pellets using the correlation in Equations (5.3) and (5.4) and values in Table 5.1.

The fluid flow model comprises momentum exchange in axial

$$\varrho_\mathrm{fl}\left(u_r\frac{\partial u_z}{\partial r} + u_z\frac{\partial u_z}{\partial z}\right) = -\frac{\partial p}{\partial z} - f_1 u_z - f_2 u u_z + \eta_\mathrm{eff}\left(\frac{1}{r}\frac{\partial}{\partial r}\left(r\frac{\partial u_z}{\partial r}\right) + \frac{\partial^2 u_z}{\partial z^2}\right) \tag{5.5}$$

and radial direction

$$\varrho_\mathrm{fl}\left(u_r\frac{\partial u_r}{\partial r} + u_z\frac{\partial u_r}{\partial z}\right) = -\frac{\partial p}{\partial r} - f_1 u_r - f_2 u u_r + \eta_\mathrm{eff}\left(\frac{\partial}{\partial r}\left(\frac{1}{r}\frac{\partial(r u_r)}{\partial r}\right) + \frac{\partial^2 u_r}{\partial z^2}\right), \tag{5.6}$$

which consistently accounts for convective transport inside packed beds [177, 192].

Equations (5.5) and (5.6) are based on non-conservative 2D Navier-Stokes equation using Darcy-Forchheimer friction parameters according to Ergun [193]

$$f_1 = 150\frac{(1 - \varepsilon(r))^2}{\varepsilon(r)^3}\frac{\eta_\mathrm{fl}}{d_\mathrm{p}^2},$$
$$f_2 = 1.75\frac{1 - \varepsilon(r)}{\varepsilon(r)^3}\frac{\varrho_\mathrm{fl}}{d_\mathrm{p}}. \tag{5.7}$$

Turbulences inside the bed are approximated using the concept of effective viscosities η_eff [179, 194]

$$\frac{\eta_\mathrm{eff}}{\eta_\mathrm{fl}} = a_{\eta_\mathrm{eff}}\exp\left(b_{\eta_\mathrm{eff}}Re\right), \tag{5.8}$$

dependent on the particle Reynolds number Re

$$Re = \frac{\varrho_{fl} u d_p}{\eta_{fl}} \tag{5.9}$$

and empirical parameters $a_{\eta_{eff}}$ and $b_{\eta_{eff}}$, listed in Table 5.1.

The pressure field is solved via mass conservation

$$\frac{1}{r}\frac{\partial(r\varrho_{fl}u_r)}{\partial r} + \frac{\partial(\varrho_{fl}u_z)}{\partial z} = 0 \tag{5.10}$$

using the ideal gas law

$$p = \frac{\varrho_{fl}\mathcal{R}T}{M} = c_{fl}\mathcal{R}T \tag{5.11}$$

as equation-of-state.

5.2.2 Species and Heat Reactor Model

A pseudo-homogeneous continuum approach for heat and species transport inside the packed bed is defined. Here, inter- and intraparticle transport effects are assumed to be negligible, which, in turn, results in an overall catalyst effectiveness factor equal to one. Convective transport is incorporated by the flow field in Equations (5.5) and (5.6). Non-convective transport phenomena arise from thermal conduction through fluid and solid, or molecular diffusion through void regions together with turbulences inside the bed. These effects are summed up in dispersive terms for axial and radial transport, respectively.

The resulting heat balance for a single reaction is given to

$$\begin{aligned} 0 = &- c_{fl}C_p^\circ u_z \frac{\partial T}{\partial z} - c_{fl}C_p^\circ u_r \frac{\partial T}{\partial r} \dots \\ &+ \frac{\partial}{\partial z}\left(\Lambda_{ax}\frac{\partial T}{\partial z}\right) + \frac{1}{r}\frac{\partial}{\partial r}\left(r\Lambda_r\frac{\partial T}{\partial r}\right) \dots \\ &+ (-\Delta_r H^\circ)\left(1 - \varepsilon(r)\right)\varrho_p\dot{r}. \end{aligned} \tag{5.12}$$

Effective thermal conductivities in radial Λ_r and axial Λ_{ax} direction reflect the dispersive heat transport inside the packed bed.

For transport and reaction of a species i a similar balance equation follows [14]

$$\begin{aligned} 0 = &- u_z\varrho_{fl}\frac{\partial}{\partial z}\left(\frac{y_i}{M}\right) - u_r\varrho_{fl}\frac{\partial}{\partial r}\left(\frac{y_i}{M}\right) \dots \\ &+ \frac{\partial}{\partial z}\left(\mathcal{D}_{ax,i}\frac{\partial(c_{fl}y_i)}{\partial z}\right) + \frac{1}{r}\frac{\partial}{\partial r}\left(r\mathcal{D}_{r,i}\frac{\partial(c_{fl}y_i)}{\partial r}\right) \dots \\ &+ (1 - \varepsilon(r))\varrho_p\dot{R}_i. \end{aligned} \tag{5.13}$$

Dispersion coefficients $\mathcal{D}_{r,i}$ and $\mathcal{D}_{ax,i}$ account for non-convective species transport inside the packed bed in radial and axial direction, respectively. The net rate of production $\dot{R}_i$ for each species i represents the chemical reaction.

5.2.3 Dispersion Model

Radial and axial dispersion of heat inside packed beds is described by the well-established $\Lambda_r(r)$ model of Winterberg et al. [182]. This model allows straightforward incorporation of radially dependent bed porosities without the need of heat transfer resistances at the tube wall. Here, effective thermal conductivities in radial Λ_r and axial Λ_{ax} direction

$$
\begin{aligned}
\frac{\Lambda_r}{\lambda_{fl}} &= \frac{\lambda_{bed}^{eff}}{\lambda_{fl}} + K_{1,h}Pe_h\frac{u(r=0)}{\bar{u}}f_h(R-r); \\
\frac{\Lambda_{ax}}{\lambda_{fl}} &= \frac{\lambda_{bed}^{eff}}{\lambda_{fl}} + \frac{Pe_h}{K_{ax}}
\end{aligned}
\tag{5.14}
$$

are both described via stagnant λ_{bed} and dynamic contributions. Here, effective thermal conductivities both in radial Λ_r and axial Λ_{ax} direction, respectively, consist of a stagnant λ_{bed} and dynamic contribution. The latter is described via an empirical Péclet expression

$$
\begin{aligned}
Pe_h &= \frac{uc_{fl}C_{p,fl}^{\circ}d_p}{\lambda_{fl}}; \\
K_{1,h} &= \frac{1}{a_{K_1}}; \\
K_{2,h} &= a_{K_2} + b_{K_2}\exp\left(-\frac{Re}{c_{K_2}}\right).
\end{aligned}
\tag{5.15}
$$

The parameter K_1 represents the slope and K_2 the damping of the dispersion in radial direction. Dispersion of species is based on the same principle

$$
\begin{aligned}
\frac{\mathcal{D}_{r,i}}{D_{fl,i}} &= \frac{\mathcal{D}_{bed,i}^{eff}}{D_{fl,i}} + K_{1,m}Pe_{m,i}\frac{u(r=0)}{\bar{u}}f_m(R-r); \\
\frac{\mathcal{D}_{ax,i}}{D_{fl,i}} &= \frac{\mathcal{D}_{bed,i}^{eff}}{D_{fl,i}} + \frac{Pe_{m,i}}{K_{ax}},
\end{aligned}
\tag{5.16}
$$

using different expressions for the transport parameters

$$
\begin{aligned}
Pe_{m,i} &= \frac{ud_p}{D_{fl,i}}; \\
K_{1,m} &= \frac{1}{a_{K_1}}\left[1 + \frac{3}{\sqrt{Pe_{m,i}(r=0)}}\right]^{-1}; \\
K_{2,m} &= a_{K_2}.
\end{aligned}
\tag{5.17}
$$

The damping function f is expressed via the respective parameter for heat and mass transfer

$$f_{h/m}(R - r) = \begin{cases} \left(\frac{R-r}{K_{2,h/m}\,d_p}\right)^2 & \text{at } 0 < R - r \le K_{2,h/m}\,d_p, \\ 1 & \text{at } K_{2,h/m}\,d_p < R - r \le R. \end{cases} \tag{5.18}$$

The coefficients $a_{K_{1/2}}$, b_{K_2} and c_{K_2} have been determined for beds of varying pellet types and are listed in Table 5.1. The stagnant contributions for heat and species transport are calculated via the model of Zehner, Bauer and Schlünder [90, 91] with detailed information given in Appendix A.5.1.

Table 5.1: Overview of selected parameters for fluid flow and heat and species dispersion of different pellet types inside packed beds.

		Ideal sphere (IS)[a]	Spherical catalyst (SC)	Cylindrical catalyst (CC)
C_f[b]		1.25	1.40	2.50
φ[b]		$7.7 \cdot 10^{-3}$	$1.0 \cdot 10^{-3}$	$1.0 \cdot 10^{-3}$
K_1[c]	a_{K_1}	8	8	6.25
	a_{K_2}	0.44	0.44	0.40
K_2[c]	b_{K_2}	4	4	1.40
	c_{K_2}	70	70	230
K_{ax}[c]		2	2	2
	ε_∞[d]	0.40	0.40	0.43
$\varepsilon(r)$	$a_{\varepsilon(r)}$	n.a.	1.36[e]	$\frac{0.65}{\varepsilon_\infty} - 1$[f]
	$b_{\varepsilon(r)}$	n.a.	5.0[e]	6.0[f]
η^{eff}[e]	$a_{\eta^{eff}}$	2.0	2.0	1.6
	$b_{\eta^{eff}}$	$3.5 \cdot 10^{-3}$	$2.0 \cdot 10^{-3}$	0

[a]A plug flow (PF) configuration with constant bed porosity $\varepsilon(r) = \varepsilon_\infty$ is used as reference case. Transport properties for PF are identical to the ideal sphere configuration.

[b]Adapted from Bauer [195].

[c]Adapted from Tsotsas [196].

[d]Adapted from Zehner and Schlünder [90].

[e]Adapted from Giese [197].

[f]Adapted from Winterberg and Tsotsas [198].

5.3 Methodology

Due to the high coupling of momentum, heat and species transport in combination with nonlinearities arising from chemical reaction, solution of integrated fixed-bed reactor models remains a challenging task.

5.3.1 Solution Routine

The system of partial differential equations (PDE) for fluid flow, Equations (5.5), (5.6) and (5.10), and chemical reaction, Equations (5.12) and (5.13), is solved by a segregated strategy [197].

The scheme in Figure 5.10 of the Supplementary Material shows the basic solution procedure. After problem initialization, nondimensionalization and domain discretization, an alternating solution of fluid flow and chemical reaction is performed. Transport and thermodynamic properties are updated after solving the fluid flow, or chemical reaction part. After every kth-loop, additionally, the convergence criterion (5.19) is checked for the dimensionless variables u_r, u_z, p, T and y_i ($i = 1, \ldots, n_{\text{species}} - 1$) at each grid point

$$
\max \left| \begin{pmatrix} u_r \\ u_r \\ p \\ T \\ y_1 \\ \vdots \\ y_{n_{\text{species}}-1} \end{pmatrix}_k - \begin{pmatrix} u_r \\ u_r \\ p \\ T \\ y_1 \\ \vdots \\ y_{n_{\text{species}}-1} \end{pmatrix}_{k-1} \right| < 10^{-3}. \tag{5.19}
$$

One common simplification in modeling of fixed-bed reactors is the negligence of coupling effects arising from reaction induced temperature and composition gradients to the fluid flow and vice versa. This so-called cold-flow assumption is equal to solving both segregated parts of the PDE system only once ($k = 2$). Its impact on the reactor behavior is part of this study.

Preliminary studies on the convergence behavior of the presented PDE system led to following discretization strategy:

1.) Fluid flow is discretized using second order finite differences method. An equally spaced, orthogonal staggered grid reduces convergence problems and oscillations arising in pressure p and velocity field $\vec{u}$ [199]. Figure 5.11 in the Supplementary Material gives information on the grid point arrangement for an exemplary 3x3 domain. For the simulations presented in this work, 48 grid points in radial and 24 grid points in axial direction per cm are applied for the fixed-bed domain to accurately resolve the inlet region and domain discontinuities. Void domains at the reactor inlet and outlet are discretized with an proportionate number of axial grid points.

2.) Heat and species transport is discretized using orthogonal collocation on finite elements [132, 149]. Roots of modified, unweighted second and fourth order Jacobi polynomials are used as internal collocation points for the axial and radial coordinate, respectively. The elements are unequally spaced in both directions. Density of elements is increased at domain discontinuities and at the reactor wall. The fixed-bed is discretized with 40 axial and 15 radial elements. At void regions ten axial elements are added. Detailed information on this methodology is given in Appendix C.

3.) C^2-continuous cubic splines are used for interpolations between the two grids.

Discretized equations and all subroutines are implemented in MATLAB v2018a. Both nonlinear systems are solved by an unconstrained *trust-region* algorithm using Cholesky factorization. Sparse Jacobian matrices are calculated by central finite differences.

5.3.2 Domain Definition and Boundary Conditions

The interplay of fluid flow and chemical reaction for pseudo-homogeneous continuum models is revisited. One major problem is the proper handling of the reactor inlet and outlet boundary conditions. The inlet is commonly represented by simple Dirichlet condition for velocities u_r and u_z as well as temperature T and mole fractions y_i. For the latter two variables, a Danckwerts step function can be used to account for axial backmixing [78, 200, 201]. The reactor outlet is often simulated by zero gradient conditions for all variables. Many researchers pointed out, that this assumption is unsuitable for chemical reactors not operating at equilibrium conversion and proposed alternatives [178, 202].

To investigate the influence of the boundary condition, void region at the front and rear part of the fixed-bed are regarded. Figure 5.2 gives a schematic overview of the resulting domains together with the appropriate boundary conditions.

For void regions, dispersion coefficients for heat $\Lambda_{r/ax}$ and species $\mathcal{D}_{r/ax}$ transport in Equations (5.12) and (5.13) as well as the effective fluid viscosity in Equations (5.5) and (5.6) are replaced by properties of the pure fluid, namely: the thermal conductivity λ_{fl}, mixture diffusion coefficient $D_{fl,i}$ and the dynamic viscosity η_{fl} of the fluid.

For sufficiently long entry and exit domains, Dirichlet condition at the inlet and zero gradients at the outlet become justifiable. Due to distinct discontinuities in the axial dispersion coefficients for heat and species transport, the flux continuities are explicitly implemented by separating the domain in three parts for the chemical reaction system.

It is noteworthy that the inlet condition for the axial velocity component can be dependent on the radial coordinate r. Assuming a fully developed laminar flow, Hagen-Poiseuille's equation

$$u_z\left(\frac{z}{L_{bed}} = -l_{in}\right) = 2\bar{u}_{in}\left(1 - \left(\frac{2r}{d_t}\right)^2\right) \tag{5.20}$$

is used. The mean inlet velocity is dependent on the fluid density $\bar{\varrho}_{in}$ at the inlet.

5.3.3 Model System

As model reaction, the single-step, irreversible reaction
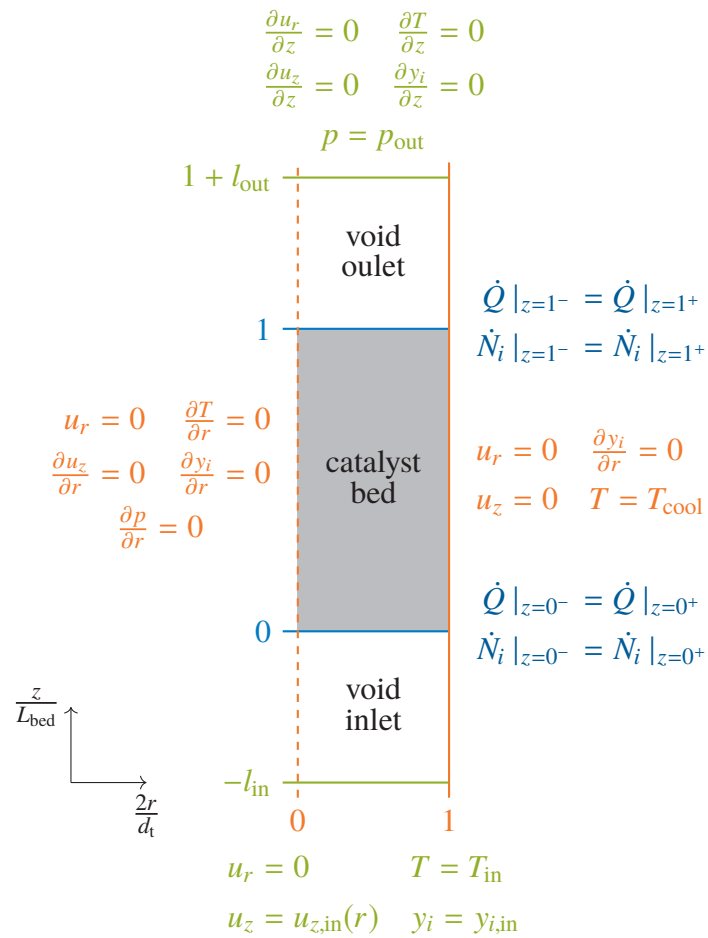
$$A \longrightarrow \nu B \tag{5.21}$$

Figure 5.2: Scheme of reactor domain with void inlet and outlet region, boundary conditions and coupling conditions for heat $\dot{Q}$ and molar fluxes $\dot{N}_i$ at domain intersections.

is applied. The parameter ν represents the stoichiometry ratio, defined as

$$\nu = \frac{\nu_B}{|\nu_A|}. \tag{5.22}$$

A simple first order rate law is applied

$$\dot{r} = A \exp\left(-\frac{E_a}{\mathcal{R}T}\right)\frac{p_A}{p^\circ} \tag{5.23}$$

using a reference pressure p° of 1 bar.

Fluid properties, are considered to be dependent on temperature using respective polynomials [144, 145], with details given in Appendix A. Both species A and B are represented by nitrogen. For non-equimolar reactions, the molar mass of the product B is adapted to conserve total mass

$$M_B = \frac{M_A}{\nu} = \frac{M_{N_2}}{\nu}. \tag{5.24}$$

Table 5.2 lists parameter values used as base case scenario, if not mentioned otherwise.

Table 5.2: Parameter values for base case scenario.

Parameter	Value
T_{in}	673.15 K
T_{cool}	T_{in}
$WHSV$	1 $kg_{feed}/(kg_{cat}$ h$)$
p_{out}	1 bar
m_{cat}	0.2 kg
d_t	2.5 cm
$\Delta_r H^\circ$	-50 kJ/mol
ν	1
A	$2 \cdot 10^{-5}$ mol/(kg$_{cat}$ s)
E_a	100 kJ/mol
ϱ_p	1500 kg/m^3
λ_p	1.0 W/(m K)
ϵ_p	0.8

5.4 Results and Discussion

In the following, a variety of different bed configurations is regarded. Besides the four types of porosity profiles, shown in Figure 5.1, computational domains (cf. Figure 5.2) with and without a void inlet region are compared. For this purpose, tube-to-particle ratios and fluid flow are

varied. Furthermore, the coupling of temperature induced density changes with the flow field are compared to cold-flow situations.

5.4.1 Flow Field

The transition of a void reactor inlet to a continuum packed-bed region is displayed in Figure 5.3 for various bed configurations. For all four configurations, the laminar and parabolic flow changes in front of the bed at $z = 0$. For the PF reference in Figure 5.3a, the flow is rapidly homogenized over the majority of the cross-section. At the tube wall the no-slip condition is fulfilled and no bypassing is observable. For ideal spheres in Figure 5.3b, distinct channeling along the radial coordinate arises inside the packed bed. Beds of spherical and cylindrical catalysts in Figures 5.3c and 5.3d have a constant axial velocity profile in the inner region and dominant bypassing close to the tube wall. Bypassing is more pronounced for the SC configuration due to higher wall porosities compared to the CC case (cf. Figure 5.1). For all four configurations, the axial dimension of the transition region remains below $0.6\,d_t$ or approximately $1.5\,cm$. Moreover, this observation of a narrow transition region could be confirmed for a broad range of Reynolds numbers and tube-to-particle ratios. Packed beds of spheres generated by discrete particle modeling show a disordered entry region of several pellet layers [203, 204], which expands over a length scale similar to the transition region shown in Figure 5.3.

So far, void inlet regions have been neglected in continuum reactor models and constant plug flow was assumed at the bed entry: $u_z(r, z = 0) = \overline{u}_{in}$. Figure 5.12 in the Supplementary Material depicts the flow field for this scenario. The plug flow is rapidly homogenized and steady profiles evolve after approximately 0.6 tube diameters. While for the void inlet in Figure 5.3 the flow field evolves in front of the bed, steady flow profiles have to form inside the packed bed, when no void inlet is considered.

By resolving the inlet transition region from void tube to the porous bed domain, there is no need of artificial boundary conditions at $z = 0$. Figure 5.4 depicts the arising radial profiles of temperature and composition at the inlet of the bed at $z = 0$ as an outcome of axial backmixing.

While for PF, IS and CC, inlet temperature profiles are very similar, temperatures of the SC configuration exceed the others. This is caused by higher wall-bypassing for the SC, which results in a lower velocity or higher residence time at the tube center. Hence, as shown in Figure 5.4b more reactant is consumed and, thus, more heat of reaction is released. In further consequence, the higher inlet temperature for the spherical catalysts slightly shifts the hotspot to the reactor entry, cf. the axial profiles in Figure 5.5a. The oscillating flow inside packed beds of ideal spheres influences both temperature and mole fraction profiles at $z = 0$. The profiles y_A indicate the differences in dispersive axial species transport, which is directly influenced by the velocity field at the bed entry. For the chosen conditions, the influence of axial backmixing of species at the reactor entry seems to be negligible. However, the presented examples are capable
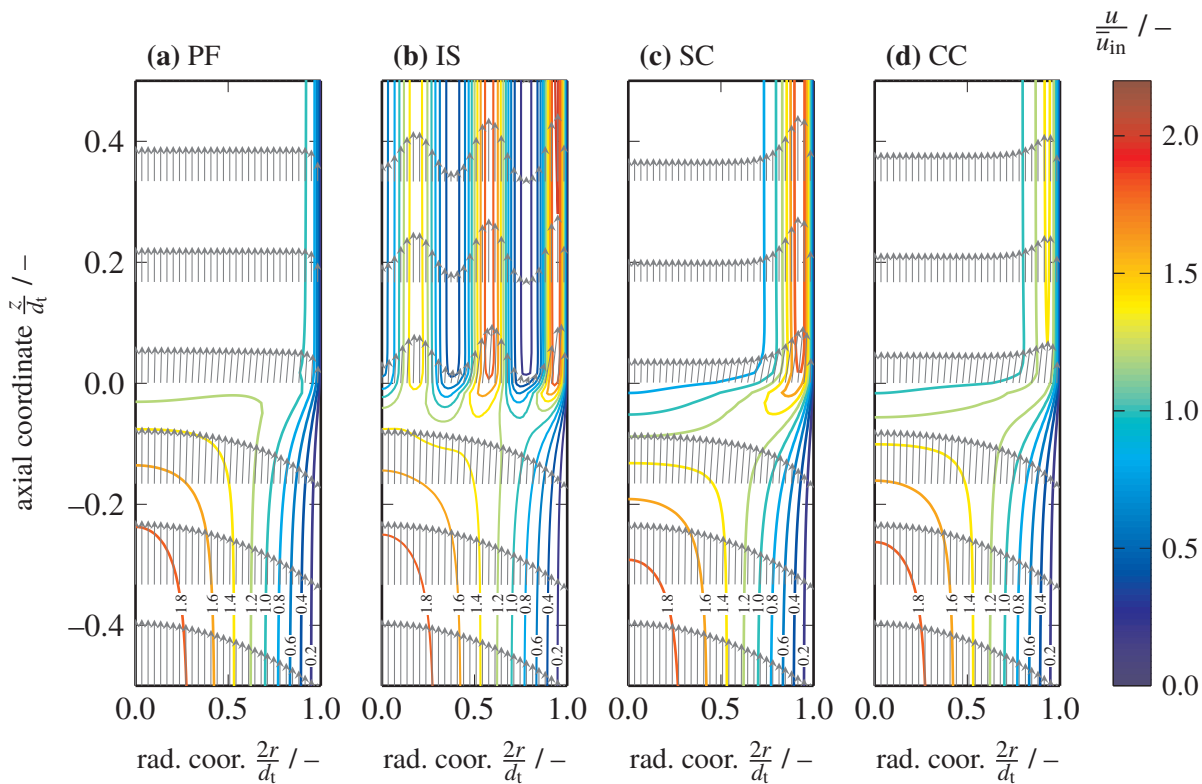
Figure 5.3: Flow field for transition region at reactor inlet for the plug flow reference case (a), a packed beds of ideal spheres (b), spherical (c) and cylindrical catalyst pellets (d) using a tube-to-particle ratio of $d_t/d_p = 5.0$.
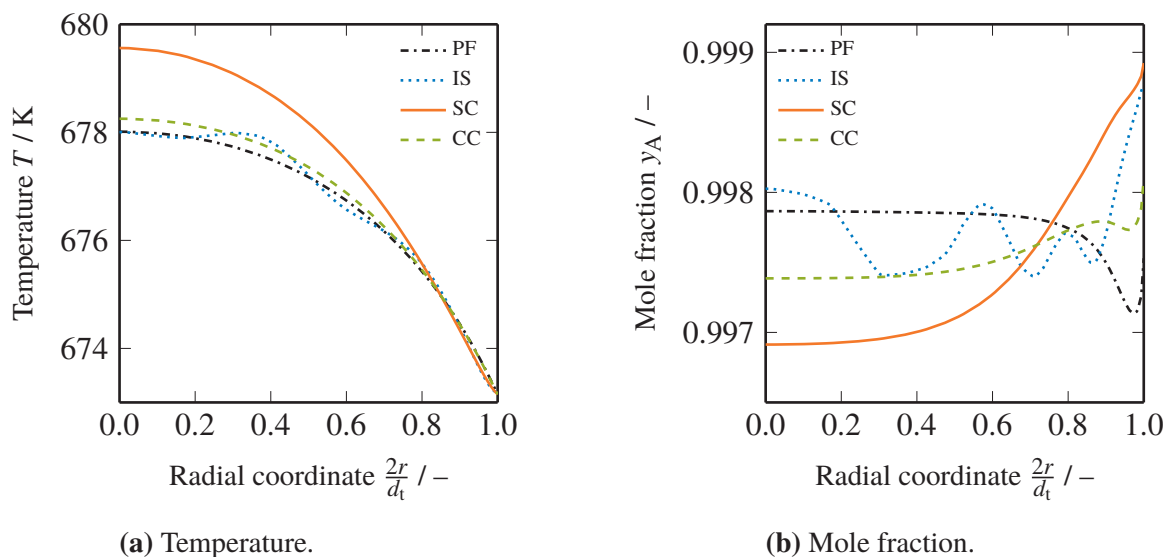

(a) Temperature.

(b) Mole fraction.

Figure 5.4: Radial reactor profiles at the reactor inlet ($z = 0$). Corresponding flow fields are given in Figure 5.3.

to demonstrate the differences to an artificial Dirichlet condition at the inlet and can be seen as an academic demonstration of the complex profiles arising at domain discontinuities.

(a) Temperature at $r = 0$.

(b) Cross-section-averaged mole fraction.
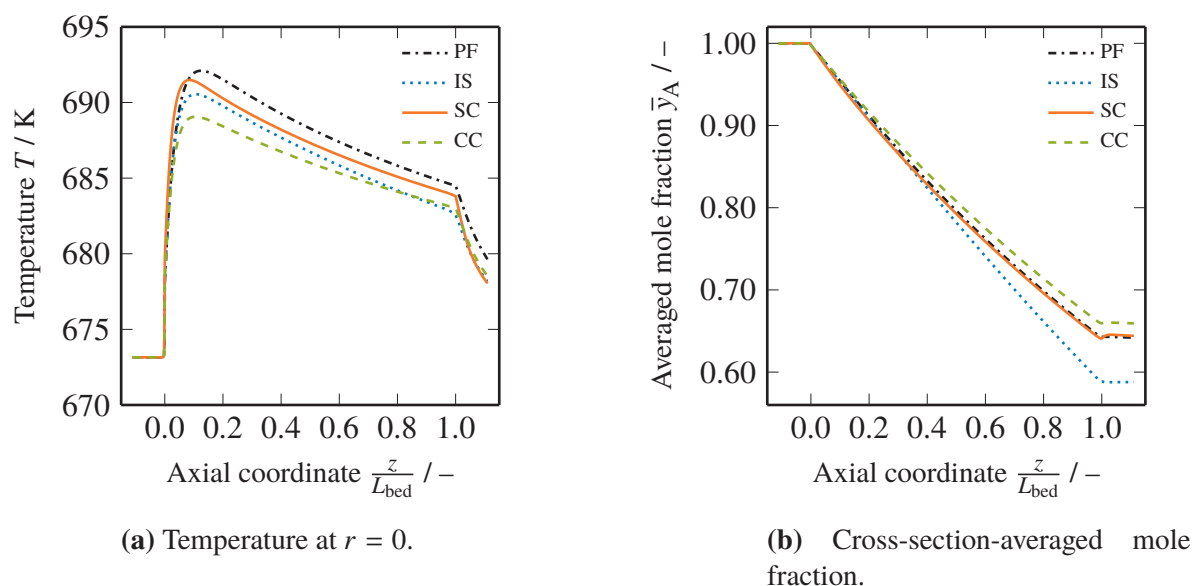
Figure 5.5: Axial reactor profiles. Corresponding flow fields are given in Figure 5.3.

Figure 5.5 shows the resulting profiles for temperature T and mole fraction y_A along the reactor axis. The four bed configurations vary in hotspot temperature ($\Delta T_{max} = \max(T) - T_{in}$) and position, Figure 5.5a, and conversion behavior, Figure 5.5b, respectively. Hotspot temperatures ΔT_{max} increase from 15.9 K for a packed bed of cylindrical catalysts up to 19.0 K for the reference PF case. The differences in radial heat dispersivity (cf. Table 5.1) in combination with the flow fields cause these variations. Interestingly, conversion behavior of the four configurations, shown in Figure 5.5b, is not directly correlated to the corresponding temperature profiles. Here, SC and PF beds exhibit very similar conversions of 35.6 % and 35.8 %, respectively. CC beds yielded a conversion of 34.1 %, while for IS 41.2 % are reached. Therefore, the choice of radial porosity profile, in combination with the shape of the particles, significantly influences the conversion behavior. The majority of this effect can be attributed to the differences in the flow field. While in PF, SC and CC beds a homogeneous velocity at the inner part of the tube is accompanied with more or less pronounced bypassing at the tube wall, in a bed of ideal spheres the strong oscillations in the radial velocity profile lead to distinct channeling. The latter causes a broadened velocity or residence time distribution and, thus, an inhomogeneous consumption of the reactant, compared to the other three configurations. In further consequence, emerging gradients enhance dispersive species fluxes in radial direction, resulting in an overall increase of conversion.

In addition, in Section 5.S.3 of the Supplementary Material a variation of the enthalpy of reaction $\Delta_r H^\circ$ is presented to assess the influence of heat sources and sinks. While hotspot temperatures only moderately depend on the bed configuration, the distribution of the catalyst material and the associated flow fields cause distinct differences in the conversion behavior.

X_A-values inside a bed of ideal spheres (IS) deviate from the other three configuration with increasing magnitude of $\Delta_r H^\circ$.

5.4.2 Space Velocity

The influence of residence time and flow conditions on the reactor characteristics are evaluated by variation of the weight hourly space velocity *WHSV*. Figures 5.6a and 5.6b visualize the changes in hotspot temperature and conversion, respectively.
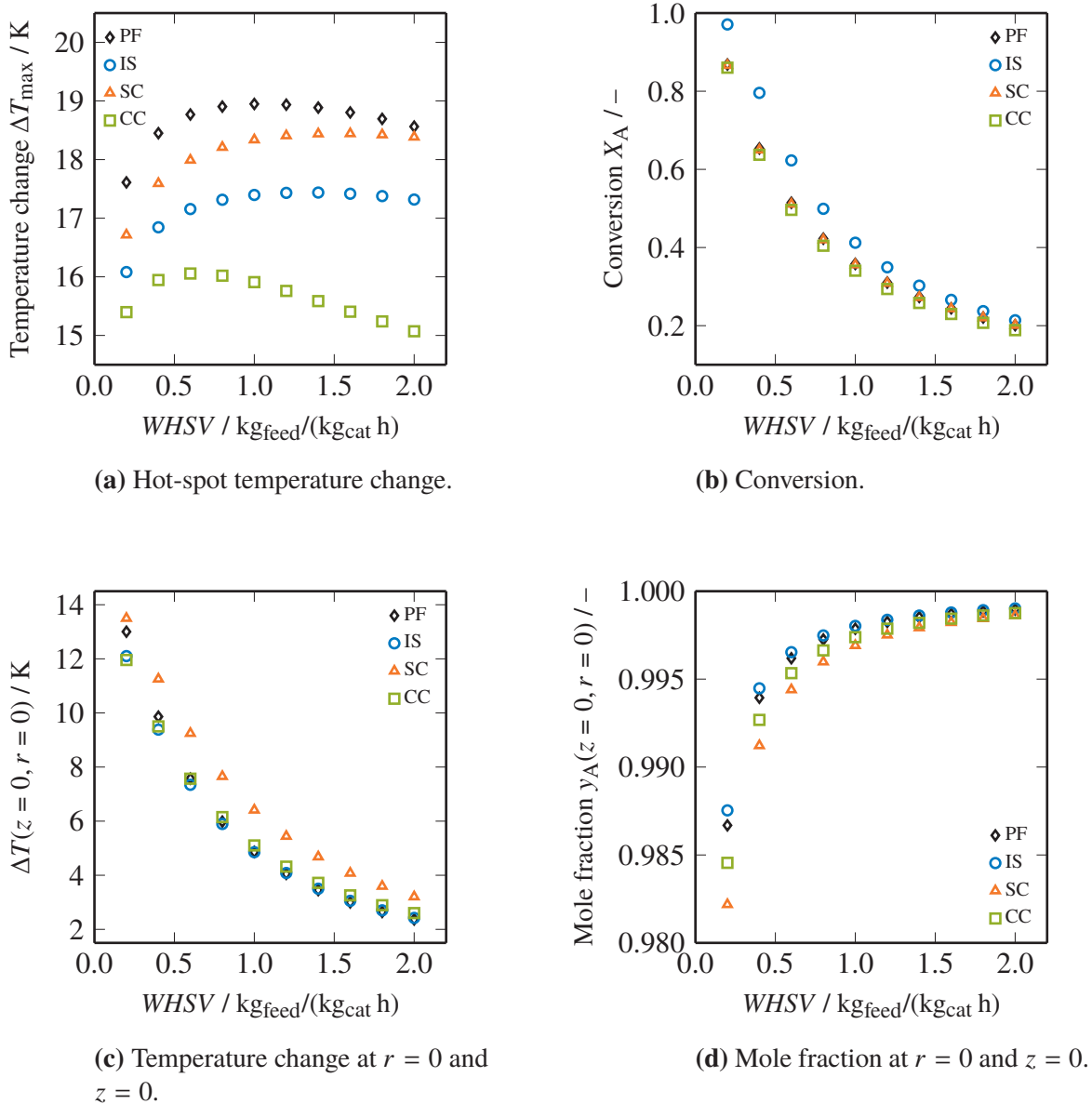

(a) Hot-spot temperature change.

(b) Conversion.

(c) Temperature change at $r = 0$ and $z = 0$.

(d) Mole fraction at $r = 0$ and $z = 0$.

Figure 5.6: Influence of weight hourly space velocity *WHSV*.

As shown in Figure 5.6b, reactant conversion X_A increases with decreasing space velocity, or raised residence time. Similar to the base case described in Section 5.4.1, beds of ideal

spheres result in slightly enhanced conversions compared to the other three configurations. Hotspot temperatures in Figure 5.6a are the result of several effects. First, a reduction of *WHSV* increases the conversion (cf. Figure 5.6b), but simultaneously the total amount of heat releasable by reaction is reduced with *WHSV*. Second, radial heat removal from the bed ascends with increased flow inside the bed. Both effects are dependent on the bed configuration, as can be seen by the trends in Figure 5.6a.

In Figures 5.6c and 5.6d, axial dispersion effects are visualized by the temperature rise ΔT and and mole fraction y_A at the tube center $r = 0$ and bed entry $z = 0$, respectively. Decreasing *WHSV* reduces convective transport inside the bed and, simultaneously lessens the dynamic contribution of the dispersive fluxes, as given in Equations (5.14) and (5.16). However, in summary the influence of dispersion drops with *WHSV*, which explains the trends shown in Figures 5.6c and 5.6d. Furthermore, comparing the hotspot temperatures ΔT_{max} in Figure 5.6a with the temperature rise at the bed entry in Figure 5.6c indicates that the hotspot position is shifted to higher axial positions for increasing *WHSV*. Furthermore, the temperature at the bed entry is not directly correlated to the trends of the respective hotspot temperatures. By contrast, mole fractions at the bed entry (cf. Figure 5.6d) are correlated to the total conversion shown in Figure 5.6b, since there is no prevalent radial gradient, as it is the case for the temperature through cooling. Furthermore, radial y_A-profiles at the bed entry (cf. Figure 5.4b) occur for all space velocities, which is why $y_A(z = 0, r = 0)$ in Figure 5.6d not necessarily depicts the minimum value of y_A. In summary, the impact of axial dispersion is reciprocally correlated to the space velocity for all four bed configurations.

5.4.3 Stoichiometry

Coupling of chemical reaction with fluid flow is mainly caused by variations in the fluid density ϱ_{fl}. For a non-adiabatic fixed bed reactor, temperature changes induced by the heat of reaction are damped along the reactor axis by external cooling or heating, respectively. In contrast, changes in the number of moles proceed with conversion and, thus, can strongly enhance the coupling of fluid flow and chemical reaction. Figure 5.7 shows this effect for a variation in mole number from -200 to $200\,\%$, simulated by adjusting the stoichiometry ratio ν from $1/3$ to $3/1$, defined in Equation (5.22).

As shown in Figure 5.7b, conversion X_A similarly decreases with increasing stoichiometry ratio ν for all four bed configurations. For reactions with volume contraction ($\nu < 1$) the flow velocity is reduced and residence times rise, respectively. Consequently, more reactant A is consumed. Neglecting the coupling of fluid flow and chemical reaction causes severe deviations for non-stoichiometric reactions ($\nu \neq 1$), as shown by the cold-flow simulations depicted with matte symbols. Here, the velocity field is not adjusted for changes in fluid density disabling mass continuity in Equation (5.10). The opposing trend demonstrates the need of a correct coupling of fluid flow and chemical reaction, especially for non-stoichiometric systems. Furthermore, in
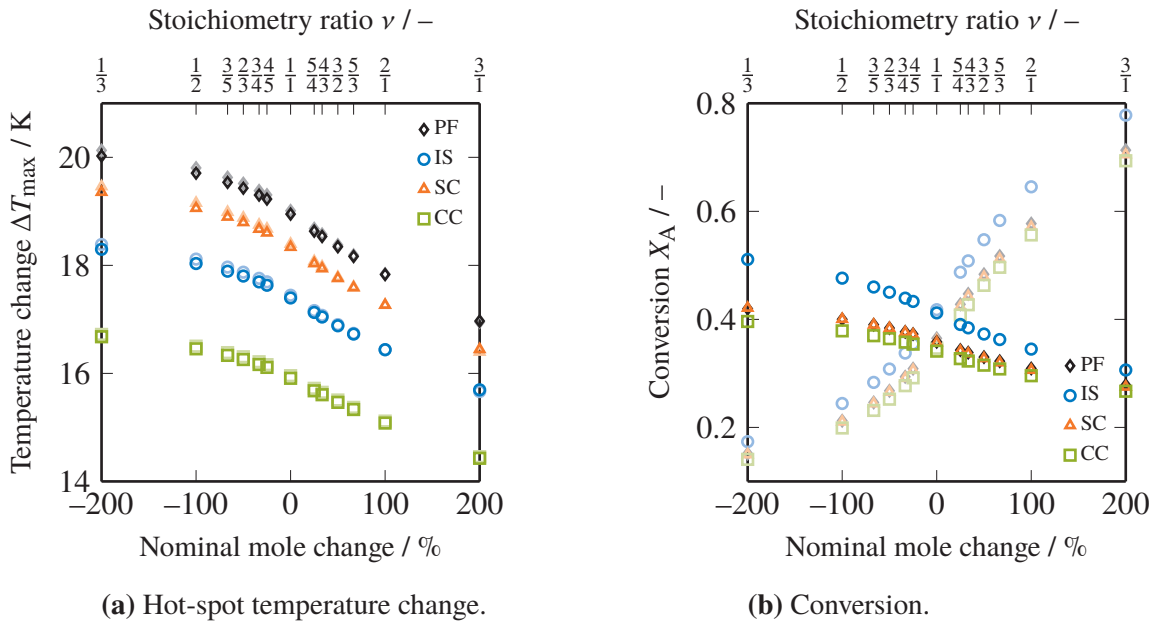
(a) Hot-spot temperature change.

(b) Conversion.

Figure 5.7: Influence of stoichiometry ratio v. Matte symbols represent cold-flow simulations neglecting coupling of fluid flow and reaction (cf. Figure 5.10).

cold-flow simulations the system mass cannot be conserved and errors up to 50 % are observed for the given example (cf. Figure 5.14a in the Supplementary Material). However, for temperature changes ΔT_{max} in Figure 5.7a, differences between coupled and cold-flow simulation become negligibly small. As hotspots evolve close to the bed entry at a moderate conversion level, the change in mole number only slightly affects the fluid density. Moreover, although there are strong deviations in the conversion X_A, axial mole fraction profiles remain comparable for coupled and cold-flow simulations in the entry-near region (cf. Figure 5.14b). In fact, the increased hotspot temperatures for low stoichiometry ratios v arise from changes in the reaction rate (5.23). In this context it is worth mentioning, the stoichiometry ratio v has no impact on a reaction order, as it would be the case for elementary reaction steps.

5.4.4 Tube-to-Particle Ratio

For industrial application, dimensioning of catalyst particles is a key design criteria for fixed-bed applications. A reduction of the particle size minimizes diffusive transport, but simultaneously increases pressure losses and, thus, operational costs. The effect of the fluid flow on varied tube-to-particle ratio is displayed in Figure 5.8.

As shown in Figure 5.8a, with increasing tube-to-particle ratio d_t/d_p hotspot temperatures rise for all configurations. In accordance to Section 5.4.1, absolute ΔT_{max}-values are the lowest for beds of cylindrical catalysts. Furthermore, with increasing d_t/d_p-values radial cooling for the SC and PF configuration seems less effective, compared to reactors consisting of CC.

(a) Hot-spot temperature change.
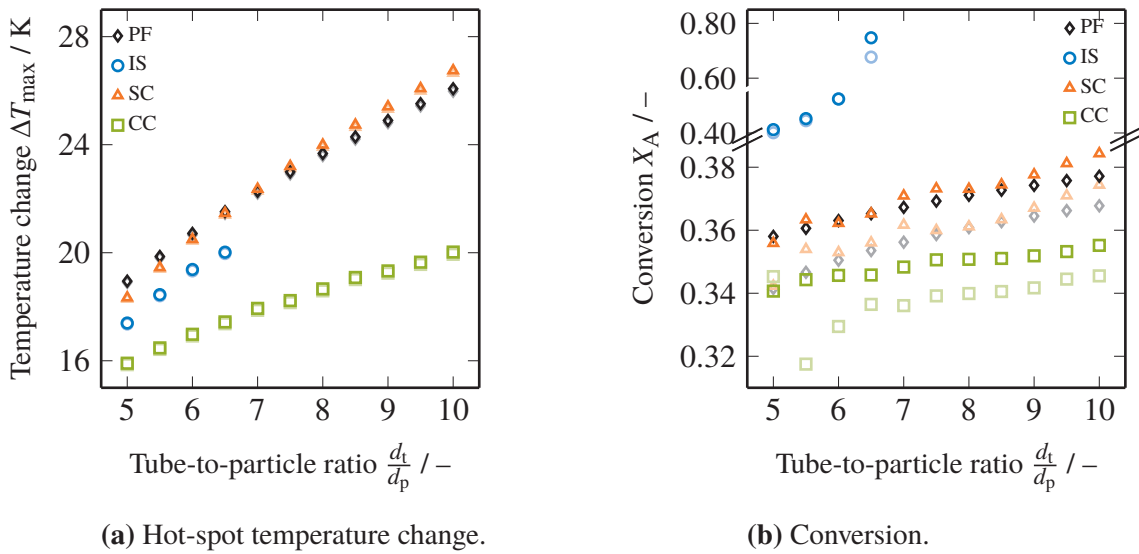
(b) Conversion.

Figure 5.8: Influence of tube-to-particle ratio $\frac{d_t}{d_p}$. Matte symbols represent configurations without void inlet region.

For all four configurations, conversion X_A increases with increasing tube-to-particle ratio d_t/d_p, or decreased pellet diameter d_p (cf. Figure 5.8b). While for PF, SC and CC only moderate changes in conversion arise, the tube-to-particle ratio has a strong impact on the conversion behavior for beds of ideal spheres. Here, the conversion rises from $X_A = 41.2\,\%$ for $d_t/d_p = 5.0$ to $74.4\,\%$ for $d_t/d_p = 6.5$ and full conversion can be observed for tube-to-particle ratios above 6.5 (not displayed). As PF and IS only differ in the underlying radial porosity profiles and flow field, respectively, the latter is responsible for the uncommon conversion behavior.

Figure 5.9 gives insights to the flow-induced differences in conversion behavior of the four configurations. For the constant porosity case PF, neither bypassing nor an oscillating radial velocity profile occurs. Hence, the slightly higher conversion in the tube center originate from the higher reaction rates due to hotspot formation. This is illustrated in temperature contour lines in Figure 5.15 of the Supplementary Material. The effect of bypassing becomes apparent by a comparison of the contour profiles of the spherical and cylindrical catalysts in Figures 5.9c and 5.9d, respectively. As described in Section 5.4.1, increased bypassing for the SC case, increases residence times at the tube center, resulting in more pronounced radial gradients compared to CC configuration. In beds of ideal spheres, distinct channeling occurs. The entailed inhomogeneous distribution in residence times is also reflected by the conversion contour lines in Figure 5.9b. These variations in porosity, velocity and mole fraction cause increased dispersive fluxes in radial direction. Strikingly, with ascending axial coordinate reversed conversion contours, having higher conversion at the tube wall not in the center, evolve. This can be explained by the predominant channeling of fluid flow and the absolute velocity minimum at $2r/d_t = 1 - d_p/d_t$ near the tube wall. The latter takes up to $20\,\%$ of the total cross-section, which significantly raises the conversion level in this region. As can be seen in the Figures 5.16 to 5.18 of the
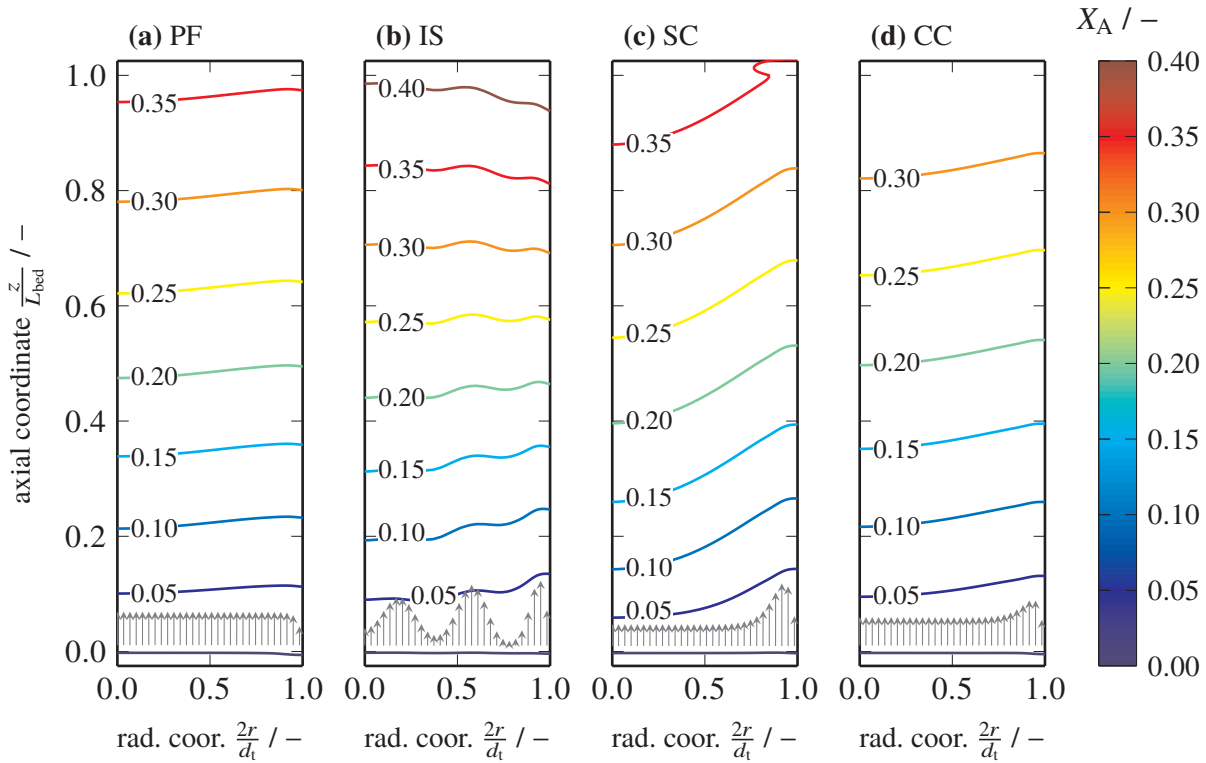
Figure 5.9: Conversion contour lines using a tube-to-particle ratio of $d_t/d_p = 5.0$.

Supplementary Material, for higher tube-to-particle ratios the above described effect becomes even more pronounced, which explains the conversion behavior of the IS configuration depicted in Figure 5.8.

Simulations without a void inlet region are depicted by the matte symbols in Figure 5.8. While hotspot temperatures ΔT_{max} in Figure 5.8a only slightly differ, conversion X_A is affected by the treatment of the inlet region. Despite for a tube-to-particle ratio of $d_t/d_p = 5.0$, the resolution of the void inlet region results in higher conversions compared to a neglected inlet region using Dirichlet boundary conditions at the bed entry. Furthermore, although macroscopically X_A-values increase with d_t/d_p for both cases, the trends exhibit variations and are not strictly monotonically increasing. This can be attributed to the complex interplay of the flow field, the dispersive transport of species and heat in axial and radial direction in combinations with nonlinearities arising from the chemical reaction.

5.5 Conclusion

A pseudo-homogeneous fixed-bed reactor continuum model, fully accounting for 2D convective and dispersive transport, is solved using an efficient numerical procedure based on two discretization techniques. The impact of fluid flow on the reactor behavior is demonstrated for four bed configurations differing in their radial porosity profiles and shape of catalyst particles. A

void inlet region in front of the bed eliminates common artificial boundary conditions giving valuable insights to the extent and form of axial dispersion at the bed entry. Strong influence on the conversion behavior arise from the oscillating porosity profile describing beds of ideal spheres. Distinct radial gradients occur due to the periodic residence time pattern, resulting in enhanced dispersive fluxes in radial direction. Furthermore, the fluid flow around the domain discontinuity at the inlet establishes within a few particle layers for all bed configurations.

A variation in the reaction stoichiometry demonstrates the effect of coupling fluid flow with chemical reaction by considering changes in fluid density. For non-equimolar reaction systems and/or reactions with significant heat of reaction consistent coupling of fluid flow and chemical reaction is inevitable. As a consequence, assuming incompressible flow and neglecting changes in fluid density or concentration are prone to fail, even qualitatively.

With this study, some of the essential points describing fluid flow in 2D fixed-bed reactor simulations are emphasized. These findings elucidate important effects of fluid flow on the fixed-bed reactor design using continuum models. The presented numerical method is a robust and efficient way to solve fluid flow and transport processes inside packed beds.

For future studies, analyses of packings consisting of more complex pellet shapes is of high interest. A combination of experimental investigations and discrete particle CFD modeling can help to evaluate such bed configurations and quantify transport process therein. Subsequently, it is possible to map these findings onto the robust 2D continuum approach presented in this study. For this purpose, it is necessary to determine averaged radial porosity profiles $\varepsilon(r)$, model parameters f_1, f_2 and η_{eff} for momentum transport, $\mathcal{D}_{\text{ax}}$ and $\mathcal{D}_{\text{r}}$ for species dispersion as well as Λ_{ax} and Λ_{r} for heat dispersion. Along this way, the established transport models can be checked and, where necessary, improved or extended. Finally, inter- and intraparticle diffusion can be incorporated to give a full-scale description of the transport phenomena inside catalytic fixed-bed reactors.

5.S Supplementary Material

5.S.1 Numerical Methods

In Figure 5.10 the segregated solution routine, described in Section 5.3.1 is presented. The staggered finite difference grid applied for the fluid flow simulation is illustrated in Figure 5.11.
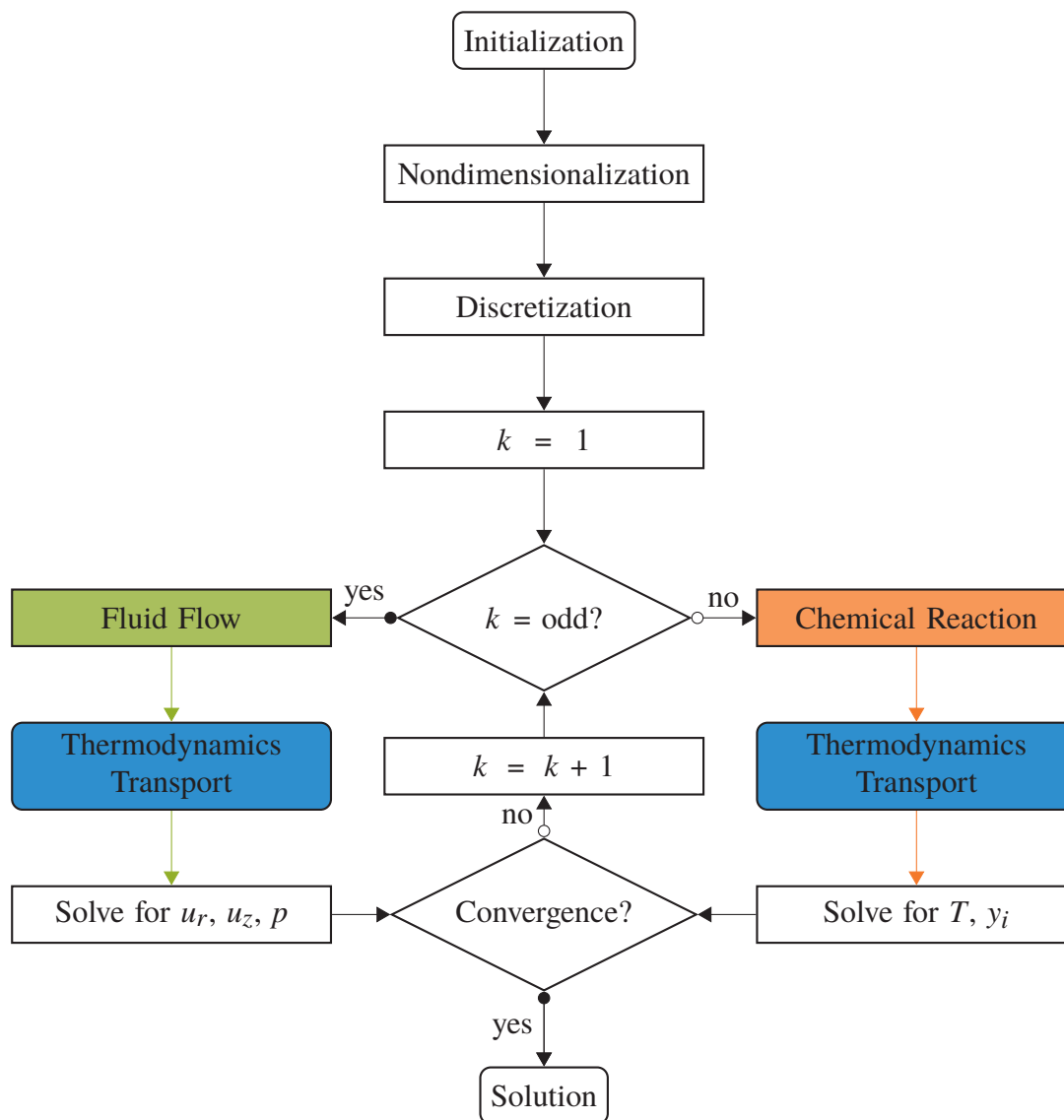
Figure 5.10: Segregated solution routine of the system of partial differential equations.

Grid convergence was confirmed by an adapted method recommended by Celik et al. [171], similar to a strategy used in a previous Chapter 4. Numerical uncertainties for the staggered finite difference grid do not exceed 5.1 % and 7.2 % for the peak velocity magnitude and the overall pressure drop, respectively. Conversion X_A and temperature change ΔT_{max} have uncertainties below 2.0 % and 0.5 % using orthogonal collocation on unequally-spaced finite elements.
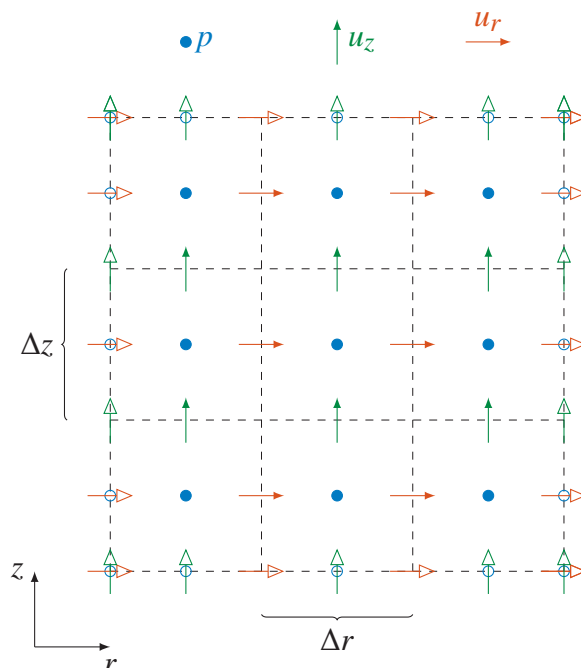
Figure 5.11: Arrangement of staggered finite difference grid used for fluid flow simulations. Filled symbols: internal grid points; open symbols: boundary grid points.

5.S.2 Fluid Flow without Void Inlet

In Figure 5.12 the flow field without void inlet region is displayed for the four bed configurations, cf. Section 5.4.1.

5.S.3 Enthalpy of Reaction

In Figure 5.13 the enthalpy of reaction $\Delta_r H^\circ$ is varied from exothermic to endothermic conditions. The hotspot temperature values in Figure 5.13a depict only slight differences between the bed configurations in line with the observations shown in Figure 5.4a for the base case of $\Delta_r H^\circ = -50\,\text{kJ/mol}$. Solely for $\Delta_r H^\circ$-values above $-60\,\text{kJ/mol}$, the non-linear acceleration of the reaction rate becomes notable and differences in heat transport properties of the four configurations become apparent. However, regarding the conversion behavior in Figure 5.13b distinct differences between the IS configuration and other three beds are observable.

5.S.4 Impact of Reaction Stoichiometry

In Figure 5.14 additional information on impact of cold-flow simulations at varied reaction stoichiometry is presented (cf. Section 5.4.3).
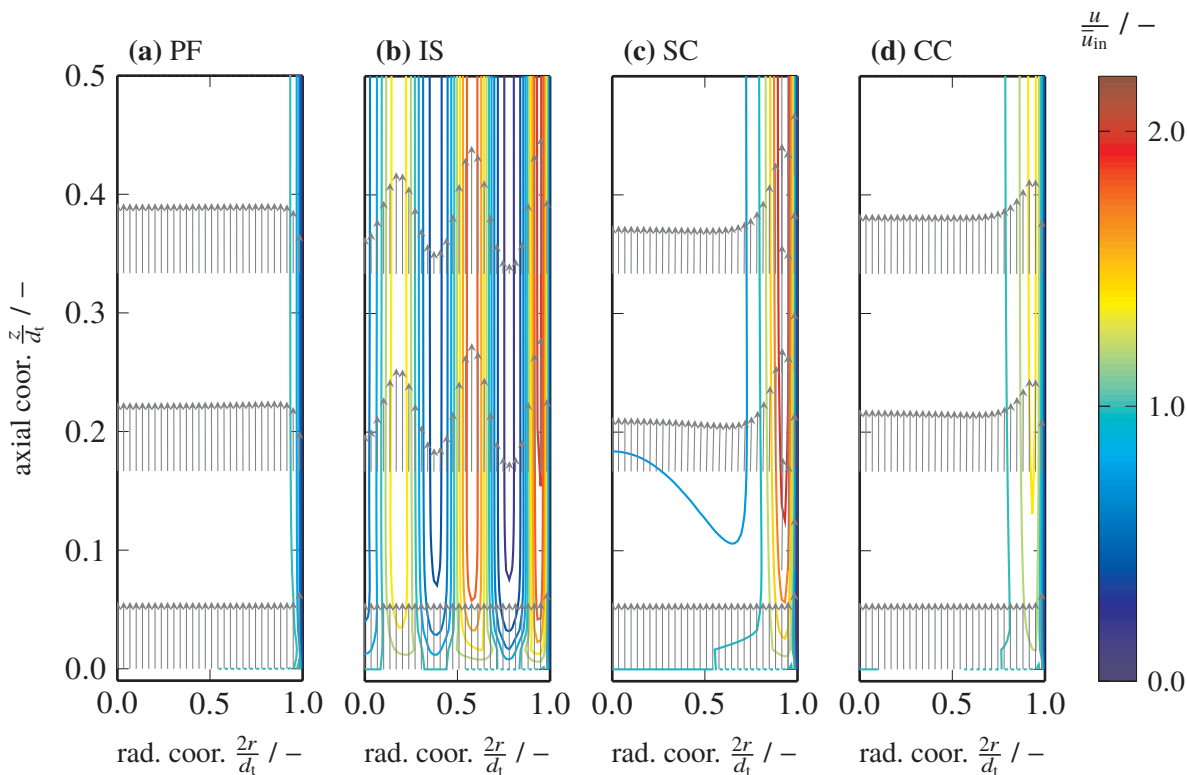
Figure 5.12: Flow field for configurations without void inlet region using a constant inlet velocity $u_z(r, z = 0) = \overline{u}_{in}$. Contour lines are equivalent to Figure 5.3.

(a) Hotspot temperature ΔT_{max}.

(b) Reactant conversion X_A.
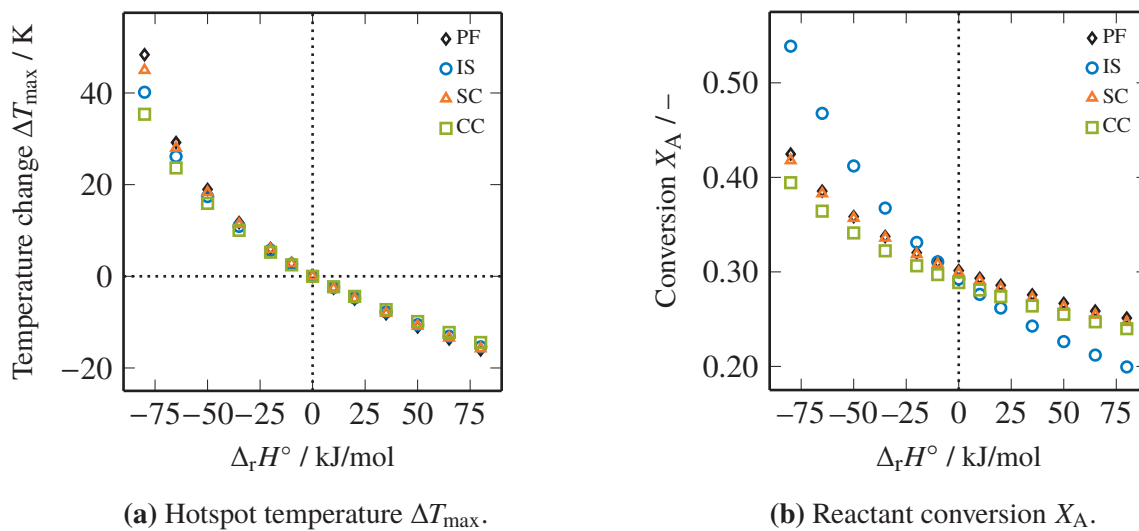
Figure 5.13: Influence of enthalpy of reaction $\Delta_r H^\circ$.
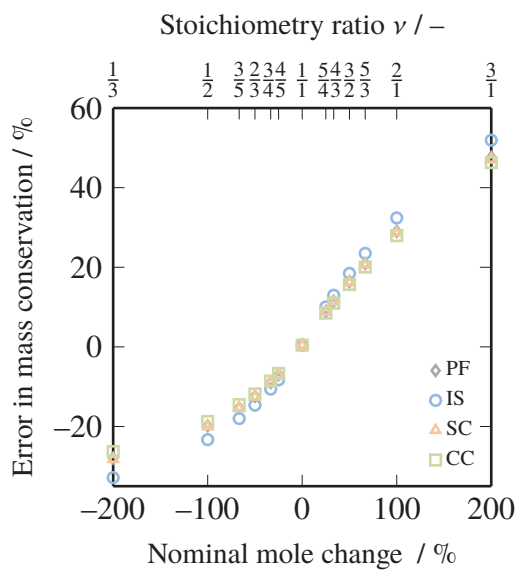
(a) Error in mass conservation for cold-flow simulations neglecting coupling of fluid flow and reaction.
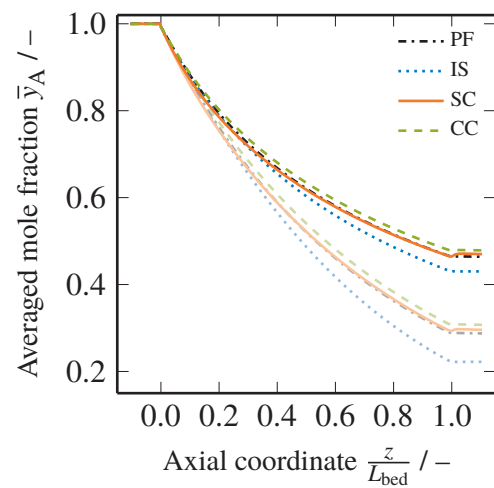
(b) Axial reactor profiles for cross-section-averaged mole fraction $\overline{y}_A$ of reactant A for $\nu = 1/3$. Matte lines represent cold-flow simulations neglecting coupling of fluid flow and reaction (cf. Figure 5.10).

Figure 5.14: Influence of stoichiometry ratio ν and cold-flow assumption using a tube-to-particle ratio of $d_t/d_p = 5.0$.

5.S.5 Temperature Contours

Temperature contour lines for the four bed configurations are displayed in Figure 5.15.
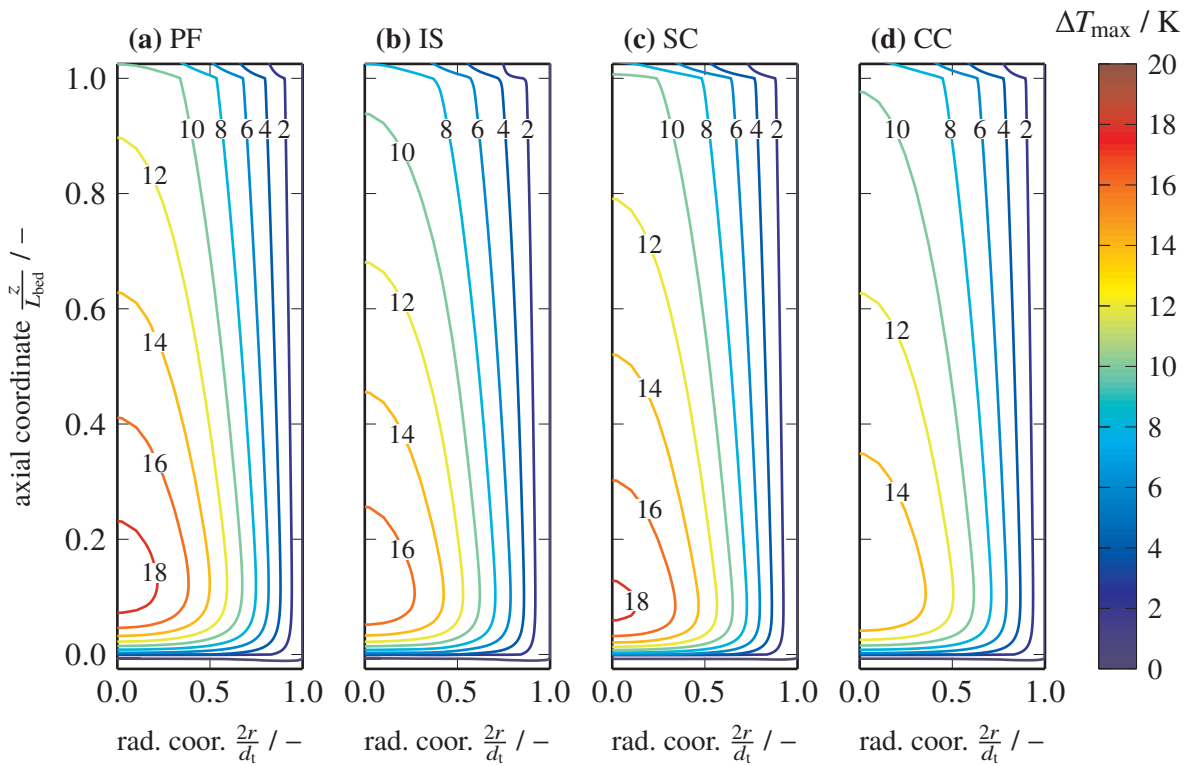
Figure 5.15: Temperature contour lines using a tube-to-particle ratio of $d_t/d_p = 5.0$.

5.S.6 Conversion Contour Lines

Conversion contour lines for tube-to-particle ratios from $d_t/d_p = 5.5$ to 6.5 are given in Figures 5.16 to 5.18.
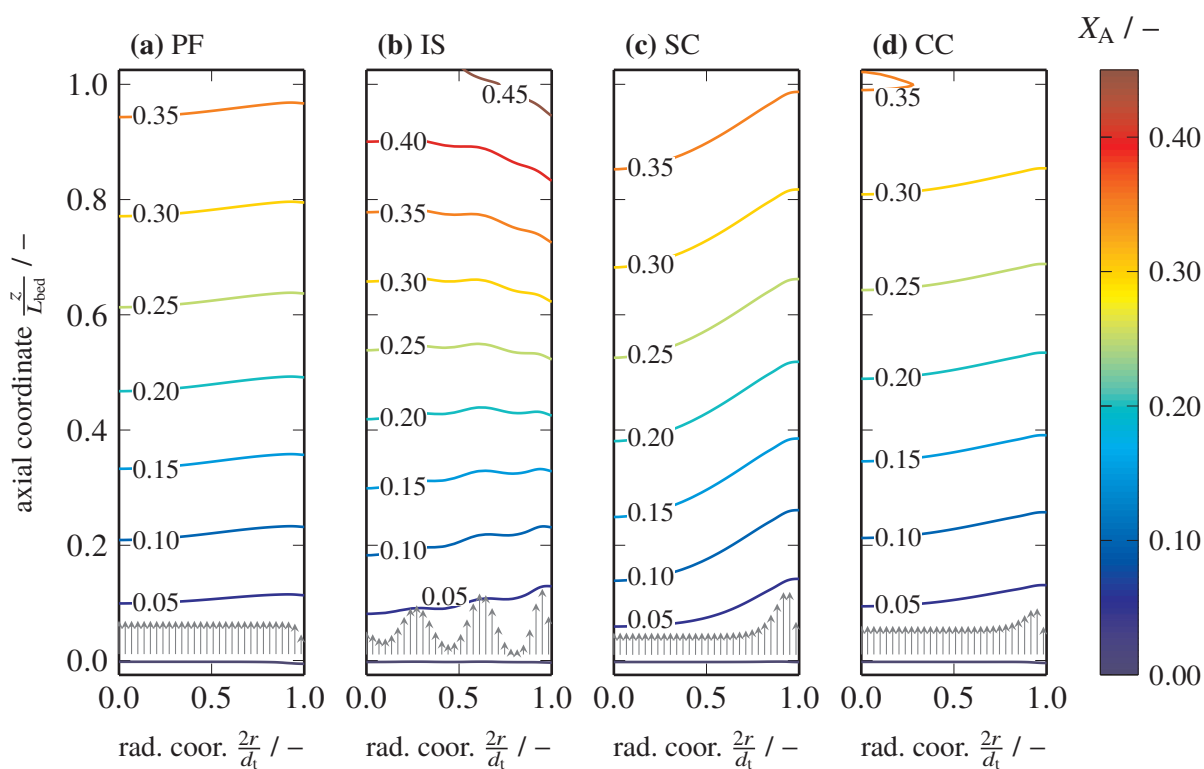
Figure 5.16: Conversion contour lines using a tube-to-particle ratio of $d_t/d_p = 5.5$.
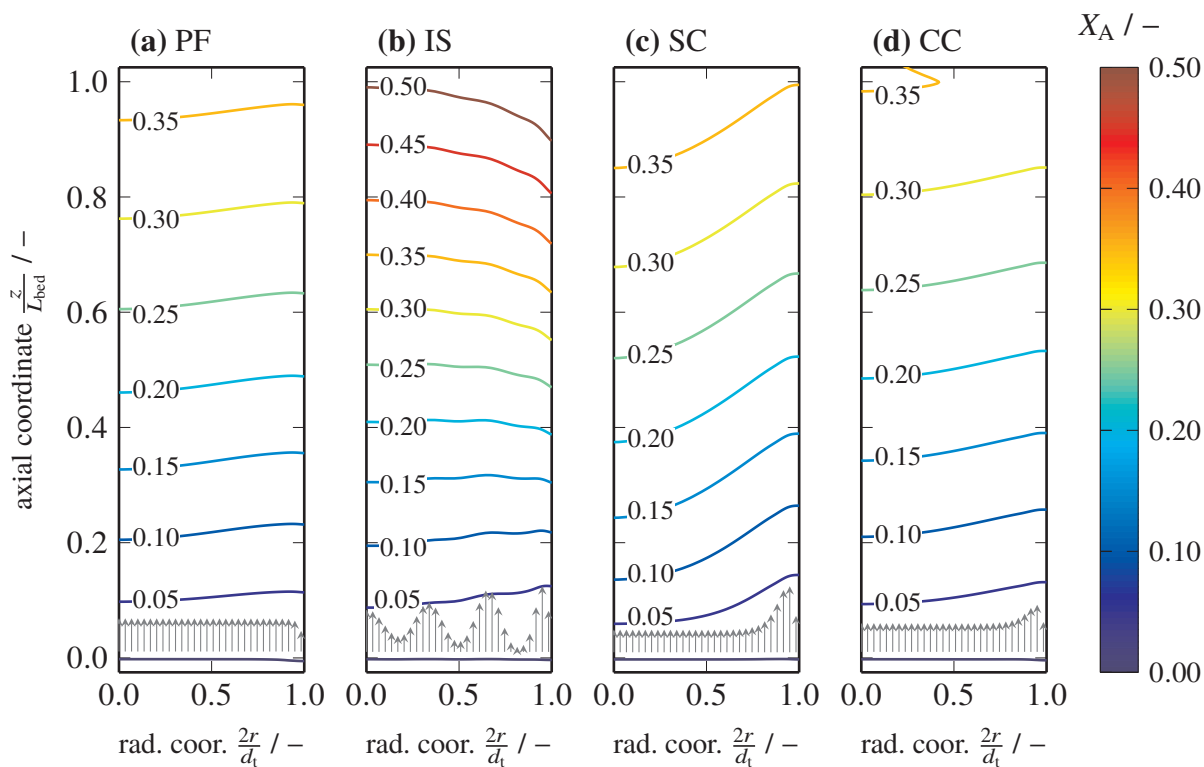
Figure 5.17: Conversion contour lines using a tube-to-particle ratio of $d_t/d_p = 6.0$.
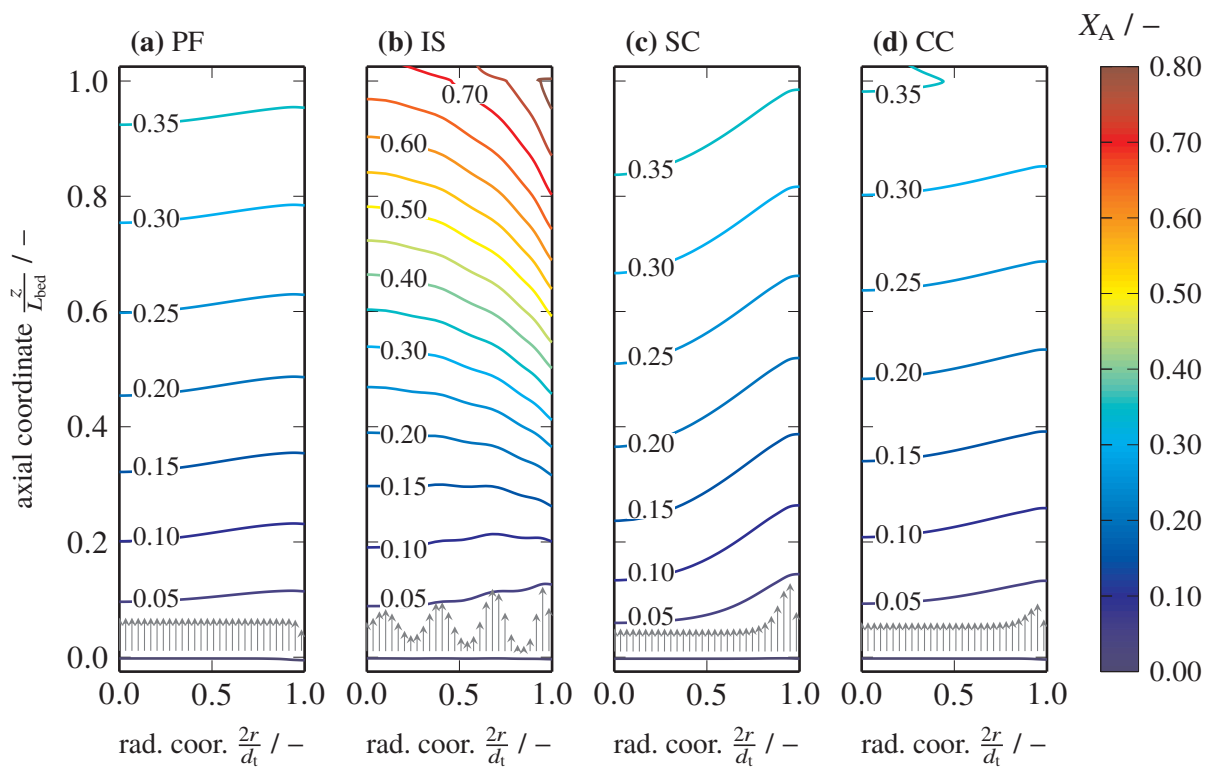
Figure 5.18: Conversion contour lines using a tube-to-particle ratio of $d_t/d_p = 6.5$.

6 Intrinsic Kinetic Model for Oxidative Dehydrogenation of Ethane

An intrinsic kinetic model for the selective production of ethene via oxidative dehydrogenation of ethane over the M1 phase of MoVTeNb mixed metal oxides is presented. Formation of acetic acid, carbon monoxide and carbon dioxide has been incorporated using a holistic reaction mechanism. The proposed model is based on two different oxygen sites, namely, lattice oxygen causing carbon-hydrogen bond cleavage and electrophilic surface oxygen responsible for the formation of carbon-oxygen bonds. It is found that carbon dioxide exclusively originates from decarboxylation of acetate species, while ethene selectively reacts to CO. Consumption and formation of all species are well predicted by the proposed model. Sensitivity analyses demonstrate the strong impact of the initial carbon-hydrogen cleavage on the net ethene production rate. Moreover, regeneration of lattice oxygen sites is found to become rate-determining at oxygen-lean conditions.
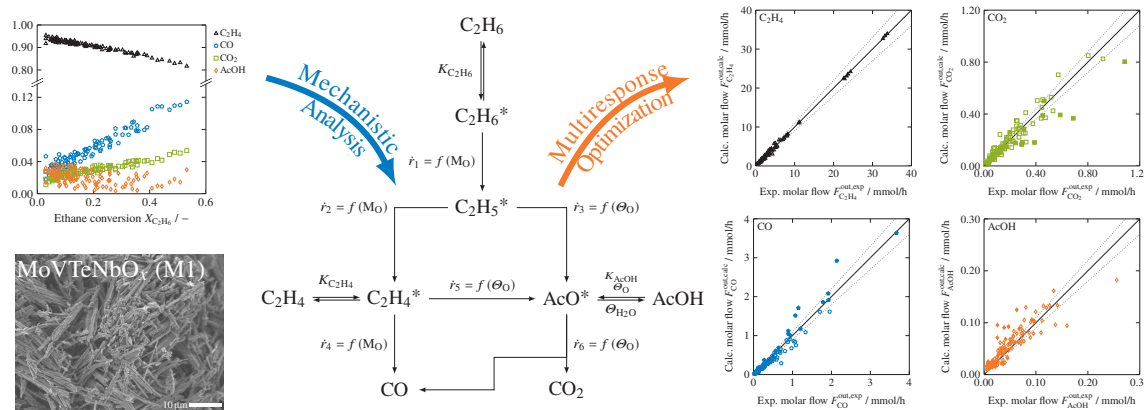
6.1 Introduction

Conventional lower olefins production via steam cracking of naphtha or ethane is a highly energy-intensive process [7, 205]. For the last two decades, oxidative dehydrogenation (ODH) evolved to be an attractive alternative for selective production of propene and, especially, ethene [8, 9, 17, 18]. A bond-strength analysis shows that selectivities to ethene can reach high values, as dissociation energy of the weakest $C-H$ bond in the product ethene exceeds those of ethane [19].

Thus, a variety of catalytic systems has been investigated [9, 20]: (1) (supported) transition metal oxides, such as V [28–30], Mo [31, 32], or rare earth metal oxides [33], as well as respective mixed metal oxides forms [34–36]; (2) NiO-based systems [21, 22]; (3) alkali oxide or chloride catalysts [23, 24]; and (4) boron containing materials [25–27].

In Figure 6.1 the M1 phase of the mixed metal oxide MoVTeNbO$_x$ is shown. This material represents one of the most promising catalysts for oxidative dehydrogenation of ethane (ODHE) [37, 38]. Its high activity and selectivity towards ethene are, amongst others, attributed to isolation of active sites [206, 207]. These site are located on the {100} basal planes and along the lateral surfaces of the crystal. On some of the lateral surfaces these exposed half-pipes [208] significantly enlarge the number of active sites [209].
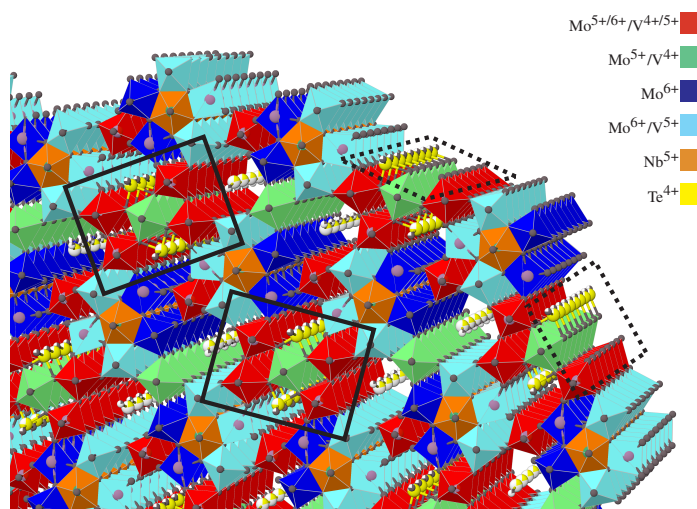
Figure 6.1: Crystal structure of MoVTeNbO$_x$ M1 phase. Proposed active regions on the basal {100} plane and on the lateral surface are indicated by solid and dotted lines, respectively. Suggested occupancies of the metal framework sites are represented by the color coding. Representation adapted from [208, 209].

Several approaches addressing the kinetics of ODHE have been published. Grabowski [210] reviewed kinetic approaches used for the description of ODH reaction of light alkanes on oxide catalysts. For vanadium-based oxides, Mars-van Krevelen (MvK) [211], Eley-Rideal (ER) [212], Langmuir-Hinshelwood(-Hougen-Watson) (LH(HW)) [34, 57, 213, 214], and combinations [215] as well as modified forms [216] have been published.

Over MoVTeNbO$_x$ catalysts, Che-Galicia, Quintana-Solórzano et al. [46, 131, 217, 218] published a collection of different models for ODHE, using a phenomenological description of ethane dehydrogenation. A multitude of models, including power-law, LH(HHW), MvK and ER mechanisms for single and dual sites have been proposed. The statistically most promising approach by Che-Galicia et al. [46] uses a reduced single site model, assuming dissociative Langmuir adsorption of oxygen accompanied by co-adsorption of product water. For this proposed model, side product formation relies on fitted orders in oxygen coverage, which is equivalent to an empirical description of the activity in oxygen.

In this study, an intrinsic kinetic model for ODHE on MoVTeNbO$_x$ M1 phase catalyst is systematically developed. Side product formation to CO, CO$_2$ and acetic acid is addressed by applying a mechanistic reaction network. Rigorous mathematical decoupling enables discrimination between lattice oxygen and electrophilic surface oxygen species. Finally, local sensitivity analyses reveal influences of obtained kinetic parameters on the overall ethene production rate.

6.2 Experimental

Catalyst synthesis, characterization and testing are described in References [219, 220]. In the following, a summary of these methods and corresponding results are given.

6.2.1 Catalyst Synthesis

The catalyst material was synthesized using an oxide based recipe [219]. For this, an aqueous mixture of MoO$_3$, V$_2$O$_5$, TeO$_2$, Nb$_2$O$_5$·1.5 H$_2$O, citric acid (CA), oxalic acid (OA) and mono ethylene glycol (EG) is used. The concentration of Mo was set to 0.5 mol/L using a metal stoichiometry of Mo:V:Te:Nb = 1:0.30:0.05:0.05. Concentration of synthesis additives relative to Mo was set to Mo:CA:OA:EG = 1:0.075:0.050:0.075. Hydrothermal synthesis was performed in an externally heated Premex Reactor AG hpm-p stainless steel autoclave using a blade stirrer at 190 °C and 17.5 bar for 48 h. The precipitates were subsequently filtered and washed with ultra-pure water. In a final step, the material was dried in air for 16 h and preconditioned at 400 °C in nitrogen atmosphere for a dwell time of 2 h (ramp 15 K/min).

6.2.2 Catalyst Characterization

An Agilent 760 ICP-OES spectrometer was used to evaluate the metal contents. X-ray diffraction analysis was performed in a 0.5 mm sealed glass capillary with a STOE Stadi P diffractometer (Cu $\left(K_{\alpha_1} \right)$, Ge(111) monochromator, 50 kV, 30 mA). In addition, Rietveld analysis, including fully crystalline r-TiO$_2$ as internal standard, was performed as described previously [209]. N$_2$-physisorption at 77 K was used for BET analysis in the reduced pressure range from 0.05 to

0.30 with a Quantachrome NOVA 4000e, with a preconditioning at 120 °C under vacuum for 3 h.

6.2.3 Kinetic Tests

Catalyst performance was tested in a glass-lined, stainless-steel tubular reactor with an inner diameter of 4 mm. The catalyst material was diluted with SiC (mass ratio: 1:5) of the same particle size range from 150 to 212 µm. Reactor entry and exit are equipped with silica wool plugs. In front of the catalyst bed 200 mg of SiC ensured an axially homogeneous heat distribution. Reaction temperature was measured at the end of the active bed. Measured temperatures exceed the set reactor temperatures by 5 to 10 K depending on the level of conversion.

Feed and product gas was analyzed using a Shimadzu GC2014 gas chromatography system equipped with TCD and FID detector capable of quantifying C_2-hydrocarbons and -oxygenates, CO and CO_2, O_2 and N_2. The latter was used as internal standard to ensure closure of the carbon balance within ±2 %. Besides CO, CO_2 and acetic acid (AcOH), no other side products were observed. Ideal gas behavior is assumed throughout this study.

Reactor temperature was varied from 290 to 370 °C. Inlet partial pressures of C_2H_6, C_2H_4 and O_2 ranged from 45 to 365 mbar, 86 to 261 mbar and 44 to 373 mbar, respectively. O_2 was diluted to ensure operation outside of flammability limits (molar ratio: O_2:(He+N_2) ≤ 1:9). The absolute pressure inside the reactor ranged from 1.5 to 4.0 bar. The catalyst mass was varied between 50 and 100 mg, resulting in mass specific space velocity ranges of 1.6 to 9.7 $g_{C_2H_6}/(g_{cat}\,h)$, 2.4 to 19.3 $g_{C_2H_4}/(g_{cat}\,h)$ and 0.9 to 10.7 $g_{O_2}/(g_{cat}\,h)$, respectively.

The conversion X_i of O_2, C_2H_6 and C_2H_4 ranged from 0.01 to 0.86, 0.03 to 0.53 and 0.02 to 0.14, respectively. A full summary of experimental selectivities is displayed in Figure 6.2 below.

Influence of inter- and intra-particle transport effects were excluded experimentally using the method of Koros and Nowak [221, 222]. In addition, the following criteria are fulfilled for all experiments.

- Interparticle mass transport: Mears [223]

$$\frac{\dot{R}_i\,\varrho_p\,d_p}{\beta_i\,c_t\,y_i} < 0.3 \tag{6.1}$$

- Interparticle heat transport: Mears [223]

$$\frac{\left|\sum \dot{R}_i \cdot H_i\right|\,\varrho_p\,d_p}{\alpha\,T} < \frac{0.3\,\mathcal{R}\,T}{E_a} \tag{6.2}$$

- Intraparticle mass transport: Weisz and Prater [224]

$$\frac{\dot{R}_i \, \varrho_\mathrm{p} \, d_\mathrm{p}^2}{4 \, c_\mathrm{t} \, y_i \, D_i^\mathrm{eff}} < 1 \tag{6.3}$$

- Intraparticle heat transport: Anderson [225]

$$\frac{\left| \sum \dot{R}_i \cdot H_i \right| \varrho_\mathrm{p} \, d_\mathrm{p}^2}{4 \, \lambda_\mathrm{p}^\mathrm{eff} \, T} < \frac{0.75 \, \mathcal{R} \, T}{E_\mathrm{a}} \tag{6.4}$$

The integral net rates of consumption for $i = C_2H_6$, C_2H_4 and O_2 were used for the mass transport criteria (6.1) and (6.3). Effective diffusion coefficients D_i^eff are estimated as described in Chapter 4. Mass β_i and heat transfer coefficients α are estimated by the correlation of Gnielinski [226], summarized in Appendix A.5.2. Total heat generated by oxidation reactions is quantified by the change in convective heat flow $\left| \sum R_i \cdot H_i \right| \varrho_\mathrm{p}$ using the respective molar enthalpies H_i for all species i. Energy of activation is conservatively assumed to be 150 kJ/mol. Catalyst density and effective thermal conductivity are approximated by 2185 $\mathrm{kg_{cat}}/\mathrm{m}^3$ (cf. Chapter 3) and 0.15 W/(m K), respectively.

Heat transport criteria (6.2) and (6.4) were at least five orders of magnitude below the respective threshold and inter-particle mass transfer (6.1) by a factor of 500. In addition, the left-hand-side of the Weisz-Prater criterion (6.3) remained below 0.57, 0.43 and 0.14 for O_2, C_2H_6 and C_2H_4, respectively.

6.3 Model Development

The reactions of partial and total oxidation of C_2H_6 over the M1 phase of $MoVTeNbO_x$ have been studied. Here, the cleavage of the first C–H bond is assumed the kinetically relevant step. The corresponding dissociation energy of C_2H_6 at 25 °C amounts to 420 kJ/(mol K), while for C_2H_4 this value is significantly higher at 464 kJ/mol [227]. This positive difference of product-reactant bond strength differences enables high C_2H_4 selectivities from a thermodynamic point of view [19].

In general, selective oxidation reactions over (mixed)metal oxides are inherently versatile due to the dynamic interplay of lattice oxygen with the surrounding gas phase [228, 229]. First of all, the origin and nature of the active oxygen species on the surface and in the outermost lattice region have to be defined. The former is described to have an electrophilic character and assumed to be, e.g. O_2^-, O_2^{2-}, O^-, or O^{2-} surface species. The latter are incorporated into the surface layers of the lattice structure of the oxide and are considered to be terminal metal-oxo groups (M=O), or bridged oxygen species (M–O–M), each having a rather nucleophilic character [229–231]. Electrophilic oxygen is assumed to catalyze the formation of fully oxidized

products CO and CO_2. In contrast, nucleophilic oxygen species are essential for high selectivity in dehydrogenation reactions [20].

Formation of C_2 oxygenates over Mo–V mixed oxides is assumed to be promoted by steam, as reported by Thorsteinson et al. [34] over $MoVNbO_x$ catalysts, Linke et al. [232] over $MoVTePdO_x$ and Sankaranarayanan et al. [233] over $MoVAlO_x$. Similarly, acrylic acid formation is enhanced by steam in propane ODH over the M1 phase of $MoVTeNbO_x$ [234]. The latter finding was accompanied by steam-induced enrichment of V^{5+} [235] and Te [234] at the oxide surface. In addition, presence of water influences the electronic structure and reduces surface polarity of the catalyst material [236]. Overall, water enhances the formation of carboxylic acids by facilitating their desorption on the one hand and directly influencing the structure of the material on the other hand. Furthermore, Linke et al. [216] proposed different sites for the formation of acetic acid (AcOH) from C_2H_6 and C_2H_4, respectively.

Decomposition of AcOH to CO and CO_2 over $MoVTeNbO_x$ was analyzed by Sobolev and Koltunov [237]. They found that decarboxylation of the acid is accompanied by oxidation of the residual C_1 surface species to CO. In addition, formic acid decomposed via dehydration to CO. Furthermore, Naumann d'Alnoncourt et al. [235] determined the rates of CO oxidation and water-gas-shift reaction to be negligibly small over the M1 phase of $MoVTeNbO_x$.

An overview of the obtained product selectivities is shown for H_2O-free C_2H_6/O_2- and C_2H_4/O_2-feed in Figure 6.2a and 6.2b, respectively. During kinetic measurements the following general observations are made:

- C_2H_6 is consumed approximately 5 to 10 times faster compared to C_2H_4 at equivalent reaction conditions.

- CO:CO_2 product ratios are above unity for all data points, which is comparable to experiments of Kube et al. [238] on pure M1 $MoVTeNbO_x$.

- CO:CO_2 product ratios for feeding C_2H_6 and C_2H_4 range from 1.1 to 2.7 and 2.5 to 4.8, respectively.

Based on these considerations and observations, the reaction network in Figure 6.3 is constructed. Major assumptions can be summarized as follows:

- Adsorption of gas-phase species is assumed to be quasi-equilibrated (⇌) and of Langmuir-type: monomolecular for C_2H_6, C_2H_4 and H_2O and dissociative for O_2.

- Desorption of AcOH is assumed to be assisted by adsorbed water resembling a dimeric structure [239, 240].

- At relevant reaction conditions, interaction of CO and CO_2 with the mixed oxide surface is small, making the respective coverages negligible [46, 235].

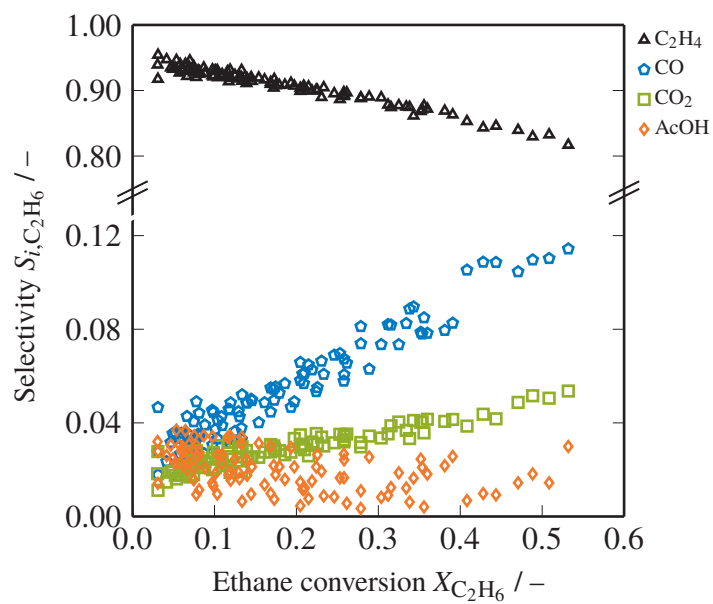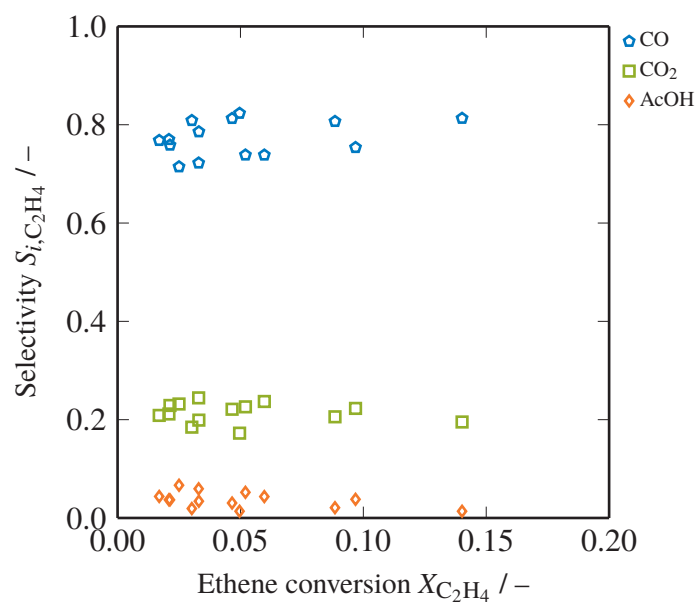- Cleavage of C–H bonds is assisted by lattice-type oxygen site M_O.

(a) C_2H_6 feed.

(b) C_2H_4 feed.

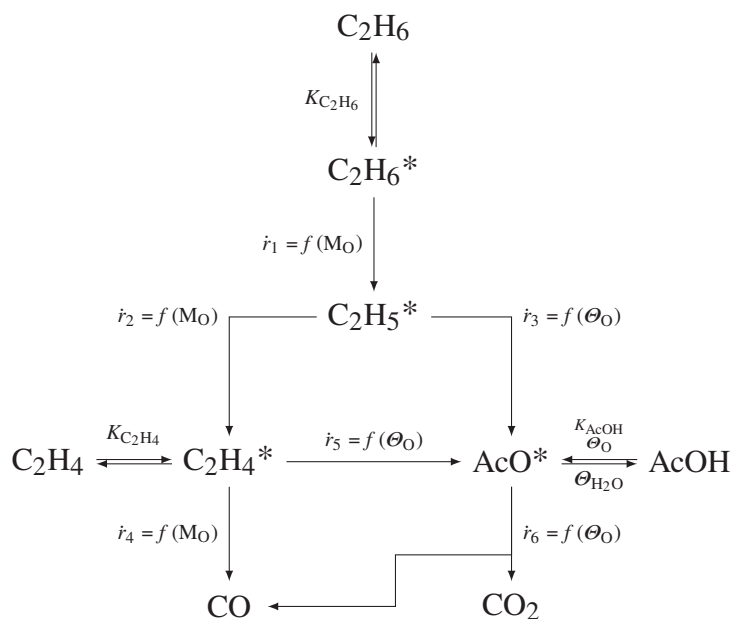**Figure 6.2:** Summary of product selectivities for all experimental data points using different carbon-feeds.

$$C_2H_6$$

$$\big\updownarrow K_{C_2H_6}$$

$$C_2H_6^*$$

$$\dot{r}_1 = f(M_O) \big\downarrow$$

$$\dot{r}_2 = f(M_O) \quad\text{———}\quad C_2H_5^* \quad\text{———}\quad \dot{r}_3 = f(\Theta_O)$$

$$C_2H_4 \underset{K_{C_2H_4}}{\rightleftharpoons} C_2H_4^* \xrightarrow{\dot{r}_5 = f(\Theta_O)} AcO^* \underset{\Theta_{H_2O}}{\overset{\substack{K_{AcOH} \\ \Theta_O}}{\rightleftharpoons}} AcOH$$

$$\dot{r}_4 = f(M_O) \big\downarrow \qquad\qquad \dot{r}_6 = f(\Theta_O) \big\downarrow$$

$$CO \longleftarrow \qquad\qquad CO_2$$

Figure 6.3: Proposed reaction network for the oxidative dehydrogenation of ethane over the M1 phase of MoVTeNb mixed metal oxides. M_O and Θ_O represent lattice and electrophilic surface oxygen sites, respectively.

- Insertion of oxygen and formation of $C-O$ bonds is based on electrophilic surface oxygen Θ_O.

- Initial activation of C_2H_6 is dependent on the cleavage of the first $C-H$ bond by M_O.

- Rate-determining reaction steps ($\text{——}\!\!\wedge\!\!\rightarrow$) are first-order in M_O and Θ_O, respectively.

- C_2H_4 either decomposes to CO by activation through $C-H$ cleavage at M_O, or interacts with electrophilic surface oxygen Θ_O to form AcO^*, which is similar to an approach made by Linke et al. [216] over $MoVTePdO_x$.

- CO_2 is exclusively formed by decarboxylation of AcO^*.

- Lattice oxygen M_O is regenerated by Θ_O, as suggested for supported VO_x [241, 242]. The resulting M_O-M_{OH}-cycle resembles the methodology of Mars and van Krevelen [243].

The obtained mechanism consists of six irreversible surface oxidation reactions and the regeneration of lattice oxygen M_O sites under H_2O release, which is summarized in Table 6.1.

Table 6.1: Summary of proposed reaction mechanism for oxidative dehydrogenation of ethane over MoVTeNb mixed metal oxides.

Reaction j	Irreversible surface reaction	Equation
1	$C_2H_6{}^* + M_O \xrightarrow{\;\;} C_2H_5{}^* + M_{OH}$	$\dot{r}_1 = k_1[M_O]\Theta_{C_2H_6}$
2	$C_2H_5{}^* + M_O \xrightarrow{\;\;} C_2H_4{}^* + M_{OH}$	$\dot{r}_2 = k_2[M_O]\Theta_{C_2H_5}$
3	$C_2H_5{}^* + O^* \xrightarrow[{-^* \;-2\,M_{OH}}]{+O^* \;+2\,M_O} AcO^* + {}^*$	$\dot{r}_3 = k_3\Theta_O\Theta_{C_2H_5}$
4	$C_2H_4{}^* + M_O \xrightarrow[{-2^* \;-3\,M_{OH}}]{+2\,O^* \;+3\,M_O} 2\,CO + M_{OH} + {}^*$	$\dot{r}_4 = k_4[M_O]\Theta_{C_2H_4}$
5	$C_2H_4{}^* + O^* \xrightarrow[{-^* \;-M_{OH}}]{+O^* \;+M_O} AcO^* + {}^*$	$\dot{r}_5 = k_5\Theta_O\Theta_{C_2H_4}$
6	$AcO^* + O^* \xrightarrow[{-3\,M_{OH}}]{+3\,M_O} CO_2 + CO + 2\,{}^*$	$\dot{r}_6 = k_6\Theta_O\Theta_{AcO}$
7	$2\,M_{OH} + O^* \xrightarrow{\;\;} 2\,M_O + H_2O^*$	$\dot{r}_7 = k_7\Theta_O[M_{OH}]^2$

Adsorptive j	Equilibrated adsorption	Equation[a]
O_2	$O_{2(g)} + 2\,{}^* \rightleftharpoons 2\,O^*$	$\Theta_O = \sqrt{K_{O_2}p'_{O_2}}\,\Theta_*$
C_2H_6	$C_2H_{6(g)} + {}^* \rightleftharpoons C_2H_6{}^*$	$\Theta_{C_2H_6} = K_{C_2H_6}p'_{C_2H_6}\Theta_*$
C_2H_4	$C_2H_{4(g)} + {}^* \rightleftharpoons C_2H_4{}^*$	$\Theta_{C_2H_4} = K_{C_2H_4}p'_{C_2H_4}\Theta_*$
H_2O	$H_2O_{(g)} + {}^* \rightleftharpoons H_2O^*$	$\Theta_{H_2O} = K_{H_2O}p'_{H_2O}\Theta_*$
$AcOH$	$2\,AcOH_{(g)} + 2\,{}^* + O^* \rightleftharpoons 2\,AcO^* + H_2O^*$	$\Theta_{AcO} = \sqrt{K_{AcOH}\dfrac{\sqrt{K_{O_2}p'_{O_2}}}{K_{H_2O}p'_{H_2O}}p'_{AcOH}}\,\Theta_*$ [b]

[a]Reduced partial pressure $p'_i = \frac{p_i}{p_i^{\circ}}$; $p_i^{\circ} = 10^5$ Pa.

[b] $\lim\limits_{p_{AcOH}\to 0} \sqrt{K_{AcOH}\dfrac{\sqrt{K_{O_2}p'_{O_2}}}{K_{H_2O}p'_{H_2O}}p'_{AcOH}} = 0$, $\quad \lim\limits_{\substack{p_{AcOH}\neq 0 \\ p_{H2O}\to 0}} \sqrt{K_{AcOH}\dfrac{\sqrt{K_{O_2}p'_{O_2}}}{K_{H_2O}p'_{H_2O}}p'_{AcOH}} = \infty \to \Theta_{AcO} = 1 \;\wedge\; \Theta_i = 0 \;\forall\, i \neq AcO.$

To allow a mathematical description of the presented reaction mechanism it is essential to decouple the two oxygen pools and, hence, the two types of active sites. By applying pseudo-steady-state approximation, the fraction of lattice hydroxyl groups M_{OH} can be approximated to (derivation in Supplementary Material 6.S.1)

$$[M_{OH}] \approx \frac{-a_M + \sqrt{a_M^2 + 4a_M}}{2},$$
$$a_M = \frac{2k_1 K_{C_2H_6} p'_{C_2H_6} + 4k_4 K_{C_2H_4} p'_{C_2H_4}}{2k_7 \sqrt{K_{O_2} p'_{O_2}}}.$$

(6.5)

Consequently, the composition of active lattice oxygen M_O is obtained from the balance

$$[M_O] = 1 - [M_{OH}].$$

(6.6)

The surface coverages Θ_i can be determined in a similar way. The coverage of the ethyl surface intermediate $\Theta_{C_2H_5}$ is given to

$$\Theta_{C_2H_5} = \frac{a_\Theta}{b_\Theta + c_\Theta \Theta_*} \Theta_*,$$
$$a_\Theta = k_1 [M_O] K_{C_2H_6} p'_{C_2H_6},$$
$$b_\Theta = k_2 [M_O],$$
$$c_\Theta = k_3 \sqrt{K_{O_2} p'_{O_2}}.$$

(6.7)

Here, the fraction of unoccupied sites Θ_* can be derived from a parabolic relation

$$\Theta_* = \frac{-e_\Theta + \sqrt{e_\Theta^2 + 4b_\Theta c_\Theta d_\Theta}}{2c_\Theta d_\Theta},$$
$$d_\Theta = 1 + \sqrt{K_{O_2} p'_{O_2}} + K_{C_2H_6} p'_{C_2H_6} + K_{C_2H_4} p'_{C_2H_4}$$
$$+ K_{H_2O} p'_{H_2O} + \sqrt{K_{AcOH} \frac{\sqrt{K_{O_2} p'_{O_2}}}{K_{H_2O} p'_{H_2O}} p'_{AcOH}},$$
$$e_\Theta = (a_\Theta + b_\Theta d_\Theta - c_\Theta).$$

(6.8)

Finally, coverages of O^*, $C_2H_6^*$, $C_2H_4^*$, H_2O^* and AcO^* are calculated by the respective Eqs. in Table 6.1 based on quasi-equilibrated sorption processes. Detailed derivations of the correlations in Eqs. (6.5), (6.7) and (6.8) are given in the Supplementary Material 6.S.1.

The system of surface reactions, shown in Table 6.1, is correlated to the net rate of production of the gas phase species by

$$\dot{R} = SRM \times \dot{r}.$$

(6.9)

The vector of surface reactions $\dot{r}$ ($[7 \times 1]$) is multiplied by the stoichiometry-reaction-matrix *SRM* to get the net rate of production for all gas phase species. This matrix is provided in Table 6.5 of the Supporting Information. Due to the approximations made for the balance of lattice oxygen and hydroxyl groups (cf. Equation (6.5) and Section 6.S.1 of the Supporting Information) the H-element balance is not fully closed. Hence, the net rates of production for H_2O and O_2 are calculated from element conservation

$$\dot{R}_{H_2O} = -\frac{1}{2} \left(6\dot{R}_{C_2H_6} + 4\dot{R}_{C_2H_4} + 4\dot{R}_{AcOH} \right)$$
$$\dot{R}_{O_2} = -\frac{1}{2} \left(\dot{R}_{H_2O} + \dot{R}_{CO} + 2\dot{R}_{CO_2} + 2\dot{R}_{AcOH} \right)$$

(6.10)

In summary, the presented model consists of 24 unknown parameters, whereof 14 represent the irreversible surface reactions (pre-exponential factors A and activation energies E_a) and 10 the sorption processes (entropy $\Delta_{ads}S^\circ$ and enthalpy of adsorption $\Delta_{ads}H^\circ$). For the hydrocarbons C_2H_6 and C_2H_4, it is possible to estimate the entropy of adsorption by the loss of $\frac{1}{3}$ of the translation entropy of the gas species [244], which can be obtained from the correlation of Sackur [245] and Tetrode [246]. Furthermore, enthalpy of adsorption for these two species was determined by microcalometric measurements in the work of Kube et al. [238]. Hence, the number of unknown parameters can be reduced to 20.

6.4 Methodology

6.4.1 Reactor Model

The experimental reactor system is described via an 1D isothermal, isobaric, pseudo-homogeneous plug-flow reactor model along the catalyst mass m_{cat}

$$\frac{dF_i}{dm_{cat}} = \dot{R}_i$$

(6.11)

for each species i, based on the respective net rate of productions R_i. To increase numerical stability, all molar flows F_i are normalized to the total flow of carbon atoms F_C^{in}, which results in a non-dimensional system of ordinary differential equations

$$\frac{dY_{i,j}}{dx} = \frac{m_{cat,j}}{F_{C,j}^{in}} \dot{R}_{i,j}$$

(6.12)

for each experiment j. Numerical integration of this stiff system is performed using a variable-step, variable-order solver based on numerical differentiation formulas [247].

6.4.2 Regression

Regression is performed by optimizing the scaled and dimensionless parameters $\Phi = [\varphi_m, \dots, \varphi_{n_{\text{para}}}]$ to minimize the residual weighted sum of squares

$$SSQ_{\text{res}} = \sum_{i=1}^{n_{\text{resp}}} \omega_i \sum_{j=1}^{n_{\text{exp}}} \left(Y_{i,j}^{\text{out,exp}} - Y_{i,j}^{\text{out,calc}} (\Phi) \right)^2 \xrightarrow{\Phi} \min. \tag{6.13}$$

at the reactor outlet, which is equivalent to a minimization of the respective negative log-likelihood function. All observed carbon-containing species (C_2H_6, C_2H_4, CO, CO_2 and AcOH) are selected as fitting responses. The diagonal entries of the inverse covariance matrix are approximated by weighting factors ω_i, defined as [248, 249]

$$\omega_i = \frac{\left(\sum_{j=1}^{n_{\text{exp}}} F_{i,j}^{\text{out,exp}} \right)^{-1}}{\sum_{i=1}^{n_{\text{resp}}} \left(\sum_{j=1}^{n_{\text{exp}}} F_{i,j}^{\text{out,exp}} \right)^{-1}}. \tag{6.14}$$

The resulting weighting factors are listed in Table 6.2.

Table 6.2: Weighting factors of carbon species obtained from Equation (6.14).

Parameter	Value / −
$\omega_{C_2H_6}$	$2.945 \cdot 10^{-3}$
$\omega_{C_2H_4}$	$8.034 \cdot 10^{-3}$
ω_{CO}	$7.710 \cdot 10^{-2}$
ω_{CO_2}	$1.820 \cdot 10^{-1}$
ω_{AcOH}	$7.299 \cdot 10^{-1}$

All model parameters φ_m are scaled and parameterized to increase numerical stability and reduce cross-correlation. Arrhenius' law is expressed as

$$k = A \exp\left(-\frac{E_a}{\mathcal{R} T} \right) = \exp\left(\varphi_{k_A} - \varphi_{k_{E_a}} \left(\frac{T_{\text{ref}}}{T} - 1 \right) \right)$$

$$\varphi_{k_A} = \ln\left(\frac{A}{\text{mmol}/(\text{g}_{\text{cat}} \, \text{h})} \right) - \varphi_{k_{E_a}} \tag{6.15}$$

$$\varphi_{k_{E_a}} = \frac{E_a}{\mathcal{R} T_{\text{ref}}}$$

using the central temperature of all experiments as reference value

$$T_{\text{ref}} = \frac{\max(T) + \min(T)}{2}. \tag{6.16}$$

Parameterization of adsorption equilibrium constants is done in a similar way

$$
\begin{aligned}
\ln(K) &= \frac{\Delta_{\text{ads}}S^{\circ}}{\mathcal{R}} - \frac{\Delta_{\text{ads}}H^{\circ}}{\mathcal{R}T} = \varphi_{K_{\Delta S}} - \varphi_{K_{\Delta H}}\left(\frac{T_{\text{ref}}}{T} - 1\right) \\
\varphi_{K_{\Delta S}} &= \frac{\Delta_{\text{ads}}S^{\circ}}{\mathcal{R}} - \varphi_{K_{\Delta H}} \\
\varphi_{K_{\Delta H}} &= \frac{\Delta_{\text{ads}}H^{\circ}}{\mathcal{R}\,T_{\text{ref}}}.
\end{aligned}
\tag{6.17}
$$

Parameter estimation is performed using a two-step procedure [216, 248]. In a first step, realistic parameter estimates were obtained by a constraint genetic algorithm [250] using a heuristic crossover-function with a crossover-fraction of 0.8. Subsequently, an unconstrained gradient-based trust-region optimization is applied to find the optimum set of parameters.

An overview of statistical methods, applied for the evaluation of the fitted parameters, is given in Appendix 6.A. Furthermore, a local sensitivity analysis procedure is presented in Appendix 6.B. Complete parameter optimization and subsequent analyses were performed using MATLAB v2019a.

6.5 Results and Discussion

6.5.1 Catalyst Characterization

The synthesized material is composed of characteristic needle-like crystals, displayed in Figure 6.4.
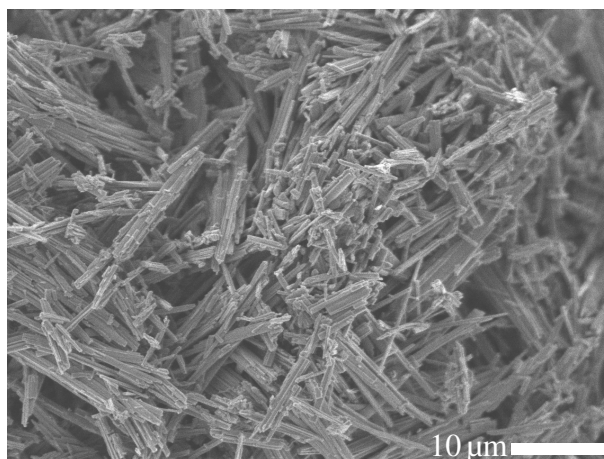
Figure 6.4: Scanning electron microscope image of the synthesized MoVTeNbO$_x$ catalyst.

The stoichiometric metal ratio of Mo:V:Te:Nb = 1:0.30:0.05:0.05 was determined by ICP-OES analysis. The resulting diffraction pattern is displayed in Figure 6.5 confirming the crystallinity of the synthesized M1 phase demonstrating the absence of major phase impurities. Rietveld

analysis yields 79 wt-% M1 and 3 wt-% of MoO_3 balanced by 18 wt-% of amorphous or rather nano-crystalline material.
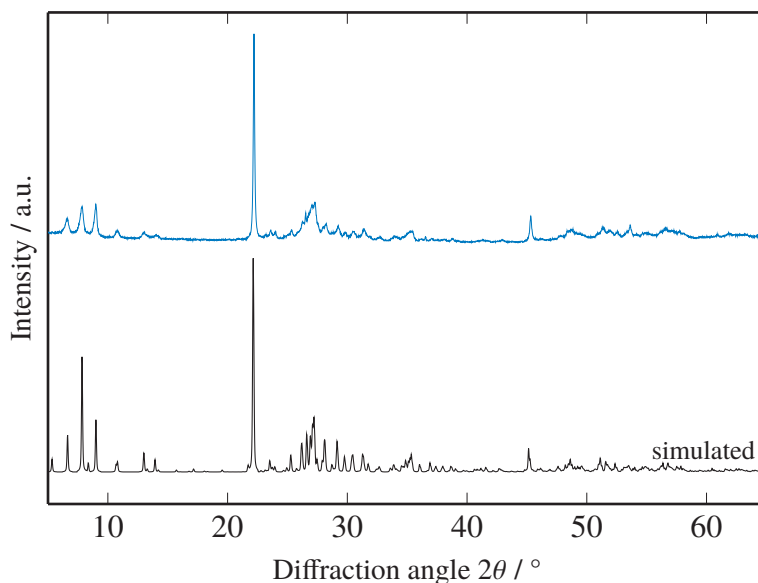
Figure 6.5: X-ray diffraction pattern of the synthesized $MoVTeNbO_x$ catalyst and the simulated pattern of the M1 phase according to Buttrey and co-workers [251, 252].

A BET-surface area of 41 m²/g$_{cat}$ was determined, which significantly exceeds values previously reported for this material [217, 234]. More detailed information on the material properties and morphology of the catalyst is given elsewhere [219, 220].

6.5.2 Model Evaluation

An overview of the optimized parameters φ_m with corresponding 95 % asymptotic confidence intervals and re-parameterized values for pre-exponential factors A, activation energies E_a, entropy $\Delta_{ads}S^\circ$ and enthalpy $\Delta_{ads}H^\circ$ of adsorption is provided in Table 6.3.

Table 6.3: Estimated parameters φ_m with 95 % asymptotic confidence intervals, corresponding t-values (6.23) and re-parameterized variables A_i, $E_{a,i}$, $\Delta_{ads}S^\circ$ and $\Delta_{ads}H^\circ$ (cf. Equations (6.15) and (6.17)) for a reference temperature of $T_{ref} = 610.125\,\mathrm{K}$.

Reaction j	$\varphi_{k_{j,A}}$ / −	t-value / −	A_j / mol/(kg$_{cat}$ s)	$\varphi_{k_{j,E_a}}$ / −	t-value / −	$E_{a,j}$ / kJ/mol
1	5.97 ± 0.01	$1.36 \cdot 10^3$	$2.99 \cdot 10^7$	19.43 ± 0.06	$1.15 \cdot 10^3$	98.57
2	9.92 ± 0.02	$1.41 \cdot 10^3$	$1.20 \cdot 10^{10}$	21.48 ± 0.06	$1.20 \cdot 10^3$	108.98
3	9.05 ± 0.02	$1.42 \cdot 10^3$	$1.11 \cdot 10^{13}$	29.17 ± 0.07	$1.33 \cdot 10^3$	148.00
4	2.59 ± 0.03	$2.78 \cdot 10^2$	$6.13 \cdot 10^6$	21.22 ± 0.18	$3.83 \cdot 10^2$	107.67
5	4.18 ± 0.15	$9.33 \cdot 10^1$	$7.12 \cdot 10^{11}$	31.30 ± 2.59	$4.01 \cdot 10^1$	158.77
6	9.86 ± 0.77	$4.22 \cdot 10^1$	$2.88 \cdot 10^{16}$	36.23 ± 1.66	$7.25 \cdot 10^1$	183.80
7	7.30 ± 0.02	$1.19 \cdot 10^3$	$3.22 \cdot 10^{10}$	25.08 ± 0.08	$1.00 \cdot 10^3$	127.24

Adsorptive j	$\varphi_{K_{j,\Delta S}}$ / −	t-value / −	$\Delta_{ads}S_j^\circ$ / J/(mol K)	$\varphi_{K_{j,\Delta H}}$ / −	t-value / −	$\Delta_{ads}H_j^\circ$ / kJ/mol
O_2	-15.55 ± 1.52	$1.28 \cdot 10^3$	-167.77	-17.87 ± 0.04	$1.51 \cdot 10^3$	-90.65
C_2H_6	n.a.	n.a.	$-55.40^{(a)}$	n.a.	n.a.	$-34.00^{(b)}$
C_2H_4	n.a.	n.a.	$-55.11^{(a)}$	n.a.	n.a.	$-41.00^{(b)}$
H_2O	-2.31 ± 0.01	$2.08 \cdot 10^1$	-179.38	-15.55 ± 1.52	$3.40 \cdot 10^1$	-78.87
AcOH	-5.63 ± 0.70	$2.68 \cdot 10^1$	-259.32	-25.56 ± 2.94	$2.89 \cdot 10^1$	-129.67

[a] Estimated by loss of $\frac{1}{3}$ of the translational entropy [244, 253] using the equation of Sackur [245] and Tetrode [246], cf. Appendix A.1.5.

[b] Heat of adsorption determined by microcalorimetry, as reported by Kube et al. [238].

The resulting activation energies range in realistic physical regions and are comparable to the values fitted by Che-Galicia et al. [131]. The energy barrier for the initial C−H cleavage is found to be 99 kJ/mol, which nicely correlates with the findings of Cheng and Goddard [254] based on quantum-mechanical calculations. They found a minimum activation energy of about 95 kJ/mol for ODHE using a crystal structure with comparable vanadium content. Evaluation of the pre-exponential factors confirms the excellent catalytic performance of the catalyst used for this study in comparison to previous ODHE studies on MoVTeNbO$_x$ [46, 131, 218].

Moreover, hydrocarbon oxidation reactions dependent on M$_O$ ($\dot{r}_1$, $\dot{r}_2$ and $\dot{r}_4$) exhibit significantly lower energy barriers and pre-exponential factors compared to the ones relying on electrophilic surface oxygen ($\dot{r}_3$, $\dot{r}_5$ and $\dot{r}_6$). This can be caused by the different nature of the respective active sites as well as differences in actual site density. However, at this point it must be stressed, that reactions 2 to 7 are not elementary impeding a detailed interpretation of the exact parameter values.

The fitted sorption parameters fulfill all four criteria of Boudart et al. [255] on the sign and magnitude of the fitted enthalpies and entropies of adsorption. For H$_2$O a enthalpy of adsorption of −79 kJ/mol is found. Applying DFT methods on a pure MoV M1 phase, Li et al. [256] reported values in the range of −68 to −106 kJ/mol, which vary with the position of adsorption on the crystal (cf. Figure 6.1). This indicates that $\Delta_{ads}H^{\circ}_{H_2O}$ lies within a realistic range, although Wernbacher et al. [257] stress the inherent differences in electronic and functional properties between M1 structures of MoV and MoVTeNb mixed metal oxides.

Table 6.4: Characteristic statistic values of the kinetic model at the parameter optimum, according to the methodology given 6.A.

Parameter	Value / −	Parameter	Value / −
dof_{res}	565	SSQ_{res}	$3.455 \cdot 10^{-4}$
dof_{pe}	35	SSQ_{pe}	$1.697 \cdot 10^{-5}$
$F_{s,crit}$	1.589	F_s	$7.470 \cdot 10^{3}$
$F_{a,crit}$	1.573	F_a	1.278
t_{crit}	1.964		

In general, small asymptotic confidence intervals are obtained for all 20 estimated parameters. Furthermore, the respective t-values all exceed a value of 20, which indicates sufficiently high relevance of each individual parameter compared to the corresponding critical value [258]. As shown by the statistical values in Table 6.4, the global significance of the kinetic model is approved, as the corresponding F_s exceeds the critical $F_{s,crit}$ by several orders of magnitude [258]. Moreover, the lack-of-fit value F_a remains below the corresponding critical value $F_{a,crit}$ proving the adequacy of the kinetic model. For nonlinear models, this adequacy test is very difficult to pass [258], which emphasizes the quality of the presented intrinsic kinetic model from a statistic point of view.

In addition, the binary correlation coefficients $\rho_{m,n}$ (6.24) between all fitted parameters are given in Table 6.6 of the Supporting Information. For 173 of the total 190 interaction between the parameters is small or moderate ($\rho_{m,n} \leq 0.5$), which confirms the successful parameterization (cf. Eqs. (6.15) and (6.17)). A medium statistical interaction ($0.5 < \rho_{m,n} \leq 0.9$) is determined for 16 parameter pairs. $\varphi_{k_{6,A}}$, $\varphi_{K_{H_2O,\Delta S}}$ and $\varphi_{K_{AcOH,\Delta S}}$ exhibit $\rho_{m,n}$ values above 0.9, indicating stronger interaction. On the one side, the inherent coupling of $\varphi_{K_{H_2O,\Delta S}}$ and $\varphi_{K_{AcOH,\Delta S}}$ through the H_2O assisted desorption of AcOH can explain these high values. On the other side, all three parameters combine the entropic influence of AcO* consumption at the catalytic surface. This could indicate that the proposed reaction scheme oversimplifies reactions of C_2-oxygenates at the surface. However, to date there is little knowledge of catalytic reactions and corresponding surface intermediates of such species on MoVTeNbO$_x$ materials and more detailed studies are required. This includes integral investigation of AcOH oxidation over the MoVTeNbO$_x$ M1 phase in combination with proper quantification of the accompanied H_2O influence.

Parity plots for the five fitting responses are given in Figures 6.6 and 6.7 in linear and logarithmic form, respectively. The kinetic model provides excellent agreement to the experimentally measured flows for C_2H_6 and C_2H_4 over a wide range of experimental conditions. Furthermore, the formation of carbon oxide products CO and CO_2 can be predicted with a sufficiently high accuracy, which is close to the precision of the measurements. Slightly higher deviations between measured and calculated flows are present for the AcOH response. This is primarily caused by missing (co)feed experiments of AcOH, which was not possible with the present experimental setup. Moreover, as assumed from the analyses of the binary correlation parameters above, there is little knowledge on the interaction of C_2-oxygenates with this catalyst.

During development of the proposed kinetic model, a multitude of potential formation mechanisms of AcOH were investigated. However, kinetically controlled desorption of AcOH, additional surface intermediates and different pathways scenarios did not allow proposing a successful or statistically adequate kinetic model. In addition, MoVTeNb mixed metal oxide catalysts exhibit a variety of different active facets due to their morphology and metal occupancy [209] (cf. Figure 6.1). The interplay of a radical character of the oxidation reactions with the variable catalytic surface enables a broad range of possible reaction pathways. Hence, a kinetic model is prone to neglect subordinate reactions, which contribute to the overall formation of CO, CO_2, or AcOH.

Analyses of the residuals allow a closer evaluation of the proposed reaction mechanism and can indicate potential deficiencies. Figures 6.11 to 6.13 in the Supporting Information show the impact of temperature, total pressure and $C_2H_{4/6}/O_2$-feed ratio on the model prediction for all five responses. Most residuals are normally distributed in terms of reaction temperature. Only for the CO and AcOH-responses slight variations are observed: with increasing reaction temperature their formation is slightly overestimated for C_2H_6-feed experiments and partly underestimated when C_2H_4 is fed. With respect to the total pressure, the residuals of all five responses show acceptable distributions. However, it is apparent, that changing the total pressure and, therefore,

(a) C_2H_6.

(b) C_2H_4.

(c) CO.

(d) CO_2.
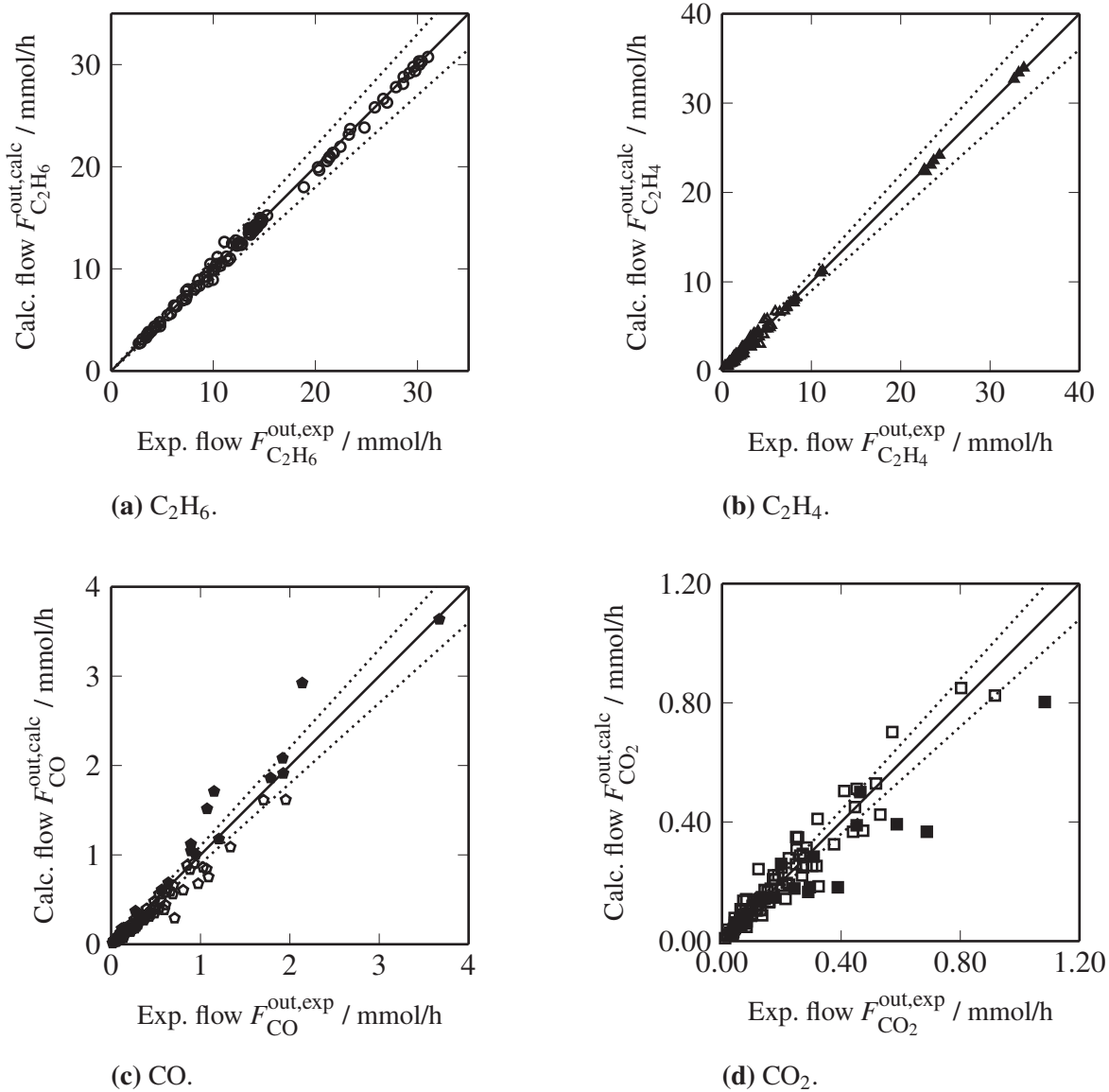
Figure 6.6: Linear parity plots comparing experimental and calculated molar flows in an unweighted form. C_2H_6 and C_2H_4 feed experiments are indicated by open and closed symbols, respectively. Dashed lines mark the $\pm 10\,\%$ region.
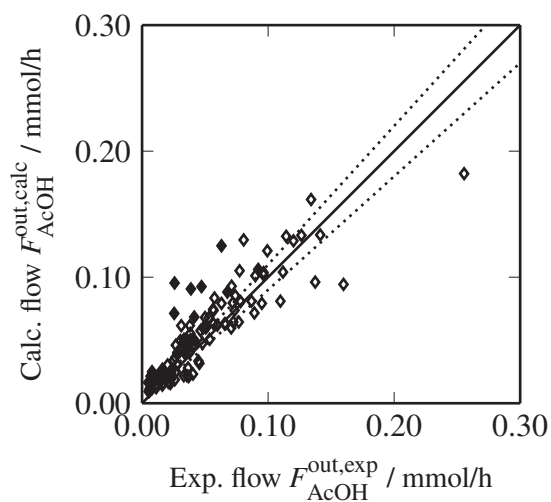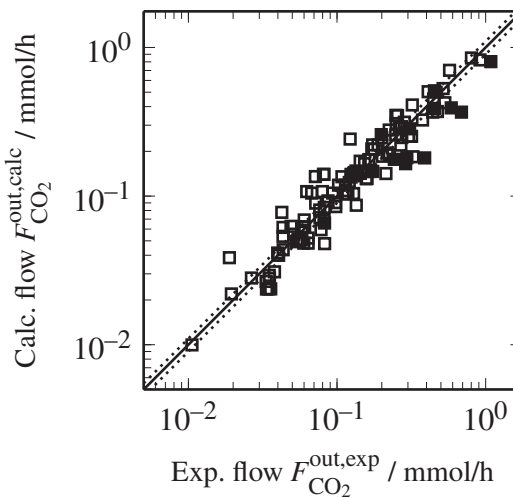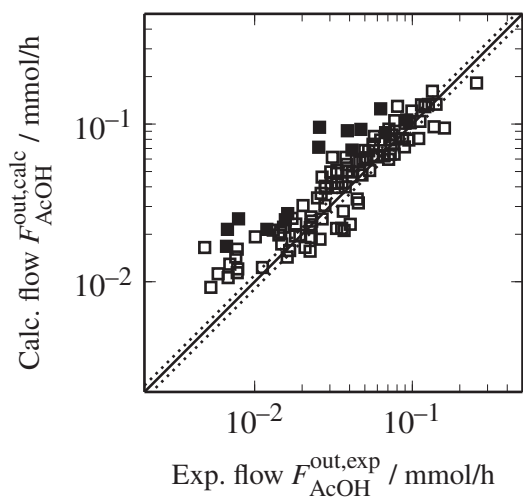
(e) AcOH.

Figure 6.6: *(continued).*
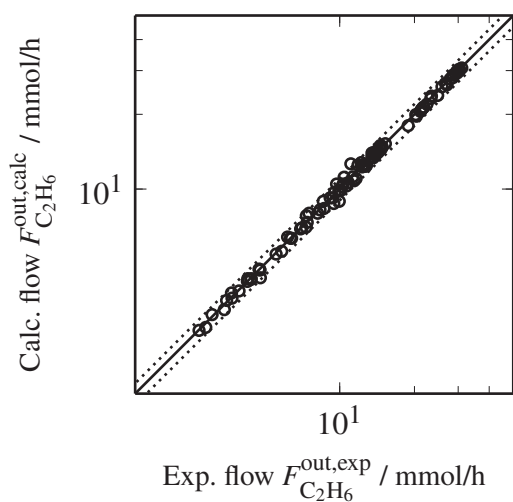
(a) C_2H_6.
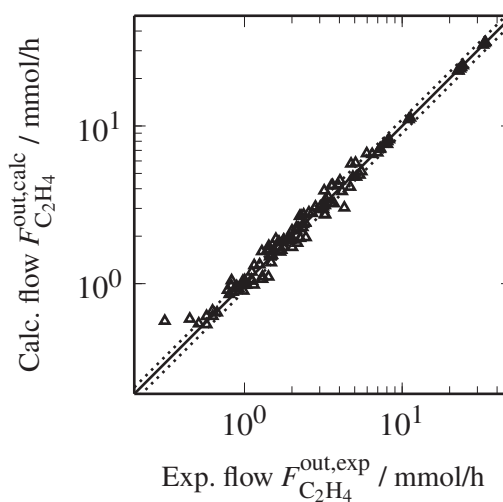
(b) C_2H_4.

Figure 6.7: Logarithmic parity plots comparing experimental and calculated molar flows in an unweighted form. C_2H_6 and C_2H_4 feed experiments are indicated by open and closed symbols, respectively. Dashed lines mark the $\pm 10\,\%$ region.

(c) CO.
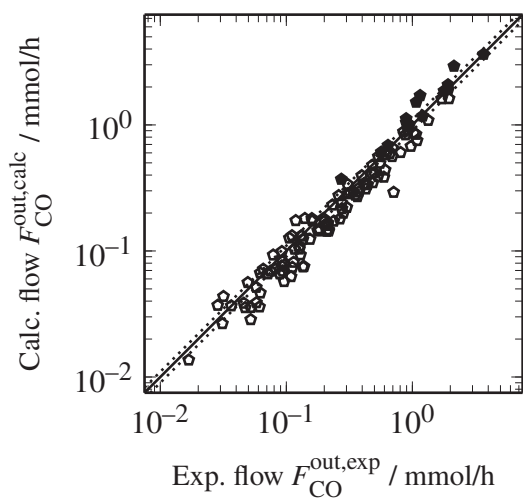
(d) CO_2.

(e) AcOH.

Figure 6.7: *(continued)*.

the reactant partial pressures, significantly influences the behavior of the reaction network. Finally, for the $C_2H_{4/6}/O_2$-feed ratio in Figure 6.13 the residuals of all five responses are well distributed. It is striking that at oxygen-rich conditions ($C_2H_{4/6}/O_2 = \frac{1}{3}$) the residuals for CO_x are more spread compared to oxygen-lean experiments. This can be attributed to the variety of possible reaction pathways on oxidic surface mentioned above. For conditions with excess oxygen, a multitude of side reactions is possible, making model predictions less reliable.

6.5.3 Sensitivity Analysis

The impact of the relevant reaction rate constants k_j and adsorption equilibria K_j on the net production rates of the desired product C_2H_4 is evaluated using a local sensitivity analysis [259], with details given in Appendix 6.B. Figure 6.8 shows the dependency of respective sensitivity values $S\left(\dot{R}_{C_2H_4}\right)$ on the reaction temperature T.

For an equimolar O_2-C_2H_6 atmosphere without any C_2H_4 product (closed symbols, solid lines), the initial $C-H$ cleavage (k_1) has the highest sensitivity value over the full temperature range, which is equivalent to the strongest influence on the C_2H_4 production rate $\dot{R}_{C_2H_4}$. In addition, regeneration of M_O by oxidation of lattice hydroxyl groups M_{OH} significantly affects C_2H_4 formation. In contrast, abstraction of the second hydrogen (k_2) can be regarded as a subordinate process. The parallel formation of the surface acetate species AcO^* (k_3) inhibits the formation of C_2H_4, which is expressed via negative S-values. Without any C_2H_4 in the reaction mixture, subsequent oxidation reactions (k_4 and k_5) do not occur, which yields zero sensitivities. Overall, temperature influences on the local sensitivity values of reaction constants k_j are marginal.

High coverages of C_2H_6 accelerate C_2H_4 formation, while the formation of electrophilic oxygen has only a minimal effect (cf. Figure 6.8b). Increasing temperature enhances the sensitivity of $K_{C_2H_6}$.

If C_2H_4 is present in the reaction mixture (open symbols, dotted lines), consumption of C_2H_4 (k_4 and k_5) does inhibit C_2H_4 net rate of production, whereas oxidation to CO (k_4) clearly dominates. As a consequence, the sensitivity of the initial $C-H$ cleavage rises to compensate for C_2H_4 consumption reactions. The presence of C_2H_4 has no significant effect on the second hydrogen abstraction k_2, the formation of AcO^* (k_3) and the oxidation of lattice hydroxyl groups (k_7). Naturally, C_2H_4 adsorption inhibits its formation, which is expressed by sensitivity values of $S\left(\dot{R}_{C_2H_4}, K_{C_2H_4}\right) \approx -0.8$.

A more detailed investigation of the reaction mixture on the sensitivity values is shown by a variable oxygen content y_{O_2} in Figure 6.9. Without any C_2H_4 in the reaction mixture (closed symbols, solid lines), the oxygen content has strong impact on the C_2H_4 formation. In oxygen-lean conditions ($y_{O_2} < 0.3$), the regeneration of lattice oxygen M_O (k_7) becomes the rate determining reaction. This is also reflected by the high sensitivity of O_2 adsorption compared to
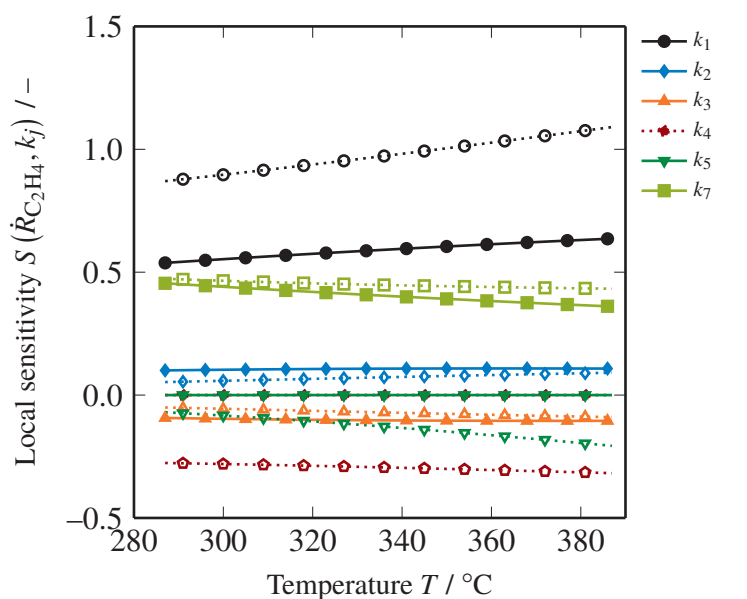
(a) Rate constants k_j.
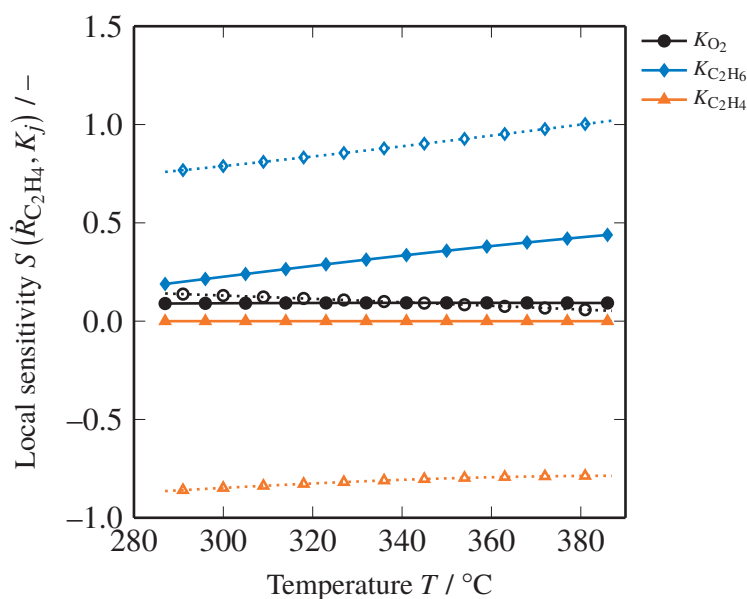
(b) Adsorption equilibrium constants K_j.

Figure 6.8: Local sensitivity of C_2H_4 net rate of production $\dot{R}_{C_2H_4}$ for varied reaction temperature T. Conditions: $p = 1\,\text{bar}$, O_2:C_2H_6:C_2H_4 = 1:1:0 (closed symbols, solid lines) and O_2:C_2H_6:C_2H_4 = 1:1:1 (open symbols, dotted lines).

C_2H_6, as displayed in Figure 6.9b. On the contrary, oxygen-rich conditions lead to a pronounced dominance of k_1 and $K_{C_2H_6}$ on the C_2H_4 sensitivity.

(a) Rate constants k_j.

(b) Adsorption equilibrium constants K_j.
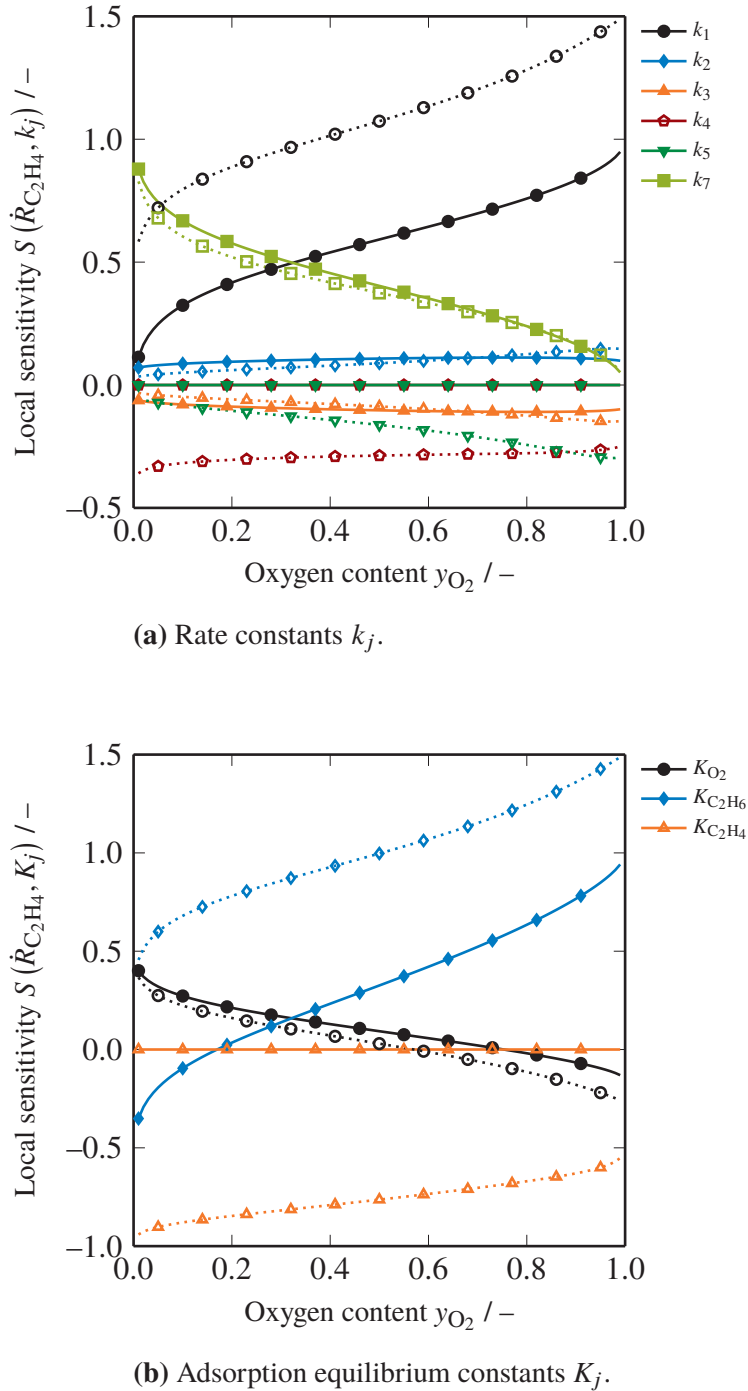
Figure 6.9: Local sensitivity of C_2H_4 net rate of production $\dot{R}_{C_2H_4}$ for varied oxygen content y_{O_2}. Conditions: $p = 1\,\text{bar}$, $T = T_{ref} = 610.125\,\text{K}$, $y_{C_2H_6} = 1 - y_{O_2}$ (closed symbols, solid lines) and $y_{C_2H_6} = y_{C_2H_4} = 0.5\left(1 - y_{O_2}\right)$ (open symbols, dotted lines).

For reaction mixtures with an equimolar content of C_2H_6 and C_2H_4 (open symbols, dotted lines), the sensitivity of k_1 is considerably enhanced, while for the formation of M_O (k_7) only a

minor effect is observable. It is noteworthy, that an increase in oxygen content provokes a higher inhibition through formation of AcO* (k_5), while it is vice-versa for the formation of CO.

In summary, the local sensitivity analyses of the proposed kinetic model verify a major influence of the initial C–H cleavage over a broad range of reaction conditions. However, for oxygen-lean atmospheres C_2H_4 formation can be controlled by the regeneration of lattice oxygen M_O.

6.6 Conclusion

Based on a thorough mechanistic evaluation, an intrinsic kinetic model for oxidative dehydrogenation of C_2H_6 over a highly active MoVTeNb mixed metal oxide M1 phase is developed. Seven surface reactions are proposed to describe the formation of C_2H_4 as well as the side products acetic acid, CO and CO_2 without using empirical parameters. The oxidation model is based on the hypothesis that lattice oxygen is responsible for C–H bond cleavage and electrophilic surface oxygen for O-insertion, as illustrated in Figure 6.10.
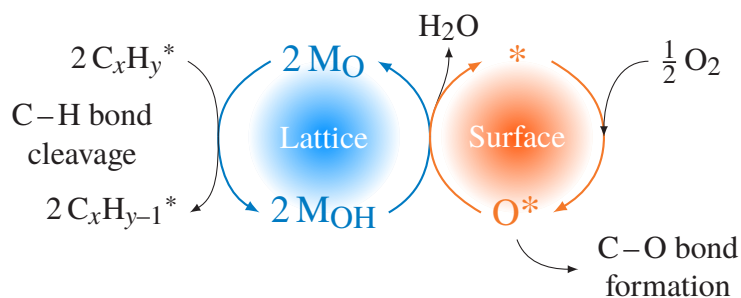
Figure 6.10: Proposed catalytic cycle for ODHE reaction on MoVTeNb mixed metal oxides.

Decarboxylation of surface acetate is hypothesized to be the single source for CO_2 formation. The resulting C_1 surface species is oxidized to CO, while additional CO is hypothesized to stem from decarbonylation of acetaldehyde speculated to be formed by oxidation of C_2H_4. Moreover, AcOH desorption is assisted by adsorbed H_2O.

An extensive statistic evaluation proved the global significance and the adequacy of the proposed kinetic model by respective F-tests. Relevance and accuracy of all 20 parameters are confirmed. It is found that the entropy terms for desorption and decarboxylation of surface acetate are correlated, which emphasizes the necessity for more detailed information on the interaction of C_2-oxygenates with the catalyst surface.

The initial C–H bond activation is established as rate determining step in C_2H_4 formation by local sensitivity analyses. However, regeneration of lattice oxygen was found to become rate determining for oxygen-lean reaction conditions.

The presented kinetic model allows an adequate description of the ODHE reaction over a broad range of reaction conditions based on a mechanistic reaction scheme. Further improvement can

be obtained by experiments and quantum chemical methods helping to decipher the complex surface morphology of the catalyst and its chemistry of elementary steps. However, for an improved description of AcOH formation the influence of H_2O on the catalytic properties has to be better resolved.

6.A Statistical Analysis

Significance and adequacy of each model are checked via two complementary F-tests, as recapitulated by Toch et al. [258]. The standard F-test compares the mean regression sum of squares to the mean residual sum of squares

$$F_s = \frac{\frac{SSQ_{reg}}{dof_{reg}}}{\frac{SSQ_{res}}{dof_{res}}} = \frac{\frac{\sum_{i=1}^{n_{resp}} \omega_i \sum_{j=1}^{n_{exp}} \left(Y_{i,j}^{out,calc}(\Phi)\right)^2}{n_{para}}}{\frac{\sum_{i=1}^{n_{resp}} \omega_i \sum_{j=1}^{n_{exp}} \left(Y_{i,j}^{out,exp} - Y_{i,j}^{out,calc}(\Phi)\right)^2}{n_{exp} \cdot n_{resp} - n_{para}}},\tag{6.18}$$

which should at a confidence level of 95 % by far exceed the corresponding critical value $F_{s,crit} = F^{-1}\left(0.95, dof_{reg}, dof_{res}\right)$ of the F-distribution to prove the significance of a model. Here, the residual degrees-of-freedom dof_{res} are dependent on the total number of experiments, the number of fitting responses n_{resp} and the total number of parameters n_{para} of the model.

The model adequacy is checked by splitting the residual sum of squares SSQ_{res} into the lack-of-fit (lof) and a pure experimental error (pe) [260]

$$SSQ_{res} = SSQ_{lof} + SSQ_{pe}.\tag{6.19}$$

The latter is calculated via n_{rep} sets of replicate experiments

$$SSQ_{pe} = \sum_{o=1}^{n_{rep}} \sum_{i=1}^{n_{resp}} \omega_i \sum_{j=1}^{n_{exp}(o)} \left(Y_{i,j}^{out,exp}(o) - \overline{Y}_j^{out,exp}(o)\right)^2\tag{6.20}$$

using deviation to the respective mean values $\overline{Y}_j^{out,exp}(o)$ for each response j and replicate set o. The respective degrees-of-freedom for this measure are given to

$$dof_{pe} = n_{resp} \sum_{o=1}^{n_{rep}} \left(n_{exp}(o) - 1\right)\tag{6.21}$$

The test yields

$$F_a = \frac{\frac{SSQ_{lof}}{dof_{lof}}}{\frac{SSQ_{pe}}{dof_{pe}}} = \frac{\frac{SSQ_{res} - SSQ_{pe}}{dof_{res} - dof_{pe}}}{\frac{SSQ_{pe}}{dof_{pe}}}\tag{6.22}$$

assessing the model to be adequate if the value F_a does not exceed the corresponding critical value $F_{a,crit} = F^{-1}\left(0.95, dof_{lof}, dof_{pe}\right)$.

Each parameter φ_m is tested on its significance via a t-test. The t value

$$t(\varphi_m) = \frac{|\varphi_m|}{\sqrt{\text{Var}(\varphi_m)}}.$$ (6.23)

is compared to the respective value of a two-sided Student's t-distribution t_{crit} with dof_{res} degrees of freedom, at 95 % confidence interval.

Finally, binary correlation coefficients allow simple estimates of the cross-correlation between two estimated parameters m and n using the respective covariances of these parameters:

$$\rho_{m,n} = \frac{\text{Cov}(\varphi_m, \varphi_n)}{\sqrt{\text{Var}(\varphi_m) \cdot \text{Var}(\varphi_n)}}$$ (6.24)

Strong interaction is evident for $|\rho_{m,n}|$-values above 0.95 [258].

The asymptotic covariance matrix $\text{Cov}(\varphi)$ of the parameters φ is used for the prediction of cross-correlation and confidence intervals. At the parameter optimum $\text{Cov}(\varphi)$ is approximated by

$$\text{Cov}(\varphi) = \frac{\left\| \omega_i \sum_{j=1}^{n_{\text{exp}}} \left(Y_{i,j}^{\text{out,exp}} - Y_{i,j}^{\text{out,calc}}(\Phi) \right)^2 \right\|}{dof_{\text{res}}} \mathcal{H}^{-1}.$$ (6.25)

For this purpose, the inverse of the Hessian $\mathcal{H}^{-1}$ at the parameter optimum is determined by QR decomposition of the respective Jacobian product $\mathcal{J}^{\mathsf{T}} \times \mathcal{J}$ [261]

$$\mathcal{H}^{-1} = (\mathcal{J}^{\mathsf{T}} \times \mathcal{J})^{-1} = R^{-1} \times Q^{\mathsf{T}}.$$ (6.26)

6.B Sensitivity Analysis

For evaluation of the proposed kinetic model a local sensitivity analysis is performed [262]. For this purpose, the 'degree of rate control' concept of Campbell [259], developed for the analysis of microkinetic models, is adapted. The sensitivity parameter

$$S\left(\dot{R}_i, k_j\right) = \frac{k_j}{\dot{R}_i} \frac{\partial \dot{R}_i}{\partial k_j}$$ (6.27)

defines the influence of the reaction rate constant k_j of reaction j on the net rate of production $\dot{R}_i$ of species i. Similarly, the impact of an adsorption constant K_j of an adsorptive j is defined to

$$S\left(\dot{R}_i, K_j\right) = \frac{k_j}{\dot{R}_i} \frac{\partial \dot{R}_i}{\partial K_j}$$ (6.28)

A value close to unity indicates the strong relevance of the parameter in the overall production of species i. Over all kinetically controlled steps k_j, the sum

$$\sum_{k_j}^{n_{\text{reactions}}} S\left(\dot{R}_i, k_j\right) = 1 \tag{6.29}$$

is conserved [263, 264], even for the mechanistic model presented here. However, as sorption process are assumed to be quasi-equilibrated, they have to be excluded from the conservation in Equation (6.29). Negative sensitivities indicate an inhibiting nature of the respective parameter on the respective production rate [263].

The partial derivatives in Equations (6.27) and (6.28) are calculated using fourth-order central finite differences at the parameter optimum.

6.S Supplementary Material

6.S.1 Model Derivation

6.S.1.1 Ethyl Surface Intermediate $C_2H_5{}^*$

The coverage of the non-desorbable $C_2H_5{}^*$ is obtained by a quasi-steady-state approximation (QSSA) of the respective surface coverage

$$\frac{\partial \Theta_{C_2H_5}}{\partial t} \approx 0 = \dot{r}_1 - \dot{r}_2 - \dot{r}_3 \tag{6.30}$$

Inserting the reaction rates and adsorption equilibria listed in Table 6.1 yields

$$0 = k_1[M_O]K_{C_2H_6}p'_{C_2H_6}\Theta_* - k_2[M_O]\Theta_{C_2H_5} - k_3\sqrt{K_{O_2}p'_{O_2}}\Theta_*\Theta_{C_2H_5} \tag{6.31}$$

Finally, the coverage of the ethyl surface intermediate $\Theta_{C_2H_5}$ can be expressed as a function of free surface sites Θ_*

$$\Theta_{C_2H_5} = \frac{k_1[M_O]K_{C_2H_6}p'_{C_2H_6}}{k_2[M_O] + k_3\sqrt{K_{O_2}p'_{O_2}}\Theta_*}\Theta_* \tag{6.32}$$

6.S.1.2 Lattice Balance

The fraction of lattice hydroxyl groups is obtained by the principle of QSSA

$$\frac{\partial [M_{OH}]}{\partial t} \approx 0 = \dot{r}_1 + \dot{r}_2 + \dot{r}_3 + 4\dot{r}_4 + \dot{r}_5 + 3\dot{r}_6 - 2\dot{r}_7. \tag{6.33}$$

Definitions from Table 6.1 and $\Theta_{C_2H_5}$ from Equation (6.32) result in

$$
\begin{aligned}
2k_7\sqrt{K_{O_2}p'_{O_2}}\,\Theta_*\,[M_{OH}]^2 = {}& k_1[M_O]K_{C_2H_6}p'_{C_2H_6}\Theta_* \\
& + \left(k_2[M_O] + 2k_3\sqrt{K_{O_2}p'_{O_2}}\,\Theta_*\right)\frac{k_1[M_O]K_{C_2H_6}p'_{C_2H_6}}{k_2[M_O] + k_3\sqrt{K_{O_2}p'_{O_2}}\,\Theta_*}\Theta_* \\
& + 4k_4[M_O]K_{C_2H_4}p'_{C_2H_4}\Theta_* + \\
& + k_5\sqrt{K_{O_2}p'_{O_2}}K_{C_2H_4}p'_{C_2H_4}\Theta_*{}^2 \\
& + 3k_6\sqrt{K_{O_2}p'_{O_2}}\sqrt{K_{AcOH}\frac{\sqrt{K_{O_2}p'_{O_2}}}{K_{H_2O}p'_{H_2O}}p'_{AcOH}}\Theta_*{}^2.
\end{aligned}
\tag{6.34}
$$

In order to derive an explicit expression for the lattice fractions $[M_O]$ and $[M_{OH}]$ it is necessary to decouple them from the number of free surface sites Θ_*. For this purpose several assumptions are made. Second order terms in Θ_* are assumed to be negligible. Together with a little rearrangement, Equation (6.34) simplifies to:

$$
\begin{aligned}
2k_7\sqrt{K_{O_2}p'_{O_2}}\,[M_{OH}]^2 \approx {}& k_1[M_O]K_{C_2H_6}p'_{C_2H_6} \\
& + k_1[M_O]K_{C_2H_6}p'_{C_2H_6}\left(1 + \frac{k_3\sqrt{K_{O_2}p'_{O_2}}}{k_2[M_O] + k_3\sqrt{K_{O_2}p'_{O_2}}\,\Theta_*}\right) \\
& + 4k_4[M_O]K_{C_2H_4}p'_{C_2H_4}
\end{aligned}
\tag{6.35}
$$

As the formation of $C_2H_4^*$ from $C_2H_5^*$ appears to be significantly faster compared to the formation AcO^*, the second term inside the brackets of Equations (6.35) vanishes

$$
[M_{OH}]^2 \approx \underbrace{\frac{2k_1 K_{C_2H_6}p'_{C_2H_6} + 4k_4 K_{C_2H_4}p'_{C_2H_4}}{2k_7\sqrt{K_{O_2}p'_{O_2}}}}_{a_M}[M_O].
\tag{6.36}
$$

The overall balance of lattice site is expressed as

$$
1 = [M_O] + [M_{OH}].
\tag{6.37}
$$

Hence, the fraction of lattice hydroxyl groups can be obtained from the solution of the quadratic relation obtained by combining Equations (6.36) and (6.37)

$$
[M_{OH}]\frac{-a_M + \sqrt{a_M{}^2 + 4a_M}}{2}
\tag{6.38}
$$

6.S.1.3 Free Surface Sites

In a last step, the coverage of free surface sites is determined. The overall balance of surface sites is given by

$$1 = \Theta_* + \Theta_O + \Theta_{C_2H_6} + \Theta_{C_2H_4} + \Theta_{H_2O} + \Theta_{AcO} + \Theta_{C_2H_5} \tag{6.39}$$

By inserting the quasi-equilibrated gas phase species, summarized in Table 6.1, and the correlation for $\Theta_{C_2H_5}$ (6.32), Equation (6.39) becomes

$$
\begin{aligned}
b_\Theta + c_\Theta \Theta_* &= (b_\Theta + c_\Theta \Theta_*) \, d_\Theta \Theta_* + a_\Theta \Theta_*, \\
a_\Theta &= k_1 \,[M_O]\, K_{C_2H_6} p'_{C_2H_6}, \\
b_\Theta &= k_2 \,[M_O], \\
c_\Theta &= k_3 \sqrt{K_{O_2} p'_{O_2}}. \\
d_\Theta &= 1 + \sqrt{K_{O_2} p'_{O_2}} + K_{C_2H_6} p'_{C_2H_6} + K_{C_2H_4} p'_{C_2H_4} \\
&\quad + K_{H_2O} p'_{H_2O} + \sqrt{K_{AcOH} \frac{\sqrt{K_{O_2} p'_{O_2}}}{K_{H_2O} p'_{H_2O}} p'_{AcOH}}.
\end{aligned}
\tag{6.40}
$$

Finally, this quadratic correlations allows to obtain the coverage of free surface sites to

$$
\begin{aligned}
\Theta_* &= \frac{-e_\Theta + \sqrt{e_\Theta^2 + 4 b_\Theta c_\Theta d_\Theta}}{2 c_\Theta d_\Theta}, \\
e_\Theta &= (a_\Theta + b_\Theta d_\Theta - c_\Theta).
\end{aligned}
\tag{6.41}
$$

6.S.1.4 Stoichiometry-Reaction-Matrix

Net rates of productions for all gaseous reactants can be obtained by Equation (6.9) using the stoichiometry-reaction-matrix in Table 6.5.

Table 6.5: Stoichiometry-reaction-matrix *SRM* for calculation of net rate of production of gas phase species.

	$\dot{r}_1$	$\dot{r}_2$	$\dot{r}_3$	$\dot{r}_4$	$\dot{r}_5$	$\dot{r}_6$	$\dot{r}_7$
$\dot{R}_{O_2}$	0	0	−0.75	−1	−0.75	−0.75	−0.5
$\dot{R}_{C_2H_6}$	−1	0	0	0	0	0	0
$\dot{R}_{C_2H_4}$	0	1	0	−1	−1	0	0
$\dot{R}_{H_2O}$	0	0	−0.5	0	−0.5	0.5	1
$\dot{R}_{CO}$	0	0	0	2	0	1	0
$\dot{R}_{CO_2}$	0	0	0	0	0	1	0
$\dot{R}_{AcOH}$	0	0	1	0	1	−1	0

6.S.2 Binary Correlation Coefficients

Binary correlation coefficients obtained from statistical analyses of the covariance matrix (cf. Equations (6.23) to (6.26)) are listed in Table 6.6.

Table 6.6: Binary correlation coefficients $\rho_{m,n}$ of fitted parameters $\varphi_{m/n}$ estimated with Equation (6.23).

$\rho_{m,n}$	$\varphi_{k_1,A}$	$\varphi_{k_2,A}$	$\varphi_{k_3,A}$	$\varphi_{k_4,A}$	$\varphi_{k_5,A}$	$\varphi_{k_6,A}$	$\varphi_{k_7,A}$	φ_{k_1,E_a}	φ_{k_2,E_a}	φ_{k_3,E_a}	φ_{k_4,E_a}	φ_{k_5,E_a}	φ_{k_6,E_a}	φ_{k_7,E_a}	$\varphi_{K_{O_2},\Delta H}$	$\varphi_{K_{H_2O},\Delta H}$	$\varphi_{K_{O_2},\Delta S}$	$\varphi_{K_{H_2O},\Delta S}$	$\varphi_{K_{AcOH},\Delta H}$	$\varphi_{K_{AcOH},\Delta S}$
$\varphi_{k_1,A}$	1	0.12	−0.34	−0.03	−0.04	0.13	0.21	−0.08	−0.19	−0.16	0.11	0.03	0.17	−0.17	−0.16	0.19	0.04	0.12	0.06	−0.14
$\varphi_{k_2,A}$		1	−0.24	0.17	0.21	−0.10	0.00	0.20	−0.29	0.19	−0.01	−0.15	0.01	−0.03	−0.28	−0.04	−0.48	−0.12	−0.04	0.08
$\varphi_{k_3,A}$			1	0.03	−0.24	0.10	0.21	−0.09	−0.35	0.45	−0.20	0.17	−0.01	0.16	0.04	0.06	−0.22	0.09	0.02	−0.08
$\varphi_{k_4,A}$				1	−0.11	−0.01	−0.02	−0.07	−0.01	−0.05	0.24	−0.01	−0.03	−0.10	−0.06	−0.04	−0.23	0.02	0.02	0.02
$\varphi_{k_5,A}$					1	−0.27	−0.07	0.05	0.08	−0.08	−0.12	−0.90	0.02	−0.04	−0.04	−0.23	−0.06	−0.36	0.10	0.09
$\varphi_{k_6,A}$						1	0.12	−0.01	−0.09	0.00	0.01	0.26	0.70	0.04	0.04	0.63	−0.01	0.97	0.78	−0.96
$\varphi_{k_7,A}$							1	0.00	−0.09	−0.15	0.29	0.04	0.16	0.58	−0.42	0.12	−0.33	0.13	0.07	−0.08
φ_{k_1,E_a}								1	−0.29	0.35	−0.06	−0.06	0.03	0.41	0.47	−0.01	0.25	−0.03	0.01	0.00
φ_{k_2,E_a}									1	−0.61	0.15	−0.03	−0.09	−0.32	−0.23	−0.11	−0.02	−0.06	−0.04	0.10
φ_{k_3,E_a}										1	−0.25	0.05	0.00	0.36	0.13	0.01	0.36	−0.02	−0.02	−0.01
φ_{k_4,E_a}											1	0.03	−0.05	0.15	−0.17	−0.04	−0.06	0.09	−0.01	0.09
φ_{k_5,E_a}												1	0.04	0.03	0.04	0.28	0.04	0.35	−0.15	−0.06
φ_{k_6,E_a}													1	0.07	−0.01	0.64	−0.03	0.65	0.66	−0.75
φ_{k_7,E_a}														1	0.20	0.04	0.22	0.05	0.02	−0.01
$\varphi_{K_{O_2},\Delta H}$															1	0.00	0.34	0.02	0.03	−0.04
$\varphi_{K_{H_2O},\Delta H}$																1	−0.01	0.53	0.13	−0.68
$\varphi_{K_{O_2},\Delta S}$																	1	0.00	−0.01	0.00
$\varphi_{K_{H_2O},\Delta S}$																		1	0.80	−0.91
$\varphi_{K_{AcOH},\Delta H}$																			1	−0.79
$\varphi_{K_{AcOH},\Delta S}$																				1

6.S.3 Residual Figures

Analyses of the residuals at the parameter optimum are displayed in Figures 6.11 to 6.13 for the bed temperature T_{bed}, the total pressure p and the $p_{C_2H_{4/6}}/p_{O_2}$ feed ratio, respectively.

(a) C_2H_6.

(b) C_2H_4.

(c) CO.

(d) CO_2.
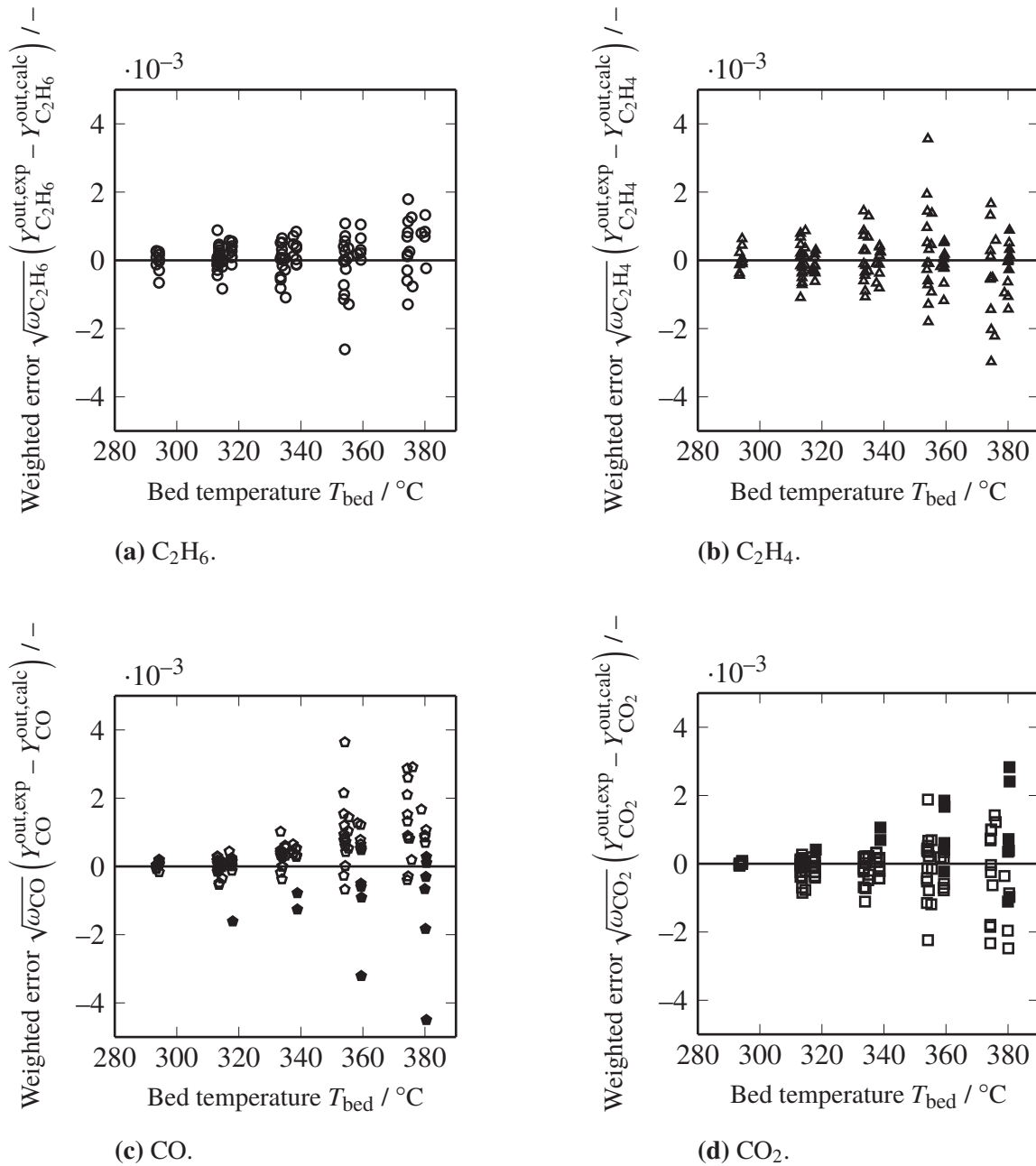
Figure 6.11: Dependency of weighted residuals $\sqrt{\omega_i}\left(Y_i^{out,exp} - Y_i^{out,calc}\right)$ on the reaction temperature T. C_2H_6 and C_2H_4 feed experiments are indicated by open and closed symbols, respectively.

133
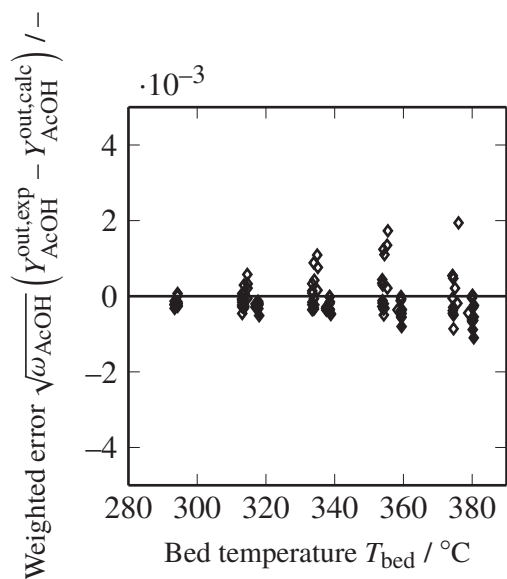
(e) AcOH.

Figure 6.11: *(continued).*
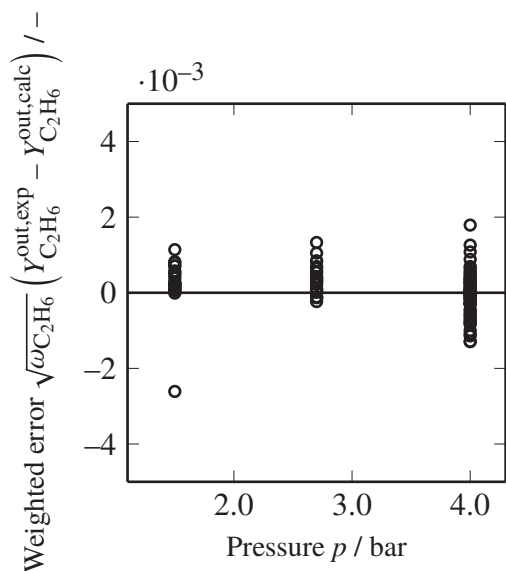
(a) C_2H_6.
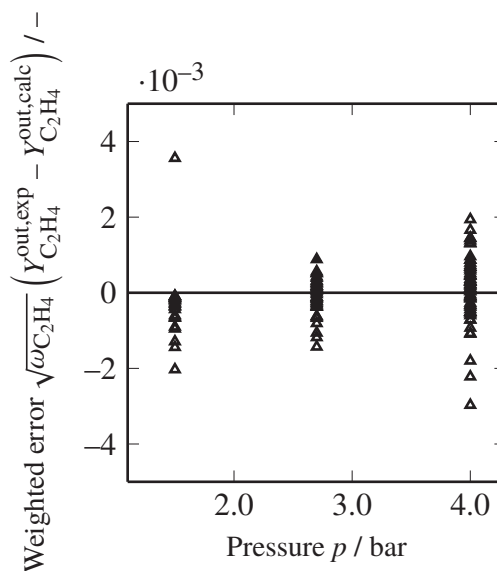
(b) C_2H_4.

Figure 6.12: Dependency of weighted residuals $\sqrt{\omega_i}\left(Y_i^{out,exp} - Y_i^{out,calc}\right)$ on the total pressure p. C_2H_6 and C_2H_4 feed experiments are indicated by open and closed symbols, respectively.

(c) CO.
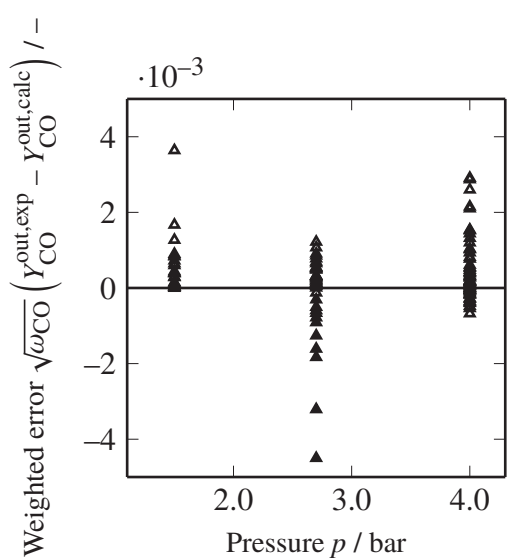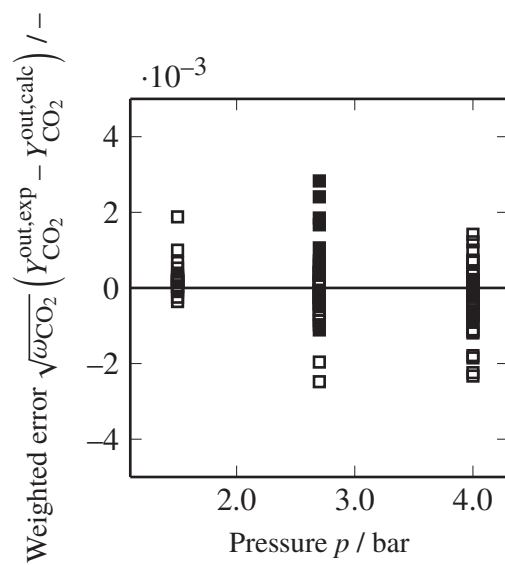
(d) CO$_2$.
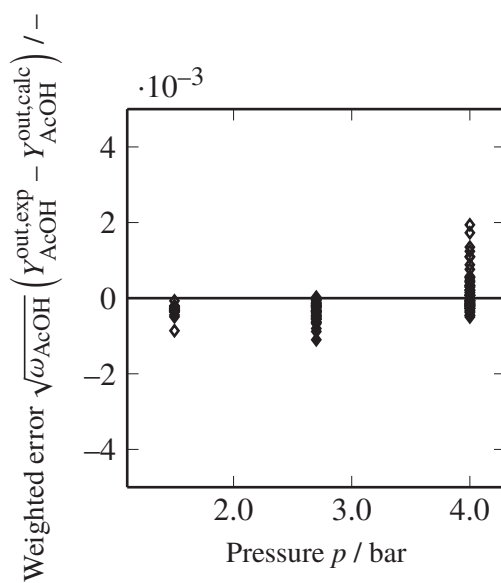
(e) AcOH.

Figure 6.12: *(continued)*.

(a) C_2H_6.

(b) C_2H_4.

(c) CO.

(d) CO_2.
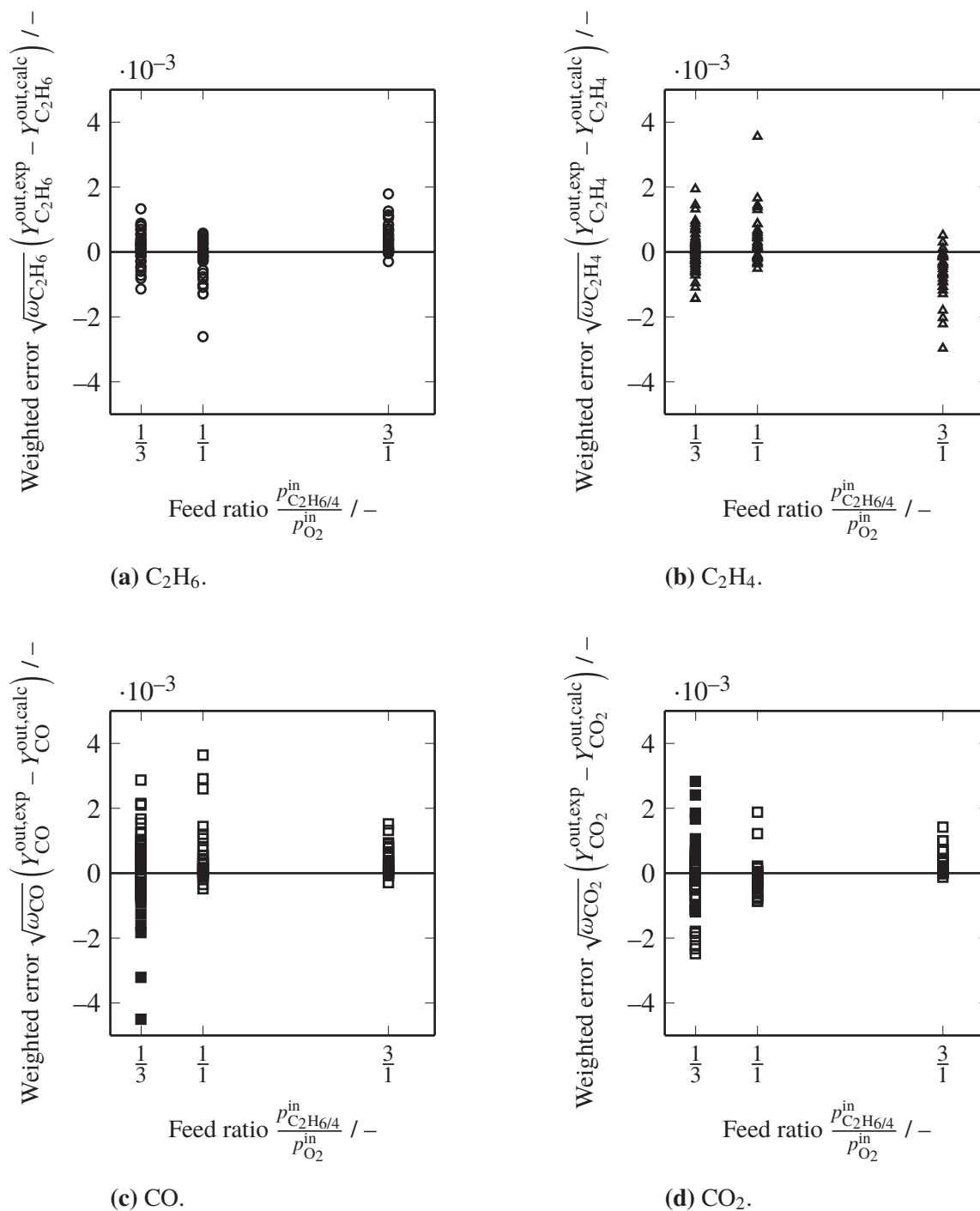
Figure 6.13: Dependency of weighted residuals $\sqrt{\omega_i}\left(Y_i^{out,exp} - Y_i^{out,calc}\right)$ on the $C_2H_{4/6}/O_2$ feed ratio $p_{C_2H_{6/4}}^{in}/p_{O_2}^{in}$. C_2H_6 and C_2H_4 feed experiments are indicated by open and closed symbols, respectively.
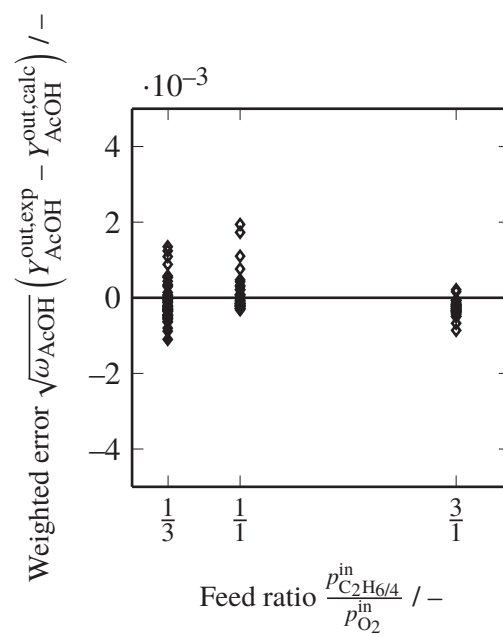
(e) AcOH.

Figure 6.13: *(continued)*.

7 Closing

7.1 Summary

In this thesis, oxidative dehydrogenation of ethane (ODHE) is examined from a multi-scale perspective, whereby the individual chapters are classified according to spacial and temporal scales of the overall process. An accurate intrinsic kinetic description is the basis of an elaborated integrated design strategy. This is superimposed by interconnected transport processes on the micro, meso and macro scale. Hereof, intraparticle transport and reactor-scale phenomena are analyzed. For this purpose, well-founded transport models are applied, coupled and developed to accurately describe this selective oxidation reaction and to advance modeling strategies for heterogeneously catalyzed systems.

In a first step, multicomponent transport processes inside one-dimensional porous catalysts are investigated. Three modeling approaches, each combining Maxwell-Stefan diffusion, Knudsen diffusion and viscous Darcy flow, are compared in terms of their impact on the overall catalyst effectiveness factor. The well-established dusty-gas model as well as the mean-transport pore model and the binary friction model yield similar profiles for mole fractions, pressure and temperature, when applied to three different heterogeneously catalyzed reactions. A global, Monte-Carlo-based sensitivity analysis enables a closer evaluation of the diffusion models by relating their differences to uncertainties in catalyst properties. If a minimal degree of uncertainty in these properties is allowed, dominating sensitivity for the pellet porosity is observable, whereas the choice of the diffusion model becomes negligible. Hence, an accurate determination of the transport parameters is found to be inevitable. In addition, the binary friction model is established as the most reliable model, due to inconsistencies in the treatment of the viscous flux terms by the other two approaches. These findings are able to generally recommend the binary friction model for simulation of multicomponent diffusion phenomena coupled with chemical reaction.

Based on this study, obtained for ideal one-dimensional spheres, a successive study on industrial scale catalysts investigated the impact of geometrical pellet features. For the first time, Maxwell-Stefan diffusion principles including pore diffusion and viscous transport, are successfully applied to multicomponent diffusion-reaction problems in complex geometries. An analytical solution of the implicit flux relations allows an efficient and robust treatment of species, mass and heat transport. Volume-to-surface ratio and curvature of the catalytic bodies are found to significantly affect the interplay of reaction and diffusion. Moreover, a one-dimensional approximation method is adopted, which reduces computational efforts by several orders of

magnitude and, hence, allows a robust and efficient coupling to reactor models. Furthermore, this approximation method outperforms classic approaches based on one-dimensional standard shapes as infinite cylinders or ideal spheres.

The third study in this thesis revisited the design and optimization of fixed-bed reactors for heterogeneously catalyzed reactions based on two-dimensional continuum models with special focus on the impact of fluid flow phenomena. Convective and dispersive transport effects are closely coupled to the radial porosity profile inside of the fixed bed. A comprehensive two-dimensional pseudo-homogeneous continuum model is solved via a segregated strategy. Here, a staggered finite difference scheme efficiently solves low-Mach compressible fluid flow, while the non-linear character of chemical reaction coupled to heat and species dispersion in axial and radial direction is handled with orthogonal collocation on finite elements. An incorporation of void inlet and outlet regions supersedes conventional artificial boundary conditions and allows a close investigation of the evolution of fluid flow in front of the bed as well as axial back-mixing of heat and species at the bed entry. The latter revealed distinct effects for packed beds of different porosity profiles applied to varying space velocity, heat of reaction, tube-to-particle ratio and reaction stoichiometry. Beds of ideal spheres exhibited deviating behavior due to distinct oscillations in the radial porosity profile compared to a plain plug-flow assumption, or beds of spherical and cylindrical catalysts. Moreover, by investigating variable reaction stoichiometries, the effect of changes in fluid density and superficial velocity highlight the importance of an adequate description of the interplay between fluid flow and chemical reaction. The proposed numerical scheme fully covers the requirements for a sophisticated design of fixed-bed reactors using continuum models.

Moreover, a kinetic model for oxidative dehydrogenation of ethane over the M1 phase of MoVTeNb mixed metal oxides is developed. Based on intrinsic kinetic measurements, it gives insights to the formation of ethene and the side products acetic acid, carbon monoxide and carbon dioxide, assuming two different oxygen sites. The formation of carbon-oxygen bonds is proposed to occur with electrophilic surface oxygen, whereas carbon-hydrogen bonds are cleaved at lattice oxygen sites. An acetate species is proposed as key surface intermediate responsible for carbon dioxide formation via decarboxylation and the production of acetic acid through a water-assisted desorption process. In contrast, ethene was found to decompose to carbon monoxide. Overall, seven surface reactions and five sorption equilibria yield a 20-parameter model of high global significance and accuracy. Moreover, sensitivity analyses establish the strong impact of the initial carbon-hydrogen cleavage of ethane on the ethene formation, whereas oxygen-lean conditions lead to a rate-determining character of the lattice oxygen regeneration. In summary, the catalytic steps on the multi-metal oxide $MoVTeNbO_x$ are well-described by the proposed model using a rigorous mechanistic analysis and accompanied mathematical treatment.

Finally, the new kinetic model can also be coupled to the above-presented strategies of intra-particle transport and fluid flow in fixed-bed reactors. Exemplary results are shown in Figure 7.1, demonstrating the arising transport limitations within a pilot-scale reactor configuration.
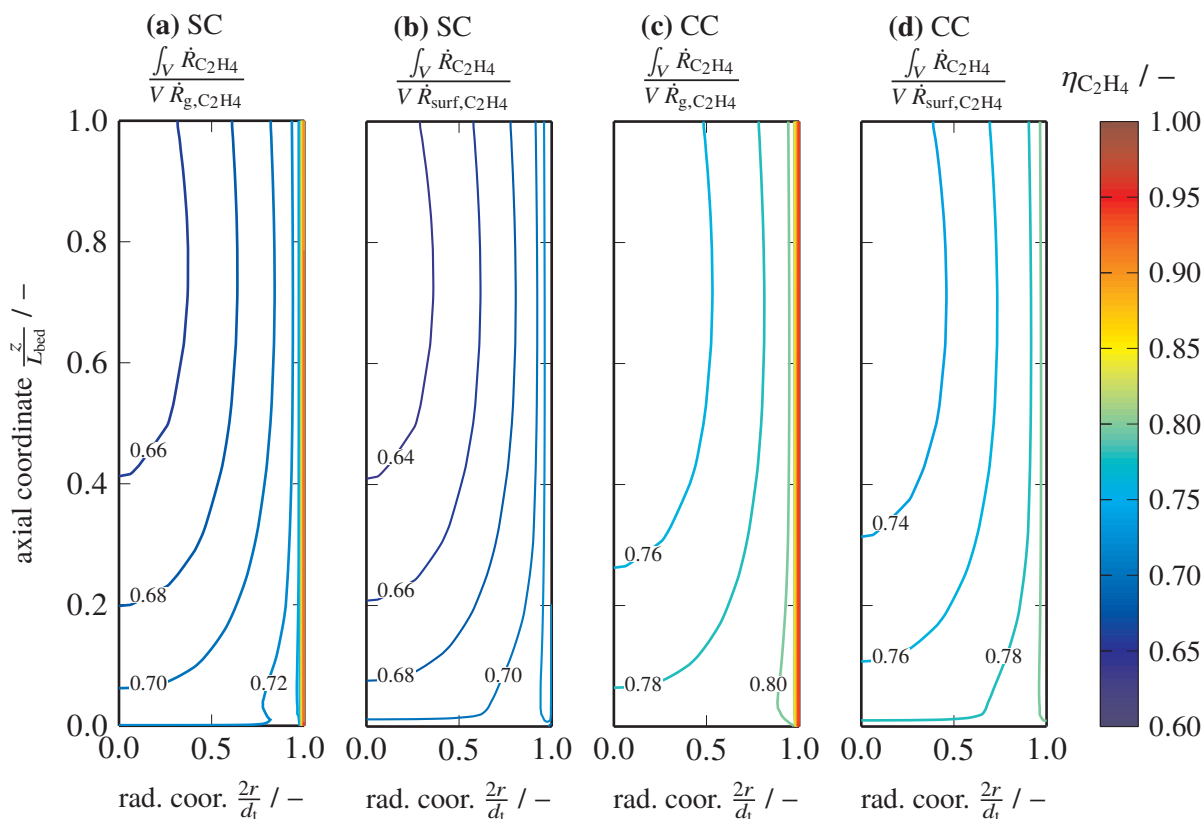
Figure 7.1: Ethene effectiveness factors for overall (a,c) and intraparticle (b,d) transport using beds of spherical SC (a,b) and cylindrical CC (c,d) catalysts (cf. Chapter 5). 1D intraparticle transport is simulated using the binary friction model (cf. Chapter 3) with adjusted shape factors (cf. Chapter 4): $\sigma_{SC} = 2$ and $\sigma_{CC} = 3.1849$ (aspect ratio = 1). Void inlet and outlet regions are neglected. Furthermore, following conditions are used: $d_t/d_p = 10$, particle Reynolds number $Re = 320$, inlet temperature $T_{in} = 300\,°C$, cooling temperature $T_{cool} = 290\,°C$, inlet air content $y_{in,air} = 0.85$, outlet pressure $p_{out} = 2\,bar$, catalyst density $\varrho_{cat} = 3500\,kg/m^3$ and total mass of catalyst $m_{cat} = 0.35\,kg_{cat}$. Other pellet-scale transport properties and reactor configurations are adapted from Chapter 3 and Chapter 5, respectively. Film theory is applied to couple fluid an solid phase, using the correlation of Gnielinski (cf. Appendix A.5.2).

By comparing the contour lines of the arising effectiveness factors in Figure 7.1b and Figure 7.1d, differences in intraparticle transport between spherical and cylindrical catalysts are observable. These originate from the corresponding shape factors, on the one hand, and differences in gas phase conditions due to respective transport properties within each bed configuration on the other hand. Moreover, the overall effectiveness factors in Figure 7.1a and 7.1c demonstrate the impact of flow channeling close to the reactor wall on the catalyst usage. In conclusion, these exemplary study summarizes the findings of this thesis in an integral reactor design and gives a perspective outline for future applications.

7.2 Outlook

As indicated in the summary, the basic findings of this thesis are versatile and can be applied to many fields of chemical reaction engineering. Explicit findings of the presented examples give direct insights to the respective research area, whereas the presented models and methods also have a universal character and can be adapted to other fields of research.

First of all, the intrinsic kinetic model for the oxidative dehydrogenation of ethane over MoVTeNbO$_x$ is capable to reliably predict the production of ethene as well as the formation of side products acetic acid, carbon monoxide and carbon dioxide and, hence, serves as a valuable tool for the scale-up of the overall production process. However, the formation and decomposition of surface acetate species and its interaction with adsorbed water need a deeper understanding. Nevertheless, the proposed two-site catalytic cycle, differentiating between electrophilic surface oxygen and lattice oxygen species, can be applied and refined as universal strategy to describe the kinetics of selective oxidation reactions over mixed metal oxides.

Despite applications to ODHE, the studies on intraparticle transport provide several universal insights. The global sensitivity analysis proved to be a robust tool for the evaluation of continuous and discrete variables in complex non-linear systems and can therefore be recommended for analysis of integrated models in the field of chemical reaction engineering. Moreover, the binary friction model outperformed two alternatives and is recommended as method of choice in modeling of diffusive transport inside porous, heterogeneously catalyzed systems.

A significant contribution to integrated reactor designs represents the one-dimensional approximation of intraparticle transport phenomena inside industrial catalyst shapes of complex geometries, by applying the binary friction model. This general procedure is applicable to any pellet geometry and for any conservation law, representing a flexible and efficient tool for the coupling of pellet and reactor scale phenomena via effectiveness factors.

The reevaluation of classical continuum models for fixed-bed reactors provides a universal procedure for modeling two-dimensional transport phenomena. The presented numerical scheme is capable to obtain effective transport parameters from either experimental investigations or discrete particle simulations.

Finally, the demonstrative case shown in Figure 7.1 touches a variety of future applications, covering an integrated fixed-bed reactor design for heterogeneously catalyzed chemical reactions.

On the one hand, these simulations indicate high computational requirements during solution of integrated reactor models for a multicomponent system like oxidative dehydrogenation of ethane. Therefore, despite a steadily increasing computing power, future research should address short-cut methods allowing for an efficient solution of such multi-dimensional designs. Valuable strategies for future research are for example multi-level optimizations [266], reducing the need of full-scale simulations to a minimal number, and artificial neural networks [267], which could be trained and potentially be applied in order to rapidly predict the behavior of individual catalyst pellets or certain reactor domains.

On the other hand, for a reliable prediction of industrial-scale configurations, it remains essential to verify each model, individually and in combined form, with experimental data. Therefore, future works should address intraparticle transport properties with regard to shape, composition and production process of the catalyst particle. Moreover, pilot-scale fixed-bed reactor experiments are necessary to obtain a realistic comparison of experimental and predicted conversions, selectivities and axial temperature profiles. Such comparisons allow to improve the presented models and provide a sound basis for future industrial application.

A Thermodynamic Principles, Physical Properties and Transport Parameter

In the following, a brief summary of relevant thermodynamic principles and physical properties is provided to give a full picture of the models used throughout this work. Additional background on the thermodynamics of mixtures is given by Walas [70]. Physical properties and transport parameter used in this study are mainly based on recommendations in the *VDI-Wärmeatlas* [268].

A.1 Caloric Parameters

Thermodynamic considerations and heat transport phenomena are fundamentally based on caloric properties. For the description of chemical reaction engineering processes, molar quantities Q, like molar heat capacity C_p, molar enthalpy H, molar entropy S, or Gibbs free energy G, are preferable. A reference state with a temperature $T^\circ = 298.15\,\text{K}$ and pressure $p^\circ = 10^5\,\text{Pa}$ is used. Here, the standard state of a quantity is referred to the standard pressure p° only, while remains a function of temperature T.

$$Q^\circ = Q^\circ(T) = Q(T, p^\circ) \tag{A.1}$$

If required, (mass) specific quantities q are calculated by

$$q = \frac{Q}{M} \tag{A.2}$$

using the respective molar weights M.

In the following, a brief description of thermodynamic principles and empirical correlations required for the description of fluid phases and its respective mixtures, is presented.

A.1.1 Pure Fluids

The properties of pure substance are functions of the two state variables T and p. Commonly these properties are split into an ideal (gas) Q° and a real contribution $\Delta_{\text{re}} Q$, as follows [70]

$$Q(T, p) = Q^{\text{ideal}}(T, p^\circ) + \Delta_{\text{re}} Q(T, p) = Q^\circ(T) + \Delta_{\text{re}} Q(T, p) . \tag{A.3}$$

A.1.2 Mixtures

Molar quantities of an n_{species}-component mixture are dependent on its composition, given by the respective mole fraction $y_1, \ldots, y_{n_{\text{species}}-1}$ and the closing condition. Furthermore, caloric properties of mixtures are expressed as a sum of ideal mixtures' (A.3) and excess' $\Delta_{\text{ex}}Q$ contributions [70].

$$Q\left(T, p, y_1, \ldots, y_{n_{\text{species}}-1}\right) = \sum_{i=1}^{n_{\text{species}}} y_i Q_i(T, p) + \Delta_{\text{ex}}Q. \tag{A.4}$$

A.1.3 Heat Capacity

The temperature dependency of the standard molar heat capacity at constant pressure C_p° is calculated using the Shomate-type polynomial [145]

$$C_p^\circ(T) = A_{C_p^\circ} + B_{C_p^\circ}T + C_{C_p^\circ}T^2 + D_{C_p^\circ}T^3 + E_{C_p^\circ}T^{-2}. \tag{A.5}$$

Parameters $A_{C_p^\circ}$ to $E_{C_p^\circ}$ are adapted from Kleiber and Joh [269].

A.1.4 Enthalpy

The ideal molar enthalpy H° is obtained from integration of Equation (A.5)

$$
\begin{aligned}
H^\circ(T) =& \Delta_f H^\circ(T^\circ) + \int_{T^\circ}^{T} C_p^\circ(T)\,\mathrm{d}T \\
=& \Delta_f H^\circ(T^\circ) + A_{C_p^\circ}(T - T^\circ) + \frac{B_{C_p^\circ}}{2}\left(T^2 - T^{\circ 2}\right) + \frac{C_{C_p^\circ}}{3}\left(T^3 - T^{\circ 3}\right) \\
&+ \frac{D_{C_p^\circ}}{4}\left(T^4 - T^{\circ 4}\right) - E_{C_p^\circ}\left(T^{-1} - T^{\circ -1}\right)
\end{aligned}
\tag{A.6}
$$

Respective standard enthalpies of formations $\Delta_f H^\circ(T^\circ)$ are listed in the *CRC Handbook of Chemistry and Physics* [227].

A.1.5 Entropy

Temperature dependence of the ideal molar entropy S° is per definition obtained by

$$
\begin{aligned}
S^\circ(T) =& S^\circ(T^\circ) + \int_{T^\circ}^{T} \frac{C_p^\circ(T)}{T}\,\mathrm{d}T \\
=& S^\circ(T^\circ) + A_{C_p^\circ}\ln\left(\frac{T}{T^\circ}\right) + B_{C_p^\circ}(T - T^\circ) + \frac{C_{C_p^\circ}}{2}\left(T^2 - T^{\circ 2}\right) \\
&+ \frac{D_{C_p^\circ}}{3}\left(T^3 - T^{\circ 3}\right) - \frac{E_{C_p^\circ}}{2}\left(T^{-2} - T^{\circ -2}\right).
\end{aligned}
\tag{A.7}
$$

Values for the molar entropy at standard temperature $S^\circ(T^\circ)$ are adopted from the *CRC Handbook of Chemistry and Physics* [227].

The empirical entropy values derived from Equation (A.7) are composed of translational, rotational and vibrational contributions. The former can be estimated using a quantum-chemical correlation introduced by Sackur [245, 270] and Tetrode [246], which for an ideal gas is defined as follows

$$S^\circ_{\text{trans}}(T) = \mathcal{R} \left[\ln \left(\frac{\mathcal{R}T}{p^\circ N_\text{A}} \left(\frac{2\pi M k_\text{B} T}{N_\text{A} h^2} \right)^{\frac{3}{2}} \right) + \frac{5}{2} \right]. \tag{A.8}$$

Here, the translational entropy S°_{trans} is solely dependent on the molar mass M of the species and the temperature T as well as on the universal gas constant $\mathcal{R}$, the Avogadro constant N_A, the Boltzmann constant k_B and Planck's constant h.

A.1.6 Chemical Equilibrium

The total Gibbs free energy G' any system is defined to [70]

$$G' = H' - TS' = U' + pV - TS' \tag{A.9}$$

consequently, changes of total Gibbs free energy $\mathrm{d}G'$ for and open system without external forces is given by

$$\mathrm{d}G' = \mathrm{d}U' + \mathrm{d}(pV) - \mathrm{d}(TS') \quad = V\mathrm{d}p - S'\mathrm{d}T + \sum_{i=1}^{n_{\text{species}}} \mu_i \mathrm{d}n_i, \tag{A.10}$$

which includes changes in the composition of a mixture by the respective mole number n_i.

At isobaric and isothermal conditions the change of the molar Gibbs free energy $\mathrm{d}G$ can be expressed through the changes of molar enthalpy H, temperature T and molar entropy S, or by the change of the chemical potential μ [70]

$$\mathrm{d}G = \mathrm{d}H - T\mathrm{d}S = \mathrm{d}\mu. \tag{A.11}$$

For a single component i, the latter is defined to

$$\mu_i = \mu_i^\circ + \mathcal{R}T \ln(a_i) = H_i^\circ - TS_i^\circ + \mathcal{R}T \ln \left(\frac{\varphi_i p y_i}{p_i^\circ} \right). \tag{A.12}$$

The standard chemical potential μ° can be expressed with the corresponding enthalpy H° (A.6) and entropy S° values (A.7). For gaseous systems, the activity a_i is calculated by the product of fugacity coefficient φ_i, the mole fraction y_i and the total pressure p related to the respective standard pressure p_i°.

At chemical equilibrium the total Gibbs free energy G' of a system becomes minimal. For a single reaction involving n_{species} species with stoichiometric coefficients v_i, this is equivalent to a zero gradient of G along the extent of the reaction ξ or a zero change of the total chemical potential

$$\left(\frac{\mathrm{d}G}{\mathrm{d}\xi}\right)_{p,T} = 0 = \mathrm{d}\mu = \sum_{i=1}^{n_{\text{species}}} v_i \mu_i. \tag{A.13}$$

From Equations (A.11), (A.12) and (A.13) the chemical equilibrium constant K_{eq} can be defined to

$$K_{\text{eq}} = \ln\left(-\frac{\Delta_r G^\circ}{\mathcal{R}T}\right) = \prod_{i=1}^{n_{\text{species}}} a_i^{v_i}$$

$$= \ln\left(-\frac{\Delta_r G^\circ}{\mathcal{R}T}\right) = \prod_{i=1}^{n_{\text{species}}} \left(\frac{\varphi_i p y_i}{p_i^\circ}\right)^{v_i} = \underbrace{\prod_{i=1}^{n_{\text{species}}} \varphi_i^{v_i}}_{K_\varphi} \cdot \overbrace{p^{\Delta v} \cdot \underbrace{\prod_{i=1}^{n_{\text{species}}} y_i^{v_i}}_{K_y}}^{K_{p_i}} \cdot \underbrace{\prod_{i=1}^{n_{\text{species}}} \left(p_i^\circ\right)^{-v_i}}_{K_{p^\circ}}. \tag{A.14}$$

A.1.7 Adsorption Equilibrium

Adsorption equilibria represent a special case of phase equilibria. For a species A adsorbing on a site *, quasi-equilibrated adsorption can be expressed as

$$A + {}^* \; \rightleftharpoons \; A^*. \tag{A.15}$$

By applying Equations (A.11) and (A.15) and assuming ideal gas behavior, the adsorption equilibrium of species A can be described by

$$K_A = \frac{k_{\text{adsorption,A}}}{k_{\text{desorption,A}}} = \exp\left(-\frac{\Delta_{\text{ads}}H^\circ}{\mathcal{R}T} + \frac{\Delta_{\text{ads}}S^\circ}{\mathcal{R}}\right) = \frac{\Theta_A}{\Theta_* \frac{p_A}{p_A^\circ}}. \tag{A.16}$$

Finally, the coverage Θ_A of species A* yields

$$\Theta_A = K_A \frac{p_A}{p_A^\circ} \Theta_*, \tag{A.17}$$

which is dependent on the partial pressure p_A, the respective standard pressure p_A° and the fraction of free surface sites Θ_*. Frequently, Equation (A.17) is expressed using a modified adsorption equilibrium constant

$$
\begin{aligned}
\Theta_A &= K_A' p_A \Theta_*, \\
K_A' &= \frac{K_A}{p_{\mathrm{ref}}}
\end{aligned}
\tag{A.18}
$$

related to a reference pressure p_{ref}.

A.2 Dynamic Viscosity

For gaseous fluids, the temperature dependency of the dynamic viscosity η is described by a polynomial correlation [145]

$$
\eta(T) = A_\eta + B_\eta T + C_\eta T^2 + D_\eta T^3 + E_\eta T^4.
\tag{A.19}
$$

Parameters A_η to E_η are summed up by Kleiber and Joh [271]. For moderate pressures the pressure-dependency can be neglected [145].

The dynamic viscosity of a gas mixture is approximated by the correlation of Wilke [147]

$$
\eta_{\mathrm{mix}} = \sum_{i=1}^{n_{\mathrm{species}}} \frac{y_i \eta_i}{\sum_{j=1}^{n_{\mathrm{species}}} y_j \zeta_{ij}}
\tag{A.20}
$$

using the respective pure-component viscosities η_i from Equation (A.19), the mole fractions y_i and mixing parameters ζ_{ij} defined to [147]

$$
\zeta_{ij} = \frac{\left[1 + \left(\frac{\eta_i}{\eta_j}\right)^{\frac{1}{2}} \left(\frac{M_j}{M_i}\right)^{\frac{1}{4}}\right]^2}{\sqrt{8\left(1 + \frac{M_i}{M_j}\right)}}.
\tag{A.21}
$$

A.3 Thermal Conductivity

A.3.1 Fluids

Similar to the dynamic viscosity in Section A.2, the temperature dependency of the thermal conductivity for fluids λ_{fl} is described by a polynomial correlation [145]

$$
\lambda_{\mathrm{fl}}(T) = A_{\lambda_{\mathrm{fl}}} + B_{\lambda_{\mathrm{fl}}} T + C_{\lambda_{\mathrm{fl}}} T^2 + D_{\lambda_{\mathrm{fl}}} T^3 + E_{\lambda_{\mathrm{fl}}} T^4.
\tag{A.22}
$$

Parameters $A_{\lambda_{\text{fl}}}$ to $E_{\lambda_{\text{fl}}}$ are summed up by Kleiber and Joh [271]. For moderate pressures, the pressure-dependency can be neglected [145].

The dynamic viscosity of a gas mixture is approximated, similar to Equation (A.20) [145, 146]

$$\lambda_{\text{fl,mix}} = \sum_{i=1}^{n_{\text{species}}} \frac{y_i \lambda_{\text{fl},i}}{\sum_{j=1}^{n_{\text{species}}} y_j \zeta_{ij}} \tag{A.23}$$

with viscosity-based mixing parameters ζ_{ij} from Equation (A.21).

A.3.2 Porous Particles

The effective thermal conductivity $\lambda_{\text{p}}^{\text{eff}}$ inside porous pellets is approximated by the method of Harriott [89]. For fused pellets, contact resistance between the solid matrix elements becomes negligible and the correlation is given to

$$\frac{\lambda_{\text{p}}^{\text{eff}}}{\lambda_{\text{s}}} = 4\chi_0^2 + \frac{\lambda_{\text{pore}}^{\text{eff}}}{\lambda_{\text{s}}}(1 - 2\chi_0)^2 + 2\left(1 + \frac{\chi_0}{0.5 - \chi_0} + \frac{\lambda_{\text{s}}}{\lambda_{\text{pore}}^{\text{eff}}}\frac{1}{2\chi_0}\right)^{-1}. \tag{A.24}$$

Here, the effective pellet thermal conductivity is dependent on thermal conductivity of the non-porous solid λ_{s} and the effective thermal conductivity inside the pores

$$\lambda_{\text{pore}}^{\text{eff}} = \frac{\lambda_{\text{fl,mix}}}{1 + \frac{2\bar{\Lambda}}{d_{\text{pore}}}}, \tag{A.25}$$

which relates the fluid thermal conductivity $\lambda_{\text{fl,mix}}$ to the pore diameter d_{pore} and the mean free path length

$$\bar{\Lambda} = \frac{\eta_{\text{fl}}}{p}\sqrt{\frac{\pi \mathcal{R} T}{2M}}. \tag{A.26}$$

The parameter χ_0 describes the geometrical arrangement of the solid matrix and pores. It can be approximated by root of

$$f(\chi) = 4\chi^3 - 3\chi^2 + \frac{1}{4}(1 - \varepsilon_{\text{p}}) \tag{A.27}$$

provided that the condition

$$\lambda_{\text{fl,mix}} \leq \lambda_{\text{p}}^{\text{eff}} \leq \lambda_{\text{s}} \tag{A.28}$$

holds.

A.4 Binary Diffusion Coefficient

The binary diffusion coefficients $Đ_{ij}$ between two species i and j are calculated by the semi-empirical correlation of Fuller et al. [73]

$$\left[\frac{Đ_{ij}}{\mathrm{m}^2/\mathrm{s}}\right] = \frac{10^{-7}\left[\frac{T}{\mathrm{K}}\right]^{1.75}\left(\left[\frac{M_i}{\mathrm{g/mol}}\right]^{-1} + \left[\frac{M_j}{\mathrm{g/mol}}\right]^{-1}\right)^{\frac{1}{2}}}{\left[\frac{p}{\mathrm{atm}}\right]\left(\left[\frac{\Delta v_i}{\mathrm{cm}^3}\right]^{\frac{1}{3}} + \left[\frac{\Delta v_j}{\mathrm{cm}^3}\right]^{\frac{1}{3}}\right)^2},$$ (A.29)

which goes back to an empirical extension of the kinetic theory of gases proposed by Gilliland [113]. Herein, temperature T, total pressure p, molar masses M and specific diffusive volumes Δv are used. Latter are defined by measured incremental values, listed in an updated publication of Fuller et al. [114], as a sum of all structural groups of the regarded species i or j. In contrast to Fickian diffusion, the symbol $Đ_{ij}$ denotes the Maxwell-Stefan representation. For ideal gases, these coefficients are symmetric and independent of composition [69].

Molecular diffusion coefficients for individual species in a mixture are approximated by the correlation of Fairbanks and Wilke [75] using binary diffusion coefficients from Equation (A.29)

$$D_{i,\mathrm{m}} = \frac{1 - y_i}{\displaystyle\sum_{\substack{j=1 \\ j \neq i}}^{n_{\mathrm{species}}} \frac{y_j}{Đ_{ij}}}.$$ (A.30)

In this context, it is emphasized that although Equation (A.30) is widely used in describing reactive media, it is only valid for the case of one species diffusing through a stagnant mixture, or highly diluted systems [14] (cf. Section 2.2.1).

A.5 Transport Properties in Packed Beds

A.5.1 Dispersion in Stagnant Packed Beds

Dispersion of heat inside packed beds filled with stagnant fluid can include thermal radiation effects, pressure dependencies, particle form and flattening. Zehner, Bauer and Schlünder [90, 91] proposed the following model for effective thermal conductivities $\lambda_{\mathrm{bed}}^{\mathrm{eff}}$ inside stagnant packed beds:

$$\frac{\lambda_{\mathrm{bed}}^{\mathrm{eff}}}{\lambda_{\mathrm{fl}}} = \left(1 - \sqrt{1 - \varepsilon(r)}\right)\varepsilon(r)\left[\frac{1}{\varepsilon(r) - 1 + \frac{1}{k_{\mathrm{G}}}} + k_{\mathrm{rad}}\right] \\ + \sqrt{1 - \varepsilon(r)}\left[\varphi k_{\mathrm{p}} + (1 - \varphi)k_{\mathrm{c}}\right].$$ (A.31)

Here, the effective thermal conductivity of the pellet, cf. Equation (A.24), is expressed via $k_p = \lambda_p^{\text{eff}}/\lambda_{\text{fl}}$. Flattening of pellets is accounted for by the flattening coefficient φ. The effective transport through the bed is described by the dimensionless thermal conductivity k_c, given to

$$
\begin{aligned}
k_c = \frac{2}{N} \Bigg\{ &\frac{B}{N^2} \frac{k_p + k_{\text{rad}} - 1}{k_G k_p} \ln \left(\frac{k_p + k_{\text{rad}}}{B \left[k_G + (1 - k_G) \left(k_p + k_{\text{rad}} \right) \right]} \right) \\
&+ \frac{B + 1}{2B} \left[\frac{k_{\text{rad}}}{k_G} - B \left(1 + \frac{1 - k_G}{k_G} \cdot k_{\text{rad}} \right) \right] - \frac{B - 1}{N k_G} \Bigg\}.
\end{aligned}
$$

(A.32)

The parameter N and the deformation factor B are calculated to

$$
N = \frac{1}{k_G} \left(1 + \frac{k_{\text{rad}} - B k_G}{k_p} \right) - B \left(\frac{1}{k_G} - 1 \right) \left(1 + \frac{k_{\text{rad}}}{k_p} \right),
$$

$$
B = C_f \left(\frac{1 - \varepsilon(r)}{\varepsilon(r)} \right)^{\frac{10}{9}}.
$$

(A.33)

Coefficient of form C_f is dependent on the particle shape. Furthermore, the heat exchange due to thermal radiation is included by

$$
k_{\text{rad}} = \frac{4\sigma_{\text{SB}}}{\frac{2}{\epsilon_p} - 1} T^3 \frac{d_p}{\lambda_{\text{fl}}}
$$

(A.34)

using the Stefan-Boltzmann constant σ_{SB} and the emissivity of the pellet surface ϵ_p. Pressure dependencies of the gaseous phase - so-called Smoluchowski effects - are considered via

$$
k_G = \frac{1}{1 + \frac{2\overline{\Lambda}_{\text{mod}}}{d_p}},
$$

(A.35)

which is equivalent to the representation of transport inside a porous pellet given in Equation (A.25). Here, a modified mean free path length $\overline{\Lambda}_{\text{mod}}$ is used [272]

$$
\overline{\Lambda}_{\text{mod}} = \frac{2 - \gamma}{\gamma} \sqrt{\frac{2\pi \mathcal{R} T}{M}} \frac{\lambda_{\text{fl}}}{p \left(2 \frac{C_{p,\text{fl}}^{\circ}}{M} - \frac{\mathcal{R}}{M} \right)}
$$

(A.36)

with the molar mass of the fluid M, temperature T, pressure p, and thermal conductivity λ_{fl}. The accommodation coefficient γ can be approximated via [273]

$$
\log \left(\frac{1}{\gamma} - 1 \right) = 0.6 - \frac{\frac{1000\,\text{K}}{T} + 1}{2.8}.
$$

(A.37)

The denominator 2.8 in Equation (A.37) is an approximate assuming air as fluid mixture [273].

Species dispersion inside packed beds is independent of contributions of the solid phase. Hence, the model reduces to

$$\frac{\mathcal{D}_{\text{bed},i}^{\text{eff}}}{D_{i,\text{m}}} = 1 - \sqrt{1 - \varepsilon(r)} \tag{A.38}$$

using an approximated diffusion coefficient $D_{i,\text{m}}$ according to Equation (A.21).

A.5.2 Fluid-Solid Interphase Transfer

Solid–fluid heat α and mass β transfer coefficients are calculated based on the film theory, using the correlations of Gnielinski [226, 265, 274]. Here, Nusselt Nu and Sherwood Sh numbers inside of packed beds are approximated by the respective single sphere values and a form factor f_a:

$$
\begin{aligned}
Nu &= \frac{\alpha d_{\text{char}}}{\lambda_{\text{fl}}} = f_\text{a}\, Nu_{\text{sphere}}, \\
Sh_i &= \frac{\beta_i d_{\text{char}}}{D_{i,\text{m}}} = f_\text{a}\, Sh_{i,\text{sphere}}.
\end{aligned}
\tag{A.39}
$$

Furthermore, a broad flow regime is captured via a combination of laminar and turbulent contributions

$$
\begin{aligned}
Nu_{\text{sphere}} &= 2 + \left[\left(0.664 \cdot Re_\varepsilon^{0.5} Pr^{\frac{1}{3}} \right)^2 + \left(\frac{0.037 \cdot Re_\varepsilon^{0.8} Pr}{1 + 2.443 \cdot Re_\varepsilon^{-0.1} \left(Pr^{\frac{2}{3}} - 1 \right)} \right)^2 \right]^{0.5}, \\
Sh_{i,\text{sphere}} &= 2 + \left[\left(0.664 \cdot Re_\varepsilon^{0.5} Sc_i^{\frac{1}{3}} \right)^2 + \left(\frac{0.037 \cdot Re_\varepsilon^{0.8} Sc_i}{1 + 2.443 \cdot Re_\varepsilon^{-0.1} \left(Sc_i^{\frac{2}{3}} - 1 \right)} \right)^2 \right]^{0.5}.
\end{aligned}
\tag{A.40}
$$

The bed Reynolds number Re_ε, the Prandtl number Pr and the Schmidt number Sc_i of the species i are defined as:

$$
\begin{aligned}
Re_\varepsilon &= \frac{\varrho_{\text{fl}}\, u\, d_{\text{char}}}{\eta_{\text{fl}} \varepsilon}, \\
Pr &= \frac{\nu_{\text{fl}}}{a_{\text{fl}}}, \\
Sc_i &= \frac{\nu_{\text{fl}}}{D_{i,\text{m}}}.
\end{aligned}
\tag{A.41}
$$

The characteristic diameter d_{char} is based on the outer particle surface A_p, via

$$d_{\text{char}} = \sqrt{\frac{A_\text{p}}{\pi}}. \tag{A.42}$$

Depending on the nature of the particles different form factors f_a have been determined. For a bed of spheres, f_a is dependent on the bed porosity ε, via

$$f_a = 1 + 1.50\,(1 - \varepsilon),\tag{A.43}$$

while for solid cylinders, with an aspect ratio from 0.24 to 1.20, a fixed value of

$$f_a = 1.60\tag{A.44}$$

is recommended [226, 274].

Fluid properties, like density ϱ_{fl}, thermal diffusivity a_{fl}, approximated diffusion coefficient $D_{i,m}$ (A.21), dynamic η_{fl} and kinematic viscosity ν_{fl}, are calculated assuming average conditions (T, p, y_i) between the bulk fluid and the solid surface.

B Kinetic Models

The studies of multicomponent mass transport and reaction in porous media presented in the Chapters 3 and 4 use mean-field kinetic models from literature, which are briefly introduced in the following.

Temperature dependence of rate constants k is generally expressed by activation energies E_a applied in Arrhenius' law

$$k = A \exp\left(-\frac{E_a}{\mathcal{R}T}\right). \tag{B.1}$$

For catalytic systems with an unknown number and/or nature of the active sites pre-exponential factors A are commonly based on the respective mass of catalyst.

B.1 Carbon Dioxide Methanation (RS1)

CO_2 methanation is a highly exothermic single reaction with four species:

$$CO_2 + 4\,H_2 \rightleftharpoons CH_4 + 2\,H_2O, \qquad\qquad \Delta_r H^\circ_{25\,^\circ C} = -165\,\frac{kJ}{mol}. \tag{B.2}$$

Langmuir-Hinshelwood-Hougen-Watson kinetics of Koschany et al. [129] are applied for a porous $NiAlO_x$ catalyst ($\varrho_s = 4700\,kg/m^3$).

The rate of reaction (B.2) is calculated via

$$\dot{r}_{RS1} = \frac{k \cdot p_{H_2}^{0.5} p_{CO_2}^{0.5} \left(1 - \frac{p_{CH_4} p_{H_2O}^2 p^{\circ 2}}{p_{CO_2} p_{H_2}^4 K_{eq,RS1}}\right)}{\left(1 + K'_{OH} \frac{p_{H_2O}}{p_{H_2}^{0.5}} + K'_{H_2} p_{H_2}^{0.5} + K'_{mix} p_{CO_2}^{0.5}\right)^2}. \tag{B.3}$$

The adsorption equilibrium constants K'_i are described by competitive adsorption using the principles given in Equations (A.15) to (A.18). The chemical equilibrium constant $K_{eq,RS1}$ is calculated as described in Section A.1.6. Model parameters are summarized in Table B.1.

Table B.1: Kinetic parameters for CO_2 methanation model of Koschany et al. [129]. The model is based on a reference pressure of 1 bar used in the rate Equation (B.3).

Parameter	Value	Unit
A	$6.81 \cdot 10^6$	$mol/(bar\,kg_{cat}\,s)$
E_a	77.50	kJ/mol
$\Delta_{ads}H_{OH}^\circ$	22.40	kJ/mol
$\Delta_{ads}S_{OH}^\circ$	34.60	J/(mol K)
$\Delta_{ads}H_{H_2}^\circ$	-6.20	kJ/mol
$\Delta_{ads}S_{H_2}^\circ$	18.00	J/(mol K)
$\Delta_{ads}H_{mix}^\circ$	-10.00	kJ/mol
$\Delta_{ads}S_{mix}^\circ$	-19.08	J/(mol K)
p_{ref}	1	bar

B.2 Methanol Synthesis (RS2)

As second model reaction system, methanol (MeOH) synthesis from CO_2 together with the reverse of the water-gas-shift reaction

$$CO_2 + 3\,H_2 \rightleftharpoons MeOH + H_2O, \qquad \Delta_r H_{25\,°C}^\circ = -49\,\frac{kJ}{mol}; \qquad (B.4)$$

$$CO_2 + H_2 \rightleftharpoons CO + H_2O, \qquad \Delta_r H_{25\,°C}^\circ = 41\,\frac{kJ}{mol}; \qquad (B.5)$$
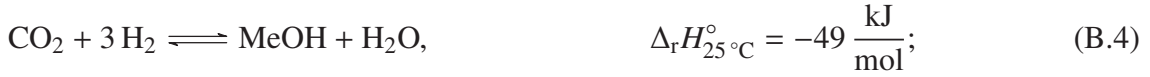
on a ternary $Cu/ZnO/Al_2O_3$ catalyst ($\varrho_s = 4500\,kg/m^3$) is used. Reaction rates are expressed by the power-law model of Peter et al. [130]

$$\dot{r}_{RS2\text{-}1} = k_1\, f_{H_2}^{m_{H2}}\, f_{CO_2}^{m_{CO2}}\, \left(C + f_{H_2O}\right)^{m_{H2O}} \cdot (1 - \beta_1), \qquad (B.6)$$

$$\dot{r}_{RS2\text{-}2} = k_2\, f_{H_2}^{n_{H2}} \cdot (1 - \beta_2). \qquad (B.7)$$

Thermodynamic equilibria is incorporated using respective approaches to equilibrium β_i

$$\beta_1 = \frac{f_{H_2O}\, f_{MeOH}\, p^{\circ 2}}{f_{H_2}^3\, f_{CO_2}\, K_{eq,RS2\text{-}1}}, \qquad (B.8)$$

$$\beta_2 = \frac{f_{H_2O}\, f_{CO}}{f_{H_2}\, f_{CO_2}\, K_{eq,RS2\text{-}2}}. \qquad (B.9)$$

Non-idealities of individual fluids (A.3) and the corresponding mixtures (A.4) are regarded by the Peng-Robinson equation-of-state [70, 142], based-on binary interaction parameters reported by Knapp et al. [143]. Equilibrium constants $K_{eq,i}$ are calculated as given in Section A.1.6.

Table B.2: Kinetic parameters for methanol synthesis model of Peter et al. [130]. The model is based on a standard pressure $p^\circ = 10^5$ Pa used in the rate Equations (B.6) and (B.7).

Parameter	Value	Unit
A_1	10.04	mol/(Pa$^{\sum_i m_i}$kg$_{cat}$s)
$E_{a,1}$	113.13	kJ/mol
m_{CO_2}	0.55	–
m_{H_2}	1.25	–
m_{H_2O}	−0.70	–
A_2	$7.36 \cdot 10^9$	mol/(Pa$^{n_{H_2}}$kg$_{cat}$s)
$E_{a,2}$	158.36	kJ/mol
n_{H_2}	0.57	–
C	316.75	Pa

B.3 Oxidative Dehydrogenation of Ethane (RS3)

Finally, the third model system is oxidative dehydrogenation of ethane on a MoVTeNbO$_x$ mixed metal oxide catalyst ($\varrho_s = 4370$ kg/m^3). The main reaction is given to

$$C_2H_6 + \frac{1}{2} O_2 \longrightarrow C_2H_4 + H_2O, \qquad \Delta_r H^\circ_{25\,°C} = -105 \, \frac{kJ}{mol}. \qquad (B.10)$$

In addition, partial and total oxidation of the C$_2$ species take place

$$C_2H_6 + \frac{7}{2} O_2 \longrightarrow 2\,CO_2 + 3\,H_2O, \qquad \Delta_r H^\circ_{25\,°C} = -1428 \, \frac{kJ}{mol}; \qquad (B.11)$$

$$C_2H_6 + \frac{5}{2} O_2 \longrightarrow 2\,CO + 3\,H_2O, \qquad \Delta_r H^\circ_{25\,°C} = -862 \, \frac{kJ}{mol}; \qquad (B.12)$$

$$C_2H_4 + 3\,O_2 \longrightarrow 2\,CO_2 + 2\,H_2O, \qquad \Delta_r H^\circ_{25\,°C} = -1323 \, \frac{kJ}{mol}; \qquad (B.13)$$

$$C_2H_4 + 2\,O_2 \longrightarrow 2\,CO + 2\,H_2O, \qquad \Delta_r H^\circ_{25\,°C} = -757 \, \frac{kJ}{mol}. \qquad (B.14)$$

A Langmuir-Hinshelwood-Hougen-Watson kinetic model published by Che-Galicia et al. [131] is applied. The adsorption equilibrium constants K'_i are described by competitive adsorption using the principles given in Equations (A.15) to (A.18).

Derived kinetic expressions for reactions (B.10) to (B.14) are

$$\dot{r}_{RS3\text{-}1} = k_1 \left(K'_{O_2} p_{O_2} \right)^{\frac{1}{2}} K'_{C_2H_6} p_{C_2H_6} \Theta_*^2, \tag{B.15}$$

$$\dot{r}_{RS3\text{-}2} = k_2 \left(K'_{O_2} p_{O_2} \right)^{\frac{m_2}{2}} K'_{C_2H_6} p_{C_2H_6} \Theta_*^{m_2+1}, \tag{B.16}$$

$$\dot{r}_{RS3\text{-}3} = k_3 \left(K'_{O_2} p_{O_2} \right)^{\frac{m_3}{2}} K'_{C_2H_6} p_{C_2H_6} \Theta_*^{m_3+1}, \tag{B.17}$$

$$\dot{r}_{RS3\text{-}4} = k_4 \left(K'_{O_2} p_{O_2} \right)^{\frac{m_4}{2}} K'_{C_2H_4} p_{C_2H_4} \Theta_*^{m_4+1}, \tag{B.18}$$

$$\dot{r}_{RS3\text{-}5} = k_5 \left(K'_{O_2} p_{O_2} \right)^{\frac{m_5}{2}} K'_{C_2H_4} p_{C_2H_4} \Theta_*^{m_5+1}. \tag{B.19}$$

The number of unoccupied surface sites is expressed as

$$\Theta_* = \left(1 + \sqrt{K'_{O_2} p_{O_2}} + K'_{C_2H_6} p_{C_2H_6} + K'_{C_2H_4} p_{C_2H_4} \right.$$
$$\left. + K'_{H_2O} p_{H_2O} + K'_{CO} p_{CO} + K'_{CO_2} p_{CO_2} \right)^{-1}. \tag{B.20}$$

Respective model parameters are summarized in Table B.3.

Table B.3: Kinetic parameters for ODHE of Che-Galicia et al. [131]. The model is based on a reference pressure of 1 Pa used in the rate Equations (B.15) to (B.19).

Parameter	Value	Unit	Parameter	Value	Unit
A_1	$5.56 \cdot 10^5$	mol/(kg$_{cat}$ s)	$\Delta_{ads} H^\circ_{O_2}$	-42.5	kJ/mol
$E_{a,1}$	76.6	kJ/mol	$\Delta_{ads} S^\circ_{O_2}$	-46.6	J/(mol K)
A_2	$3.90 \cdot 10^3$	mol/(kg$_{cat}$ s)	$\Delta_{ads} H^\circ_{C_2H_6}$	-42.7	kJ/mol
$E_{a,2}$	149.0	kJ/mol	$\Delta_{ads} S^\circ_{C_2H_6}$	-57.1	J/(mol K)
m_2	0.142	–	$\Delta_{ads} S^\circ_{C_2H_4}$	-61.5	J/(mol K)
A_3	$1.86 \cdot 10^4$	mol/(kg$_{cat}$ s)	$\Delta_{ads} H^\circ_{C_2H_4}$	-90.1	kJ/mol
$E_{a,3}$	132.0	kJ/mol	$\Delta_{ads} S^\circ_{H_2O}$	-90.0	J/(mol K)
m_3	0.549	–	$\Delta_{ads} S^\circ_{H_2O}$	-51.7	J/(mol K)
A_4	$6.94 \cdot 10^4$	mol/(kg$_{cat}$ s)	$\Delta_{ads} H^\circ_{CO}$	-88.0	kJ/mol
$E_{a,4}$	120.0	kJ/mol	$\Delta_{ads} S^\circ_{CO}$	-83.4	J/(mol K)
m_4	0.130	–	$\Delta_{ads} H^\circ_{CO_2}$	-72.6	kJ/mol
A_5	$3.11 \cdot 10^5$	mol/(kg$_{cat}$ s)	$\Delta_{ads} S^\circ_{CO_2}$	-66.1	J/(mol K)
$E_{a,5}$	109.0	kJ/mol			
m_5	0.492	–	p_{ref}	1	Pa

C Orthogonal Collocation on Finite Elements

The non-linear character of chemical reaction engineering problems requires an accurate and robust numerical treatment of the (partial) derivatives. For this purpose, orthogonal collocation on finite elements (OCFE) is a classic strategy, which will be briefly introduced in the following.

Orthogonal collocation (OC) is a special form of the method of weighted residuals [275]. Here, the differential equation L of the form

$$L\left(s(x)\right) = 0 \tag{C.1}$$

is approximated by a polynomial $\widetilde{s}(x)$

$$\widetilde{s}(x) = a_0 + a_1 x + a_2 x^2 + \cdots + a_m x^m = \sum_{i=0}^{m} a_i x^i \tag{C.2}$$

of the order m. Substituting the approximation (C.2) into the differential equation L yields a residual

$$res\left(x\right) = L\left(\widetilde{s}(x)\right) \tag{C.3}$$

The weighted integral of the residual $res\left(x\right)$

$$\int \omega(x) \cdot res\left(x\right) dx \xrightarrow{\text{min}} 0 \tag{C.4}$$

is minimized by an adequate choice of the coefficients a_i and the weighting function $\omega(x)$. Equation (C.4) shows the general representation of the method of weighted residuals.

In the following, the principle of orthogonal collocation is introduced following the representation of Finlayson [275, 276]. The solution $s(x)$ of problem (C.1) can be expressed through a product sum of the coefficients a_i and the known test functions s_i

$$s(x_j) = \sum_{i=1}^{n_{OC}} a_i s_i(x_j) \tag{C.5}$$

at n_{OC} grid points x_j. These test functions s_i are expressed through series of orthogonal polynomials P_j of the form

$$
\begin{aligned}
P_0(x) &= c_0, \\
P_1(x) &= c_0 + c_1 x^1, \\
P_2(x) &= c_0 + c_1 x^1 + c_2 x^2, \\
&\vdots \\
P_m(x) &= \sum_{j=0}^{m} c_j x^j.
\end{aligned}
\tag{C.6}
$$

The coefficients c_j are defined through the orthogonality conditions

$$
\int_{x_a}^{x_b} \omega(x) P_{m-1}(x) P_m(x) \mathrm{d}x, \quad n = 1, \ldots, m - 1, \quad \omega(x) > 0, \quad P_0 = 1,
\tag{C.7}
$$

within the borders x_a and x_b. Hence, the polynomial $P_m(x)$ is orthogonal to each lower order polynomial from P_0 to P_{m-1}. Examples for these kind of functions are the Jacobi ($\omega(x) = 1 - x^2$) or Legendre polynomial ($\omega(x) = 1$) series [276]. The unknown coefficients a_i are determined by using the roots of P_m as grid points x_j for Equation (C.5).

Applying the above introduced principle on a domain from $x_a = 0$ to $x_b = 1$ yields

$$
s(x) = x + x(1 - x) \cdot \sum_{i=1}^{n_{OC}} a_i P_i - 1(x)
\tag{C.8}
$$

with $n_{OC} + 2$ unknown coefficients d_i. The parameters a_1 to $a_{n_{OC}}$ are given through Equation (C.7), while the remaining two depend on the boundary conditions at the domain borders. Hence, for the inner collocation points x_j, Equation (C.8) can be expressed through

$$
s(x_j) = \sum_{i=1}^{n_{OC}+2} d_i x_j^{i-1}.
\tag{C.9}
$$

Derivation of Equation (C.9) yields approximations for the derivative of the solution $s(x)$, e.g.

$$
\begin{aligned}
\frac{\mathrm{d}}{\mathrm{d}x} s(x_j) &= \sum_{i=1}^{n_{OC}+2} d_i \, (i - 1) \, x_j^{i-2}, \\
\frac{\mathrm{d}^2}{\mathrm{d}x^2} s(x_j) &= \sum_{i=1}^{n_{OC}+2} d_i \, (i - 1) \, (i - 2) \, x_j^{i-3} \\
&\vdots
\end{aligned}
\tag{C.10}
$$

In matrix notation Equation (C.10) is expressed as

$$s = [D_0]d, \qquad D_{0,ij} = x_j^{i-1};$$
$$\frac{\mathrm{d}}{\mathrm{d}x}s = [D_1]d, \qquad D_{1,ij} = (i-1)\,x_j^{i-2}; \qquad (C.11)$$
$$\frac{\mathrm{d}^2}{\mathrm{d}x^2}s = [D_2]d, \qquad D_{2,ij} = (i-1)(i-2)\,x_j^{i-3}.$$

Replacing the unknown placeholder vector d through the inverse of the matrix $[D_0]$ allows an explicit representation of the derivatives by the solution vector s

$$\frac{\mathrm{d}}{\mathrm{d}x}s = [D_1][D_0]^{-1}s = [A]s;$$
$$\frac{\mathrm{d}^2}{\mathrm{d}x^2}s = [D_2][D_0]^{-1}s = [B]s. \qquad (C.12)$$

Equation (C.12) is the general representation of orthogonal collocation as discretization technique.

If the overall domain along a coordinate x is divided into $k = 1,\ldots,n_{\mathrm{FE}}$ finite elements of the size Δx_k, the above presented strategy can be extended to so-called orthogonal collocation on finite elements method. Each individual element is coupled to its neighbor through C^1-continuity conditions, ensuring a continuous and differentiable discretization method. Between the k-th and $(k+1)$-th element this conditions can be expressed as [132]

$$s\left(x_{k,i=n_{\mathrm{OC}}+2}\right) = s\left(x_{k+1,i=1}\right), \qquad k = 1,\ldots,n_{\mathrm{FE}}-1;$$
$$\frac{1}{\Delta x_k}\sum_{i=1}^{n_{\mathrm{OC}}+2} A_{n_{\mathrm{OC}}+2,i}\, s\left(x_{k,i}\right) = \frac{1}{\Delta x_{k+1}}\sum_{i=1}^{n_{\mathrm{OC}}+2} A_{1,i}\, s\left(x_{k+1,i}\right), \quad k = 1,\ldots,n_{\mathrm{FE}}-1. \qquad (C.13)$$

Within each element any required derivative is incorporated using the principles given in Equation (C.12), scaled with the respective element length Δx_k. Finally, the external element boundaries at $x_a = x_{k=1,i=1}$ and $x_b = x_{k=n_{\mathrm{FE}},i=n_{\mathrm{OC}}+2}$ are used for the boundary conditions of the system. Using an orthogonal coordinate system, OCFE can be extended to multiple dimension in a straightforward manner [149].

D Bibliography

[1] H. Zimmermann, R. Walzl, "Ethylene" in *Ullmann's Encyclopedia of Industrial Chemistry*, (Ed.: B. Elvers), Wiley-VCH, Weinheim, DE, **2014**, DOI 10.1002/14356007.a10_045.pub3.

[2] A. M. Gaffney, O. M. Mason, "Ethylene Production via Oxidative Dehydrogenation of Ethane using M1 Catalyst", *Catal. Today* **2017**, *285*, 159–165, DOI 10.1016/j.cattod.2017.01.020.

[3] J. A. Moulijn, M. Makkee, A. E. van Diepen, *Chemical Process Technology*, 2nd Edition, Wiley & Sons, Chichester, UK, **2013**.

[4] I. Amghizar, L. A. Vandewalle, K. M. van Geem, G. B. Marin, "New Trends in Olefin Production", **2017**, *3*, 171–178, DOI 10.1016/j.eng.2017.02.006.

[5] C. Baroi, A. M. Gaffney, R. Fushimi, "Process Economics and Safety Considerations for the Oxidative Dehydrogenation of Ethane using the M1 Catalyst", *Catal. Today* **2017**, *298*, 138–144, DOI 10.1016/j.cattod.2017.05.041.

[6] R. B. Jackson, A. Vengosh, J. W. Carey, R. J. Davies, T. H. Darrah, F. O'Sullivan, G. Pétron, "The Environmental Costs and Benefits of Fracking", *Annu. Rev. Environ. Resour.* **2014**, *39*, 327–362, DOI 10.1146/annurev-environ-031113-144051.

[7] T. Ren, M. K. Patel, K. Blok, "Olefins from Conventional and Heavy Feedstocks: Energy Use in Steam Cracking and Alternative Processes", *Energy* **2006**, *31*, 425–451, DOI 10.1016/j.energy.2005.04.001.

[8] F. Cavani, N. Ballarini, A. Cericola, "Oxidative Dehydrogenation of Ethane and Propane: How Far from Commercial Implementation?", *Catal. Today* **2007**, *127*, 113–131, DOI 10.1016/j.cattod.2007.05.009.

[9] C. A. Gärtner, A. C. van Veen, J. A. Lercher, "Oxidative Dehydrogenation of Ethane: Common Principles and Mechanistic Aspects", *ChemCatChem* **2013**, *5*, 3196–3217, DOI 10.1002/cctc.201200966.

[10] R. Schlögl, "Heterogeneous Catalysis", *Angew. Chem., Int. Ed.* **2015**, *54*, 3465–3520, DOI 10.1002/anie.201410738.

[11] K. F. Kalz, R. Kraehnert, M. Dvoyashkin, R. Dittmeyer, R. Gläser, U. Krewer, K. Reuter, J.-D. Grunwaldt, "Future Challenges in Heterogeneous Catalysis: Understanding Catalysts under Dynamic Reaction Conditions", *ChemCatChem* **2017**, *9*, 17–29, DOI 10.1002/cctc.201600996.

[12] F. J. Keil, "Molecular Modelling for Reactor Design", *Annu. Rev. Chem. Biomol. Eng.* **2018**, *9*, 201–227, DOI 10.1146/annurev-chembioeng-060817-084141.

[13] M. Andersen, C. Panosetti, K. Reuter, "A Practical Guide to Surface Kinetic Monte Carlo Simulations", *Front. Chem.* **2019**, *7*, 1–24, DOI 10.3389/fchem.2019.00202.

[14] G. F. Froment, K. B. Bischoff, J. de Wilde, *Chemical Reactor Analysis and Design*, 3rd Edition, Wiley & Sons, Hoboken (NJ), US, **2011**.

[15] M. Nijemeisland, A. G. Dixon, "Comparison of CFD Simulations to Experiment for Convective Heat Transfer in a Gas–Solid Fixed Bed", *Chem. Eng. J.* **2001**, *82*, 231–246, DOI 10.1016/S1385-8947(00)00360-0.

[16] A. G. Dixon, "Fixed Bed Catalytic Reactor Modelling: the Radial Heat Transfer Problem", *Can. J. Chem. Eng.* **2012**, *90*, 507–527, DOI 10.1002/cjce.21630.

[17] F. Cavani, F. Trifirò, "The Oxidative Dehydrogenation of Ethane and Propane as an Alternative Way for the Production of Light Olefins", *Catal. Today* **1995**, *24*, 307–313, DOI 10.1016/0920-5861(95)00051-G.

[18] M. M. Bhasin, J. H. McCaina, B. V. Vora, T. Imai, P. R. Pujadó, "Dehydrogenation and Oxydehydrogenation of Paraffins to Olefins", *Appl. Catal., A* **2001**, 397–419, DOI 10.1016/S0926-860X(01)00816-X.

[19] C. Batiot, B. K. Hodnett, "The Role of Reactant and Product Bond Energies in Determining Limitations to Selective Catalytic Oxidations", *Appl. Catal., A* **1996**, *137*, 179–191, DOI 10.1016/0926-860X(95)00322-3.

[20] J. T. Grant, J. M. Venegas, W. P. McDermott, I. Hermans, "Aerobic Oxidations of Light Alkanes over Solid Metal Oxide Catalysts", *Chem. Rev.* **2018**, *118*, 2769–2815, DOI 10.1021/acs.chemrev.7b00236.

[21] E. Heracleous, A. A. Lemonidou, "Ni-Nb-O Mixed Oxides as Highly Active and Selective Catalysts for Ethene Production via Ethane Oxidative Dehydrogenation: Part I. Characterization and Catalytic Performance", *J. Catal.* **2006**, *237*, 162–174, DOI 10.1016/j.jcat.2005.11.002.

[22] B. Solsona, P. Concepción, J. M. López Nieto, A. Dejoz, J. A. Cecilia, S. Agouram, M. D. Soriano, V. Torres, J. Jiménez-Jiménez, E. Rodríguez-Castellón, "Nickel Oxide Supported on Porous Clay Heterostructures as Selective Catalysts for the Oxidative Dehydrogenation of Ethane", *Catal. Sci. Technol.* **2016**, *6*, 3419–3429, DOI 10.1039/C5CY01811K.

[23] B. Tope, Y. Zhu, J. A. Lercher, "Oxidative Dehydrogenation of Ethane over Dy_2O_3/MgO Supported LiCl Containing Eutectic Chloride Catalysts", *Catal. Today* **2007**, *123*, 113–121, DOI 10.1016/j.cattod.2007.02.020.

[24] C. A. Gärtner, A. C. van Veen, J. A. Lercher, "Oxidative Dehydrogenation of Ethane on Dynamically Rearranging Supported Chloride Catalysts", *J. Am. Chem. Soc.* **2014**, *136*, 12691–12701, DOI 10.1021/ja505411s.

[25] Y. Murakami, K. Otsuka, Y. Wada, A. Morikawa, "Partial Oxidation of Ethane over Boron Oxide Added Catalysts", *Chem. Lett.* **1989**, *18*, 535–538, DOI 10.1246/cl. 1989.535.

[26] J. T. Grant, C. A. Carrero, F. Goeltl, J. M. Venegas, P. Mueller, S. P. Burt, S. E. Specht, W. P. McDermott, A. Chieregato, I. Hermans, "Selective Oxidative Dehydrogenation of Propane to Propene using Boron Nitride Catalysts", *Science* **2016**, *354*, 1570–1573, DOI 10.1126/science.aaf7885.

[27] R. Huang, B. Zhang, J. Wang, K.-H. Wu, W. Shi, Y. Zhang, Y. Liu, A. Zheng, R. Schlögl, D. S. Su, "Direct Insight into Ethane Oxidative Dehydrogenation over Boron Nitrides", *ChemCatChem* **2017**, *9*, 3293–3297, DOI 10.1002/cctc.201700725.

[28] J. Le Bars, A. Auroux, M. Forissier, J. C. Védrine, "Active Sites of V_2O_5/γ-Al_2O_3 Catalysts in the Oxidative Dehydrogenation of Ethane", *J. Catal.* **1996**, *162*, 250–259, DOI 10.1006/jcat.1996.0282.

[29] J. M. López Nieto, J. Soler, P. Concepción, J. Herguido, M. Menéndez, J. Santamaría, "Oxidative Dehydrogenation of Alkanes over V-Based Catalysts: Influence of Redox Properties on Catalytic Performance", *J. Catal.* **1999**, *185*, 324–332, DOI 10.1006/ jcat.1999.2467.

[30] M. D. Argyle, K. Chen, A. T. Bell, E. Iglesia, "Effect of Catalyst Structure on Oxidative Dehydrogenation of Ethane and Propane on Alumina-Supported Vanadia", *J. Catal.* **2002**, *208*, 139–149, DOI 10.1006/jcat.2002.3570.

[31] E. Heracleous, A. A. Lemonidou, J. A. Lercher, "Mechanistic Features of the Ethane Oxidative Dehydrogenation by In Situ FTIR Spectroscopy over a MoO_3/Al_2O_3 Catalyst", *Appl. Catal., A* **2004**, *264*, 73–80, DOI 10.1016/j.apcata.2003.12.030.

[32] E. Heracleous, J. Vakros, A. A. Lemonidou, C. Kordulis, "Role of Preparation Parameters on the Structure–Selectivity Properties of MoO_3/Al_2O_3 Catalysts for the Oxidative Dehydrogenation of Ethane", *Catal. Today* **2004**, *91-92*, 289–292, DOI 10.1016/j. cattod.2004.03.046.

[33] P. Ciambelli, L. Lisi, R. Pirone, G. Ruoppolo, G. Russo, "Comparison of Behaviour of Rare Earth Containing Catalysts in the Oxidative Dehydrogenation of Ethane", *Catal. Today* **2000**, *61*, 317–323, DOI 10.1016/S0920-5861(00)00391-6.

[34]   E. Thorsteinson, T. P. Wilson, F. G. Young, P. H. Kasai, "The Oxidative Dehydrogenation of Ethane over Catalysts Containing Mixed Oxides of Molybdenum and Vanadium", *J. Catal.* **1978**, *52*, 116–132, DOI 10.1016/0021-9517(78)90128-8.

[35]   K. Ruth, R. Burch, R. Kieffer, "Mo-V-Nb Oxide Catalysts for the Partial Oxidation of Ethane: I. Preparation and Structural Characterisation", *J. Catal.* **1998**, *175*, 16–26, DOI 10.1006/jcat.1998.1975.

[36]   M. Roussel, M. Bouchard, K. Karim, S. Al-Sayari, E. Bordes-Richard, "MoVO-Based Catalysts for the Oxidation of Ethane to Ethylene and Acetic Acid", *Appl. Catal., A* **2006**, *308*, 62–74, DOI 10.1016/j.apcata.2006.04.017.

[37]   W. Ueda, K. Oshihara, "Selective Oxidation of Light Alkanes over Hydrothermally Synthesized Mo-V-M-O (M=Al, Ga, Bi, Sb, and Te) Oxide Catalysts", *Appl. Catal., A* **2000**, *200*, 135–143, DOI 10.1016/S0926-860X(00)00627-X.

[38]   P. Botella, E. García-González, A. Dejoz, J. M. López Nieto, M. I. Vázquez, J. M. González-Calbet, "Selective Oxidative Dehydrogenation of Ethane on MoVTeNbO Mixed Metal Oxide Catalysts", *J. Catal.* **2004**, *225*, 428–438, DOI 10.1016/j.jcat.2004.04.024.

[39]   S. Rebsdat, D. Mayer, "Ethylene Oxide" in *Ullmann's Encyclopedia of Industrial Chemistry*, (Ed.: B. Elvers), Wiley-VCH, Weinheim, DE, **2014**, DOI 10.1002/14356007.a10_117.

[40]   K. Lohbeck, H. Haferkorn, W. Fuhrmann, N. Fedtke, "Maleic and Fumaric Acids" in *Ullmann's Encyclopedia of Industrial Chemistry*, (Ed.: B. Elvers), Wiley-VCH, Weinheim, DE, **2014**, DOI 10.1002/14356007.a16_053.

[41]   P. M. Lorz, F. K. Towae, W. Enke, R. Jäckh, N. Bhargava, W. Hillesheim, "Phthalic Acid and Derivatives" in *Ullmann's Encyclopedia of Industrial Chemistry*, (Ed.: B. Elvers), Wiley-VCH, Weinheim, DE, **2014**, DOI 10.1002/14356007.a20_181.pub2.

[42]   M. L. Rodríguez, D. E. Ardissone, A. A. Lemonidou, E. Heracleous, E. López, M. N. Pedernera, D. O. Borio, "Simulation of a Membrane Reactor for the Catalytic Oxidehydrogenation of Ethane", *Ind. Eng. Chem. Res.* **2009**, *48*, 1090–1095, DOI 10.1021/ie800564v.

[43]   G. Eigenberger, W. Ruppel, "Catalytic Fixed-Bed Reactors" in *Ullmann's Encyclopedia of Industrial Chemistry*, (Ed.: B. Elvers), Wiley-VCH, Weinheim, DE, **2014**, DOI 10.1002/14356007.b04_199.pub2.

[44]   E. López, E. Heracleous, A. A. Lemonidou, D. O. Borio, "Study of a Multitubular Fixed-Bed Reactor for Ethylene Production via Ethane Oxidative Dehydrogenation", *Chem. Eng. J.* **2008**, *145*, 308–315, DOI 10.1016/j.cej.2008.08.029.

[45] M. Fattahi, M. Kazemeini, F. Khorasheh, A. Darvishi, A. M. Rashidi, "Fixed-Bed Multi-Tubular Reactors for Oxidative Dehydrogenation in Ethylene Process", *Chem. Eng. Technol.* **2013**, *36*, 1691–1700, DOI 10.1002/ceat.201300148.

[46] G. Che-Galicia, R. S. Ruiz-Martínez, F. López-Isunza, C. O. Castillo-Araiza, "Modeling of Oxidative Dehydrogenation of Ethane to Ethylene on a MoVTeNbO/TiO$_2$ Catalyst in an Industrial-Scale Packed Bed Catalytic Reactor", *Chem. Eng. J.* **2015**, *280*, 682–694, DOI 10.1016/j.cej.2015.05.128.

[47] G. Che-Galicia, R. S. Ruiz-Martínez, D. Rios-Morales, J. A. Ayala-Romero, C. O. Castillo-Araiza, "Kinetic and Reactor Performance of a Ni-Based Catalyst during the Production of Ethene", *Chem. Eng. Commun.* **2018**, *205*, 372–386, DOI 10.1080/00986445.2017.1396538.

[48] S. Thomas, C. Hamel, A. Seidel-Morgenstern, "Basic Problems of Chemical Reaction Engineering and Potential of Membrane Reactors" in *Membrane Reactors*, (Ed.: A. Seidel-Morgenstern), Wiley-VCH, Weinheim, DE, **2010**, pp. 1–27, DOI 10.1002/9783527629725.ch1.

[49] A. Fazlinezhad, A. Naeimi, E. Yasari, "Theoretical Investigation of Ethane Oxidative Dehydrogenation over MoVTeNbO Catalyst in Fixed-Bed Reactors with Intermediate Water Removal", *Chem. Eng. Res. Des.* **2019**, *146*, 427–435, DOI 10.1016/j.cherd.2019.04.028.

[50] F. Klose, C. Hamel, A. Seidel-Morgenstern, "Comparison of Different Membrane Reactors" in *Membrane Reactors*, (Ed.: A. Seidel-Morgenstern), Wiley-VCH, Weinheim, DE, **2010**, pp. 263–267, DOI 10.1002/9783527629725.ch9.

[51] E. Gobina, R. Hughes, "Ethane Dehydrogenation Using a High-Temperature Catalytic Membrane Reactor", *J. Membr. Sci.* **1994**, *90*, 11–19, DOI 10.1016/0376-7388(94)80030-8.

[52] J. Coronas, M. Menéndez, J. Santamaría, "Use of a Ceramic Membrane Reactor for the Oxidative Dehydrogenation of Ethane to Ethylene and Higher Hydrocarbons", *Ind. Eng. Chem. Res.* **1995**, *34*, 4229–4234, DOI 10.1021/ie00039a011.

[53] C. Hamel, Á. Tóta, F. Klose, E. Tsotsas, A. Seidel-Morgenstern, "Analysis of Single and Multi-Stage Membrane Reactors for the Oxidation of Short-Chain Alkanes: Simulation Study and Pilot Scale Experiments", *Chem. Eng. Res. Des.* **2008**, *86*, 753–764, DOI 10.1016/j.cherd.2008.03.025.

[54] M. L. Rodríguez, D. E. Ardissone, E. Heracleous, A. A. Lemonidou, E. López, M. N. Pedernera, D. O. Borio, "Oxidative Dehydrogenation of Ethane to Ethylene in a Membrane Reactor: a Theoretical Study", *Catal. Today* **2010**, *157*, 303–309, DOI 10.1016/j.cattod.2010.01.053.

[55] J. H. Teles, I. Hermans, G. Franz, R. A. Sheldon, "Oxidation" in *Ullmann's Encyclopedia of Industrial Chemistry*, (Ed.: B. Elvers), Wiley-VCH, Weinheim, DE, **2014**, DOI 10.1002/14356007.a18_261.pub2.

[56] J. Werther, "Fluidized-Bed Reactors" in *Ullmann's Encyclopedia of Industrial Chemistry*, (Ed.: B. Elvers), Wiley-VCH, Weinheim, DE, **2014**, DOI 10.1002/14356007.b04_239.pub2.

[57] S. A. Al-Ghamdi, M. M. Hossain, H. I. de Lasa, "Kinetic Modeling of Ethane Oxidative Dehydrogenation over VO_x/Al_2O_3 Catalyst in a Fluidized-Bed Riser Simulator", *Ind. Eng. Chem. Res.* **2013**, *52*, 5235–5244, DOI 10.1021/ie303305c.

[58] I. A. Bakare, S. A. Mohamed, S. A. Al-Ghamdi, S. A. Razzak, M. M. Hossain, H. I. de Lasa, "Fluidized Bed ODH of Ethane to Ethylene over VO_x-MoO_x/γ-Al_2O_3 Catalyst: Desorption Kinetics and Catalytic Activity", *Chem. Eng. J.* **2015**, *278*, 207–216, DOI 10.1016/j.cej.2014.09.114.

[59] J. Rischard, C. Antinori, L. Maier, O. Deutschmann, "Oxidative Dehydrogenation of *n*-Butane to Butadiene with Mo-V-MgO Catalysts in a Two-Zone Fluidized Bed Reactor", *Appl. Catal., A* **2016**, *511*, 23–30, DOI 10.1016/j.apcata.2015.11.026.

[60] S. N. Khadzhiev, N. Y. Usachev, I. M. Gerzeliev, E. P. Belanova, V. P. Kalinin, V. V. Kharlamov, A. V. Kazakov, S. A. Kanaev, T. S. Starostina, A. Y. Popov, "Oxidative Dehydrogenation of Ethane to Ethylene in a System with Circulating Microspherical Metal Oxide Oxygen Carrier: 1. Synthesis and Study of the Catalytic System", *Pet. Chem.* **2015**, *55*, 651–654, DOI 10.1134/S0965544115080125.

[61] I. M. Gerzeliev, A. Y. Popov, V. A. Ostroumova, "Oxidative Dehydrogenation of Ethane to Ethylene in a System with Circulating Microspherical Metal Oxide Oxygen Carrier: 2. Ethylene Production in a Pilot Unit with a Riser Reactor", *Pet. Chem.* **2016**, *56*, 724–729, DOI 10.1134/S0965544116080053.

[62] M. C. Huff, L. D. Schmidt, "Ethylene Formation by Oxidative Dehydrogenation of Ethane over Monoliths at Very Short Contact Times", *J. Phys. Chem.* **1993**, *97*, 11815–11822, DOI 10.1021/j100147a040.

[63] T. Liu, V. Gepert, G. Veser, "Process Intensification through Heat-Integrated Reactors for High-Temperature Millisecond Contact-Time Catalysis", *Chem. Eng. Res. Des.* **2005**, *83*, 611–618, DOI 10.1205/cherd.05026.

[64] P. Brussino, J. Bortolozzi, V. G. Milt, E. D. Banús, M. A. Ulla, "NiCe/γ-Al_2O_3 Coated onto Cordierite Monoliths Applied to Oxidative Dehydrogenation of Ethane (ODE)", *Catal. Today* **2016**, *273*, 259–265, DOI 10.1016/j.cattod.2016.02.055.

[65] S. A. R. K. Deshmukh, S. Heinrich, L. Mörl, M. van Sint Annaland, J. A. M. Kuipers, "Membrane Assisted Fluidized Bed Reactors: Potentials and Hurdles", *Chem. Eng. Sci.* **2007**, *62*, 416–436, DOI `10.1016/j.ces.2006.08.062`.

[66] S. R. de Groot, P. Mazur, *Non-Equilibrium Thermodynamics*, North-Holland Publishing Company, Amsterdam, NL, **1962**.

[67] L. Onsager, "Reciprocal Relations in Irreversible Processes: I", *Phys. Rev.* **1931**, *37*, 405–426, DOI `10.1103/PhysRev.37.405`.

[68] L. Onsager, "Reciprocal Relations in Irreversible Processes: II", *Phys. Rev.* **1931**, *38*, 2265–2279, DOI `10.1103/PhysRev.38.2265`.

[69] R. Taylor, R. Krishna, *Multicomponent Mass Transfer*, Wiley-VCH, New York (NY), US, **1993**.

[70] S. M. Walas, *Phase Equilibria in Chemical Engineering*, Butterworth Publishers, Stoneham (MA), US, **1985**.

[71] J. C. Maxwell, FRS FRSE, "On the Dynamical Theory of Gases", *Philos. Mag.* **1868**, *35*, 185–217, DOI `10.1080/14786446808639963`.

[72] J. Stefan, "Über das Gleichgewicht und die Bewegung, insbesondere die Diffusion von Gasen", *Sitzungsber. Akad. Wiss. Wien, Math.-Natur. Cl., Abt. 2* **1871**, *63*, 63–124.

[73] E. N. Fuller, P. D. Schettler, J. C. Giddings, "New Method for Prediction of Binary Gas-Phase Diffusion Coefficients", *Ind. Eng. Chem.* **1966**, *58*, 18–27, DOI `10.1021/ie50677a007`.

[74] A. Fick, "Über Diffusion", *Ann. Phys.* **1855**, *170*, 59–86, DOI `10.1002/andp.18551700105`.

[75] D. F. Fairbanks, C. R. Wilke, "Diffusion Coefficients in Multicomponent Gas Mixtures", *Ind. Eng. Chem.* **1950**, *42*, 471–475, DOI `10.1021/ie50483a022`.

[76] J. B. Duncan, H. L. Toor, "An Experimental Study of Three Component Gas Diffusion", *AIChE J.* **1962**, *8*, 38–41, DOI `10.1002/aic.690080112`.

[77] R. B. Bird, W. E. Stewart, E. N. Lightfoot, *Transport Phenomena*, rev. 2nd Edition, Wiley & Sons, New York (NY), US, **2007**.

[78] P. V. Danckwerts, "Continuous Flow Systems: Distribution of Residence Times", *Chem. Eng. Sci.* **1953**, *2*, 1–13, DOI `10.1016/0009-2509(53)80001-1`.

[79] G. Taylor, "Dispersion of Soluble Matter in Solvent Flowing Slowly through a Tube", *Proc. R. Soc. London, Ser. A* **1953**, *219*, 186–203, DOI `10.1098/rspa.1953.0139`.

[80] R. Aris, "On the Dispersion of a Solute in a Fluid Flowing through a Tube", *Proc. R. Soc. London, Ser. A* **1956**, *235*, 67–77, DOI `10.1098/rspa.1956.0065`.

[81] G. Taylor, "The Dispersion of Matter in Turbulent Flow through a Pipe", *Proc. R. Soc. London, Ser. A* **1954**, *223*, 446–468, DOI `10.1098/rspa.1954.0130`.

[82] K. B. Bischoff, O. Levenspiel, "Fluid Dispersion-Generalization and Comparison of Mathematical Models: I Generalization of Models", *Chem. Eng. Sci.* **1962**, *17*, 245–255, DOI `10.1016/0009-2509(62)85003-9`.

[83] K. B. Bischoff, O. Levenspiel, "Fluid Dispersion-Generalization and Comparison of Mathematical Models: II Comparison of Models", *Chem. Eng. Sci.* **1962**, *17*, 257–264, DOI `10.1016/0009-2509(62)85004-0`.

[84] O. Levenspiel, *Chemical Reaction Engineering*, 3rd Edition, Wiley & Sons, Hoboken (NJ), US, **1999**.

[85] W. E. Ranz, "Friction and Transfer Coefficients for Single Particles and Packed Beds", *Chem. Eng. Prog.* **1952**, *48*, 247–253.

[86] N. O. Lemcoff, S. I. Pereira Duarte, O. M. Martínez, "Heat Transfer in Packed Beds", *Rev. Chem. Eng.* **1990**, *6*, 22–292.

[87] S. Das, N. G. Deen, J. Kuipers, "A DNS Study of Flow and Heat Transfer through Slender Fixed-Bed Reactors Randomly Packed with Spherical Particles", *Chem. Eng. Sci.* **2017**, *160*, 1–19, DOI `10.1016/j.ces.2016.11.008`.

[88] J. B. J. Fourier, *Théorie Analytique de la Chaleur*, Reprint from 1822, Jacques Gabay, Paris, FR, **1989**.

[89] P. Harriott, "Thermal Conductivity of Catalyst Pellets and Other Porous Particles: Part I: Review of Models and Published Results", *Chem. Eng. J.* **1975**, *10*, 65–71, DOI `10.1016/0300-9467(75)88018-X`.

[90] P. Zehner, E.-U. Schlünder, "Einfluß der Wärmestrahlung und des Druckes auf den Wärmetransport in nicht durchströmten Schüttungen", *Chem. Ing. Tech.* **1972**, *44*, 1303–1308, DOI `10.1002/cite.330442305`.

[91] R. Bauer, E.-U. Schlünder, "Effective Radial Thermal Conductivity of Packings in Gas Flow: 2. Thermal-Conductivity of Packing Fraction without Gas-Flow", *Int. Chem. Eng.* **1978**, *18*, 189–204.

[92] G. Damköhler, "Einfluß von Diffusion, Strömung und Wärmetransport auf die Ausbeute bei chemisch-technischen Reaktionen" in *Physikalisch-chemische und wirtschaftliche Gesichtspunkte für die Durchführung chemischer Operationen*, (Eds.: A. Eucken, B. Jakob), Der Chemie-Ingenieur, **1937**, pp. 359–485.

[93] E. W. Thiele, "Relation between Catalytic Activity and Size of Particle", *Ind. Eng. Chem.* **1939**, *31*, 916–920, DOI `10.1021/ie50355a027`.

[94] R. Aris, *The Mathematical Theory of Diffusion and Reaction in Permeable Catalysis: the Theory of Steady State*, *Vol. 1*, Clarendon Press, Oxford, GB, **1975**.

[95]   R. Aris, *The Mathematical Theory of Diffusion and Reaction in Permeable Catalysis: Questions of Uniqueness, Stability, and Transient Behaviour*, *Vol. 2*, Clarendon Press, Oxford, GB, **1975**.

[96]   G. Emig, "Diffusion und Reaktion in porösen Kontakten" in *Angewandte Physikalische Chemie*, (Eds.: G. Emig, G. M. Schneider, H. Jüntgen, K. H. Heek), Fortschritte der Chemischen Forschung, Springer, Berlin, DE, **1970**, pp. 451–558, DOI `10.1007/BFb0051223`.

[97]   R. Krishna, "Problems and Pitfalls in the Use of the Fick Formulation for Intraparticle Diffusion", *Chem. Eng. Sci.* **1993**, *48*, 845–861, DOI `10.1016/0009-2509(93)80324-J`.

[98]   R. Krishna, J. A. Wesselingh, "The Maxwell-Stefan Approach to Mass Transfer", *Chem. Eng. Sci.* **1997**, *52*, 861–911, DOI `10.1016/S0009-2509(96)00458-7`.

[99]   R. B. Evans, III., G. M. Watson, E. A. Mason, "Gaseous Diffusion in Porous Media at Uniform Pressure", *J. Chem. Phys.* **1961**, *35*, 2076–2083, DOI `10.1063/1.1732211`.

[100] R. B. Evans, III., G. M. Watson, E. A. Mason, "Gaseous Diffusion in Porous Media. II. Effect of Pressure Gradients", *J. Chem. Phys.* **1962**, *36*, 1894–1902, DOI `10.1063/1.1701287`.

[101] E. A. Mason, R. B. Evans, III., G. M. Watson, "Gaseous Diffusion in Porous Media. III. Thermal Transpiration", *J. Chem. Phys.* **1963**, *38*, 1808–1826, DOI `10.1063/1.1733880`.

[102] E. A. Mason, A. P. Malinauskas, "Gaseous Diffusion in Porous Media. IV. Thermal Diffusion", *J. Chem. Phys.* **1964**, *41*, 3815–3819, DOI `10.1063/1.1725819`.

[103] E. A. Mason, A. P. Malinauskas, *Gas Transport in Porous Media: the Dusty-Gas Model*, Elsevier, Amsterdam, NL, **1983**.

[104] E. A. Mason, A. P. Malinauskas, R. B. Evans, III., "Flow and Diffusion of Gases in Porous Media", *J. Chem. Phys.* **1967**, *46*, 3199–3216, DOI `10.1063/1.1841191`.

[105] H. S. Nan, M. M. Dias, A. E. Rodrigues, "Effect of Forced Convection on Reaction with Mole Changes in Porous Catalysts", *Chem. Eng. J.* **1995**, *57*, 101–114, DOI `10.1016/0923-0467(94)02930-X`.

[106] K. R. Rout, M. Hillestad, H. A. Jakobsen, "A Numerical Study of Pellet Model Consistency with Respect to Molar and Mass Average Velocities, Pressure Gradients and Porosity Models for Methanol Synthesis Process: Effects of Flux Models on Reactor Performance", *Chem. Eng. Res. Des.* **2013**, *91*, 296–317, DOI `10.1016/j.cherd.2012.09.003`.

[107] J. Solsvik, H. A. Jakobsen, "Modeling of Multicomponent Mass Diffusion in Porous Spherical Pellets: Application to Steam Methane Reforming and Methanol Synthesis", *Chem. Eng. Sci.* **2011**, *66*, 1986–2000, DOI 10.1016/j.ces.2011.01.060.

[108] J. W. Veldsink, R. van Damme, G. F. Versteeg, W. van Swaaij, "The Use of the Dusty-Gas Model for the Description of Mass Transport with Chemical Reaction in Porous Media", *Chem. Eng. J.* **1995**, *57*, 115–125, DOI 10.1016/0923-0467(94)02929-6.

[109] A. Bertei, C. Nicolella, "Common Inconsistencies in Modeling Gas Transport in Porous Electrodes: the Dusty-Gas Model and the Fick Law", *J. Power Sources* **2015**, *279*, 133–137, DOI 10.1016/j.jpowsour.2015.01.007.

[110] A. Bertei, C. Nicolella, "Dusty-Gas Model with Uniform Pressure: a Numerical Study on the Impact of a Frequent Inconsistent Assumption in SOFC Electrode Modeling", *ECS Trans.* **2015**, *68*, 2887–2895, DOI 10.1149/06801.2887ecst.

[111] I. K. Kookos, "On the Diffusion in Porous Electrodes of SOFCs", *Chem. Eng. Sci.* **2012**, *69*, 571–577, DOI 10.1016/j.ces.2011.11.013.

[112] K. Tseronis, I. K. Kookos, C. Theodoropoulos, "Modelling Mass Transport in Solid Oxide Fuel Cell Anodes: a Case for a Multidimensional Dusty Gas-Based Model", *Chem. Eng. Sci.* **2008**, *63*, 5626–5638, DOI 10.1016/j.ces.2008.07.037.

[113] E. R. Gilliland, "Diffusion Coefficients in Gaseous Systems", *Ind. Eng. Chem.* **1934**, *26*, 681–685, DOI 10.1021/ie50294a020.

[114] E. N. Fuller, K. Ensley, J. C. Giddings, "Diffusion of Halogenated Hydrocarbons in Helium: the Effect of Structure on Collision Cross Sections", *J. Phys. Chem.* **1969**, *73*, 3679–3685, DOI 10.1021/j100845a020.

[115] N. Epstein, "On Tortuosity and the Tortuosity Factor in Flow and Diffusion through Porous Media", *Chem. Eng. Sci.* **1989**, *44*, 777–779, DOI 10.1016/0009-2509(89)85053-5.

[116] R. Dittmeyer, G. Emig, "Simultaneous Heat and Mass Transfer and Chemical Reaction" in *Handbook of Heterogeneous Catalysis*, *Vol. 3*, (Eds.: G. Ertl, H. Knözinger, F. Schüth, J. Weitkamp), Wiley-VCH, Weinheim, DE, **2008**, pp. 1727–1784, DOI 10.1002/9783527610044.hetcat0094.

[117] D. Arnošt, P. Schneider, "Dynamic Transport of Multicomponent Mixtures of Gases in Porous Solids", *Chem. Eng. J.* **1995**, *57*, 91–99, DOI 10.1016/0923-0467(94)02900-8.

[118] P. Fott, G. Petrini, P. Schneider, "Transport Parameters of Monodisperse Porous Catalysts", *Collect. Czech. Chem. Commun.* **1983**, *48*, 215–227, DOI 10.1135/cccc19830215.

[119] P. Schneider, "Multicomponent Isothermal Diffusion and Forced Flow of Gases in Capillaries", *Chem. Eng. Sci.* **1978**, *33*, 1311–1319, DOI `10.1016/0009-2509(78)85112-4`.

[120] P. Schneider, D. Gelbin, "Direct Transport Parameters Measurement versus their Estimation from Mercury Penetration in Porous Solids", *Chem. Eng. Sci.* **1985**, *40*, 1093–1099, DOI `10.1016/0009-2509(85)85067-3`.

[121] O. Šolcová, H. Šnajdaufová, V. Hejtmánek, P. Schneider, "Textural Properties of Porous Solids in Relation to Gas Transport", *Chem. Pap.* **1999**, *53*, 396–402.

[122] P. J. A. M. Kerkhof, "A Modified Maxwell-Stefan Model for Transport through Inert Membranes: the Binary Friction Model", *Chem. Eng. J.* **1996**, *64*, 319–343, DOI `10.1016/S0923-0467(96)03134-X`.

[123] P. J. A. M. Kerkhof, "New Light on Some Old Problems: Revisiting the Stefan Tube, Graham's Law, and the Bosanquet Equation", *Ind. Eng. Chem. Res.* **1997**, *36*, 915–922, DOI `10.1021/ie960542i`.

[124] P. J. A. M. Kerkhof, "New Developments in Membrane Transport Phenomena", *Lat. Am. Appl. Res.* **1998**, *28*, 15–24.

[125] P. Čapek, A. Seidel-Morgenstern, "Multicomponent Mass Transport in Porous Solids and Estimation of Transport Parameters", *Appl. Catal., A* **2001**, *211*, 227–237, DOI `10.1016/S0926-860X(00)00867-X`.

[126] P. Čapek, V. Hejtmánek, O. Šolcová, K. Klusáček, P. Schneider, "Gas Transport in Porous Media under Dynamic Conditions", *Catal. Today* **1997**, *38*, 31–38, DOI `10.1016/S0920-5861(97)00036-9`.

[127] R. Jackson, *Transport in Porous Catalysts*, Elsevier, Amsterdam, NL, **1977**.

[128] P. J. A. M. Kerkhof, M. A. M. Geboers, "Analysis and Extension of the Theory of Multicomponent Fluid Diffusion", *Chem. Eng. Sci.* **2005**, *60*, 3129–3167, DOI `10.1016/j.ces.2004.12.042`.

[129] F. Koschany, D. Schlereth, O. Hinrichsen, "On the Kinetics of the Methanation of Carbon Dioxide on Coprecipitated NiAl(O)$_x$", *Appl. Catal., B* **2016**, *181*, 504–516, DOI `10.1016/j.apcatb.2015.07.026`.

[130] M. Peter, M. B. Fichtl, H. Ruland, S. Kaluza, M. Muhler, O. Hinrichsen, "Detailed Kinetic Modeling of Methanol Synthesis over a Ternary Copper Catalyst", *Chem. Eng. J.* **2012**, *203*, 480–491, DOI `10.1016/j.cej.2012.06.066`.

[131] G. Che-Galicia, R. Quintana-Solórzano, R. S. Ruiz-Martínez, J. S. Valente, C. O. Castillo-Araiza, "Kinetic Modeling of the Oxidative Dehydrogenation of Ethane to Ethylene over a MoVTeNbO Catalytic System", *Chem. Eng. J.* **2014**, *252*, 75–88, DOI `10.1016/j.cej.2014.04.042`.

[132] G. F. Carey, B. A. Finlayson, "Orthogonal Collocation on Finite Elements", *Chem. Eng. Sci.* **1975**, *30*, 587–596, DOI `10.1016/0009-2509(75)80031-5`.

[133] A. Saltelli, M. Ratto, S. Tarantola, F. Campolongo, "Sensitivity Analysis for Chemical Models", *Chem. Rev.* **2005**, *105*, 2811–2828, DOI `10.1021/cr040659d`.

[134] A. Janon, T. Klein, A. Lagnoux, M. Nodet, C. Prieur, "Asymptotic Normality and Efficiency of Two Sobol Index Estimators", *ESAIM: P&S* **2014**, *18*, 342–364, DOI `10.1051/ps/2013040`.

[135] A. Saltelli, "Making Best Use of Model Evaluations to Compute Sensitivity Indices", *Comput. Phys. Commun.* **2002**, *145*, 280–297, DOI `10.1016/S0010-4655(02)00280-1`.

[136] I. M. Sobol', "Sensitivity Estimates for Nonlinear Mathematical Models", *Math. Model. Comput. Exp.* **1993**, *1*, 407–414.

[137] I. M. Sobol', "Global Sensitivity Indices for Nonlinear Mathematical Models and their Monte Carlo Estimates", *Math. Comput. Simul.* **2001**, *55*, 271–280, DOI `10.1016/S0378-4754(00)00270-6`.

[138] H. Monod, C. Naud, D. Makowski, "Uncertainty and Sensitivity Analysis for Crop Models" in *Working with Dynamic Crop Models*, (Eds.: D. Wallach, D. Makowski, J. W. Jones), Elsevier, Amsterdam, NL, **2006**, pp. 55–100.

[139] *CRC Materials Science and Engineering Handbook*, 3rd Edition, (Eds.: J. F. Shackelford, W. Alexander), CRC Press, Boca Raton (FL), US, **2001**.

[140] J. Barrientos, N. González, M. Lualdi, M. Boutonnet, S. Järås, "The Effect of Catalyst Pellet Size on Nickel Carbonyl-Induced Particle Sintering under Low Temperature CO Methanation", *Appl. Catal., A* **2016**, *514*, 91–102, DOI `10.1016/j.apcata.2015.12.034`.

[141] P. B. Weisz, "Zeolites - New Horizons in Catalysis: When a Murphree Medalist Discusses the Ins and Outs of Zeolites Catalysts the Knowledgeable Listen.", *Chemtech* **1973**, *3*, 498–505.

[142] D.-Y. Peng, D. B. Robinson, "A New Two-Constant Equation of State", *Ind. Eng. Chem. Fund.* **1976**, *15*, 59–64, DOI `10.1021/i160057a011`.

[143] H. Knapp, R. Döring, L. Oellrich, U. Plöcker, J. M. Prausnitz, *Vapor-Liquid Equilibria for Mixtures of Low Boiling Substances: Binary Systems*, Dechema, Frankfurt (Main), DE, **1982**.

[144] M. Kleiber, R. Joh, "Berechnungsmethoden für Stoffeigenschaften" in *VDI-Wärmeatlas*, *Vol. Da1*, (Ed.: S. Kabelac), Springer, Berlin, DE, **2006**, pp. 103–132, DOI `10.1007/978-3-540-32218-4_10`.

[145] M. Kleiber, R. Joh, "Berechnungsmethoden für Stoffeigenschaften" in *VDI-Wärmeatlas*, *Vol. D1*, (Ed.: VDI-Gesellschaft Verfahrenstechnik und Chemieingenieurwesen), Springer, Berlin, DE, **2013**, pp. 137–174, DOI 10.1007/978-3-642-19981-3_11.

[146] E. A. Mason, S. C. Saxena, "Approximate Formula for the Thermal Conductivity of Gas Mixtures", *Phys. Fluids* **1958**, *1*, 361–396, DOI 10.1063/1.1724352.

[147] C. R. Wilke, "A Viscosity Equation for Gas Mixtures", *J. Chem. Phys.* **1950**, *18*, 517–519, DOI 10.1063/1.1747673.

[148] S. Weber, "Über den Zusammenhang zwischen der laminaren Strömung der reinen Gase durch Rohre und dem Selbstdiffusionskoeffizienten", *Mat.-Fys. Medd. - K. Dan. Vidensk. Selsk.* **1954**, *28*, 1–138.

[149] B. A. Finlayson, "Orthogonal Collocation on Finite Elements: Progress and Potential", *Math. Comput. Simul.* **1980**, *22*, 11–17, DOI 10.1016/0378-4754(80)90097-X.

[150] M. Gao, H. Li, M. Yang, J. Zhou, X. Yuan, P. Tian, M. Ye, Z. Liu, "A Modeling Study on Reaction and Diffusion in MTO Process over SAPO-34 Zeolites", *Chem. Eng. J.* **2019**, *377*, 119668, DOI 10.1016/j.cej.2018.08.054.

[151] F. J. Keil, *Diffusion und Chemische Reaktionen in der Gas/Feststoff-Katalyse*, Springer, Berlin, DE, **1999**, DOI 10.1007/978-3-642-60224-5.

[152] J. B. Young, B. Todd, "Modelling of Multi-Component Gas Flows in Capillaries and Porous Solids", *Int. J. Heat Mass Transfer* **2005**, *48*, 5338–5353, DOI 10.1016/j.ijheatmasstransfer.2005.07.034.

[153] R. Aris, "On Shape Factors for Irregular Particles–I: the Steady State Problem. Diffusion and Reaction", *Chem. Eng. Sci.* **1957**, *6*, 262–268, DOI 10.1016/0009-2509(57)85028-3.

[154] N. J. Mariani, S. D. Keegan, O. M. Martínez, G. F. Barreto, "A One-Dimensional Equivalent Model to Evaluate Overall Reaction Rates in Catalytic Pellets", *Chem. Eng. Res. Des.* **2003**, *81*, 1033–1042, DOI 10.1205/026387603322482266.

[155] C. Mocciaro, N. J. Mariani, O. M. Martínez, G. F. Barreto, "A Three-Parameter One-Dimensional Model to Predict the Effectiveness Factor for an Arbitrary Pellet Shape", *Ind. Eng. Chem. Res.* **2011**, *50*, 2746–2754, DOI 10.1021/ie101296d.

[156] N. J. Mariani, M. J. Taulamet, S. D. Keegan, O. M. Martínez, G. F. Barreto, "Prediction of Effectiveness Factor Using One-Dimensional Approximations for Complex Pellet Shapes and Abnormal Kinetics Expressions", *Ind. Eng. Chem. Res.* **2013**, *52*, 15321–15329, DOI 10.1021/ie4005805.

[157] M. J. Taulamet, N. J. Mariani, O. M. Martínez, G. F. Barreto, "Prediction of Effective Reaction Rates in Catalytic Systems of Multiple Reactions Using One-Dimensional Models", *Chem. Eng. J.* **2018**, *335*, 876–886, DOI 10.1016/j.cej.2017.10.186.

[158] A. G. Dixon, D. L. Cresswell, "Model Reduction for Two-Dimensional Catalyst Pellets with Complex Kinetics", *Ind. Eng. Chem. Res.* **1987**, *26*, 2306–2312, DOI `10.1021/ie00071a022`.

[159] A. G. Dixon, M. Nijemeisland, "CFD as a Design Tool for Fixed-Bed Reactors", *Ind. Eng. Chem. Res.* **2001**, *40*, 5246–5254, DOI `10.1021/ie001035a`.

[160] G. D. Wehinger, T. Eppinger, M. Kraume, "Detailed Numerical Simulations of Catalytic Fixed-Bed Reactors: Heterogeneous Dry Reforming of Methane", *Chem. Eng. Sci.* **2015**, *122*, 197–209, DOI `10.1016/j.ces.2014.09.007`.

[161] G. M. Karthik, V. V. Buwa, "Effect of Particle Shape on Fluid Flow and Heat Transfer for Methane Steam Reforming Reactions in a Packed Bed", *AIChE J.* **2017**, *63*, 366–377, DOI `10.1002/aic.15542`.

[162] A. G. Dixon, M. E. Taşkin, M. Nijemeisland, E. H. Stitt, "CFD Method to Couple Three-Dimensional Transport and Reaction inside Catalyst Particles to the Fixed Bed Flow Field", *Ind. Eng. Chem. Res.* **2010**, *49*, 9012–9025, DOI `10.1021/ie100298q`.

[163] M. E. Taşkin, A. Troupel, A. G. Dixon, M. Nijemeisland, E. H. Stitt, "Flow, Transport, and Reaction Interactions for Cylindrical Particles with Strongly Endothermic Reactions", *Ind. Eng. Chem. Res.* **2010**, *49*, 9026–9037, DOI `10.1021/ie1003619`.

[164] B. Partopour, A. G. Dixon, "*n*-Butane Partial Oxidation in a Fixed Bed: a Resolved Particle Computational Fluid Dynamics Simulation", *Can. J. Chem. Eng.* **2018**, *96*, 1946–1956, DOI `10.1002/cjce.23130`.

[165] R. H. Hite, R. Jackson, "Pressure Gradients in Porous Catalyst Pellets in the Intermediate Diffusion Regime", *Chem. Eng. Sci.* **1977**, *32*, 703–709, DOI `10.1016/0009-2509(77)80117-6`.

[166] A. Nagaraj, S. Bikkina, P. L. Mills, "Analysis of Heat, Mass Transport, & Momentum Transport Effects in Complex Catalyst Shapes for Gas-Phase Heterogeneous Reactions Using COMSOL Multiphysics", COMSOL Conference, Boston (MA), US, **2008**.

[167] A. Nagaraj, P. L. Mills, "Modeling Transport-Kinetics Interactions in Commercial Catalyst Shapes for SO_2 Oxidation to SO_3", 24th International Symposium on Chemical Reaction Engineering (ISCRE 24), Minneapolis (MN), US, **2016**.

[168] C. H. Bosanquet, "The Optimum Pressure for a Diffusion Separation Plant", British Technical Assistance Report, *BR 507*, London, GB, **1944**.

[169] K. R. Kaza, J. V. Villadsen, R. Jackson, "Intraparticle Diffusion Effects in the Methanation Reaction", *Chem. Eng. Sci.* **1980**, *35*, 17–24, DOI `10.1016/0009-2509(80)80065-0`.

[170] A. Reitzmann, W. M. Brandstädter, L. Streifinger, M. Estenfelder, "Shaped Catalyst Body for Flow-through Fixed-Bed Reactors", Patent WO 2012/069481, **2012**.

[171]   I. B. Celik, U. Ghia, P. J. Roache, C. J. Freitas, H. Coleman, P. E. Raad, "Procedure for Estimation and Reporting of Uncertainty Due to Discretization in CFD Applications: Announcement", *J. Fluids Eng.* **2008**, *130*, 078001-1–078001-4, DOI `10.1115/1.2960953`.

[172]   A. Burghardt, A. Kubaczka, "Generalization of the Effectiveness Factor for Any Shape of a Catalyst Pellet", *Chem. Eng. Process.* **1996**, *35*, 65–74, DOI `10.1016/0255-2701(95)04115-X`.

[173]   S. D. Keegan, N. J. Mariani, O. M. Martínez, G. F. Barreto, "Behaviour of Smooth Catalysts at High Reaction Rates", *Chem. Eng. J.* **2005**, *110*, 41–56, DOI `10.1016/j.cej.2005.04.013`.

[174]   S. D. Keegan, N. J. Mariani, O. M. Martínez, G. F. Barreto, "Behavior of Catalytic Pellets at High Reaction Rates: the Effect of Edges", *Ind. Eng. Chem. Res.* **2006**, *45*, 85–97, DOI `10.1021/ie050740m`.

[175]   L. Kwaśniewski, "Application of Grid Convergence Index in FE Computation", *Bull. Pol. Acad. Sci.: Tech. Sci.* **2013**, *61*, 123–128, DOI `10.2478/bpasts-2013-0010`.

[176]   V. Hlaváček, J. A. Puszynski, H. J. Vijoen, J. E. Gatica, "Model Reactors and Their Design Equations" in *Ullmann's Encyclopedia of Industrial Chemistry*, (Ed.: B. Elvers), Wiley-VCH, Weinheim, DE, **2014**, DOI `10.1002/14356007.b04_121`.

[177]   T. Daszkowski, G. Eigenberger, "A Reevaluation of Fluid Flow, Heat Transfer and Chemical Reaction in Catalyst Filled Tubes", *Chem. Eng. Sci.* **1992**, *47*, 2245–2250, DOI `10.1016/0009-2509(92)87042-O`.

[178]   S. Hein, D. Vortmeyer, "Wandgekühlte chemische Festbettreaktoren und deren Modellierung mit Ein-und Zweiphasenmodellen", *Z. Naturforsch., A: Phys. Sci.* **1995**, *50*, DOI `10.1515/zna-1995-0608`.

[179]   M. Giese, K. Rottschäfer, D. Vortmeyer, "Measured and Modeled Superficial Flow Profiles in Packed Beds with Liquid Flow", *AIChE J.* **1998**, *44*, 484–490, DOI `10.1002/aic.690440225`.

[180]   D. Schlereth, O. Hinrichsen, "A Fixed-Bed Reactor Modeling Study on the Methanation of CO_2", *Chem. Eng. Res. Des.* **2014**, *92*, 702–712, DOI `10.1016/j.cherd.2013.11.014`.

[181]   J. Maußner, A. Pietschak, H. Freund, "A New Analytical Approximation to the Extended Brinkman Equation", *Chem. Eng. Sci.* **2017**, *171*, 495–499, DOI `10.1016/j.ces.2017.06.005`.

[182]   M. Winterberg, E. Tsotsas, A. Krischke, D. Vortmeyer, "A Simple and Coherent Set of Coefficients for Modelling of Heat and Mass Transport with and without Chemical Reaction in Tubes Filled with Spheres", *Chem. Eng. Sci.* **2000**, *55*, 967–979, DOI 10.1016/S0009-2509(99)00379-6.

[183]   A. G. Dixon, M. Nijemeisland, E. H. Stitt, "Packed Tubular Reactor Modeling and Catalyst Design using Computational Fluid Dynamics" in *Computational Fluid Dynamics*, (Ed.: G. B. Marin), Advances in Chemical Engineering, Elsevier, Amsterdam, NL, **2006**, pp. 307–389, DOI 10.1016/S0065-2377(06)31005-8.

[184]   A. G. Dixon, "Local Transport and Reaction Rates in a Fixed Bed Reactor Tube: Endothermic Steam Methane Reforming", *Chem. Eng. Sci.* **2017**, *168*, 156–177, DOI 10.1016/j.ces.2017.04.039.

[185]   B. Partopour, A. G. Dixon, "Computationally Efficient Incorporation of Microkinetics into Resolved-Particle CFD Simulations of Fixed-Bed Reactors", *Comput. Chem. Eng.* **2016**, *88*, 126–134, DOI 10.1016/j.compchemeng.2016.02.015.

[186]   B. Partopour, A. G. Dixon, "Integrated Multiscale Modeling of Fixed Bed Reactors: Studying the Reactor under Dynamic Reaction Conditions", *Chem. Eng. J.* **2018**, *377*, 119738, DOI 10.1016/j.cej.2018.08.124.

[187]   M. Behnam, A. G. Dixon, M. Nijemeisland, E. H. Stitt, "A New Approach to Fixed Bed Radial Heat Transfer Modeling Using Velocity Fields from Computational Fluid Dynamics Simulations", *Ind. Eng. Chem. Res.* **2013**, *52*, 15244–15261, DOI 10.1021/ie4000568.

[188]   A. G. Dixon, N. J. Medeiros, "Computational Fluid Dynamics Simulations of Gas-Phase Radial Dispersion in Fixed Beds with Wall Effects", *Fluids* **2017**, *2*, 56, DOI 10.3390/fluids2040056.

[189]   M. Zhang, H. Dong, Z. Geng, "Computational Study of Flow and Heat Transfer in Fixed Beds with Cylindrical Particles for Low Tube to Particle Diameter Ratios", *Chem. Eng. Res. Des.* **2018**, *132*, 149–161, DOI 10.1016/j.cherd.2018.01.006.

[190]   A. B. Hamzah, S. Ookawara, S. Yoshikawa, H. Matsumoto, "CFD Modelling of Mass and Heat Dispersion in Sphere Fixed Bed with Porosity-Dependent Segmented-Continuum Approaches", *Chem. Eng. Res. Des.* **2019**, *141*, 93–114, DOI 10.1016/j.cherd.2018.10.022.

[191]   O. Bey, G. Eigenberger, "Fluid Flow through Catalyst Filled Tubes", *Chem. Eng. Sci.* **1997**, *52*, 1365–1376, DOI 10.1016/S0009-2509(96)00509-X.

[192]   E. Haidegger, D. Vortmeyer, P. Wagner, "Simultane Lösung von Energie-, Stoff-und Impulsgleichungen für wandgekühlte chemische Festbettreaktoren", *Chem. Ing. Tech.* **1989**, *61*, 647–650, DOI 10.1002/cite.330610822.

[193] S. Ergun, "Fluid Flow through Packed Columns", *Chem. Eng. Prog.* **1952**, *48*, 89–94.

[194] D. Vortmeyer, J. Schuster, "Evaluation of Steady Flow Profiles in Rectangular and Circular Packed Beds by a Variational Method", *Chem. Eng. Sci.* **1983**, *38*, 1691–1699, DOI 10.1016/0009-2509(83)85026-X.

[195] R. Bauer, *Effektive radiale Wärmeleitfähigkeit gasdurchströmter Schüttungen mit Partikeln unterschiedlicher Form und Größenverteilung: Dissertation, Universität Karlsruhe, 1976*, VDI-Verlag, Düsseldorf, DE, **1977**.

[196] E. Tsotsas, "Wärmeleitung und Dispersion in durchströmten Schüttungen" in *VDI-Wärmeatlas*, *Vol. M7*, (Ed.: VDI-Gesellschaft Verfahrenstechnik und Chemieingenieurwesen), Springer, Berlin, DE, **2013**, pp. 1517–1534, DOI 10.1007/978-3-642-19981-3_102.

[197] M. Giese, "Strömung in porösen Medien unter Berücksichtigung effektiver Viskositäten", Ph.D. Thesis, Technische Universität München, München, DE, **1998**.

[198] M. Winterberg, E. Tsotsas, "Correlations for Effective Heat Transport Coefficients in Beds Packed with Cylindrical Particles", *Chem. Eng. Sci.* **2000**, *55*, 5937–5943, DOI 10.1016/S0009-2509(00)00198-6.

[199] J. H. Ferziger, M. Perić, *Computational Methods for Fluid Dynamics*, 3rd, rev. Edition, Springer, Berlin, DE, **2002**, DOI 10.1007/978-3-642-56026-2.

[200] J. F. Wehner, R. H. Wilhelm, "Boundary Conditions of Flow Reactor", *Chem. Eng. Sci.* **1956**, *6*, 89–93, DOI 10.1016/0009-2509(56)80014-6.

[201] R. A. Novy, H. Davis, L. E. Scriven, "Upstream and Downstream Boundary Conditions for Continuous-Flow Systems", *Chem. Eng. Sci.* **1990**, *45*, 1515–1524, DOI 10.1016/0009-2509(90)80003-W.

[202] T. Salmi, J. J. Romanainen, "A Novel Exit Boundary Condition for the Axial Dispersion Model", *Chem. Eng. Process.* **1995**, *34*, 359–366, DOI 10.1016/0255-2701(94)00531-1.

[203] R. Zou, A. B. Yu, "The Packing of Spheres in a Cylindrical Container: the Thickness Effect", *Chem. Eng. Sci.* **1995**, *50*, 1504–1507, DOI 10.1016/0009-2509(94)00483-8.

[204] J. Reimann, J. Vicente, E. Brun, C. Ferrero, Y. Gan, A. Rack, "X-Ray Tomography Investigations of Mono-Sized Sphere Packing Structures in Cylindrical Containers", *Powder Technol.* **2017**, *318*, 471–483, DOI 10.1016/j.powtec.2017.05.033.

[205] T. Ren, M. K. Patel, K. Blok, "Steam Cracking and Methane to Olefins: Energy Use, CO_2 Emissions and Production Costs", *Energy* **2008**, *33*, 817–833, DOI 10.1016/j.energy.2008.01.002.

[206] R. K. Grasselli, "Fundamental Principles of Selective Heterogeneous Oxidation Catalysis", *Top. Catal.* **2002**, *21*, 79–88, DOI `10.1023/A:1020556131984`.

[207] R. K. Grasselli, "Site Isolation and Phase Cooperation: Two Important Concepts in Selective Oxidation Catalysis: a Retrospective", *Catal. Today* **2014**, *238*, 10–27, DOI `10.1016/j.cattod.2014.05.036`.

[208] R. Schlögl, "Active Sites for Propane Oxidation: Some Generic Considerations", *Top. Catal.* **2011**, *54*, 627–638, DOI `10.1007/s11244-011-9683-0`.

[209] D. Melzer, P. Xu, D. Hartmann, Y. Zhu, N. D. Browning, M. Sanchez-Sanchez, J. A. Lercher, "Atomic-Scale Determination of Active Facets on the MoVTeNb Oxide M1 Phase and Their Intrinsic Catalytic Activity for Ethane Oxidative Dehydrogenation", *Angew. Chem., Int. Ed.* **2016**, *55*, 8873–8877, DOI `10.1002/anie.201600463`.

[210] R. Grabowski, "Kinetics of Oxidative Dehydrogenation of C_2-C_3 Alkanes on Oxide Catalysts", *Catal. Rev.* **2006**, *48*, 199–268, DOI `10.1080/01614940600631413`.

[211] J. Le Bars, J. C. Védrine, A. Auroux, S. Trautmann, M. Baerns, "Role of Surface Acidity on Vanadia/Silica Catalysts used in the Oxidative Dehydrogenation of Ethane", *Appl. Catal., A* **1992**, *88*, 179–195, DOI `10.1016/0926-860X(92)80214-W`.

[212] F. Rahman, K. F. Loughlin, M. A. Al-Saleh, M. R. Saeed, N. M. Tukur, M. M. Hossain, K. Karim, E. A. Mamedov, "Kinetics and Mechanism of Partial Oxidation of Ethane to Ethylene and Acetic Acid over MoV Type Catalysts", *Appl. Catal., A* **2010**, *375*, 17–25, DOI `10.1016/j.apcata.2009.11.026`.

[213] S. T. Oyama, A. M. Middlebrook, G. A. Somorjai, "Kinetics of Ethane Oxidation on Vanadium Oxide", *J. Phys. Chem.* **1990**, *94*, 5029–5033, DOI `10.1021/j100375a049`.

[214] M. D. Argyle, K. Chen, A. T. Bell, E. Iglesia, "Ethane Oxidative Dehydrogenation Pathways on Vanadium Oxide Catalysts", *J. Phys. Chem. B* **2002**, *106*, 5421–5427, DOI `10.1021/jp0144552`.

[215] F. Klose, M. Joshi, C. Hamel, A. Seidel-Morgenstern, "Selective Oxidation of Ethane over a VO_x/γ-Al_2O_3 Catalyst: Investigation of the Reaction Network", *Appl. Catal., A* **2004**, *260*, 101–110, DOI `10.1016/j.apcata.2003.10.005`.

[216] D. Linke, D. Wolf, M. Baerns, S. Zeyß, U. Dingerdissen, "Catalytic Partial Oxidation of Ethane to Acetic Acid over $Mo_1V_{0.25}Nb_{0.12}Pd_{0.0005}O_x$: II. Kinetic Modelling", *J. Catal.* **2002**, *205*, 32–43, DOI `10.1006/jcat.2001.3368`.

[217] J. S. Valente, R. Quintana-Solórzano, H. Armendáriz-Herrera, G. Barragán-Rodríguez, J. M. López Nieto, "Kinetic Study of Oxidative Dehydrogenation of Ethane over MoVTeNb Mixed-Oxide Catalyst", *Ind. Eng. Chem. Res.* **2014**, *53*, 1775–1786, DOI `10.1021/ie402447h`.

[218] R. Quintana-Solórzano, G. Barragán-Rodríguez, H. Armendáriz-Herrera, J. M. López Nieto, J. S. Valente, "Understanding the Kinetic Behavior of a Mo-V-Te-Nb Mixed Oxide in the Oxydehydrogenation of Ethane", *Fuel* **2014**, *138*, 15–26, DOI 10.1016/j.fuel.2014.07.051.

[219] G. Mestl, K. Wanninger, D. Melzer, M. Sanchez-Sanchez, J. Tseglakova, J. A. Lercher, "Synthesis of a MoVTeNb Catalyst from Low-Cost Metal Oxides", Patent WO 2018/141654 (A1), **2018**.

[220] D. Melzer, G. Mestl, K. Wanninger, Y. Zhu, N. D. Browning, M. Sanchez-Sanchez, J. A. Lercher, "Design and Synthesis of Highly Active MoVTeNb-Oxides for Ethane Oxidative Dehydrogenation", *Nat. Commun.* **2019**, *10*, 4012, DOI 10.1038/s41467-019-11940-0.

[221] R. M. Koros, E. J. Nowak, "A Diagnostic Test of the Kinetic Regime in a Packed Bed Reactor", *Chem. Eng. Sci.* **1967**, *22*, 470, DOI 10.1016/0009-2509(67)80134-9.

[222] R. J. Madon, M. Boudart, "Experimental Criterion for the Absence of Artifacts in the Measurement of Rates of Heterogeneous Catalytic Reactions", *Ind. Eng. Chem. Fund.* **1982**, *21*, 438–447, DOI 10.1021/i100008a022.

[223] D. E. Mears, "Tests for Transport Limitations in Experimental Catalytic Reactors", *Ind. Eng. Chem. Process Des. Dev.* **1971**, *10*, 541–547, DOI 10.1021/i260040a020.

[224] P. B. Weisz, C. D. Prater, "Interpretation of Measurements in Experimental Catalysis" in, (Eds.: W. G. Frankenburg, V. I. Komarewsky, E. K. Rideal), Advances in Catalysis, Academic Press, New York (NY), US, **1954**, pp. 143–196, DOI 10.1016/S0360-0564(08)60390-9.

[225] J. B. Anderson, "A Criterion for Isothermal Behavior of a Catalyst Pellet", *Chem. Eng. Sci.* **1963**, *18*, 147–148, DOI 10.1016/0009-2509(63)80023-8.

[226] V. Gnielinski, "Berechnung des Wärme- und Stoffaustauschs in durchströmten ruhenden Schüttungen", *VT, Verfahrenstech.* **1982**, *16*, 36–39.

[227] W. M. Haynes, *CRC Handbook of Chemistry and Physics*, 95th Edition, CRC Press, Hoboken (NJ), US, **2015**.

[228] A. Bielański, J. Haber, *Oxygen in Catalysis*, Dekker, New York (NY), US, **1991**.

[229] J. Haber, "Molecular Mechanism of Heterogeneous Oxidation: Organic and Solid State Chemists' Views" in *Third World Congress on Oxidation Catalysis*, (Eds.: S. T. Oyama, A. M. Gaffney, J. E. Lyons), Studies in Surface Science and Catalysis, Elsevier, Amsterdam, NL, **1997**, pp. 1–17, DOI 10.1016/S0167-2991(97)80966-4.

[230] J. Haber, W. Turek, "Kinetic Studies as a Method to Differentiate between Oxygen Species Involved in the Oxidation of Propene", *J. Catal.* **2000**, *190*, 320–326, DOI 10.1006/jcat.1999.2764.

[231] H. Tsuji, H. Hattori, "Oxide Surfaces that Catalyse an Acid-Base Reaction with Surface Lattice Oxygen Exchange: Evidence of Nucleophilicity of Oxide Surfaces", *ChemPhysChem* **2004**, *5*, 733–736, DOI `10.1002/cphc.200400009`.

[232] D. Linke, D. Wolf, M. Baerns, O. Timpe, R. Schlögl, S. Zeyß, U. Dingerdissen, "Catalytic Partial Oxidation of Ethane to Acetic Acid over $Mo_1V_{0.25}Nb_{0.12}Pd_{0.0005}O_x$: I. Catalyst Performance and Reaction Mechanism", *J. Catal.* **2002**, *205*, 16–31, DOI `10.1006/jcat.2001.3367`.

[233] T. M. Sankaranarayanan, R. H. Ingle, T. B. Gaikwad, S. K. Lokhande, T. Raja, R. N. Devi, V. Ramaswamy, P. Manikandan, "Selective Oxidation of Ethane over Mo-V-Al-O Oxide Catalysts: Insight to the Factors Affecting the Selectivity of Ethylene and Acetic Acid and Structure-Activity Correlation Studies", *Catal. Lett.* **2008**, *121*, 39–51, DOI `10.1007/s10562-007-9289-0`.

[234] M. Hävecker, S. Wrabetz, J. Kröhnert, L.-I. Csepei, R. Naumann d'Alnoncourt, Y. V. Kolen'ko, F. Girgsdies, R. Schlögl, A. Trunschke, "Surface Chemistry of Phase-Pure M1 MoVTeNb Oxide during Operation in Selective Oxidation of Propane to Acrylic Acid", *J. Catal.* **2012**, *285*, 48–60, DOI `10.1016/j.jcat.2011.09.012`.

[235] R. Naumann d'Alnoncourt, L.-I. Csepei, M. Hävecker, F. Girgsdies, M. E. Schuster, R. Schlögl, A. Trunschke, "The Reaction Network in Propane Oxidation over Phase-Pure MoVTeNb M1 Oxide Catalysts", *J. Catal.* **2014**, *311*, 369–385, DOI `10.1016/j.jcat.2013.12.008`.

[236] C. Heine, M. Hävecker, A. Trunschke, R. Schlögl, M. Eichelbaum, "The Impact of Steam on the Electronic Structure of the Selective Propane Oxidation Catalyst MoVTeNb Oxide (Orthorhombic M1 Phase)", *Phys. Chem. Chem. Phys.* **2015**, *17*, 8983–8993, DOI `10.1039/c5cp00289c`.

[237] V. I. Sobolev, K. Y. Koltunov, "Oxidative and Non-Oxidative Degradation of C_1-C_3 Carboxylic Acids over V_2O_5/TiO_2 and MoVTeNb Oxides: a Comparative Study", *Appl. Catal., A* **2013**, *466*, 45–50, DOI `10.1016/j.apcata.2013.06.018`.

[238] P. Kube, B. Frank, S. Wrabetz, J. Kröhnert, M. Hävecker, J. Velasco-Vélez, J. Noack, R. Schlögl, A. Trunschke, "Functional Analysis of Catalysts for Lower Alkane Oxidation", *ChemCatChem* **2017**, *9*, 573–585, DOI `10.1002/cctc.201601194`.

[239] S. M. Lofgren, P. R. Mahling, J. B. Togeas, "Acetic Acid Vapor: 1. Statistical/Quantum Mechanical Models of the Ideal Vapor", *J. Phys. Chem. A* **2005**, *109*, 5430–5437, DOI `10.1021/jp058003r`.

[240] J. B. Togeas, "Acetic Acid Vapor: 2. a Statistical Mechanical Critique of Vapor Density Experiments", *J. Phys. Chem. A* **2005**, *109*, 5438–5444, DOI `10.1021/jp058004j`.

[241] V. I. Avdeev, V. M. Tapilin, "Water Effect on the Electronic Structure of Active Sites of Supported Vanadium Oxide Catalyst VO$_x$/TiO$_2$(001)", *J. Phys. Chem. C* **2010**, *114*, 3609–3613, DOI 10.1021/jp911145c.

[242] E. M. Sadovskaya, V. B. Goncharov, Y. K. Gulyaeva, G. Y. Popova, T. V. Andrushkevich, "Kinetics of the H$_2$^{18}O/H$_2$^{16}O Isotope Exchange over Vanadia–Titania Catalyst", *J. Mol. Catal. A: Chem.* **2010**, *316*, 118–125, DOI 10.1016/j.molcata.2009.10.009.

[243] P. Mars, D. W. van Krevelen, "Oxidations Carried out by Means of Vanadium Oxide Catalysts", *Chem. Eng. Sci.* **1954**, *3*, 41–59, DOI 10.1016/S0009-2509(54)80005-4.

[244] P. Kumar, J. W. Thybaut, S. Svelle, U. Olsbye, G. B. Marin, "Single-Event Microkinetics for Methanol to Olefins on H-ZSM-5", *Ind. Eng. Chem. Res.* **2013**, *52*, 1491–1507, DOI 10.1021/ie301542c.

[245] O. Sackur, "Die Anwendung der kinetischen Theorie der Gase auf chemische Probleme", *Ann. Phys.* **1911**, *341*, 958–980, DOI 10.1002/andp.19113411505.

[246] H. Tetrode, "Die chemische Konstante der Gase und das elementare Wirkungsquantum", *Ann. Phys.* **1912**, *343*, 434–442, DOI 10.1002/andp.19123430708.

[247] L. F. Shampine, M. W. Reichelt, "The MATLAB ODE Suite", *SIAM J. Sci. Comput.* **1997**, *18*, 1–22, DOI 10.1137/S1064827594276424.

[248] T.-Y. Park, G. F. Froment, "Kinetic Modeling of the Methanol to Olefins Process: 2. Experimental Results, Model Discrimination, and Parameter Estimation", *Ind. Eng. Chem. Res.* **2001**, *40*, 4187–4196, DOI 10.1021/ie000854s.

[249] J. W. Thybaut, G. B. Marin, G. V. Baron, P. A. Jacobs, J. A. Martens, "Alkene Protonation Enthalpy Determination from Fundamental Kinetic Modeling of Alkane Hydroconversion on Pt/H–(US)Y-Zeolite", *J. Catal.* **2001**, *202*, 324–339, DOI 10.1006/jcat.2001.3292.

[250] D. E. Goldberg, *Genetic Algorithms in Search, Optimization, and Machine Learning*, 24th Edition, Addison-Wesley, Boston (MA), US, **2003**.

[251] P. DeSanto, Jr., D. J. Buttrey, R. K. Grasselli, C. G. Lugmair, A. F. Volpe, Jr., B. H. Toby, T. Vogt, "Structural Aspects of the M1 and M2 Phases in MoVNbTeO Propane Ammoxidation Catalysts", *Z. Kristallogr.* **2004**, *219*, 152–165, DOI 10.1524/zkri.219.3.152.29091.

[252] X. Li, D. J. Buttrey, D. A. Blom, T. Vogt, "Improvement of the Structural Model for the M1 Phase Mo-V-Nb-Te-O Propane (Amm)oxidation Catalyst", *Top. Catal.* **2011**, *54*, 614–626, DOI 10.1007/s11244-011-9684-z.

[253] J. A. Dumesic, D. F. Rudd, L. M. Aparicio, J. E. Rekoske, A. A. Treviño, *The Microkinetics of Heterogeneous Catalysis*, American Chemical Society, Washington (DC), US, **1993**.

[254] M.-J. Cheng, W. A. Goddard, III., "The Mechanism of Alkane Selective Oxidation by the M1 Phase of Mo-V-Nb-Te Mixed Metal Oxides: Suggestions for Improved Catalysts", *Top. Catal.* **2016**, *59*, 1506–1517, DOI `10.1007/s11244-016-0669-9`.

[255] M. Boudart, D. E. Mears, M. A. Vannice, "Kinetics of Heterogeneous Catalytic Reactions", *Ind. Chim. Belge* **1967**, *32*, 281–284.

[256] W.-Q. Li, T. Fjermestad, A. Genest, N. Rösch, "Reactivity Trends of the MoVO$_x$ Mixed Metal Oxide Catalyst from Density Functional Modeling", *Catal. Sci. Technol.* **2019**, *9*, 1559–1569, DOI `10.1039/C8CY02545B`.

[257] A. M. Wernbacher, P. Kube, M. Hävecker, R. Schlögl, A. Trunschke, "Electronic and Dielectric Properties of MoV-Oxide (M1 Phase) under Alkane Oxidation Conditions", *J. Phys. Chem. C* **2019**, *123*, 13269–13282, DOI `10.1021/acs.jpcc.9b01273`.

[258] K. Toch, J. W. Thybaut, G. B. Marin, "A Systematic Methodology for Kinetic Modeling of Chemical Reactions Applied to *n*-Hexane Hydroisomerization", *AIChE J.* **2015**, *61*, 880–892, DOI `10.1002/aic.14680`.

[259] C. T. Campbell, "Future Directions and Industrial Perspectives Micro- and Macro-Kinetics: Their Relationship in Heterogeneous Catalysis", *Top. Catal.* **1994**, *1*, 353–366, DOI `10.1007/BF01492288`.

[260] J. R. Kittrell, "Mathematical Modeling of Chemical Reactions" in *Advances in Chemical Engineering*, (Eds.: T. B. Drew, G. R. Cokelet, J. W. Hoopes, T. Vermeulen), Advances in Chemical Engineering, Elsevier, **1970**, pp. 97–183, DOI `10.1016/S0065-2377(08)60184-2`.

[261] G. A. F. Seber, C. J. Wild, *Nonlinear Regression*, Wiley & Sons, Hoboken (NJ), US, **2003**.

[262] H. Rabitz, M. Kramer, D. Dacol, "Sensitivity Analysis in Chemical Kinetics", *Annu. Rev. Phys. Chem.* **1983**, *34*, 419–461, DOI `10.1146/annurev.pc.34.100183.002223`.

[263] C. T. Campbell, "Finding the Rate-Determining Step in a Mechanism: Comparing DeDonder Relations with the "Degree of Rate Control": Letter to the Editor", *J. Catal.* **2001**, *204*, 520–524, DOI `10.1006/jcat.2001.3396`.

[264] C. Stegelmann, A. Andreasen, C. T. Campbell, "Degree of Rate Control: How Much the Energies of Intermediates and Transition States Control Rates", *J. Am. Chem. Soc.* **2009**, *131*, 8077–8082, DOI `10.1021/ja9000097`.

[265] V. Gnielinski, "Gleichungen zur Berechnung des Wärme und Stoffaustausches in durchströmten ruhenden Kugelschüttungen bei mittleren und großen Pécletzahlen", *VT, Verfahrenstech.* **1978**, *12*, 363–366.

[266] A. Peschel, H. Freund, K. Sundmacher, "Methodology for the Design of Optimal Chemical Reactors Based on the Concept of Elementary Process Functions", *Ind. Eng. Chem. Res.* **2010**, *49*, 10535–10548, DOI `10.1021/ie100476q`.

[267] D. M. Himmelblau, "Accounts of Experiences in the Application of Artificial Neural Networks in Chemical Engineering", *Ind. Eng. Chem. Res.* **2008**, *47*, 5782–5796, DOI `10.1021/ie800076s`.

[268] *VDI-Wärmeatlas*, 11., bearb. und erw. Auflage, (Ed.: VDI-Gesellschaft Verfahrenstechnik und Chemieingenieurwesen), Springer, Berlin, DE, **2013**, DOI `10.1007/978-3-642-19981-3`.

[269] M. Kleiber, R. Joh, "Stoffwerte von sonstigen chemisch einheitlichen Flüssigkeiten und Gasen" in *VDI-Wärmeatlas*, *Vol. Dca1*, (Ed.: S. Kabelac), Springer, Berlin, DE, **2006**, pp. 249–294, DOI `10.1007/978-3-540-32218-4_18`.

[270] O. Sackur, "Die universelle Bedeutung des sog. elementaren Wirkungsquantums", *Ann. Phys.* **1913**, *345*, 67–86, DOI `10.1002/andp.19133450103`.

[271] M. Kleiber, R. Joh, "Stoffwerte von sonstigen reinen Fluiden" in *VDI-Wärmeatlas*, *Vol. D3*, (Ed.: VDI-Gesellschaft Verfahrenstechnik und Chemieingenieurwesen), Springer, Berlin, DE, **2013**, pp. 357–488, DOI `10.1007/978-3-642-19981-3_20`.

[272] E. Tsotsas, "Wärmeübergang von einer Heizfläche an ruhende oder mechanisch durchmischte Schüttungen" in *VDI-Wärmeatlas*, *Vol. M6*, (Ed.: VDI-Gesellschaft Verfahrenstechnik und Chemieingenieurwesen), Springer, Berlin, DE, **2013**, pp. 1499–1516, DOI `10.1007/978-3-642-19981-3_101`.

[273] H. Martin, "Wärme- und Stoffübertragung in der Wirbelschicht", *Chem. Ing. Tech.* **1980**, *52*, 199–209, DOI `10.1002/cite.330520303`.

[274] V. Gnielinski, "Wärmeübertragung Partikel–Fluid in durchströmten Haufwerken" in *VDI-Wärmeatlas*, *Vol. G9*, (Ed.: VDI-Gesellschaft Verfahrenstechnik und Chemieingenieurwesen), Springer, Berlin, DE, **2013**, pp. 839–840, DOI `10.1007/978-3-642-19981-3_50`.

[275] B. A. Finlayson, *Nonlinear Analysis in Chemical Engineering*, McGraw-Hill, New York (NY), US, **1980**.

[276] B. A. Finlayson, *The Method of Weighted Residuals and Variational Principles: with Application in Fluid Mechanics, Heat and Mass Transfer*, Academic Press, New York (NY), US, **1972**.

Nomenclature

Latin Symbols

a_i-e_i	placeholder	a.u.
A_i-E_i	placeholder	a.u.
a	(thermodynamic) activity	–
a	thermal diffusivity	$\mathrm{m^2/s}$
A	area	$\mathrm{m^2}$
A	pre-exponential factor in Arrhenius' law	$\mathrm{mol/(kg_{cat}\,s)}$
B	deformation factor in stagnant packed-bed dispersion model (cf. Section A.5.1)	–
B_0	permeability of porous medium	$\mathrm{m^2}$
B_i	individual permeability parameter of porous medium	$\mathrm{m^2/s}$
c	molar concentration	$\mathrm{mol/m^3}$
C_p°	standard molar heat capacity at constant pressure	$\mathrm{J/(mol\,K)}$
$[C]$	transport matrix for multicomponent diffusion model	s/m
$c_{i,i}$	diagonal entries of $[C]$	s/m
$c_{i,j}$	entries in i-th row and j-th column of $[C]$	s/m
C_f	form factor in stagnant packed-bed dispersion model (cf. Section A.5.1)	–
$\mathrm{Cov}(\dots)$	covariance of ...	a.u.
d	diameter	m
$Đ_{ij}$	Maxwell-Stefan binary diffusion coefficient between components i and j	$\mathrm{m^2/s}$
$D_{i,\mathrm{Kn}}$	Knudsen diffusion coefficient of species i	$\mathrm{m^2/s}$
$D_{i,\mathrm{m}}$	average molecular diffusion coefficient of species i	$\mathrm{m^2/s}$
$\mathcal{D}$	dispersion coefficient	$\mathrm{m^2/s}$
dof	degrees-of-freedom	–
E_a	activation energy	J/mol
$\mathrm{E}(\dots)$	expected value of ...	a.u.
f_i	fugacity of species i	Pa

f	damping function in dynamic packed-bed dispersion model (cf. Section 5.2.3)	–
F	molar flow	mol/s
$F_{a/s}$	value of F-test	–
G	molar Gibbs' free energy	J/mol
G'	(total) Gibbs' free energy	J
h	Planck's constant	J s
H	molar enthalpy	J/mol
H'	(total) enthalpy	J
$\Delta_r H^\circ$	enthalpy of reaction	J/mol
$\Delta_{ads} H^\circ$	enthalpy of adsorption	J/mol
$\mathcal{H}$	Hessian matrix	a.u.
i	index variable	–
j	index variable	–
$\widetilde{J}$	general flux	a.u.
$\mathcal{J}$	Jacobian matrix	a.u.
k	rate constant	$mol/(kg_{cat} \, s)$
K	equilibrium constant	–
k_B	Boltzmann constant	J/K
k_i	dimensionless thermal conductivity $k_i = \lambda_i / \lambda_{fl}$	–
K_1	slope parameter in dynamic packed-bed dispersion model (cf. Section 5.2.3)	–
K_2	damping parameter in dynamic packed-bed dispersion model (cf. Section 5.2.3)	–
K_{ax}	parameter for axial dispersion in dynamic packed-bed dispersion model (cf. Section 5.2.3)	–
l	dimensionless length	–
L	length	m
L	phenomenological coefficients in non-equilibrium thermodynamics	a.u.
$L(s(x))$	differential equation with the solution $s(x)$	a.u.
m_{cat}	catalyst mass	kg
M	molar mass	kg/mol
$MAPE$	mean absolute percentage error	%
$MaxAPE$	maximum absolute percentage error	%
$[M_i]$	lattice site fraction of i	–
n	mole number	mol
n_i	number of i	–
N	molar flux	$mol/(m^2 \, s)$

N	parameter in stagnant packed-bed dispersion model (cf. Section A.5.1)	–
N_A	Avogadro constant	1/mol
p	pressure	Pa
p_i	partial pressure of species i	Pa
p'_i	reduced pressure of species i: $p'_i = p/p_{\mathrm{ref},i}$	–
p°	standard pressure $p^\circ = 10^5\,\mathrm{Pa}$	Pa
P_i	polynomial of degree i	a.u.
Pe	Péclet number	–
PE	percentage error	%
Pr	Prandtl number	–
Q	general molar quantities	a.u.
$\dot{Q}$	heat flux	W/m^2
r	radial coordinate	m
$\dot{r}_j$	reaction rate of reaction j	mol/(kg$_{\mathrm{cat}}$ s)
R	tube radius	m
$\dot{R}_i$	net rate of production of species i	mol/(kg$_{\mathrm{cat}}$ s)
$\mathcal{R}$	ideal gas constant	J/molK
R/H	pellet aspect ratio	–
Re	Reynolds number	–
$s(x)$	solution of a differential equation	a.u.
S_X	Sobol' index of parameter X	–
S	molar entropy	J/(mol K)
S'	(total) entropy	J/K
S_{ij}	selectivity of product species i with respect to reactant j	–
$S(i,j)$	sensitivity of i with regard to j	–
$\Delta_{\mathrm{ads}}S^\circ$	entropy of adsorption	J/(mol K)
Sc	Schmidt number	–
Sh	Sherwood number	–
SRM	stoichiometry-reaction-matrix	–
t	Student's t-value	–
T	temperature	K
u	superficial velocity	m/s
Δv	specific diffusive volumes	m^3
V	volume	m^3
Var(...)	variance of ...	a.u.
$WHSV$	weight hourly space velocity	kg$_{\mathrm{feed}}$/(kg$_{\mathrm{cat}}$ h)
x	dimensionless coordinate	–

X	parameter for sensitivity analysis	a.u.
X_i	conversion of species i	–
y_i	mole fraction of species i	–
Y_i	carbon fraction of species i	–
Y	output function for sensitivity analysis	a.u.
Y^X	output function with frozen parameter X for sensitivity analysis	a.u.
z	axial coordinate	m

Greek Symbols

α	heat transfer coefficient	W/(m^2 K)
α	placeholder for diffusion model	–
β	mass transfer coefficient	m/s
β	placeholder for diffusion model	s/m^2
β	approach to equilibrium (cf. Appendix B.2)	
γ	accommodation coefficient	–
δ	thermodynamic forces	a.u.
δ	thickness of boundary layer	m
$\Delta\ldots$	change of . . .	a.u.
ε	porosity	–
ϵ_p	particle emissivity	–
ζ_{ij}	mixing parameter according to Wilke [147] (cf. Equation (A.21))	–
η	dynamic viscosity	Pa s
η	catalyst effectiveness factor	–
Θ	surface coverage	–
2θ	diffraction angle	°
κ_i	fractional viscous contributions of component i, defined for the BFM	s
λ	thermal conductivity	W/(m K)
Λ	thermal dispersion	W/(m K)
$\overline{\Lambda}$	mean free path length	m
μ	chemical potential	J/mol
ν	kinematic viscosity	m^2/s
ν_{ij}	stoichiometric coefficient of species i in reaction j	–
ν	stoichiometry ratio	–

ξ	uncertainty	–
ϱ	density	kg/m^3
$\rho_{m,n}$	binary correlation coefficient	–
σ	standard deviation	a.u.
σ	shape factor	–
σ_S	entropy production	J/(K s)
σ_{SB}	Stefan-Boltzmann constant	W/(m^2 K^4)
τ^2	tortuosity factor	–
φ_i	fugacity coefficient of species i	–
φ	flattening coefficient	–
φ	parameterized variable	–
ϕ	electric potential	V
χ_p	shape-material parameter	(kg/m)$^{0.5}$
χ	geometry factor for effective thermal conductivity inside porous pellets (cf. Appendix A.3.2)	–
ω	weighting factor	–

Sub- and Superscript

$\sim$	dimensionless variable	
$\rightarrow$	vector for all species	
—	averaged value	
0	pure component	
0	root	
$\circ$	standard state	
ax	axial direction	
bed	packed bed/catalyst bed	
c	core of bed in stagnant packed-bed dispersion model (cf. Section A.5.1)	
calc	calculation	
cat	catalyst	
char	characteristic value	
cool	cooling/coolant	
crit	critical	
eff	effective value	
exp	experiment	
fl	fluid	
G	pressure dependence/Smoluchowski effect (Section A.5.1)	

h	parameter for heat transport
ideal	ideal fluid
in	inlet
lof	lack-of-fit
m	parameter for mass transport
max	maximum value
mod	modified
out	outlet
p	particle/pellet
pore	catalyst pore
para	parameter
pe	pure experimental
r	radial direction
rad	radiation
ref	reference value
reg	regression
rep	replicate
res	residual
resp	response
s	solid
species	species in mixture
surf	surface conditions
t	total
t	tube
trans	translational
visc	viscous

Abbreviations

∗	surface site
3H1	three hole cylinder
3H2	indented three hole cylinder
4H1	four hole cylinder
4H2	indented four hole cylinder
AcO*	surface acetate species
AcOH	acetic acid
BFM	binary friction model

CC	cylindrical catalyst
CYL	cylinder
DGM	dusty-gas model
DM	diffusion model
DAL	double alpha pellet shape [170]
FE	finite elements
IS	ideal sphere
MTPM	mean-transport pore model
OC	orthogonal collocation
OCFE	orthogonal collocation on finite elements
ODE	ordinary differential equation
ODH	oxidative dehydrogenation
ODHE	oxidative dehydrogenation of ethane
PBMR	packed-bed membrane reactor
PDE	partial differential equation
PF	plug flow
RHS	right-hand-side
RIF	ring filet
RIN	ring
RS	reaction system
SC	spherical catalyst
vWB	viscous Wilke-Bosanquet
WAW	wagon wheel
WB	Wilke-Bosanquet

List of Figures

List of Tables

List of Publications

Journal Publications

- P. J. Donaubauer, O. Hinrichsen, "A Monte-Carlo-Based Sensitivity Analysis of Multi-component Diffusion in Porous Catalysts", *Chem. Eng. Sci.* **2018**, *185*, 282–291, DOI `10.1016/j.ces.2018.03.048`.

- P. J. Donaubauer, O. Hinrichsen, "Evaluation of Effectiveness Factors for Multicomponent Diffusion Models inside 3D Catalyst Shapes", *Ind. Eng. Chem. Res.* **2019**, *58*, 110–119, DOI `10.1021/acs.iecr.8b04922`.

- P. J. Donaubauer, U. Cardella, L. Decker, H. Klein, "Kinetics and Heat Exchanger Design for Catalytic Ortho-Para Hydrogen Conversion during Liquefaction", *Chem. Eng. Technol.* **2019**, *42*, 669–679, DOI `10.1002/ceat.201800345`.

- P. J. Donaubauer, L. Schmalhorst, O. Hinrichsen, "2D Flow Fields in Fixed-Bed Reactor Design: a Robust Methodology for Continuum Models", *Chem. Eng. Sci.* **2019**, *208*, 115137, DOI `10.1016/j.ces.2019.07.055`.

- P. J. Donaubauer, D. Melzer, K. Wanninger, G. Mestl, M. Sanchez-Sanchez, J. A. Lercher, O. Hinrichsen, "Intrinsic Kinetic Model for Oxidative Dehydrogenation of Ethane over MoVTeNb Mixed Metal Oxides: a Mechanistic Approach", *Chem. Eng. J.* **2020**, *383*, 123195, DOI `10.1016/j.cej.2019.123195`.

Oral Presentations

- P. J. Donaubauer, O. Hinrichsen, "Multicomponent Diffusion in Porous Catalysts", Jahrestreffen Reaktionstechnik, Würzburg, DE, **2017**.

- P. J. Donaubauer, O. Hinrichsen, "Sensitivity Analysis for Multicomponent Diffusion Models in Porous Catalysts", 8th Asian-Pacific Chemical Reaction Engineering Symposium (APCRE), Shanghai, CN, **2017**.

- P. J. Donaubauer, L. Schmalhorst, O. Hinrichsen, "2D Continuum Models for Fixed-Bed Reactor Design: Impact of 2D Flow Field on Inlet Region Characteristics", XXIII International Conference on Chemical Reactors (CHEMREACTOR-23), Ghent, BE, **2018**.

Poster Presentations

- P. J. Donaubauer, O. Hinrichsen, "Multicomponent Diffusion in Porous Catalysts", Colloquium on Chemical Reaction Engineering at the First Symposium on Chemical Research in Flanders, Blankenberge, BE, **2016**.

- P. J. Donaubauer, M. Kutscherauer, O. Hinrichsen, "Oxidative Dehydrogenation of Ethane over Mixed Metal Oxides: a Kinetic Literature Survey", 8th World Congress on Oxidation Catalysis (WCOC), Cracow, PL, **2017**.

- P. J. Donaubauer, L. Schmalhorst, O. Hinrichsen, "2D Fixed-Bed Reactor Modeling Study on Oxidative Dehydrogenation of Ethane", Jahrestreffen Reaktionstechnik, Würzburg, DE, **2018**.

- P. J. Donaubauer, S. Steck, L. U. Hartley, O. Hinrichsen, "Modeling of 3D Catalyst Pellets using Multicomponent Diffusion Models", 25th International Symposium on Chemical Reaction Engineering (ISCRE 25), Florence, IT, **2018**.

- P. J. Donaubauer, D. Melzer, M. Sanchez-Sanchez, K. Wanninger, G. Mestl, J. A. Lercher, O. Hinrichsen, "Oxidative Dehydrogenation of Ethane over MoVTeNb Mixed Metal Oxides: Kinetic Investigation and Modeling", Jahrestreffen Deutscher Katalytiker, Weimar, DE, **2019**.

- P. J. Donaubauer, D. Melzer, M. Sanchez-Sanchez, K. Wanninger, G. Mestl, J. A. Lercher, O. Hinrichsen, "Oxidative Dehydrogenation of Ethane over MoVTeNb Mixed Metal Oxides: Kinetic Investigation and Modeling", EuropaCat, Aachen, DE, **2019**.